

University of Strathclyde
Faculty of Engineering
Department of Biomedical Engineering

Biocompatibility assessment of a sol-gel
modified electrospun ventricular shunt
catheter

Davide Erbogasto

A thesis presented in fulfillment for the requirements
of the degree of Doctor of Engineering

2020

This thesis is the result of the author's original research. It has been composed by the author and has not been previously submitted for examination which has led to the award of a degree.

The copyright of this thesis belongs to the author under the terms of the United Kingdom Copyright Acts as qualified by University of Strathclyde Regulation 3.50. Due acknowledgement must always be made of the use of any material contained in, or derived from, this thesis.

Signed *Daide Erbogato*

Date

ABSTRACT

Hydrocephalus is a clinical condition that usually originates from a reduced passage of cerebrospinal fluid from one brain ventricle to another. The main procedure to treat this condition involves the insertion of a shunt catheter to bypass the blockage and allow the CSF to flow from the ventricles, thus avoiding a possible build-up of intracranial pressure. Such catheters, which are commonly made from medical grade silicone, are known to be affected by mechanical failures, infection and blockage owing to cerebral tissue infiltration and bacterial colonisation.

To decrease cell adhesion and at the same time increase resistance to bacterial colonisation, medical grade polyurethane was modified with the addition of inorganic modifiers (titanium and zinc) via a sol-gel process.

Both titanium and zinc were successfully incorporated into the polyurethane in an amorphous form, having a strong impact on the microstructure of the fibres, as the presence of the inorganic phase affects the degree of segregation of hard and soft segments typical of polyurethanes, and changes the diameter size and distribution of the fibres, with modified materials exhibiting a narrower diameter distribution. Titanium is well dispersed within the fibres, while zinc tends to segregate on the surface. All electrospun materials are effective at absorbing fluid quickly.

The co-action of morphological factors and chemistry is effective in controlling cell adhesion and bacterial colonisation. Upon exposure to human immortalised astrocyte cultures, modified electrospun materials exhibit a significantly lower viability than the positive control, and a higher apoptotic rate than the negative control (PDMS). Preliminary results suggest that cell adhesion is lower for materials with smaller fibre diameters.

Furthermore, results from bacterial colonisation studies show that nanostructured surfaces are effective in controlling and reducing *Staphylococcus aureus* colonisation (1 log₁₀ unit reduction), as compared to the standard silicone.

ACKNOWLEDGMENTS

The work presented in this thesis would not have been possible without my supervisor, Dr Richard Black, who generously believed in me more than I believed in myself, encouraging, mentoring and giving me opportunities to travel, explore and meet people during my four years at Strathclyde. I have learned much and grown a lot, scientifically and personally, during that time.

I am grateful for a scholarship granted by the Engineering and Physical Sciences Research Council (EPSRC), which allowed me to pursue my research, and to Biomer Technology Ltd. for making polymers available for this research.

I am indebted to two colleagues who first introduced me to electrospinning and cell culture, Tom Harrison, Supraja Suresh and Milovan Cardona. Thank you Milovan for the uncountable hours spent discussing issues, fixing equipment, when you shared your knowledge and precious tips. Your kindness and generosity made a big difference in the lab.

I would like to thank those from the department who have supported me in various capacities. Research is not the result of a single mind, and I found many practical solutions and ideas, as and much inspiration (as well as company) through discussion with fellow students in the lab and in the office, both lecturers and researchers, masters students and admin staff (who created a thriving and positive environment).

I wish to thank Katie Henderson, Anne Goudie and Brian Cartlidge for their patient and enduring technical support: you saved the day more than once. I am grateful to Andrew Ward for dedicating his time and expertise to the work on the bacterial studies. The Advanced Materials Research Laboratory provided the equipment for the Thermal Analysis, and the CMAC National Facility provided the equipment for the FT-IR and Contact Angle Goniometer. Silvia Piccinini supported me during a particular difficult moment.

Thanks to my extended support network of my family, friends and others I met during my Glaswegian years, as well as my work colleagues and bosses at Incorez and KCI. Their non-judgemental, genuine interest meant a lot to me.

And finally Nick, thanks for encouraging me at critical moments and for patiently listening to me talking about things that are not quite your cup of tea, and for your gentle nudging, enduring support and love.

This thesis is dedicated to the memory of Margaret, who caringly and proudly assisted me throughout, and dad, a curious man who first sowed seeds of good hope.

TABLE OF CONTENTS

List of Figures	x
List of Tables	xv
1 HYDROCEPHALUS AND ITS DIAGNOSIS AND TREATMENT	1
1.1 Introduction	1
1.2 Hydrocephalus: overview	2
1.2.1 Clinical issue	2
1.2.2 Definition of hydrocephalus	3
1.2.3 Ventricle system	3
1.2.4 Cerebrospinal fluid production	4
1.2.5 Cerebrospinal fluid composition	7
1.2.6 Symptoms and morbidity of hydrocephalus	7
1.2.7 Types of hydrocephalus	8
1.2.8 Hydrocephalus causes	9
1.2.9 Diagnosis and investigation of hydrocephalus	10
1.2.10 Mortality	10
1.3 Shunt catheters: overview	12
1.3.1 Hydrocephalus treatments	12
1.3.2 Endoscopic third ventriculostomy	13
1.3.3 Shunt catheter	13
1.3.4 History and development of ventricular shunt catheterisation	15
1.4 Shunt failure	16
1.4.1 Investigation of shunt malfunction	17
1.4.2 Obstruction of the shunt catheter	17
1.4.3 Protein occlusion	18
1.4.4 Bacterial contamination	19
1.5 Modification of the traditional shunt catheter	22
1.5.1 Modifications with antibacterial applications	25
1.5.2 Drug delivery solutions	27
1.5.3 Catheter design	27

1.5.4	Alternative catheter design	29
1.6	Polyurethanes and their biomedical applications	32
1.6.1	Polyurethanes	32
1.6.2	Macrodiols	34
1.6.3	Diisocyanates	35
1.6.4	Chain extender	35
1.6.5	Chemical structure of polyurethanes	36
1.6.6	Physical properties of polyurethanes	38
1.6.7	Biomedical applications of polyurethanes	40
1.6.8	Degradation of polyurethanes for medical applications	40
1.6.9	Polyurethanes for antibacterial applications	42
1.6.10	Biomer Technology polyurethane	43
1.6.11	Thermal analysis of polyurethane	44
1.7	Electrospinning: overview	48
1.7.1	Electrostatic spinning	48
1.7.2	Electrospinning principles and process	48
1.7.3	Influence of parameters on electrospinning	51
1.7.4	Morphological considerations	55
1.7.5	Applications of electrospinning	57
1.8	Wettability	59
1.8.1	Hydrophilicity	59
1.9	Sol-gel route to inorganic polymers	60
1.9.1	Sol-gel and electrospinning	63
1.10	Research aims	67
1.11	Thesis outline	70
2	FABRICATION AND CHARACTERISATION OF MODIFIED ELECTROSPUN POLYURETHANE	71
2.1	Introduction	71
2.1.1	Materials selection	71
2.1.2	Electrospinning	72
2.1.3	Differential scanning calorimetry	73
2.1.4	Thermogravimetric analysis of polymers	73
2.2	Materials and methods	75
2.2.1	Polyurethane selection criteria	75
2.2.2	Cast films	75

2.2.3	Electrospinning of the reference sample (ES)	76
2.2.4	Electrospinning of modified materials	77
2.2.5	Scanning Electron Microscopy and Energy Dis- persion Spectroscopy	80
2.2.6	Fourier-transform Infrared spectroscopy	81
2.2.7	Thermal analysis	82
2.2.8	Statistical analysis	82
2.3	Results	83
2.3.1	Scanning Electron Microscopy	83
2.3.2	Energy Dispersion Spectroscopy	87
2.3.3	FT-IR	87
2.3.4	Differential Scanning Calorimetry	90
2.3.5	Thermogravimetric Analysis	93
2.3.6	Mass loss	95
2.4	Discussion	97
2.5	Conclusions	107
3	FUNCTIONAL PROPERTIES OF MODIFIED ELECTROSPUN SURFACES	109
3.1	Introduction	109
3.1.1	Contact Angle Goniometer	109
3.1.2	Atomic Force Microscopy	110
3.1.3	Force mapping	116
3.2	Materials and methods	119
3.2.1	Materials	119
3.2.2	Contact angle	119
3.2.3	Atomic Force Microscopy	120
3.2.4	Statistical analysis	121
3.3	Results	122
3.3.1	Contact angle	122
3.3.2	Atomic Force Microscopy	123
3.3.3	Phase retrace images	124
3.4	Discussion	134
3.5	Conclusions	139
4	BIOCOMPATIBILITY ASSESSMENT	140
4.1	Introduction	140

4.1.1	Cell apoptosis	140
4.1.2	Cell adhesion	141
4.1.3	Cell motility	143
4.2	Materials and methods	144
4.2.1	Viability and apoptosis assays	144
4.2.2	Cell type and culturing methods	145
4.2.3	Bacterial cultures	152
4.2.4	Statistical analysis	154
4.3	Results	156
4.3.1	Mammalian cell viability	156
4.3.2	Cell apoptosis	158
4.3.3	Live/dead and DAPI assays	162
4.3.4	Cell adhesion	162
4.3.5	Cell motility	166
4.3.6	Bacteria morphology and biofilm formation	168
4.3.7	Bacteria viability	171
4.4	Discussion	174
4.5	Conclusions	182
5	CONCLUSIONS	184
5.1	General conclusions	184
5.1.1	Successful modification of the surface of a bio-compatible polyurethane	184
5.1.2	Cell viability is lower on modified electrospun materials	186
5.1.3	Colonisation of <i>S. aureus</i> is lower on modified electrospun materials	188
5.2	Recommendations	188
5.3	Future work	190
	REFERENCES	192
A	APPENDIX	208
A.1	Time lapse images of cell populations	208
A.1.1	Methods	208
A.1.2	Results and discussion	209
A.2	Energy Dispersion Spectroscopy	211

A.3	FT-IR	212
A.4	Thermogravimetric analysis	213

LIST OF FIGURES

Figure 1.1	Anatomy of the ventricle system in the human brain.	4
Figure 1.2	Schematic of the CSF circulation in the ventricle system.	5
Figure 1.3	Schematic of a unidirectional valve as a part of a shunt catheter.	14
Figure 1.4	Schematic of the shunt catheter system.	15
Figure 1.5	Schematic of a ventricular (proximal) catheter, with the details of holes.	28
Figure 1.6	Schematic of Rivulet, a ventricular (proximal) catheter by Medtronic.	29
Figure 1.7	Mechanism of action of ReFlow, a ventricular (proximal) catheter by Anuncia.	30
Figure 1.8	Schematic of the basic structures of polyurethane and nylon	33
Figure 1.9	Structure of polyethylene oxide (PEO) and poly-(tetramethylene oxide) (PTMO), both polyethers.	34
Figure 1.10	Structure of 4,4-diphenylmethane diisocyanate (MDI).	35
Figure 1.11	Structure of 1,2-butanediol.	36
Figure 1.12	Schematic of polyurethanes as a “composite” made by hard segments immersed in a soft “matrix”.	37
Figure 1.13	Schematic of hydrogen bonds between adjacent polyurethane chains and the formation of hard and soft segments.	37
Figure 1.14	Schematic model for the morphological changes that occur during DSC scans of polyurethane elastomers.	46
Figure 1.15	Thermogravimetric curve for a polyurethane.	47
Figure 1.16	Electrospinning apparatus and process.	49

Figure 1.17	Taylor cone.	51
Figure 1.18	Effect of applied potential (V) on charged solution drops (V_c)	51
Figure 1.19	Scanning electron micrograph of splining and branching on a polyurethane sample.	56
Figure 1.20	Schematic of the sessile contact angle.	60
Figure 1.21	Schematic of the sol-gel process.	62
Figure 1.22	Chemical structures of Ti and Zn organic precursors.	64
Figure 2.1	SEM images of ES, Ti2, Ti3, Ti7, Zn3, Zn5, Zn10, at x1000, x5000 and x10000 magnification respectively.	84
Figure 2.2	An example of gaussian interpolation of distribution histograms of the diameters of the following samples: a) ES, b) Ti2 and c) Zn3.	85
Figure 2.3	Average diameter of the first peak plotted against the molar concentration of modifier precursor for each of the two sets of materials, Ti and Zn.	86
Figure 2.4	Selected Energy Dispersion Spectrogram for titanium and zinc-modified electrospun mats, representing Ti2 and Zn3.	87
Figure 2.5	a) Absorbance ATR-IR spectra of cast, ES, Ti2 and Zn3 modified samples taken in the 4000 cm^{-1} to 400 cm^{-1} region. Inserts b) show details for N-H and C=O vibrational modes. Additional spectrograms pertaining to the remaining samples are to be found in Appendix A.3.	89
Figure 2.6	Thermograms (DSC) of modified samples plotted against the unmodified sample, ES.	91
Figure 2.7	DTG curves for electrospun materials modified a) with Ti, b) with Zn, against the unmodified samples ES.	94
Figure 2.8	Illustration of how the positive charged needle (b) can attract the negatively charged polymers to the surface during the electrospinning process (a).	107

Figure 3.1	Tip-surface interaction graphs.	111
Figure 3.2	Cantilever Olympus AC160TS used in the present work.	112
Figure 3.3	Basic diagram of an AFM.	112
Figure 3.4	Development of contact angle over time on ES polyurethane, Ti2 and Zn3 modified surfaces.	122
Figure 3.5	Contact angle measurements and SD ($n = 5$) for cast and ES polyurethane, Ti2 and Zn3 (modified electrospun).	123
Figure 3.6	AFM scans of cast Z6A1 at lower and higher resolution, on both glass and air-exposed side, and an example of the height profile of the glass side.	125
Figure 3.7	10x10 μm AFM scans of electrospun materials, height profile on the left and phase retrace on the right.	126
Figure 3.8	20x20 μm AFM scans of Z6A1 electrospun.	127
Figure 3.9	5x5 μm AFM scans of electrospun materials, height profile on the left and phase retrace on the right.	128
Figure 3.10	Example of height profile of selected pores (marked) on Ti2 scan.	129
Figure 3.11	Profile of selected single fibres on Ti2 and Zn3.	130
Figure 3.12	Adhesion force mapping scans (on the right) along with a low-resolution AFM height scan produced by the software together with the force map (on the left).	132
Figure 3.13	Adhesion force values and SD ($n = 3$) for cast and ES polyurethane, Ti2 and Zn3 (modified electrospun).	133
Figure 4.1	Example of calibration curve for AlamarBlue assay.	147
Figure 4.2	Schematic of the centrifuge setting.	149

Figure 4.3	Quantification of viability in U373 cells grown on cast PU, untreated ES PU, positive control (tissue culture plastic, TCP) and negative control (PDMS) evaluated after 48, 96 and 216 h in culture.	157
Figure 4.4	Quantification of apoptotic rates in U373 cells, evaluated after 48, 96 and 216 h in culture.	159
Figure 4.5	Brightfield images of U373 cells grown on a) tissue culture plastic, b) PDMS and c) cast polyurethane for 9 days (final time point) and stained with apoptosis assay.	160
Figure 4.6	Ratio of apoptotic cells versus viable cells on each substrate at each time point.	161
Figure 4.7	Fluorescence images of U373 astrocytes taken after 48, 96 and 216 h in culture on cast polyurethane, PDMS, TCP and tape samples. Nuclei of fixed cells are stained blue with DAPI.	163
Figure 4.8	Fluorescence images of U373 astrocytes taken after 48, 96 and 216 h in culture on cast polyurethane, PDMS, TCP and tape samples. Live cells are stained green (Calcein-AM) and dead cells are stained red (ethidium homodimer-1).	164
Figure 4.9	Orthogonal detachment force, as obtained via a centrifugation assay, expressed in relative centrifuge force (RCF).	165
Figure 4.10	Average detachment force plotted against the feature size for all substrates.	167
Figure 4.11	Brightfield image of U373 cells after 60 minutes incubation at 37 °C, 20x magnification.	168
Figure 4.12	U373 cells cultivated on ES, PDMS and Ti2 and recorded under a time-lapse microscope every 60 seconds at a 40x magnification for at least 3 hours.	169
Figure 4.13	Single cell moving on Zn3 fibres electrospun on a glass microscope slides.	170

Figure 4.14	Scanning electron micrographs of bacterial cultures on different materials, gold-coated, after 24 hr.	171
Figure 4.15	Comparison of the Colony Forming Units, on TCP (positive control), electrospun PU (ES), Ti and Zn-doped electrospun PU, cast PU and PDMS, with and without exposure to UV light.	172
Figure 4.16	Plot of <i>S. aureus</i> colony forming units (expressed in log units of CFU/mL) against morphological surface feature size for non-flat surfaces (cast, ES, Ti ₂ and Zn ₃).	173
Figure A.1	Paths of cells moving on TCP (a), PDMS (b), cast polyurethane (c), ES (d), Ti ₂ (e) and Zn ₃ (f), as tracked with Fiji/Manual Tracking software on videos of multiple cells, magnification x10, sampling frequency=15 minutes over 20 hours.	210
Figure A.2	Energy Dispersion Spectrogram for titanium and zinc-modified electrospun mats, representing Ti ₂ and Zn ₃ . a) Ti ₂ , b) Ti ₃ , c) Ti ₇ , d) Zn ₃ , e) Zn ₅ , f) Zn ₁₀ . The elemental peaks for Ti and Zn, respectively, are indicated.	211
Figure A.3	Additional Absorbance ATR-IR spectrograms of Ti ₂ and Zn ₃ modified samples taken in the 4000 cm ⁻¹ to 400 cm ⁻¹ region.	212
Figure A.4	TGA thermograms for electrospun materials modified a) with Ti, b) with Zn, against the unmodified samples ES.	213

LIST OF TABLES

Table 1.1	Electrophoretic separation of spinal fluid proteins.	7
Table 1.2	Diagnosis tools for hydrocephalus.	11
Table 1.3	Factors influencing microbial attachment to artificial surfaces.	20
Table 1.4	Properties of Biomer Technology b ₉ polyurethanes, series 'A'.	44
Table 1.5	Wettability of a surface.	61
Table 2.1	Electrospinning parameters for the production of each sample.	79
Table 2.2	Mass and molar quantities of metal precursors for each sample.	80
Table 2.3	Average fibre diameter for Ti and Zn-modified electrospun materials, and unmodified electrospun polyurethane.	86
Table 2.4	FT-IR peak positions for N–H and C=O groups of cast, ES and Ti and Zn-modified samples.	88
Table 2.5	Temperature points for peak II and peak III and, in brackets, melting enthalpy for reported samples, as determined from DSC curves.	92
Table 2.6	Temperature for each mass loss stage for cast, electrospun and modified materials, as determined from peaks in the TGA graphs.	93
Table 2.7	Mass percentage of char in the pan as determined by TGA curves.	95
Table 4.1	Antibacterial efficiency (ABE%).	173
Table 5.1	Comparison between selected materials for shunt catheters: PDMS, ES medical grade polyurethane, electrospun polyurethane modified with Ti and Zn.	189

ACRONYMS

AB	AlamarBlue Assay
AB%	AlamarBlue Percent Reduction
AFM	Atomic Force Microscopy
CSF	Cerebrospinal Fluid
CFU	Colony Forming Unit
DMEM	Dulbecco Modified Eagle's Medium
DMF	N,N-Dimethylformamide
DSC	Differential Scanning Calorimetry
DTC	Derivative Thermogravimetry
ES	Electrospun Scaffold
FT-IR	Fourier Transform Infra-red Spectroscopy
HS	Hard Segment
ICP	Intracranial Pressure
LB	Lysogeny Broth
MRSA	Methicillin-Resistant <i>Staphylococcus aureus</i>
NPH	Normal Pressure Hydrocephalus
PBS	Phosphate-Buffered Saline
PDMS	Poly(dimethylsiloxane)
PEG	Poly(ethyleneglycol)
PEO	Poly(ethyleneoxide)
PU	Polyurethane

SEM	Scanning Electron Microscopy
SS	Soft Segment
TCP	Tissue Culture Plastic
TGA	Thermogravimetric Analysis
Ti	Titanium
UV	Ultraviolet Light or Radiation
Z6A1	Polyurethane of the A1 range, series b9 TM , provided by Biomer Technology Ltd.
Zn	Zinc

SAMPLE DESCRIPTORS

Cast	Unmodified cast Z6A1
ES	Unmodified electrospun Z6A1
Ti2	Titanium-modified electrospun Z6A1, 1:2 w/w (PU:Ti precursor)
Ti3	Titanium-modified electrospun Z6A1, 1:3 w/w (PU:Ti precursor)
Ti7	Titanium-modified electrospun Z6A1, 1:7 w/w (PU:Ti precursor)
Zn3	Zinc-modified electrospun Z6A1, 1:3 w/w (PU:Zn precursor)
Zn5	Zinc-modified electrospun Z6A1, 1:5 w/w (PU:Zn precursor)
Zn10	Zinc-modified electrospun Z6A1, 1:10 w/w (PU:Zn precursor)

HYDROCEPHALUS AND ITS DIAGNOSIS AND TREATMENT

1.1 INTRODUCTION

Hydrocephalus is a rare cerebrospinal condition which affects around 2 people in 1000, and can be described as an abnormal absorption of the cerebrospinal fluid (CSF). CSF is generated in the brain ventricles and is normally reabsorbed by the cerebral tissues. If the fluid is not re-absorbed, it accumulates, creating a rise in the internal cerebral pressure, resulting in damage to the brain tissue and permanent impairment to the patient [1].

While there is no effective pharmaceutical cure for hydrocephalus, the current (and preferred) treatment option involves surgically inserting of a flexible catheter through the skull of the patient into the third ventricle. The catheter, through a passive valve, drains the excess fluid from the brain into one of the heart chambers or into the abdominal cavity. The shunt catheter in its current form was first introduced in 1957. The proximal and distal catheters are generally made of medical grade silicone, which is biocompatible, non toxic and flexible [2].

The shunt catheter, however, suffers from a high failure rate. Device failure can occur at different stages. Whereas the valve can malfunction and cause overdrainage or become blocked, the catheter fails mainly because of infection and obstruction. Infection occurs principally in the first few months after insertion, and is usually caused by bacteria from the skin of the patient or the surgeon that are transferred to the implant. Blockage can be caused by growth of healthy or inflammatory cells or tissue around the catheter. The catheter can fail mechanically as well, as the material degrades over time. As PDMS degrades, its surface roughness increases favouring cell adhesion and bacteria ingrowth, which can lead to mechanical malfunction and failure, such as occlusion of one or more fenestrations, or downstream

on the components of the valve, calcification, overdrainage or underdrainage [3]. The design of the catheter has been scrutinised as well, with the number and position of holes being criticised [4].

In case of a malfunctioning or infected catheter, the device needs to be revised. The average lifespan of a catheter does not exceed 10 years, which requires patients to undergo several operations in their lifetime.

While most of research is focused on improving valve performance, innovations to the proximal and distal catheters have not been able to improve its lifespan significantly. Given its high rate of failure, a review of materials and possibly a general redesign of the medical device is long overdue.

The present thesis proposes a new design for the proximal catheter, namely an electrospun ventricular catheter as opposed to a fenestrated one, which was first proposed in the article by Suresh & Black [5]. In order to make the antimicrobial properties of such microfibrinous catheter more effective, justified by the fact it exhibits a larger surface area to volume ratio, the base material (medical grade polyurethane) was subjected to modifications with titanium and zinc.

1.2 HYDROCEPHALUS: OVERVIEW

Hydrocephalus is a medical condition that is generally associated with a build-up of cerebrospinal fluid in the ventricles, an increase in intracranial pressure and neuronal development issues. Hydrocephalus can be congenital (and often associated to other malformations) or acquired, and must be treated urgently to avoid permanent damages to the brain tissue.

1.2.1 *Clinical issue*

Hydrocephalus is a medical condition caused by a build-up of cerebrospinal fluid (CSF) within the ventricles in the brain. Such accumulation damages the tissues of the brain, can be debilitating and, if left untreated, fatal. Historically and etymologically, hydrocephalus

is linked with “water on the brain”, because CSF has the appearance of a clear liquid.

Hydrocephalus affects around 0.5-2.5 in 1000 people (and as many as 6 in 1000 in 2003 in USA) [3]. It is commonly regarded as a disorder affecting mainly infants and children, but adolescents and adults are also affected (especially when normal pressure hydrocephalus, NPH, is considered, see Section 1.2.7).

1.2.2 *Definition of hydrocephalus*

Hydrocephalus is defined as a debilitating neurological disorder involving an active and abnormal distension and enlargement of the ventricular system of the brain resulting from inadequate passage of cerebro-spinal fluid (CSF) from its point of production within the cerebral ventricles to its point of absorption into systemic circulation.

This updated definition, reported in the work by ReKate [6], identifies hydrocephalus as an active condition, and recognises an underlying cause common to all the different types of hydrocephalus, namely a mismatch between the volumes of CSF that are produced and re-absorbed within the nervous system, and therefore it excludes other issues such as enema and hydrocephalus *ex vacuo*. Furthermore, according to this definition, hydrocephalus requires ventriculomegaly, or extension of the ventricles, while an abnormal intracranial pressure (ICP) is not required as one of the symptoms, which would not include NPH.

1.2.3 *Ventricle system*

The ventricles are a system of four interconnecting chambers or cavities at the base of the brain (Fig. 1.1). The first two ventricles (*lateral*) develop parallel to each other, and are located in their respective hemisphere. The lateral ventricles present projections, called horns, into the frontal, occipital and temporal areas. The two lateral ventricles are then connected to the third one by the *foramen of Monro*. The third ventricle is situated between the right and left thalamus, and is further connected to the fourth by the *cerebral aqueduct*. This fourth

ventricle is connected to the central spinal canal and to the subarachnoid cistern [7].

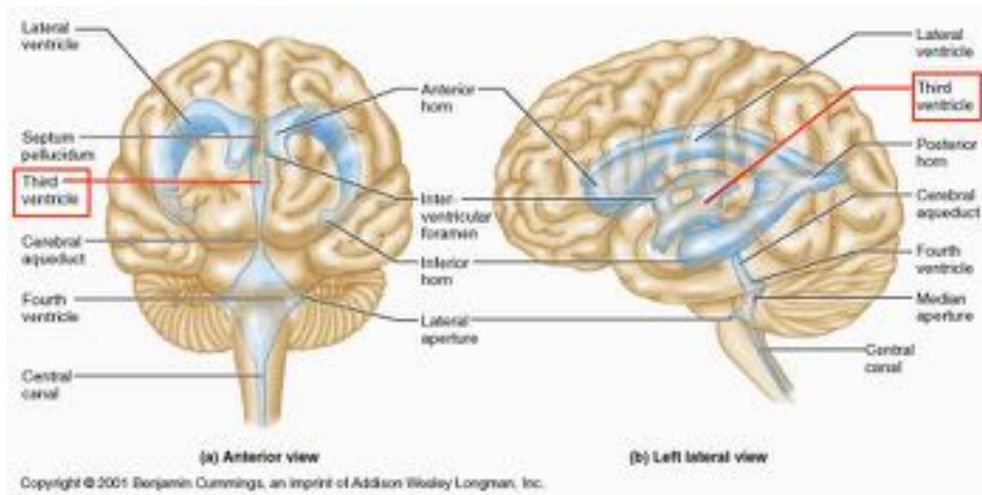


Figure 1.1: Anatomy of the ventricle system in the human brain [8].

1.2.4 Cerebrospinal fluid production

Cerebrospinal fluid (CSF) is a clear fluid with the same composition as plasma (although 50 times more diluted). It circulates around the brain and the spinal cord, with functions of damping, protection, chemical buffering, acting as a diffusion medium for nutrients, gases and chemical messengers, waste removal and buoyancy (sustaining the brain weight) [9].

CSF is produced by *cuboidal ependymal cells*, which are ciliated cells during embryonic development and early childhood, but lose their cilia during development, except for some small areas where they persist in order to help circulate the CSF. Some ependymal cells, concentrated in a spot on the internal layer of each ventricle, have a specialised function. Altogether, they form what is called the *choroid plexus*. The plexus originates from the roof of the third ventricle and then folds out into the two lateral ventricles. A choroid plexus is present on the roof of the fourth ventricle as well, between the pons and the cerebellum. The choroid plexus secretes sodium inside the ventricle space, thus increasing the internal osmotic pressure and causing water to enter from the blood vessel through osmotic ex-

change. Ependymal cells on the choroid plexus are connected by tight junctions and surround capillaries deriving from the pia mater [10].

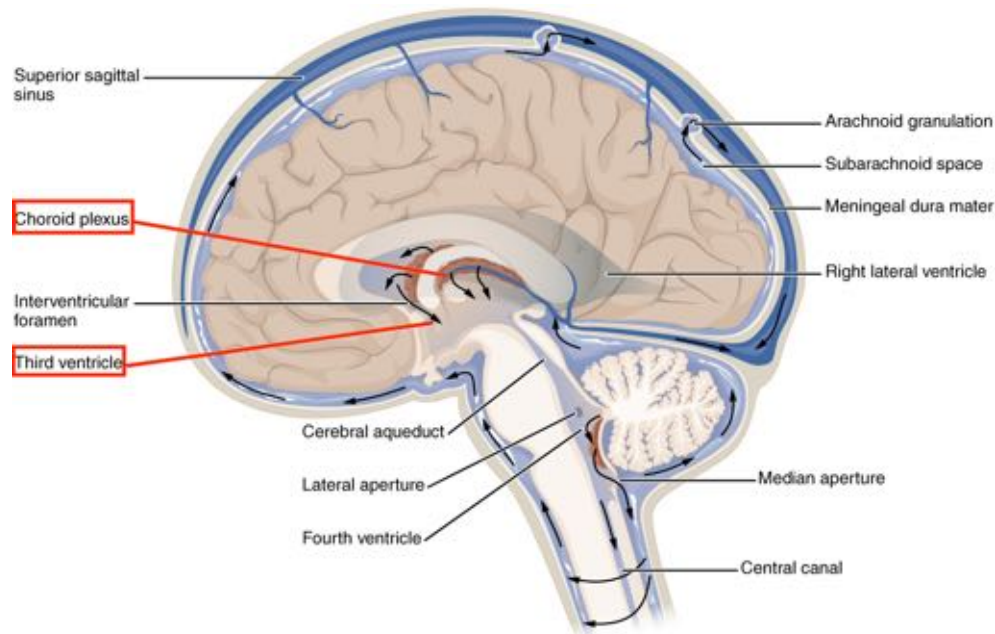


Figure 1.2: Schematic of the CSF circulation in the ventricle system. CSF is produced by the choroid plexus, and moves along the four ventricles, into the spinal canal and finally into the subarachnoid system, where it is reabsorbed by the tissues [11].

The normal route of CSF from production to clearance is as follows (see Fig. 1.2): produced by the choroid plexus, the CSF flows to fill the lateral ventricles, then flows through the interventricular foramen of Monro, the third ventricle, the cerebral aqueduct of Sylvius, the fourth ventricle, the two lateral foramina of Luschka and one medial foramen of Magendie, the subarachnoid space, the arachnoid granulations, the dural sinus, and finally the CSF is naturally reabsorbed into the venous drainage bathing the spinal cord and the brain. It is then absorbed by the lymphatic system at the level of the arachnoid granulations, which are large fingerlike extensions (villi) of the arachnoid membrane, between the arachnoid mater and pia mater.

1.2.4.1 Cerebrospinal fluid volume and Intracranial Pressure

In adults, about 500 mL of CSF is secreted per day by the ependymal cells of the choroid plexus, an amount that equates to 20 mL/h, or 0.35 mL/min. The capacity of normal lateral and third ventricles is

approximately 20 mL, whereas the total CSF volume in an adult is 120-150 mL. Hence, in normal circumstances CSF is recycled over three times each day [12].

CSF flow is not steady, but proceeds with a pulsation rate of 280 pulses/min [13, 14]. The pulsatile flows is generated by a combination of the transient change in volume of blood vessels in the closed craniospinal spaces, with a superimposition of the respiratory cycle, abdominal pressure, jugular venous pressure, physical activity and posture [15, 16]. While in the rest of the body the arterial pulsation is dissipated by the tissues compliance, the brain cannot dissipate it as it is enclosed in a rigid compartment, the skull, therefore the pulsation is dissipated by an overall intracranial compliance, to which four elements contribute: brain tissue compliance, arterial compliance, venous compliance and spinal thecal compliance through the cerebrospinal fluid vessels [17].

Intracranial pressure (ICP) rises if production of CSF exceeds absorption, but CSF production will fall as ICP rises to high levels, and compensation (stabilisation of hydrocephalus to a new ICP level) may occur through transventricular absorption of CSF. Dural absorption may also be important through nerve root sleeves and unrepaired meningocoeles. Of vital significance is the fact that compensated hydrocephalus (for example, in patients with a longstanding non-functional shunt) is not necessarily permanent because of the sometimes precarious nature of the balance between production and absorption of CSF. Clinicians involved in the care of patients with so-called stable hydrocephalus should always be alert to the possibility of insidious subclinical progression or late decompensation of this condition, which may occur spontaneously or after a minor head injury.

Normal ICP values are between 10 and 15 mmHg for adults and 3 and 4 mmHg in infants [15]. ICP over 15 mmHg at frequent intervals overnight or while resting is considered to be abnormal [18].

1.2.5 Cerebrospinal fluid composition

CSF presents the same composition as plasma, with the difference that it is around 500 times less concentrated. Unlike plasma, however, CSF is excreted by the choroid plexus by increasing the concentration of sodium ions in the ventricle space, therefore CSF has a higher concentration of sodium (and its counter-ion chloride) than plasma, but a lower concentration of potassium, calcium, glucose and proteins. The main protein is albumin, and then, in a decreasing order of prevalence, gamma-globulin, transferrin, haptoglobulin and tau-proteins [19]. Physiological protein concentration is between 20.8 and 240 mg/dL [13].

Table 1.1: Electrophoretic separation of spinal fluid proteins (% range of total protein concentrations) [20, 21].

Protein	%
Prealbumin	2-7
Albumin	56-76
α 1 globulin	2-7
α 2 globulin	3.5-12
β globulin	8-18
γ globulin	7-12

Protein levels vary according to the patient age, being lower at a younger age and increasing thereafter. Protein levels vary along the CSF pathway as well: the concentration is lower inside the ventricles, and increases while passing from the cisterna magna to the lumbar thecal sac.

1.2.6 Symptoms and morbidity of hydrocephalus

The accumulation of CSF causes a build-up of internal cranial pressure (ICP) in the ventricular cavities, leading to the dilation of the ventricles, which in turn can press onto and damage the brain tissue. In infants and toddlers, the bones of the skull are not yet fused, and they may dilate and bulge under the internal pressure (macrocephaly), making hydrocephalus obvious.

Other symptoms include vomiting, lethargy, headache, failing and blurred vision, drowsiness, fatigue and convulsions, poor feeding, irritability and listlessness, constant downward gaze of the eyes, and occasional seizures [18].

In many cases, because of cognitive impairments, the lives of patients can be affected to various degrees, as well as their work life achievements.

1.2.7 *Types of hydrocephalus*

Hydrocephalus can be classified into three categories:

1. High pressure hydrocephalus: it can be either congenital or acquired.
 - a) Non-communicating (obstructive) hydrocephalus: it occurs when cerebrospinal fluid flow is blocked within the ventricular system. Obstruction can happen at the following sites: foramen of Monro (the connection between the two lateral ventricles and the third), aqueduct of Sylvius, outlets of the fourth ventricle, basal cisterns or arachnoid granulations [6].
 - b) Communicating (non-obstructive) hydrocephalus: it occurs where there is inadequate cerebrospinal fluid absorption and a full communication between the ventricles and the sub-arachnoid space fails, therefore making it difficult for reabsorption to occur at all or in part. It may happen because of inflammatory processes such as meningitis, or else haemorrhage, which damage the subarachnoid granulation, where the majority or reabsorption occurs. Another instance arises when CSF is overproduced and the rate of reabsorption is lower than the production rate.
2. Normal pressure Hydrocephalus (NPH): an increase in the amount of cerebrospinal fluid in the brain's ventricles with little or no increase in the pressure inside the head; most often seen in adults over age 60. It may be owed to other diseases, for example heart

conditions, that affect the flow of blood in the brain. It is accompanied by dementia, mobility issues and incontinence, but they appear over an amount of time and they can be confused with other common conditions, for example Alzheimer. Patients with NPH do not show a raise in intercranial pressure, because of gradual build up of the CSF and pressure, which occurs over months or years.

1.2.8 *Hydrocephalus causes*

Hydrocephalus has a complicated aetiology.

Hydrocephalus is often congenital and it arises from malformations of the ventricles, especially involving the ducts that connect the ventricles [22]. Only rarely it occurs for genetic reasons.

Possible causes are infections of the mother during pregnancy, such as rubella (German measles) or mumps, or connected to other cerebrospinal conditions such as spina bifida.

Hydrocephalus can be originated by an aneurysm of the vein of Galen, or benign intracranial cysts, by craniofacial anomalies, or brain tumours. Usually children affected by tumors tend not to receive a pre-operation shunting, as the removal of the tumor should be effective in opening the CSF pathway.

Chiari malformation occurs when two protrusions from the cerebellum, called cerebellar tonsils, push into the foramen of Magendie, blocking the effective flow between ventricles and spine. Some forms of the Chiari malformation are accompanied by spina bifida.

Among the causes of hydrocephalus are cysts, which are pockets of tissue filled with fluid, that can be located inside the brain or even inside the ventricles. Another cause is the Dandy-Walker malformation, which is a cyst of the posterior fossa, next to the cerebellum. An enlarged fourth ventricle is usually accompanied to the Dandy-Walker cyst [1].

Adult or acquired hydrocephalus can origin from injuries to the skull, traumas, tumor or cysts, inflammations such as meningitis, granulomatous, or stroke.

1.2.9 *Diagnosis and investigation of hydrocephalus*

There are several tests that can help in diagnosing hydrocephalus, and they have been briefly summarised in Table 1.2. These same diagnostic tools can also help evaluate the shunt in case of malfunction or infection.

Clinical features of hydrocephalus are extremely variable in onset and timing, due to the difference in the physiology of the brain at different ages. While a colloid cyst in young adults causing the third ventricle become blocked leads to a sudden increase in ICP and sudden death, NPH is difficult to spot as a softer, more compliant brain on old age leads to a delay in the occurrence of brain damages, usually as a slowing of gait or dementia. Head injuries or subarachnoid haemorrhage usually lead to a slow presentation of symptoms as well. Acute hydrocephalus occurs over days, subacute over weeks, and chronic over months and years [18].

1.2.10 *Mortality*

As outlined by Vinchon *et al.* [24], it is important to determine when the death of the patient is related to hydrocephalus and not, instead, to a number of pathologies associated with hydrocephalus, for example brain tumors, unrelated events, or related conditions, for example infection in an already debilitated patient. When death occurs after surgery or because of a failed shunt systems, the relation is sure. Some deaths cannot be ascribed to a single cause or remain unexplained. The authors therefore propose to consider these deaths in shunted-patients as shunt-related by default.

In any case, if untreated, hydrocephalus degenerates and cause the decease of the patient. One common route is respiratory arrest due to tonsillar herniation and compression of the brain stem.

Table 1.2: Diagnosis tools for hydrocephalus [23].

Computed Tomography	Computed Tomography (CT) is required to determine the overall size of the ventricles, and check for the presence of periventricular oedema (also-called lucency). A CT scan is required for the size of the fourth ventricle, which gives an insight into the nature of the hydrocephalus, communicating (and a ventriculostomy might be chosen over a shunt) or non-communicating. One of the concerns linked with CT are the ionising radiations. As patients need long-term, continuous monitoring of the shunt, an accumulation can be harmful to the developing brain and can be associated with an increased occurrence of cancer.
Neuroimaging	Magnetic Resonance Imaging (MRI) and Diffusion Tensor Imaging can detect a Chiari malformation or tumors, which sometimes are not visible on CT.
Intracranial pressure monitoring	These techniques are used for patients with mild symptoms and NHP. ICP monitoring can reveal an abnormal pressure. Lumbar CSF infusion measures CSF outflow resistance. A continuous flow of saline solution is infused via a lumbar puncture needle, while the rise in the ICP is recorded.
Transcranial Doppler	Middle cerebral artery flow velocity and pulsatile index. It is not always reliable but it is non-invasive.
Tympanic membrane displacement	Communication of pressure waves between the intracranial space to the middle ear. It is not always reliable and indirect but non-invasive.
CSF sample	Used to determine cell count, protein concentration, ongoing infection.
Psychometric analysis	Hand-eye coordination and visual-spatial problems.

1.3 SHUNT CATHETERS: OVERVIEW

Generally, hydrocephalus is treated surgically by inserting a shunt catheter that drains the excess cerebrospinal fluid into a heart chamber or the patient's abdomen. A shunt catheter is comprised of three parts: a proximal catheter, with a number of holes distributed in proximity of the tip, a passive valve, and a distal catheter. The rate of failure for shunt catheters is quite high, and it is owed to a number of causes, including high bacterial colonisation rates, blockage from healthy or inflamed tissue, valve under- or overdrainage, or mechanical failure.

1.3.1 *Hydrocephalus treatments*

If untreated, hydrocephalus can cause severe damage to the brain tissue and can even be fatal, but if it is treated timely, the patients usually recovers completely and they can lead a normal life, albeit hydrocephalus is often accompanied by cognitive issues and vision problems, which do not always disappear after the treatment.

To date, there is no effective long-term medical treatment for hydrocephalus. While the use of some drugs have been tried, such as carbonic anhydrase inhibitors (e.g., acetazolamide) and loop diuretics (e.g., furosemide), their use is discouraged and they must be considered only as a temporary, acute measure in order to delay the surgical intervention [25].

Usually, the most common treatment for hydrocephalus is the surgical insertion of a shunt catheter to drain the excess fluid from the brain to another area of the body, where it will be reabsorbed by the tissues into the circulatory system. 75% of all cases of hydrocephalus, and up to 50% of children with communicating hydrocephalus, is treated with shunt catheter.

Given the high rate of malfunctions of the shunt catheter, an alternative way to treat hydrocephalus is a surgical procedure called Endoscopic Third Ventriculostomy (ETV), which allows fluid to pass through the wall of the ventricle. With recent improved surgical techniques, ETV is regarded as a viable alternative in specific cases, and

is briefly discussed in the following paragraph, while the rest of this section will be devoted to the shunt catheter.

1.3.2 *Endoscopic third ventriculostomy*

Given the high incidence of failure for the shunt catheter, an alternative endoscopic treatment, the third ventriculostomy, has seen some resurgence in recent years. Third ventriculostomy consists of making a hole on the floor of the skull, in correspondence of the third ventricle, in order to create a direct communication between the third ventricle and the subarachnoid space, to allow the extra fluid to escape the brain. The surgical procedure starts with a burr-hole in the frontal region, followed by cannulation and introduction of an endoscope [26].

Given the availability of smaller endoscopes, better optics and brighter lights, nowadays neurosurgeons feel more confident to follow this procedure in all safety of the patient, and the number of procedures is increasing steadily [18]. A more detailed analysis of this technique is beyond the scope of this thesis, though.

1.3.3 *Shunt catheter*

A schematic of the structure of the shunt is shown in Figure 1.4.

A shunt comprises three parts, depicted in Figure 1.3:

- a ventricular (proximal) catheter which drains the fluid from the ventricle cavities;
- a unidirectional valve; and
- a distal catheter which ends either in the abdominal cavity, in the peritoneal cavity (ventriculo-peritoneal, VP) or in the jugular vein on a heart chamber (ventriculo-atrial, VA), where the excess fluid is then reabsorbed and recycled by the body [3]. VP is preferred over VA since it reduces risks of life-threatening complications such as pulmonary emboli or shunt nephritis [18].

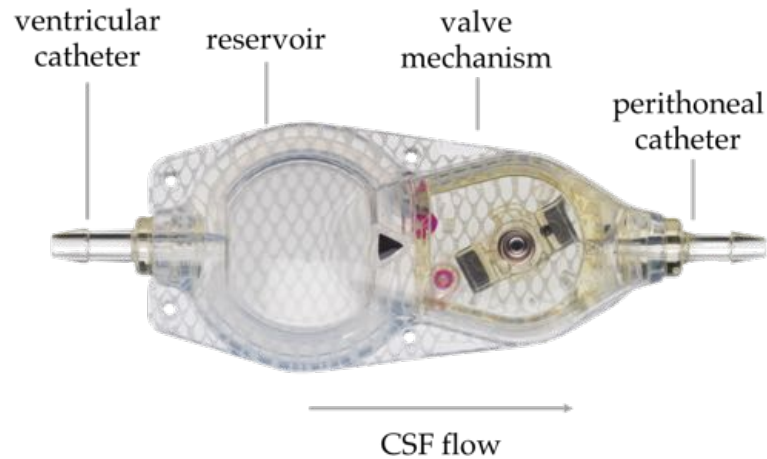


Figure 1.3: Schematic of a unidirectional valve as a part of a shunt catheter. The direction of the CSF flow is highlighted (Codman Certas Plus Programmable Valve, product 828800, adapted from Codman catalogue available at [27]).

The valve is placed halfway between the two ends and connects the catheters and controls the flow once the ICP rises. The valve includes a reservoir, but sometimes a reservoir is separate and is housed along the catheter. The reservoir is useful to the surgeon to take samples of CSF from the patient, as it can be accessed with a needle. The flow can be not constant, following changes in posture of the patient.

A variety of designs are available on the market, but typically, on one end of the proximal catheter 32 holes of 500 μm diameter are punched, grouped into four rows. The proximal catheter passes from a cerebral ventricle, normally the frontal horn of the lateral ventricle, through hemispheric parenchyma and meninges, and eventually exits from the cranial cavity via a hole to finally connect to one port in the valve. All three parts usually carry radiopaque marks to be detected through radiography [28].

The shunt catheter is surgically introduced into the patient from two points: frontal or parieto-occipital. The site is chosen each time according to the surgeon's preference. Many papers report different opinions as to which site is optimal. Nakahara *et al.* [30] recommends the parieto-occipital choice as it should reduce the shortening of the catheter and therefore grant a long-term function.

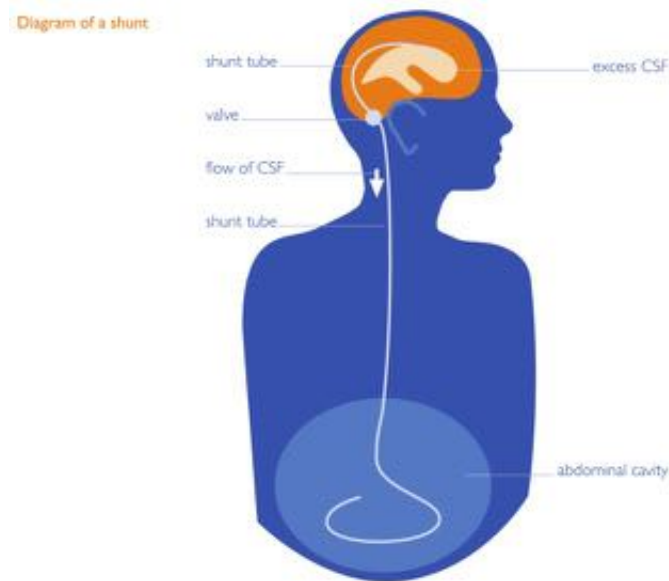


Figure 1.4: Schematic of the shunt catheter system [29].

1.3.4 History and development of ventricular shunt catheterisation

The history of the shunt catheter procedure dates from 1881, when Carl Wernicke performed the first sterile ventricular puncture and external ventricular drain, after which various catheter-like devices, such as horsehair, silk, and catgut wicks, became popular. Given the risks that an open drainage would pose, early 20th century saw the attempt to use internal drainage devices. For example, Jan Mikulicz-Radecki successfully inserted a nail made of glass wool into the ventricles of a child in order to re-route CSF to the subdural space in 1893. This led to 1903, when Nicholas Senn inserted a perforated rubber tube. Most of these procedures were unsuccessful, and patients died because of infections and blockage of the device. Other forms of devices included gold and glass tubes, silver tubes, and even omentum (peritoneal tissue), linen and transplanted human calf vessel. Arne Torkildsen introduced a rubber catheter to divert the CSF from the lateral ventricle to the cisterna magna in 1939 [2].

Finally, in 1951 Nulsen and Spitz published a paper reporting the first successful procedure of treating hydrocephalus by means of a ventriculojugular shunt, introducing both a one-way flow regulating device (the invention of a machinist who created a one-way valve to

help doctors save his child's life, who had spina bifida) and the use of soft rubber. In the meanwhile, alongside with rubber, other materials were being experimented, such as polyethylene and finally PDMS, with the introduction of a shunt made of silicone in 1957 by Robert Pudenz [31].

1.4 SHUNT FAILURE

Shunt systems, in their current form and design, suffer from many imperfections and are affected by a high rate of failure. Analysis of patient outcomes reveals that one third of children undergo revision of the shunt in the first year after surgery [32], 40% fail within two years [33] and up to 85% fail within 10 years after implantation [28]. This implies the necessity of frequent revision surgery needed to replace the implant while the patient grows (an average of two shunt revisions has been reported by Kehler *et al.* [34]), which imply discomfort for the patient. Around 30% of the revisions occur during the growth of the child [35].

Ventricular shunt catheters can fail either at the valve, at the proximal or distal catheter, and the failures can have multiple causes:

- aseptic:
 - mechanical malfunction, such as calcification, overdrainage, underdrainage, cell obstruction, and the need for revision to adjust the length of the distal catheter;
 - obstruction originating from choroid plexus tissue growing in or around the three parts of the catheter;
 - reasons related to the complex nature of the disorder itself.
- septic (infection-related).

The causes of catheter obstruction will be the subject of the following section, especially as far as the proximal catheter (VP) is concerned. Shunt valve obstruction have been specifically excluded in the discussion.

1.4.1 *Investigation of shunt malfunction*

Shunt failure can be normally detected using a CT scan. Sometimes, palpation of the shunt reservoir is used, however this method is not reliable. Other indicators of possible failure of the shunt are white cell count of peripheral blood (unless there has been a recent surgery) to determine the presence of internal infection, ICP monitoring and lumbar infusion test (see Pople [18] and Section 1.2.9).

1.4.2 *Obstruction of the shunt catheter*

Occlusion of catheter is the primary cause of shunt failure and accounts for 40% of the shunts revisions within 2 years of the implant in the USA, and for up to the 54% of the total revisions in the sub-Saharan Africa. The sources of obstruction can be mainly classified as: pathological or inflammatory tissue, or normal brain tissue.

1.4.2.1 *Normal brain tissue*

Healthy tissue infiltrates the catheter as a single cell, as an aggregate of cells or as a whole tissue.

Insertion of the catheter plays a role in obstruction by whole tissue, such as choroid plexus, connective tissue, white or grey matter. Normal cells present in the brain can be shed from the internal surface of the ventricles as a result of stretching or compression during or after the insertion of the catheter. Mechanical blockage of the proximal holes can result from re-expansion of the cortical tissue. Other tissue can be pulled in by a negative pressure in the catheter [3].

1.4.2.2 *Pathological tissue*

A number of inflammatory cells originating either in the blood or in the subventricular zone, such as red blood cells, platelets and cell debris, can be commonly found in the first millimetres of revised catheters. They infiltrate the ventricular space as a result of the surgery (injury response) or from the hydrocephalus itself.

Some specific inflammatory cells are found as a response of hydrocephalus, for example proliferative glial cells, giant cells, exfoliated ependymal cells, monocyte and macrophage, neural progenitor cells, lymphocytes. These cells reach the ventricle by chemotactic drive or by shedding or breaking the blood vessel. Once in contact with the catheter, they bind to the surface and multiply [3].

1.4.2.3 *Inflammatory cells*

Pathological inflamed cells and tissue develop in or around a number of obstructed shunt catheters. The cause of inflammation is twofold: it can be a result of the surgical injury to introduce the catheter, or what is called Foreign Body Response, that is, the natural immune response of the patient's organism to an externally introduced device. Patients develop an immune reaction to the shunt system, therefore it is expected that the inflammatory response will be stronger with every revision [3].

1.4.3 *Protein occlusion*

It has been thought that protein adhering on the internal lumen of the shunt catheter or on the valve might cause occlusion, or increasing the viscosity of the CSF so much to reduce the flow. All three of these mechanisms, however, have been dismissed [36–38]. The CSF protein concentration is indeed very low to justify an accumulation on the catheter components.

It has been reported elsewhere, however, that a higher concentration of proteins might stimulate cell attachment (macrophage and neural-glial) and indirectly cause obstruction down the line. Albumin and γ -globulin, which are the proteins present in highest concentration in the CSF, adsorb the most on hydrophobic surfaces such as the lumen of the ventricular catheter [39].

1.4.4 *Bacterial contamination*

Bacterial colonisation is one of the major issues for medical devices and implants, and accounts for 11.7% per patient and 7.2% per procedure [3]. Almost all the contamination cases for shunt catheters occur during the surgical operation, and are caused by bacteria present on the patient's skin. Following disinfection, the skin flora returns to original levels after only 15-20 min, resulting in contamination of the incision, instruments and the catheter itself. This is particularly dangerous for such an implant as shunt catheters, as the internal lumen is inaccessible to the immunitary system [40].

Statistics about contamination of the shunt system vary hugely, with reported rates ranging between 2 and 27% [41, 42]. Few hospital centres have achieved an infection rate lower than 1%.

Usually, infection-related revisions are performed during the first months after implantation. Up to 90% of the colonised shunts are removed before the first year, with more than 60% being diagnosed after the very first month following the procedure [41]. It is easy to observe that colonisation episodes must be related to hospital procedures themselves.

Some categories of patients are more affected by contamination, such as neonates up to 1 year and patients that have been previously treated with an external ventricular drain (EVD).

Catheter colonisation leads to rehospitalisation, treatment with antibiotics, surgery to remove the colonised device and a second intervention to replace the failed catheter with a new one.

Bacteria belonging to the skin flora, especially *Staphylococcus* spp (first coagulase-negative *Staphylococcus*, followed by *Staphylococcus aureus*), account for up to 70% of colonisation, while gram-negative bacteria such as *Escherichia coli* and *Klebsiella* for another 20%. Some colonisations (between 10 and 15%) have been reported to be caused by multiple bacteria, at least one of which are Staph or *E. Choli*. A small percentage (around 5%) of colonisation are originated by anaerobic bacteria, which may cause meningitis as well (*Haemophilus influenzae*, *Streptococcus pneumoniae*, *Neisseria meningitidis*) [41].

Colonisation of a device surface by bacterial strains is influenced by different factors that can be grouped into three classes:

1. the properties of the surface;
2. host factors;
3. factors intrinsic to the microorganisms themselves (e.g. the ability of the colony itself to produce a biofilm).

These various factors are summarised in Table 1.3.

Table 1.3: Factors influencing microbial attachment to artificial surfaces [43].

Class	Factors
Chemical properties	Wettability Charged groups Polarity
Physical properties	Roughness Porosity
Host conditions	Protein layer pH, ionic concentration, temperature shear rate
Pathogen characters	Gram positive/negative Species Bacteria surface charge Biofilm formation

Bacterial colonisation follows four stages:

1. adhesion: bacteria need first to adhere to a surface. Adhesion occurs via a range of interactions: Van der Waals forces, electrostatic interactions, hydrophobic forces, hydrogen bonding, and ligand-receptor interactions. The latter occur especially when the surface is coated with a layer of biological molecules, namely proteins, which adhere to the surface immediately once immersed in a biological fluid;
2. multiplication: bacteria multiply rapidly and increase in number;

3. biofilm formation: at this stage, the bacteria clump together in a continuous colony and start develop a dense biofilm, made of polysaccharides and proteins, that swells in water and acts as an effective protective barrier against the penetration of external biocides, antibiotics and against phagocytosis by white cells. Once a mature biofilm has been created, conventional antibiotic therapies are not efficient any more to eradicate the colony;
4. spreading: bacteria leave the biofilm and are ready to spread and colonise other areas, thus starting the cycle again.

1.4.4.1 Contamination routes

Contamination occurs via four different routes:

- bacterial colonisation of the surface of the catheter during the surgical procedure, which is related to direct manipulation of the device before surgery. While Pople *et al.* [44] demonstrated a correlation between the density of skin bacteria to the population of bacteria on the infected device, other studies have shown that less than 50% of the bacteria can be traced back to the patient [45];
- retrograde colonisation from the distal catheter;
- inoculation through the operation wound and skin; and
- dissemination through blood vessels, which are quite rare but at the same time difficult to identify.

Borges [46] argues that catheters interfere with the natural population of neutrophils, therefore limiting their role in phagocytosis.

Symptoms of infection are pain and fever. Proximal colonisation may be easier to detect but might lead to life-threatening conditions such as meningitis and ventriculitis.

The best way to treat patients showing the symptoms of catheter colonisation is the removal of the catheter and a prompt antibiotic therapy. A new catheter, however, cannot be inserted straight away, as the non sterile tissue could lead to a re-colonisation. At the same time, this may pose the risk of a rise in intercranial pressure.

1.5 MODIFICATION OF THE TRADITIONAL SHUNT CATHETER

Silicone (polydimethylsilyoxane, PDMS) elastomer has traditionally been used as the standard material for the catheter. It exhibits high tensile strength, good flexibility and tear resistance. At the same time, it is inert and stable in a biological environment [47]. All these properties make PDMS the standard biomaterial for shunt catheters. Silicone polymers find a wide range of applications in medical devices, for example in implants for ophthalmology, orthopaedic surgery, reconstructive surgery, microfluidics and cardiovascular devices.

Nevertheless, silicone is affected by several issues. It can arise a series of foreign body reactions. Polymer degradation occurs over time, and it is accelerated by the inflammatory process and mechanical wear in areas where the catheter is subjected to regular movements [48]. Upon degradation, several byproducts are liberated into the host's body and an inflammatory response is triggered. Unpolymerised oligomers and monomers may be released from a newly implanted device and elicit the same kind of inflammatory response. Fractures and corrosion often occurs, and in the worst cases, the catheter undergoes calcification and fixation, as reported by Boch *et al.* [35]. Barium sulphate, the radio-opaque filler used to facilitate the localisation of the catheter inside the patient's body, can cause cracking of the silicone and initiate an inflammatory response [49].

Furthermore, PDMS is hydrophobic, exhibiting an advancing angle of $105.58 \pm 5.38^\circ$ and a receding angle of $71.34 \pm 7.88^\circ$ [13]. Because of its hydrophobic interactions, though, it leads to undesired protein adsorption, cell adhesion and scarring.

In order to limit the host's body reaction, several solutions have been proposed. Research has focussed on three properties: surface charge, roughness and wettability. The effectiveness of each modification is ultimately related to the type of cells and the environment PDMS is exposed to, though.

Harris *et al.* [13] describes an oxidative process using plasma, in order to create hydrophilic hydroxy-groups on the surface of standard catheters and improve wettability. Other examples of surface functionalisation include silanes, heparin and hyaluronic acid. Achyuta

et al. [50] reports the covalent bonding of the catalytic enzyme trypsin on the catheter surface with the goal to inhibit cell adhesion.

In another study by Harris & McAllister [3], silicone was first coated with pHEMA (poly-2-hydroxyethyl methacrylate), which is highly hydrophilic (its water uptake is up to 40% in weight) and turns into a gel-like material in contact with water. It originates a milder reaction but at the same time it integrates too well into the body, and connective tissue was found all around the catheter, and therefore it was abandoned, although, given its successful use for intraocular lenses and contact lenses against protein adhesion and cell adhesion, further studies should be carried out.

Instead of focusing on the surface, several materials alternative to silicone have been proposed for catheters, including polyethylene, expanded polytetrafluoroethylene (e-PTFE), polyether sulfone, cellulose acetate, silver-impregnated polyurethane and polyethylene oxide (PEO) [2].

Another available alternative material is polyvinyl pyrrolidone (PVP), which is a water-soluble, hydrophilic polymer, which creates a hydrogel when immersed in water. PVP-coated catheters were commercialised as BioGlide by Medtronic (Minneapolis, Minnesota, USA), where PVP was covalently bound to the silicone surface. BioGlide was initially marketed as a catheter with enhanced lubricity, with the benefit to provide a smoother insertion in the patient. Besides, an additional higher resistance to bacterial colonisation was later observed. Owing to its very lubricity, however, it was withdrawn from the market in 2010, as the catheter lumen tended to slip out of the connector with the valve, leading to the failure of the device [2]. Nonetheless, a study published by Çağavi *et al.* [51] brings further evidence to the hypothesis that, when comparing antibiotics-impregnated catheters and PVP-coated catheters, coated catheters are superior to the other group in preventing bacterial colonisation, and surface hydration seems to be an efficient mechanism as an antimicrobial barrier.

To avoid colonisation and obstruction, the use of hydrophilic surfaces (presenting high surface wettability) have indeed gained momentum as a possible solution [13]. Under such CSF rates, hydrophobic materials apparently elicit more cell adhesion than hydrophilic

surfaces, although this effect is highly dependent on cell type and surface coating [3]. In general, higher wettability enhance bacterial resistance by creating a layer that makes the surface smooth and less prone to be colonised by bacteria.

According to Arima & Iwata [52], epithelial cells spread out poorly on $-OH$ group, while they adhere preferentially on $-COOH$ and $-NH_2$ groups. Cox *et al.* [53] show that glial cells are more adherent on hydrophobic surfaces and highlight that probably different cell-surface adhesion mechanisms intervene at different time points. Their conclusion is that during the first minutes and hours the direct cell-surface interaction influences the adhesion, while, on a longer time scale, other factors, such as protein adsorption/desorption curves, are more important.

Hydrophilic surfaces have been shown to be able to inhibit non specific protein adsorption. Proteins are indeed made of different domains, both hydrophilic and hydrophobic, and a uniform surface is less able to grant adsorption. Each protein is then attracted by one surface or another. For example, albumin is adsorbed more easily on hydrophobic surfaces [54]. Since albumin is a non-adherent protein, it inhibits following cell adhesion. If albumin is adsorbed on an hydrophilic surface, though, it can be displaced (since it is only loosely bound to the surface) by other proteins such as fibronectin (which is called *Vroman effect*), which is protein-adherent, and therefore cell adhesion is enhanced. Therefore amphiphilic surfaces promote higher adsorption than hydrophilic or hydrophobic ones. It has been reported that a wettability between 40 and 60° is the most favourable for cell adhesion [52].

Several papers seem to suggest that surface wettability has a different effect depending on the cell line they are exposed to. In general, cells are influenced by the density of hydrophilic/hydrophobic functional groups, their polarity and the way charge is distributed on the surface.

1.5.1 *Modifications with antibacterial applications*

An increase in the roughness of the surface has been linked to a higher risk of bacterial colonisation, as a smooth surface reduces the chances of adhesion and bacterial adhesion is limited. Increased roughness is connected with ageing of the catheter [55]. However, Epstein *et al.* [56] explored the effectiveness of high-aspect-ratio features (HAR), a term used to describe structures with a dimension more developed than the other: typically, needle-like nanotubes. One of the findings of their study is that HAR nanostructures generally inhibit bacterial growth independently of their mechanical stiffness; it has been shown, however, that the surface roughness is efficient only within a certain range, that is, between 1 and 5 μm . They argue that when the nanostructures are smaller than 1 μm in height, the surface presents a small area accessible to bacteria, the point of contact between the bacterial membrane and the surface itself being limited to the top of the features, and is less energetically favourable for bacterial interactions [56]. Scardino & de Nys [57] report that both natural surfaces and artificial bio-inspired surfaces have shown successful decrease in adhesion for protruding structures that are smaller than the settling organism. In particular, the highest efficacy is achieved when the size of the structure is between 50 and 90% of the diameter or length of the settling organism, therefore, bacterial adhesion is inhibited.

The change in the surface structure may induce a change in surface energy. Surface energy is linked with wettability. One theory to account for the change in wettability as a function of the surface morphology is the Wenzel and Cassie-Baxter method, which takes into account the microbubbles of air trapped between the cavities of the surface.

Many studies agree that an increase in hydrophilicity leads to a decrease in bacteria adhesion. Therefore much of the literature has focused on modifying the surface chemistry in order to make it more hydrophilic. A simple and effective method is the modification of the surface with polyethyleneglycol (PEG), which confers hydrophilicity, it is a non charged polymeric molecule, and is an hydrogen-bond ac-

ceptor. Ostuni *et al.* [58] underlines how these three conditions, when present together, are the most effective to offer protection against bacterial adhesion. Chitosan is a valid alternative to PEG.

However, the interaction between bacteria and polymeric surface is always mediated, in a physiological environment, by adherent proteins, mainly albumin, fibronectin and fibrinogen. Apparently, albumin has a general effect of decreasing bacteria adhesion, probably by increasing the overall hydrophilicity of the surface.

Bacteria bear a net negative charge on the surface, are small and move with brownian motion, hence they can be modelled as spheres or nanoparticles and their interaction with a surface can be described as a colloidal fluid according the DLVO theory (named after Derjaguin, Landau, Verway, and Ocerbeek). The interaction between bacteria and a biomaterial surface is the sum of net charges, dipolar and dispersive forces present on both bacteria and the surface. Therefore, if the net charge on the surface of the polymer is zero and the polymer is neutral, van der Waals forces are predominant in driving bacteria adhesion.

Another way to reduce bacterial contamination is the chemical modification of the surface, for example, effective antibacterial coatings incorporate metal ions such as silver, copper, zinc, and titanium dioxide, or quaternary amines and other cationic organic compounds, drugs and biological molecules [59].

The antimicrobial activity of a surface can be defined not only by its ability to limit or completely eradicate bacterial proliferation, but more generally by its prevention of bacterial adhesion onto the surface, limitation of proliferation of adherent bacterial and prevention of film formation, even when the surface itself does not prove to be bactericidal [60].

Finally, it should be remarked that the effect of the surface does not depend on one factor only, but on the complex contributions of a number of them combining together: charges, hydrophilicity of the surface, morphology, the static or dynamic conditions. For example, hydrophobic surfaces are generally less bacteria-conductive. However, the size of the pattern plays a significant role, as submicron patterns on a hydrophobic surface are reported to decrease bacterial adhesion

by reducing the available contact surface, while micrometer patterned surfaces lead to increased bacterial adhesion [61].

1.5.2 Drug delivery solutions

On top of perioperative antibiotic prophylaxis, the introduction of antimicrobial-impregnated and -coated catheters (AICs) have had a positive impact on reducing the rate of colonisation [62, 63].

Impregnation with antibiotics should address both uniformity issue (distribution of the antibiotic both on the inner and on the outer surface), and a time dependence effect (released time). Antibiotics are introduced into the material either by immersing it into a chloroform solution, or mixing them in the pre-polymerized silicone via a cast-moulding method, so that they get trapped inside the polymeric network and are released slowly over time [64].

Hayhurst *et al.* [65] reports that antibiotic impregnated shunt catheters can reduce bacterial colonisation from 27% down to 10.4%. Bayston *et al.* [40] registers a successful antibacterial activity of such catheter, although this is not accompanied by a lesser bacterial adhesion to the shunt. *Staphylococcus* can be reduced by the 99.97% for rifampin and trimethoprim sulfomethaxazole-impregnated shunt catheters [66], while Gower *et al.* [67] reports a decrease by 54% in adherence of *Staphylococcus epidermidis* by soaking the catheter in bacitracin A solution (50,000 units in 250 ml).

1.5.3 Catheter design

The number of holes, their size, contribution to roughness, distance and distribution varies according to the manufacturer, and each of these factors may influence the mechanisms of obstruction. Normally there are 12- to 32-hole perforation patterns. For example, a standard 16-hole catheter manufactured by Miethke-Aesculap has eight pairs of perforations distributed opposite to each other along a 12.8 mm-long segment at the proximal end [68]. Holes have a tapered shape (that is, a truncated conical shape) with an external diameter (on the outer surface of the catheter) of 0.5 mm, which corresponds to an area of

0.2 mm. The internal diameter ranges from 0.18 to 0.35 mm depending on the model, which corresponds to an area between 0.1 mm and 0.38 mm, which, multiplied by the 16 holes, amounts to a combined absorbing area of 1.63 mm² to 6.16 mm². The intersegment distance between holes ranges from 1 to 2.5 mm according to the model [69].

An example of ventricular catheter is depicted in Fig. 1.5.

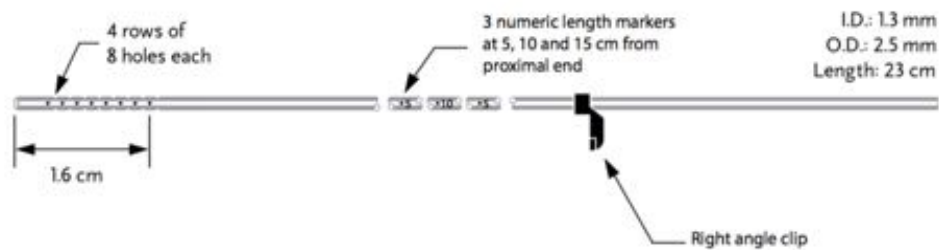


Figure 1.5: Schematic of a ventricular (proximal) catheter, with the details of holes (Ares Ventricular Catheter by Medtronic, from Medtronic Product Catalogue, p. 18, available from *Ares Antibiotic-Impregnated Catheters - Overview | Medtronic* [70]).

There is no scientific evidence regarding the number, disposition, area, shape and grouping. Number of holes is arbitrary and their distribution does not guarantee an even flow of CSF. It has been proven that, in an eight-holes catheter design, more than 75% of the holes (those which are distal) are not in use at any time, and that the proximal ones, being subjected to the majority of the flow, become obstructed with cells [71]. Papers report some trials where a lower number of holes and a different size distribution would provide a more homogeneous flow, after observing that only the first 2 holes of each row (or 6, according to Thomale *et al.* [68]) actually contribute to the inflow [71].

Thereafter some studies have introduced a 6-holes catheter (manufactured by Miethke-Aesculap), and all of them appear to be functional and contribute to the flow [68]. The perforations are distributed for a total 3.8 mm length pair-wise.

Medtronic has therefore introduced a new model in 2007 called Rivulet (whose diagram is showed in Figure 1.6). On this device, holes of decreasing size along the distal-proximal axis are distributed on 4 parallel rows. The flow is supposed to be more uniform and

this has been verified by computational simulations carried out by Galarza *et al.* [69]. The proximal inlets are placed a little further away from the tip, in order to prevent invasion from the choroid plexus.

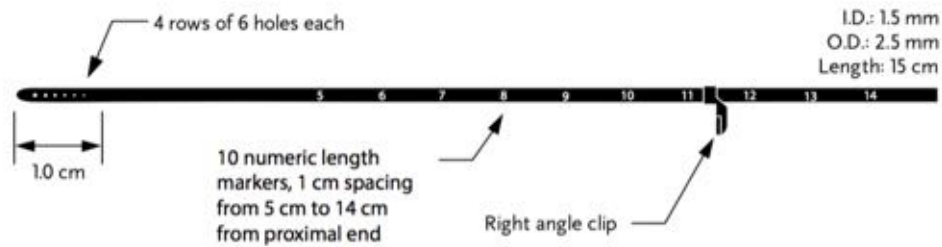


Figure 1.6: Schematic of Rivulet, a ventricular (proximal) catheter by Medtronic (product number 41701, available from their products catalogue [72]).

More specifically, it has been shown with theoretical and experimental data that more than 80% of total fluid mass flows into the two most proximal holes of a hydrocephalus shunt [71]. Catheters with variable sized holes, with its largest one situated at the catheter tip, would redistribute the flow more evenly along the entire length of the catheter. Some studies suggest the smaller holes, with a higher shear stress, increase adhesion of macrophage and astrocytes, probably depending on a threshold. A relationship between size of holes and astrocytes attachment has been noticed [73].

A new technology has been introduced by Anuncia via the ReFlow Ventricular System, whereby the blockage, once identified by a healthcare specialist, can be removed by operating a special valve, called flusher, which momentarily reverses the CSF flow and, through a precise pulse, removes the occluding cells and tissue. If the occlusion is severe and cannot be removed, a secondary membrane can be opened, and the CSF flow can continue through this alternative pathway (Fig. 1.7, [74]).

1.5.4 Alternative catheter design

It is evident that the current designs for ventricular catheters can be improved, especially on the number, distribution and design of the fenestrations. Most of the holes, in the current design, play no

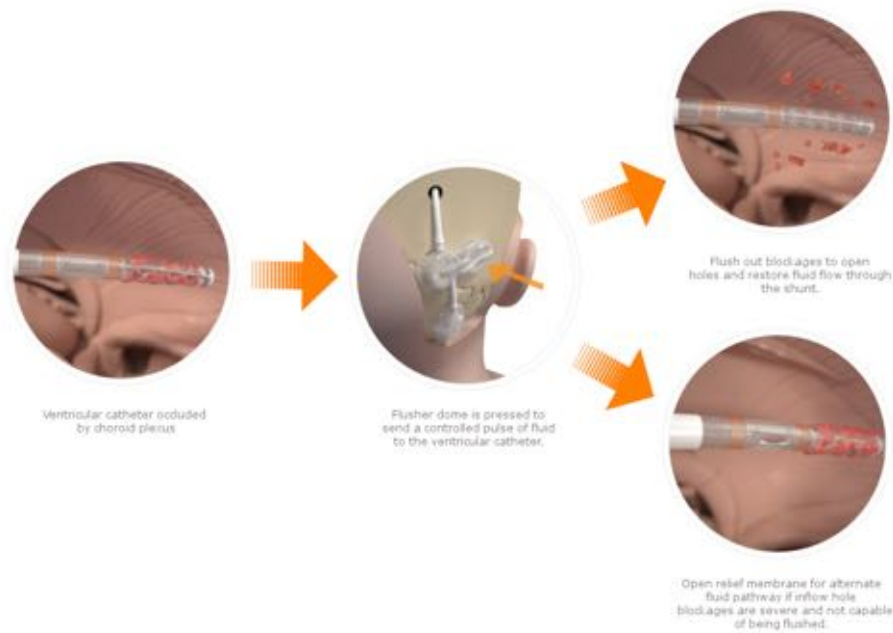


Figure 1.7: Mechanism of action of ReFlow, a ventricular (proximal) catheter by Anuncia [74].

active role, while at the same time being prone to stimulate cellular ingrowth and leading to occlusion. Research published by Go *et al.* [75] reports necrotic tissue causing obstruction of the wholes punched on the shunt catheter surface.

A totally alternative approach to this sub-optimal design has been described in Suresh & Black [5] and it is based on the idea that the a continuous, solid surface with a limited number of interspersed fenestrations should be substituted with a microporous surface, capable of absorption across the whole surface.

This would allow for a continuous inflow of CSF throughout the whole surface, redistributing the absorption pressure on the whole surface, whereas in the current model pressure is concentrated on few spots. A distributed porosity all over the surface would reduce therefore the shear force in proximity of the holes and the risk of obstruction associated.

Furthermore, a permeable device that allows to drain the CSF through the walls of the catheter itself would at the same time create a tortuous environment for the cells to pass through and decreasing the

shear force on cells in the area close to the holes so to reduce the rate of obstruction and ingrowth [76]. Inhibition of cell growth in the proximity of the fenestrations would decrease the risk of cells obstructing them, and reduce the number of failed devices.

This innovative design represents the basis for the work in this thesis. Rather than a continuous surface with few holes, a microporous surface will be fabricated.

In order to fabricate such a microporous surface, electrospinning technique will be used. Electrospinning is described in 1.7. Electrospinning is a versatile technique that allows control over several parameters of the process and on the final properties of the device, in particular, porosity. Pores in electrospun items are interconnected, thus creating a complex structure than cannot be achieved with other traditional techniques, such as casting or injection moulding, which are currently used to fabricate the catheters.

In case of electrospun surfaces, pore diameter is significantly proportional to the size of the fibres, network porosity and the number of layers, and that is explained by the physical packing during the deposition of the fibres [77]. Fibre diameter is usually in the nano- and micrometre range, therefore it is expected that pores will be in the same range, thus much smaller than conventional fenestrations. However, pores are interconnected across the third dimension of the electrospun device (thickness), and density of electrospun materials is low, providing effectively a device that is in good part void and permeable.

As silicone, the conventional material used for catheters, cannot be electrospun, another material had to be used in order to achieve this kind of microporous, electrospun surface. Polyurethanes are excellent alternatives, as described in section 1.6. Polyurethanes can be electrospun, are biocompatible and, at the same time, are biologically inert, therefore not supporting the proliferation of cells once implanted. The work with polyurethane would continue and expand research started and presented by Suresh & Black [5].

1.6 POLYURETHANES AND THEIR BIOMEDICAL APPLICATIONS

Polyurethanes are a class of segmented organic polymeric materials whose backbone is comprised of two blocks with very different chemical properties, that tend to segregate in the solid form and create distinct domains. Thanks to this internal microstructure, polyurethanes are thermoplastic polymers with very good flexibility associated to good mechanical properties, making them able to withstand repeated mechanical solicitations. Furthermore, they have excellent biocompatibility, and they have found several medical applications, especially for cardiovascular devices. Given their proven history in medical devices, polyurethane represents an ideal substitute for the current material used in catheter manufacturing, that is, silicone.

1.6.1 *Polyurethanes*

In organic chemistry, polymers are a class of materials based on the repetition of a fundamental unit, called a monomer. Polymers can be classified via the bond that joins monomers together. Accordingly, polyurethane is a class of polymers defined by the urethane bond ($-\text{NHCO}(=\text{O})-$) [78].

Polyurethanes were first synthesised in the 1930s by Otto Bayer in order to compete with the newly-developed nylon 6,6. While the structure of nylon and polyurethane differs by only two extra oxygen atoms in the polyurethane chain (highlighted in red in Fig. 1.8), the properties of these two classes of materials are very distinct.

1.6.1.1 *Synthesis reaction*

The majority of commercially available polyurethanes are block copolymers, which means they are composed of alternating distinct segments. Strictly speaking, a polyurethane is made of two main components, a diisocyanate and diol, while usually a third component, namely a chain extender, is introduced to alter and tailor its chemical-physical properties [80].

The polymerisation occurs by step reaction. Each monomer carries two reactive sites, that can be reactive functional sites, in the form

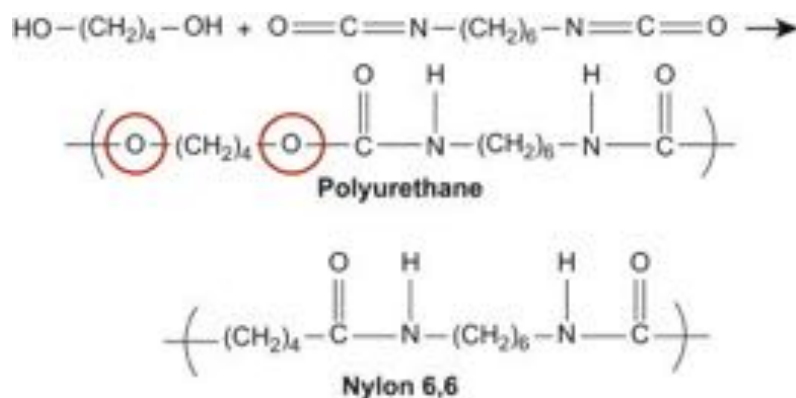


Figure 1.8: Schematic of the basic structures of polyurethane and nylon [79]. Even though the structure is similar and they differ only for two oxygen atoms, their properties are very different.

of ions, radicals or complex, so that monomers can grow on both sides by reacting with other species, and create oligomers that will further react into polymers. The reaction can be by condensation, when two moieties react by releasing a small molecule (H_2O or CO_2), or by addition, when no molecule is released.

Polymerisation reaction occurs between the cyanate group ($-\text{N}=\text{C}=\text{O}$) and the hydroxyl group ($-\text{OH}$), therefore stoichiometry is constrained by the number of reacting bonds; namely, the number of diisocyanates must at least equal to the total number of molecules of diols and chain extenders combined. This prepolymer is usually 5-6 units long, and by using an excess of diisocyanates, it will be terminated at both ends by cyanate moieties, so that it can further react with chain extenders. Chain extenders will join several prepolymers into a longer chain of the desired molecular weight. The final polyurethane chain might look like a similar sequence: $\text{ABC}(\text{BAB})_n\text{C}$, where A is the diol, B the isocyanate and C the chain extender.

A second method, whereby all the three ingredients are mixed together and made react at once, yields less ordered structures and there is less control over the final properties of the polymer [81].

1.6.2 Macrodiols

The main component of a polyurethane by weight is a macrodiol, a long-chain molecule terminating on each extremity with an $-OH$ group.

The molecular weight of such long chains ranges usually between 500 and 5000 dalton, although the most frequent molecular weights range between 1000 and 2000. Depending on their molecular weight, polyols can appear as waxes or more or less viscous oils. Shorter chains deliver stiffer polyurethanes, while long chain polyols can form semicrystalline domains [81]. These components have a typical glass transition temperature below zero, namely between -70°C and -30°C , and are therefore amorphous at room temperature and have a rubber-like nature. The long aliphatic backbone has a certain degree of flexibility and it is what constitute what is called “soft segment” (SS).

Polyols can be of different types according to the kind of bonds and functional groups they exhibit along the chain, but they mainly belong to the families of polyether (basically a polymerisation of polyethylene glycol), polyester, polycarbonate, or copolymers of those as di- or tri-blocks. Polyesters tend to be more hydrophobic and crystalline, while polyethers instead have lower moduli, thus providing the final polyurethane with improved flexibility, stretchability and hydrophilicity. Some polyether diols are polyethylene oxide (PEO), polypropylene oxide (PPO), poly(tetramethylene oxide) (PTMO), poly(hexamethylene oxide) (PHMO) (Fig. 1.9).

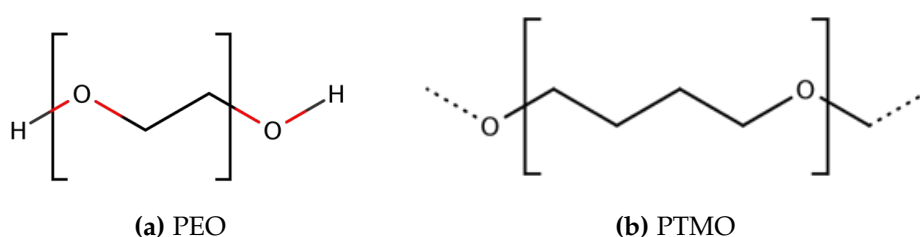


Figure 1.9: Structure of polyethylene oxide (PEO) and poly(tetramethylene oxide) (PTMO), both polyethers.

Diols can be branched and bear more than two hydroxy functionalities, to create interchain networks. Polyurethanes made from inter-

networking are harder, but they still preserve a certain flexibility degree.

1.6.3 Diisocyanates

Diisocyanates are usually short molecules terminating at both ends with the isocyanate group, $\text{N}=\text{C}=\text{O}$. Diisocyanates can be either aromatic or aliphatic according to the chemical nature of the molecule itself. Of the most common aromatic diisocyanates, it is worth mentioning 2,4-tolylene diisocyanate (TDI) and 4,4-diphenylmethane diisocyanate (MDI, Fig. 1.10). MDI has low cost, high reactivity and ability to form crystalline domains, resulting in harder polyurethanes. Aliphatic diisocyanates are less prone to yellowing and degrading oxidation upon exposure to UV radiation instead.

Because they are usually short aromatic molecules, which have no rotational freedom around their bonds, such molecules are quite rigid and tend to form hydrogen bonds with other groups on neighbouring chains, stacking together to create what is called “hard segment” (HS), that have a glass temperature above room temperature and therefore are in a ordered state most of the time [82].

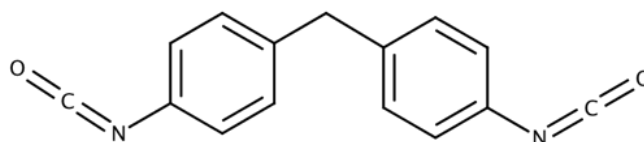


Figure 1.10: Structure of 4,4-diphenylmethane diisocyanate (MDI).

1.6.4 Chain extender

Small chain extenders can be diols, or a diamine with a 2-6 carbon chain in length, either aliphatic or aromatic (an example is 1,2-butanediol, Figure 1.11). Diols will create urethane bonds, whereas amines will make urea bonds, giving room for bidentate hydrogen bonding. Diamines yield higher moduli and tensile strength. Chain extenders are employed to reach the final desired molecular weight.

Higher molecular weight chain extenders can be used to increase flexibility of the final polyurethane [81].

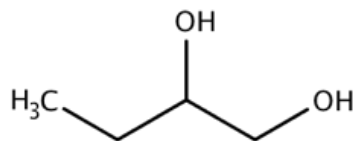


Figure 1.11: Structure of 1,2-butanediol.

1.6.5 Chemical structure of polyurethanes

Polyurethanes are segmented polymers. Their structure is made up of alternating building blocks, one defined as soft segment (SS), because it is made of polyolephines (linear organic macromolecules) that, thanks to their linear carbon chain, are flexible and can move, the other called hard segment (HS). The hard segments are usually made of two short chain components that are not flexible: one is the diisocyanate and the other a short chain extender.

The two types of segments tend to segregate into domains with distinct properties. Hard segments stack into crystalline domains, surrounded by amorphous soft segments. Because of their particular structure, PU look like composite materials, with the HS domains acting as the reinforcement fillers in a softer matrix [79]. The mechanical properties of polyurethanes are determined by the crystallinity percentage. It is therefore of key interest to be able to characterise the polymers according to the hard segment content.

Usually hard and soft segments are carefully chosen for their different chemical properties so that they will be incompatible and segregate. Macrophase separation is impossible because of the covalent bonds that join together the incompatible elements. However, the two blocks tend to separate as much as possible and segregate into microdomains.

HS tend to stack together (Fig. 1.13), helped by secondary forces and hydrogen bonds between a $-NH$ group on one molecule and $-C(O)O$ group on the other (urethane-ester bond, urethane-ether, with

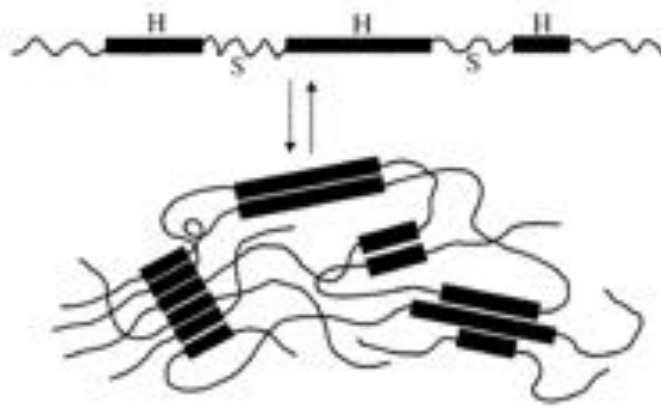


Figure 1.12: Schematic of polyurethanes as a “composite” made by hard segments immersed in a soft “matrix” [83].

neighbouring extenders, or inter-urethane, with neighbouring urethane bonds), and create ordinate structures surrounded by the soft segments, which are flexible and long enough to bend and allow for the hard segments to pair together. These bonds can be destroyed by either thermal energy or solvents.

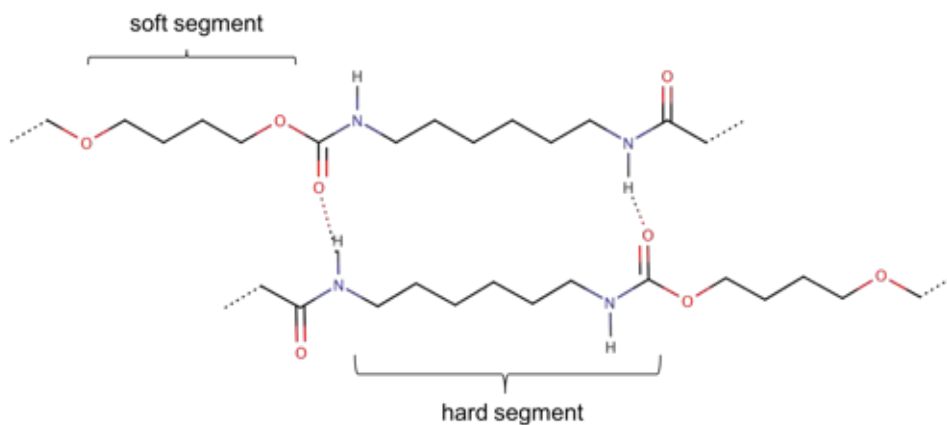


Figure 1.13: Schematic of hydrogen bonds between adjacent polyurethane chains and the formation of hard and soft segments. This model polyurethane chain is made of hexanediol and 1,6-hexamethylene diisocyanate (HDI).

The bulk of the polymer is therefore not homogeneous, with regions rich in HS and other regions rich in SS. Segregation occurs because of the very different properties of the two blocks which make

them incompatible. Hard segments are more polar, while SS are made of apolar, carbon-rich chains.

The degree of segregation depends on both the thermodynamic forces driving the separation and the kinetic pathways of the process. For example, using particularly hydrophobic SS, less prone to making hydrogen bonds, the segregation can be higher. When the relative concentration of the hard segments increases, HS domains become larger and assume a spherulitic-like structure, while at the same time they become less dispersed in the SS domains. HS domains have size that range from tens to hundreds of angstrom [83].

At high hard segment concentration, hard segments can organise into crystallites called *lamellae* and then further into macroaggregates called *spherulites*.

While usually polyurethanes are linear polymers, cross-linkers can be introduced by means of segments with more than two reactive moieties in order to increase a stronger polymeric network through connecting joints. As polyurethane chains end with a reactive cyanate group, absorbed moisture must be avoided, because adventitious (casual) cross-linking can be introduced by reaction with water molecules.

1.6.6 *Physical properties of polyurethanes*

Polyurethanes exhibit good fatigue resistance and are used as coating, adhesives, sealants, rigid and flexible foams, and textiles [80]. Many properties derive from the PU characteristic biphasic structure. PUs act as a composite material, with a harder phase mixed with a softer matrix. One phase provides reinforcement to the elasticity. HS serve as weak net points and as rigid filler at the same time [81]. The relative amount of HS, as well as its size, and its relative length to the diol segment, determine the mechanical modulus. By changing the HS/SS ratio, a whole range of properties can be obtained, going from soft elastomers to hard reinforced rubbers.

Polyurethanes have an elastomeric mechanical behaviour. Unlike natural rubber, which are cross-linked through a process called vulcanisation, the reason for such properties is not to be found in cross-

linking, though. In fact, in the case of polyurethanes, the linear segment will stretch, while the HS and the hydrogen bonding provides the sort of cross linking that allows the material to recover back after being stretch.

Depending on the distribution of SS/HS, two regimes can be described:

1. for low HS concentration, the fibrillar regime is in place: SS comprise almost all of the material, and they uncoil and stretch first. The HS are diluted and already loosely distributed along the main chain and they can be easily orientated parallel to the axis of elongation;
2. for high HS concentrations, a lamellar regime is in place: as soon as the SS are uncoiled, the HS are stacked and closely packed, so that the major axis is perpendicular to the polymeric chain and therefore to the stretching direction. The initial energy is therefore spent to rotate the domains so that they are parallel to the elongation. However, after all the domains are aligned, the strain leads to the progressive destruction of the stacks of the domains and the disruption of the hydrogen bonds [83].

The mechanism is not quite this simple, however, as polymer chains show a certain distribution of the HS along the chains itself, given by the peculiar polymerisation reaction of the PU. Therefore, the strain will be distributed accordingly as well, creating non-homogeneity along the chains, with areas where the load is higher and reorientation is required to minimise the stress. In high-load conditions, strain-induced recrystallisation in soft-segments occurs, resulting in formations called nanofibrils [83]. Hysteresis in the stress-strain cycles is attributed to breaking-down of the HS domains.

The weak hydrogen bonding of the HS can be broken by application of heat, and then reformed upon cooling. HS are dynamic; they can be broken and reformed upon application of heat and stress. Therefore, PU are thermoplastic, as the hydrogen bonds in the HS can be melted and PU can be processed, extruded and melted.

1.6.7 *Biomedical applications of polyurethanes*

Polyurethanes are particularly attractive for medical devices and tissue regeneration thanks to their biocompatible properties. Their good mechanical properties, good fatigue resistance and elastomeric properties are the main reasons behind the range of biomedical applications.

Polyurethane are especially employed in vascular applications, such as permanent pacemakers lead insulators and implantable cardioverter defibrillators, catheters, artificial hearts bladders, balloon pumps and vascular grafts [80].

Beside good tear resistance and their tensile properties, they exhibit an excellent blood compatibility. The accepted explanation for this lies in the microphase separation that occurs for block polymers such as polyurethanes. The thrombogenic properties of the hard domains have been researched, and it has been proposed that the crystalline structure of the domains and their ability to make hydrogen bonds is involved in promoting platelet adhesion [84]. Blood compatibility can be increased by incorporating siloxanes.

Furthermore, given their flexibility, or the possibility to turn them into foams, they are often used as external devices such as wound dressings.

1.6.8 *Degradation of polyurethanes for medical applications*

Polyurethanes are a class of organic macromolecules and, as such, undergo a series of chemical reactions in the host bodies that degrade them over time.

Four degradation routes can be identified:

- hydrolysis (reaction with the water present in the biological environment);
- oxidation (oxidants produced by the host tissues, especially when inflamed);
- enzymatic degradation; and

- physical degradation (water swelling, mechanical loading, wearing and stress cracking).

Degradation leads to the mechanical failure of the device, for example in pacemaker lead insulators, with environmental stress cracking appearing on the surface of the polyurethane outer coating. The mechanism originates from mechanical or endogenous stress and contact with adherent phagocytic cells [85].

The unintended degradation of polyurethanes is a limit to their application in medical devices, and the duration that a polyurethane can maintain their function under use conditions is an important measure of their properties, and is called functional time.

Polyurethanes have found application in several cardiovascular devices, including heart valves and artificial ventricles, however their use for the latter has been discontinued because of their lack of long-term performance and permeability to water and water vapour [43].

A more detailed work on the biostability of Biomer's b₉ series of polymers was carried out by Cardona [86]. Modifications to the surface after exposure to a simulated biological environment (physiological solution) and an oxidative solution were investigated. Biomer polyurethanes did show changes in surface topography in oxidative solution, while there were no significant changes in physiological solution after 90 days.

When designing a polyurethane for biomedical applications, MDI is the preferred choice for the hard segment, and polyether diols as the SS because they are more resistant to hydrolysis and have good mechanical properties. Another diisocyanate, TDI, can degrade into toluene diamine, which is toxic and its use in biomedical field has been limited. Furthermore, as aromatic isocyanates are potentially toxic and carcinogenic, there is still debate about the aromatic byproducts, other class are used, for example hexamethylene diisocyanate and 1,4-diisocyanatobutane and lysine diisocyanate [81]. Aliphatic isocyanates however do not match the mechanical properties of the aromatic ones. Lysine diisocyanate is thought to be better for its lysine-based degradation pathway.

When devising a degradable scaffolds, for example in tissue engineering as resorbable scaffolds, several properties of the PU account

for the degradation rate. For example, polyether backbones increase hydrophilic characteristics and are less exposed to hydrolytic degradation. However, they can be oxidised by adherent inflammatory cells, thus becoming degraded in shorter time. On the other side, a higher presence of crystalline domains slows the water diffusion and therefore, potentially, the hydrolytic degradation of the scaffold [61].

1.6.9 Polyurethanes for antibacterial applications

Polyurethanes are known for performing only moderately well when compared to other biomaterials for bacterial adhesion. The interaction between bacteria and thrombogenic materials can be describe in thermodynamic terms by considering bacteria as colloids, given their small size, low density and net negative surface charge. Therefore, the distribution of charges on the surface of polyurethanes can influence bacterial adhesion and viability [43].

Usually, infection is treated with post-operational antibiotic treatment, and antibiotic-impregnated polyurethane catheters are available. On the other hand, strategies that do not involve drug release are ever more important, as the activity of the device does not exhaust over time and, furthermore, does not promote bacterial resistance, unlike the use of drugs. For example, *S. aureus* strains with increasing resistance to antibiotics (called Methicillin-resistant Staphylococcus aureus, MRSA) are becoming an increasing widespread issue in clinical practice, and naturally-resistant materials may provide an alternative to the prophylactic use of antibiotics [87].

The main strategies to prevent infection with intrinsically resistant PUs are based on limiting microbial adhesiveness by increasing the antifouling properties or antimicrobial properties of the polyurethanes themselves.

Antifouling properties are obtained by decreasing unspecific interactions of the material with microorganisms and reduce the chance that bacteria adhere on the surface and form a colony. The antifouling properties can be improved either by increase the surface hydrophilicity, introducing negatively charged groups, or decreasing the free energy of the surface.

Materials can be modified chemically, by creating a buffer layer that separates the bacteria from the surface. For example, by grafting PEG (polyethylene glycol) onto the surface of a polyurethane, PEG creates a sort of molecular brush that keeps proteins and bacteria away from the surface. PEG and PEO cannot be used as bulk materials on their own, given their lack of mechanical properties, but they can easily be grafted or covalently bound to a surface. They are highly hydrophilic polymers which create a water layer and form a sort of barrier on the surface of the polyurethane that works via steric hindrance [88].

Another method to improve the surface antifouling properties is to use different physical treatments to modify the surface roughness at the micro and nano scale to reduce the bacterial adhesion. A number of publications show the influence of micro-patterning on proteins adsorption and bacterial adhesion, reporting an effective decrease in bacterial colonies density (*S. epidermidis*, *E. coli*).

Other treatments aim specifically at killing bacteria, rather than limiting their adhesion. Antimicrobial properties can be achieved by adsorbing or grafting antimicrobial drugs on the surface, or incorporating them in the bulk of the material, from which they are leaked and released over time, or by introducing side-chain functionalities that disrupt the bacteria membrane, for example phosphonate or quaternary amine groups [43].

1.6.10 Biomer Technology polyurethane

Biomer Technology Ltd. provides a range of thermoplastic polyetherurethanes in pellets that are usually flexible and exhibit different hardness through the range. They are based on poly(tetramethylene oxide) (PTMO) and 4,4-diphenylmethane diisocyanate (MDI) (see Fig. 1.9b and 1.10). They are hydrolytically stable and are compatible with a range of fillers, including dyes and radio-opaque fillers. They have been developed especially for biomedical applications and cardiovascular devices, such as catheter balloons and heart valves, and have a proved history of biocompatibility.

Table 1.4 reports selected physical and mechanical properties. While the melting and degradation temperature is similar across the range,

the ultimate tensile strength increases quite sensibly going from Z1 to Z9, whereas elongation decreases, suggesting an increase in density of HS along the range, achieved by decreasing the length of the SS.

Table 1.4: Biomer Technology b₉ polyurethanes, series 'A'. Selected properties are reported (not all could be retrieved).

name	melt- ing point [°C]	degra- dation point [°C]	shore hard- ness	ultimate tensile strength [MPa]	ulti- mate elonga- tion [%]	density [g/cm ³]
Z1A1	190-235	280	80A	39.6	555	1.10
Z2A1	-	-	-	-	-	-
Z3A1	200-235	280	55D	46.7	410	1.15
Z4A1	200-235	280	-	-	-	-
Z6A1	220-235	-	70D	57.0	305	1.18
Z9A1	220-235	280	78D	58.0	280	1.20

Of all the available grades provided by Biomer Technologies Ltd., Z6A1 in particular was selected for use in this research.

Z6A1 exhibits better mechanical properties as compared to softer polyurethanes such as Z1A1 and Z2A1, while at the same time proving not to be as rigid as other polymers in the range (Z9A1).

The choice of this particular polyurethane grade was based in part on the ease with which each polymer could be electrospun: the range of available polyurethanes was tested and ranked according to their propensity to being electrospun, and while some grades were more difficult to be electrospun at the conditions of the laboratory environment (in particular, they proved to be particularly sensitive to humidity and voltage set-up), some others were more versatile and workable, in particular Z6A1, providing reproducible results.

1.6.11 *Thermal analysis of polyurethane*

1.6.11.1 *Differential scanning calorimetry*

From DSC curves it is possible to determinate the crystalline structure of semi-crystalline polymers and the impact of modifications on

internal structure of the material: for example, in composites the melting point and decomposition temperature are modified by the interaction between the matrix and the filler (illustrated in Figure 1.14) [89–92].

In particular, a DSC thermograph for biphasic polymers, such as polyurethane, shows four typical peaks:

1. the first relevant feature is actually a change in the slope of the curve of the DSC and corresponds to the glass transition temperature (T_g). Glass transition is a second-order phase transformation and describes the passage from a hard, brittle state to a soft and plastic regime;
2. 30 °C–80 °C, also defined as annealing endotherm, corresponds to the melting of soft domain crystals (pertaining to the soft segments, or the “rubbery” domains). Other sources have attributed it to the disruption and rearrangement of short-range ordered hard domains;
3. 120 °C–190 °C: this peak corresponds to the dissolution of interurethane hydrogen bonds within the HS, or the rearrangement of hard segment long-range ordering, with the onset of microphase mixing;
4. 200 °C–240 °C: this usually corresponds to the softening, or final melting of hard segments, with a complete mixing of SS and HS.

For low-HS content polyurethanes, only region I and III usually appear, with region II featuring at higher HS concentrations instead. Annealing (a post-process thermal treatment consisting in raising the temperature beyond the glass transition, so that chains are flexible enough to be able to reorganise themselves) encourages alignment and order at longer-range, increasing the crystalline domains and merging the relative DSC curves. If the polymer is annealed, curve I moves up until it merges with II, and upon extreme annealing, only curve III can be observed [94].

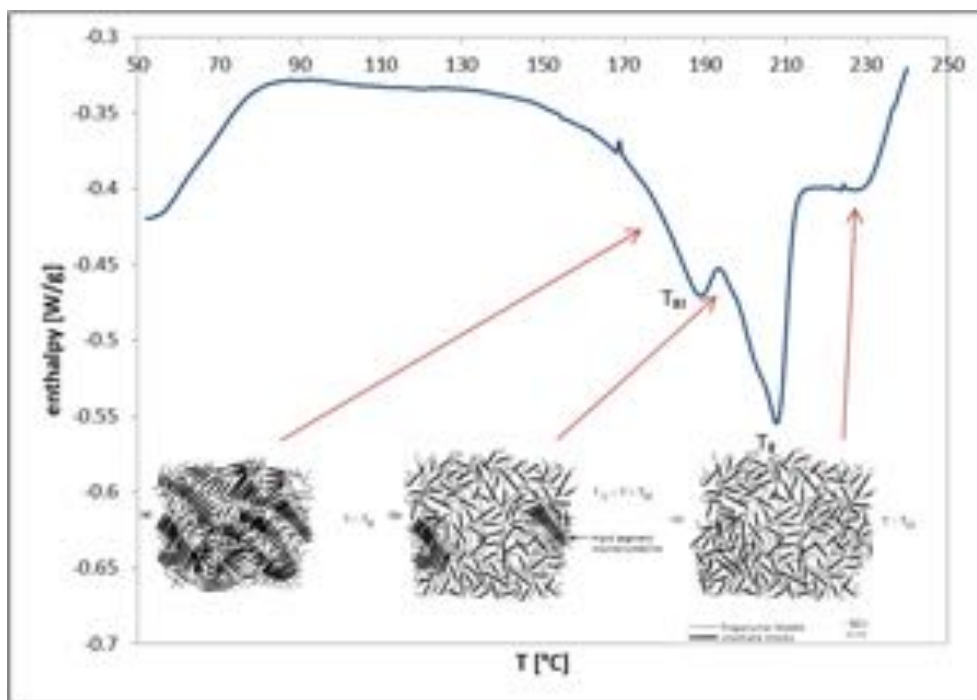


Figure 1.14: Schematic model for the morphological changes that occur during DSC scans of polyurethane elastomers: (a) below the microphase mixing transition temperature; (b) between the microphase mixing temperature and the melting temperature; and (c) above the melting temperature. The microcrystalline hard-segment domains are indicated [93].

1.6.11.2 Thermal degradation of polyurethanes

The thermal degradation of segmented biphasic polymers is well documented in the literature [95–97]. The process usually occurs in three stages: degradation (depolymerisation), dimerisation and oxidation.

A TGA curve is a plot of the mass loss (calculated as a percentage on the original mass) versus temperature. An example of a TGA curve for a polyurethane is reported in Figure 1.15. The three stages described above correspond to three changes in the curve slope, therefore, by taking the first derivative of the curve, also called derivative thermogravimetry (DTG), a characteristic plot with three peaks is observed for polyurethanes (also illustrated in Fig.1.15) [98, 99].

1. In the first stage, which occurs between 200 and 250 °C, urethane bonds break down to release the monomers, alcohols and

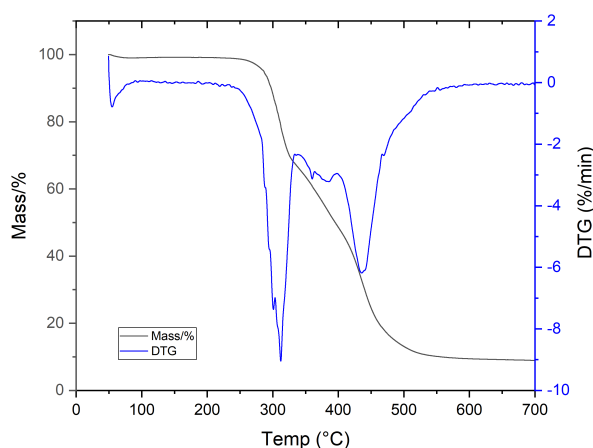


Figure 1.15: Thermogravimetric curve for a polyurethane. Each step in the curve corresponds to part of the sample leaving the heating pan and therefore to a mass loss. The final plateau, at very high temperatures, is the mass of what cannot be burnt or decomposed into volatile molecules: charred organic components or inorganic compounds.

isocyanates, with a reaction which is the reverse of the polymerization itself;

2. In the second stage, the monomers cannot leave the sample because secondary reactions and rearrangements occur between them, leading to more complex and heavier compounds; in particular, isocyanates dimerize into carbodiimides, which then react with the alcohols forming substituted ureas. At this stage, cyclic trimers of the isocyanates may form as well (isocyanurate rings). This kind of side reactions induces a change in the molecular weight and molecular weight distribution of the samples;
3. The third stage is the thermal decomposition (oxidation) of such ureas to give volatile products, which leave the TGA pan, leaving behind as a result a small amount of carbonaceous char as well, especially when the sample chains contains cyclic monomers.

1.7 ELECTROSPINNING: OVERVIEW

Electrospinning is a versatile technique to produce nano e microfibrres starting from polymers dissolved in organic solvent. Given the resemblance of such non-woven fibrous environment to extracellular matrix, electrospun surfaces find application in tissue engineering, but such highly porous materials, with high specific surface, have a much wider potential.

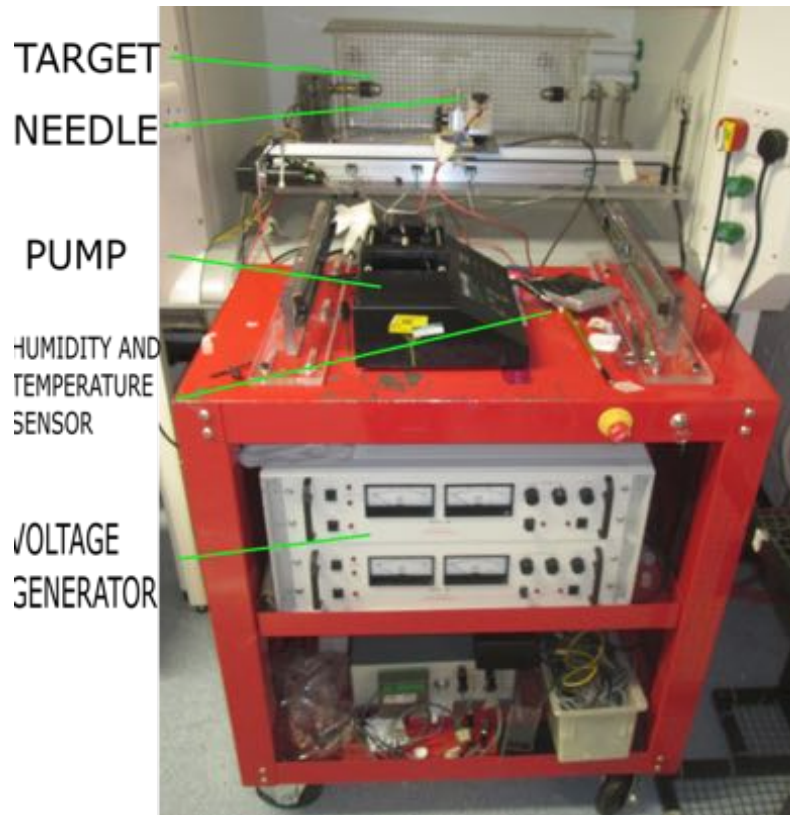
1.7.1 *Electrostatic spinning*

Electrostatic spinning, or electrospinning (ES), is a versatile technique for producing small fibres, whose diameter can range from the nanoscale to the micrometer scale, thus spanning more than four orders of magnitude in size [100]. It has started and gained popularity in the 1990s and it is gaining momentum along with the development of nanoscience and innovative materials. Its set up is flexible and a number of different materials, from plastics to biological to ceramics, can be processed, although the main application is for macromolecules and polymers [101]. For the purpose of the present thesis, the focus will be mainly on synthetic polymeric systems. Normally, polymers are dissolved into a volatile solvent, but they can be melted as well. Melt electrospinning is beyond the scope of this thesis and will not be discussed.

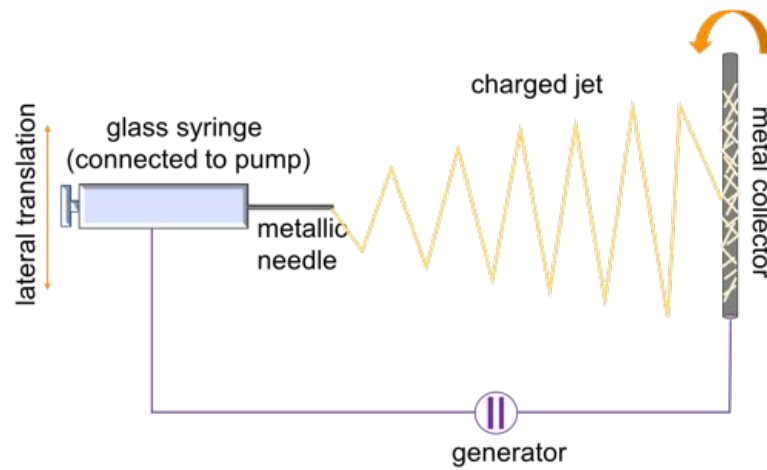
1.7.2 *Electrospinning principles and process*

An electrospinning apparatus is described in Figure 1.16a and is comprised of a metallic needle, fed by a pump, and a target. Electrospinning process is based on an electrostatic field that is generated between the needle and the target, therefore either the needle, the target or both must be connected to a generator (Fig. 1.16b).

A material dissolved in a solvent, usually a polymer, is charged into a reservoir or a syringe connected to a pump. The pump controls the flow of the polymeric solution in a precise way. By pushing the polymeric solution through the nozzle, a droplet will form on the tip



(a) An electrostatic spinning apparatus.



(b) Schematic of the electrospinning process.

Figure 1.16: Electrospinning apparatus and process.

of the needle. The droplet, under the influence of the electrostatic field, whose voltage is in the order of the kilovolts, is elongated into a jet, assuming a conical shape called Taylor cone.

This jet is initially straight, then an instability occurs and the polymeric jet starts bending and coiling into a spiral shape that develops along a conical surface. A second bending instability occurs, and the bending fibre starts coiling on itself, forming a new coil. When a third instability sets in, a further coiling occurs, in a fractal way that stretches the fibre. Sometimes a fourth instability occurs (Fig. 1.17). The whipping movements are extremely fast given the instability of the system, and the fibre is stretched and elongated until it leaves the nozzle [101].

The whipping movements are distributed along a conical shape called Taylor cone, from the name of the first to describe the shape of a charged drop in an electric field. During such process, solvent evaporation rate increases dramatically. The multiple coiling allows the fibre to elongate and increase in length in a small amount of space. At the same time, the energy provided by the electric field is enough to keep the fibre aloft, while, if it was straight, much more would be needed to keep it in air [102]. The whole process takes few milliseconds to occur. Electrospinning is a kinetic reaction rather than thermodynamic.

In order for the droplet to be deformed by the electrostatic field, the solution must be charged. Free charges occur in solution as excess or uncompensated charges, usually in the form of ions, but sometimes originating from the fixed charges on larger molecules, which are less mobile than smaller ions and diffuse slower. Sources of charges are the solvent itself; charges present on the polymer in solution and ionic solutes; impurities coming from the solution container or other sources. Protic solvents, that is, when it has a hydrogen proton bound to an oxygen or nitrogen atom that can be easily donated in solution (H^+), are typical sources of charges.

Surface tension tends to create small droplets, with a smaller surface/volume ratio. When an electric polarity is applied to a charged liquid, the electric forces act upon the droplet until breaking the surface tension and finally a fibre is ejected. Electrospinning is the result

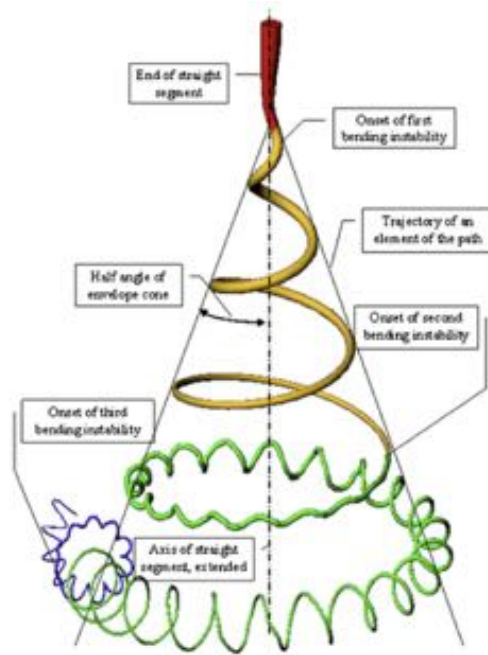


Figure 1.17: Taylor cone [103].

of the balance between electric forces and surface tension (Fig. 1.18). When the first overcome the latter, a droplet forms, which then goes through the space between the needle and the target and lands on the target. Evaporation occurs very quickly and most of the solvent is lost before the fibres reach their target, therefore fibres do not usually undergo major deformation after being deposited [102].

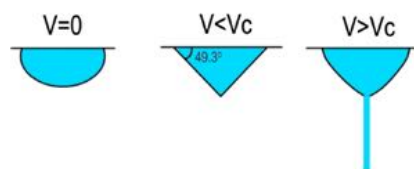


Figure 1.18: Effect of applied potential (V) on charged solution drops (V_c) [102].

1.7.3 Influence of parameters on electrospinning

The production of fibres is a statistical method and the main aim of the technique is to control the distribution of the fibre diameter. Because the technique relies on many different parameters, it is not straightforward to predict the final diameter distribution, and the con-

control on the process is very limited [104]. Electrospinning is the result of the complex interaction of many elements contributing to the process, including electric charges, rheology, shape geometry and properties of the surfaces involved [100].

1.7.3.1 *Voltage*

The effect of the voltage and field intensity are controversial and heavily varying according to the system. Some groups have reported bigger fibres for higher voltages, while other groups report thinner fibres and argue that higher voltages increase the charge density on the surface of the fibres and therefore fibre-fibre repulsion [105].

1.7.3.2 *Needle-target distance*

Several papers have reported opposite effects on the fibre diameter from the distance. On the one side it can be argued that the higher the distance, the more time for the solvent to dry, leading to thinner fibres. On the other hand, a longer distance makes the field weaker by a power factor of two, so electric field is much less strong and fibres are not pulled and stretched in the same way [104].

1.7.3.3 *Flow rate and nozzle diameter*

The flow feed of the needle is influential on the fibre diameter. A higher flow rate produces bigger fibres as the feeding rate produces bigger droplets. At the same time, however, electrospinning cannot occur beyond a critical flow rate. When gravity force is bigger than the electric force, the droplets cannot be supported by the electric field and drop. For some systems, it is possible to determine a flow rate/charge ratio to determine the fibre volume [106].

1.7.3.4 *Relative humidity and temperature*

Relative humidity, as well as temperature, pressure and atmospheric composition, should be strictly controlled in order to obtain reproducible results. Temperature affects directly the system by increasing the evaporation rate, solution density (and viscosity) and relaxation

time. The dew point and therefore the vapour pressure on the solution alters the evaporation rate, which, in turn, influence the charge density on the fibre and finally its diameter. Furthermore, if the atmospheric humidity is high, evaporation from the fibres is more difficult and fibres fuse together, and are deposited in bundles or bend. Atmospheric moisture can increase the occurrence of cross-linking or gellation in the polymer. Such side reactions lead to a higher molecular weight of the polymer chains, which are more difficult to be electrospun. Some research groups have shown how humidity can affect the morphology of the fibres and contribute to porosity [105].

1.7.3.5 *Solvent volatility*

Polarity of the solvent has an important influence as well, as the vapour point is important in determining how quickly the solvent evaporates from the droplet to make fibres. By varying the volatility of the solvent and consequently its evaporation rate, the thickness of the final fibres can be tuned. Volatile solvents contribute towards thinner, neat fibres. In order to control the evaporation rate, tertiary systems can be used, where a high boiling point solvent is coupled with a lower point one to increase or decrease the evaporation rate.

All traces of solvent should be removed by the time the fibres land on the collector, to avoid the fibres to fuse together and form a melded or reticular mat. Incomplete solvent evaporation can lead to change in mass, shrinkage of the final scaffold, porous fibres and faster degradation [104].

1.7.3.6 *Solution concentration and viscosity*

Polymeric solutions concentration varies considerably, and value as low as 1.0% and as high as 40% have been reported, although typical concentrations are lower than 30% to obtain a workable solution. Viscosity depends on the molecular weight of the polymer as well as on the concentration of the solution, temperature and solution system (solvent-polymer interactions, presence of thickening additives). Molecular weight contributes to viscosity by way of the polymeric chains entanglement. Without a certain degree of chain entanglement, however, electrospinning cannot occur [107].

Viscosity has a direct effect on fibre thickness. A certain critical viscosity needs to be achieved in order for electrospinning to occur. At the lower end of the spectrum, electrospinning turns into electro-spraying, a coating process whereby the droplets are not elongated into thin fibres and are deposited directly onto the target. On the other side of the spectrum, electrospinning does not occur when the surface tension cannot be broken by the electric forces. Sometimes very large and irregular ribbons can be produced. In between these two extremes, electrospinning occurs, with the formation of straight fibres [105].

In general, it has been observed that, for a given stable solution, a high concentration or a high viscosity tends to produce larger fibres. Demir *et al.* [108] reports a cubic relation between the average fibre diameter and concentration.

1.7.3.7 Charge

One of the major parameters controlling the results of electrospinning is the magnitude and direction of the electrostatic field. At the same time, the volume charge density of the solution itself has a strong impact on the fibre diameter, as reported by Thompson *et al.* [104]. An increase in charge is one of the factors that contribute to produce straight fibres, as well as to contribute to a smaller diameter.

Charges in solution come from several sources. If the solvent is protic, charges are linked to the pH of the solution. If the solvent is aprotic, the polarity of the solution influences the distribution of charges. It has been observed that the higher the electric constant of the solvent, the smaller the diameter of the resulting fibres, because the solution will be more polarisable and achieve a better distribution of charges.

In addition to the charges of the solution and the characteristics of the applied electric field, polarity of the capillary (whether the nozzle is charged or not, and the sign and magnitude of the charge) and the dielectric properties of the collector can have dramatic effects on the final product.

1.7.4 *Morphological considerations*

1.7.4.1 *Bead formation*

When the solution viscosity is sub-optimal, a bead-on-a-string morphology might occur, whereby the solution surface tension is dominant over the applied field. Fibre formation remains the main process, and intermittently beads are formed. The final result is thin fibres exhibit spherical enlargements (beads) along their axis. This scenario represents a transition between the individual droplets typical of electrospraying and the neat fibres of electrospinning. However, this phenomenon is highly unstable [105].

Beads are common when very dilute solutions or polymers with low molecular weight are used, because their short chains are not able to entangle and cannot form long strings and fibres. A transition regime can be observed, from essentially an all-bead formation (electrospray) – to spindle-like structures – to beads-on-a-string

Possible routes to avoid bead formation are:

- increase concentration or viscosity of the solution;
- increase the molecular weight of the polymer;
- decrease feed rate (the feeding rate should always match the extraction rate, otherwise beads are formed as the voltage cannot form a field strong enough to stretch the fibres);
- increase applied voltage (so that it can create a stronger field and stretch better the fibres);
- increase surface charges on the jet by mixing additives to the solution; or
- decrease surface tension by adding surfactants.

1.7.4.2 *Branching or splining*

Charges are responsible for the a phenomenon called splining, whereby a single fibres branches and a secondary, smaller fibre generates from the main one (see SEM micrograph shown in Fig. 1.19).

Branching occurs when the charge density is too high, causing instability. The excess charge generates undulations on the surface of the coiling jet. Such undulations become high enough to cause a branch of the fibre to become unstable and generate a secondary fibre branching out of the main one. Therefore branching occurs especially at high polymer concentrations and with viscous solutions. In these systems, charges redistribution happens at a slower rate and local concentration may occur. Because of this, the fibre population will exhibit a bimodal size distribution, with thinner fibres branching and sprouting from thicker ones [100].

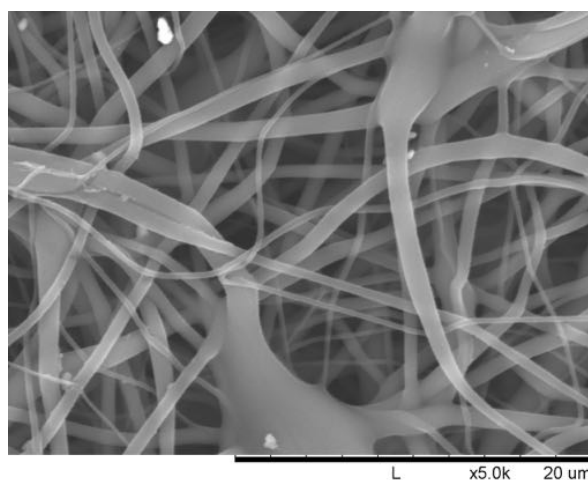


Figure 1.19: Scanning electron micrograph of splining and branching on a polyurethane sample. It is possible to see clearly a bi-modal distribution of smaller fibres alongside with thicker fibres. Some of the smaller fibres originate from the sides of thicker ones.

1.7.4.3 *Fibre alignment*

Electrospun materials are typically a layer of stacked fibres in random directions, creating a non-woven surface. However, techniques have been developed to obtain orientated fibres, for example axially or bi-axially aligned. By acting upon the electric field, fibres can be directed along special force lines. The ability to control the direction of the fibres is fundamental to influence the properties of the materials (mechanical, optical and electric) [109].

1.7.5 Applications of electrospinning

Electrostatic spinning is a technique that is typically used to produce two-dimensional objects, i.e., thin, microporous membranes or sheets. Taking a closer inspection, electrospinning produces “two and a half dimensional” surfaces, because fibres stack on each other and the interconnecting holes makes the surface highly irregular and not strictly flat. However, several techniques have been developed to make fully three-dimensional forms.

Electrospinning is of great industrial interest as a cost-effective manufacturing process. However, the volume production rates are still limited. Given the the large surface/volume ratio of fibres, which increase all those phenomenon occurring at the surface or interface, electrospinning is of particular interest for applications such as catalysis or filtering [110].

Several are the application of electrospinning in regenerative medicine and medical devices, from textiles for wound healing, to the production of scaffolds to mimic the extra cellular matrix.

1.7.5.1 Electrospinning for antibacterial applications

Topography can be modified to increase bactericidal activity of the material. A micro-patterned surface whose dimensions are slightly smaller (50-90%) than the adherent organism can reduce bacterial adhesion. For example, shark-skin inspired micropatterning on PDMS increases the time for biofilms to be formed. In general, a number of polymers work well as antimicrobial surfaces with no need to add any antimicrobial agent or modification, among which PLA, PA, PU and cellulose [59].

Therefore, electrospun surfaces, which show an intrinsic roughness, are promising to offer defence against bacterial colonisation, provided the fibre diameter exhibits the right dimensions. For example, it has been reported in Ogushi *et al.* [111] that submicrometer patterns (<800 nm) lead to decrease in adhesion, while micrometer patterns favour adhesion [61]. The reasons have not been investigated thoroughly, but it might be a combination of surface area and functional

groups pertaining to each polymer (carbonyl, amide, phenyl, nitrile, halogen) [59].

One of the challenges that a shunt catheter faces is degradation over time and the surface changes it entails, which eventually seems to encourage bacteria adhesion [41]. There is still no agreement, however, over how surface roughness influences bacteria adhesion.

It is generally believed that roughness does increase adhesion, although some other studies found that roughness does not influence bacterial attachment significantly. These controversial reports are probably dependent on the bacteria species, the roughness size, how the size is determined, and finally how the adhesion itself is measured. For example, Francolini & Piozzi [43] observes there exists a roughness threshold of 200 nm, above which adhesion increases and below which surface roughness does not influence bacteria adhesion.

1.8 WETTABILITY

In Section 1.6 it was discussed how increasing the surface hydrophilicity as one of the strategies to improve the antibacterial properties of biomedical materials and decrease infection rate.

In order to reduce protein and cell adhesion (inert surfaces), Ostuni *et al.* [58] mentions three characteristics a surface should:

1. have an overall surface charge that is neutral;
2. be hydrophilic;
3. be able to accept hydrogen bonds; but
4. not include hydrogen-bond donors.

Furthermore, a hydrophilic surface should enable the absorbency efficacy of the catheter to be increased, as compared to the traditional design of the catheter.

Wettability is a measurement of the affinity of a surface with a liquid. A material is called hydrophilic when it bears a high affinity with water. Some materials, such as zinc or titanium oxide, are hydrophilic, and turn superhydrophilic (contact angle next to 180°) when irradiated with ultraviolet light. Titanium and zinc oxides can be produced at low temperatures via a sol-gel route.

1.8.1 *Hydrophilicity*

Wettability is a way to measure how the surface interacts with a liquid. For example, if a drop of water (a polar solvent) is deposited on a polar surface, the molecules of water will tend to spread out in order to interact with as much as surface as possible. If, on the contrary, there is less affinity, the molecules will prefer to keep away and the drop will retain its rounded shape. When a droplet of water is laid on a surface in normal atmosphere, the tangent to the droplet profile, where three elements, water, air and material, meet, will set an angle. By observing the angle tangent to the surface of the drop of water, a surface can be defined as hydrophilic when the angle is lower

than 90° , whereas it is hydrophobic when the angle is higher than 90° (Fig. 1.20).

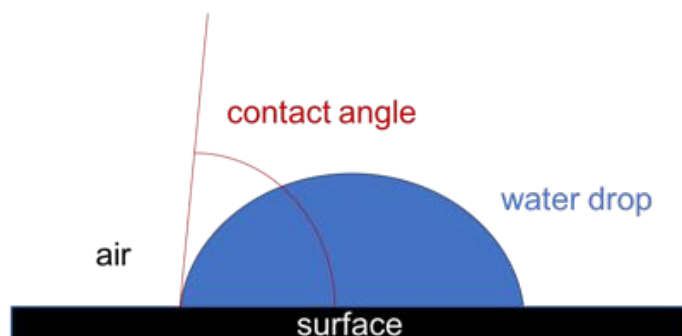


Figure 1.20: Schematic of the sessile contact angle: a drop of liquid is deposited on a surface and the angle between three phases, solid, liquid and air, is measured.




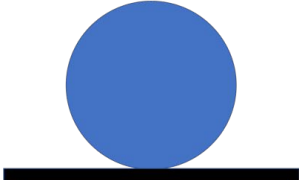
Wettability is a measurement of the collective contribution of polarity and charges on the surface. Polar groups, such as $-\text{OH}$, $-\text{NH}_2$, $-\text{COOH}$, and charged surfaces are more hydrophilic than apolar functionalities (for example, long aliphatic chains or apolar groups such as silicone).

When the surface is so hydrophilic that the droplet will spread and angle will tend to 0° , such phenomenon is called superhydrophilicity, and superhydrophobicity describes its opposite, with contact angles approaching 180° (see Table 1.5).

1.9 SOL-GEL ROUTE TO INORGANIC POLYMERS

The so called sol-gel method is a convenient route to produce a range of solid inorganic oxides, starting from precursors in a solvent (a solution) [112]. The precursors are usually small metallorganic compounds that undergo a series of condensation reactions that create an extensive networking until a final stage of gel is reached. A gel is an amorphous form of oxide. The resulting oxide is not crystalline and the network is usually open and poorly organised, given that the condensation reaction is never fully undergone and it occurs at low temperatures and the energy is not enough to bring the material to a better organised state. This gel can be the starting point for further material transformation.

Table 1.5: Wettability of a surface. Reference liquid (blue droplet) is water.

Contact angle		Description
$\alpha \approx 0$		superhydrophilic
$\alpha < 90$		hydrophilic (good wettability)
$\alpha > 90$		hydrophobic (poor wettability)
$\alpha \approx 180$		superhydrophobic

Sol-gel reaction has been widely employed to make a variety of materials, especially in the form of coatings (thin layers).

The sol-gel reaction follows two routes:

1. metal alkoxide in organic solvent
2. inorganic salt in aqueous solution

Water is usually necessary for such reactions, as it is the source of the oxygen bridging the metal atoms.

The sol-gel process occurs in two steps (illustrated in Figure 1.21):

1. the precursor undergoes hydroxylation, which breaks the M–O–C bonds to create M–OH bonds. This occurs either by changing the pH of the aqueous solution, or by adding water to the organic solvent in the case of alkoxides;
2. condensation stage: from M–OH to M–O–M bonds.

Since condensation process never achieves a yield of 100%, a certain number of M–OH and M–C bonds are retained in the network and therefore the final material assumes an open structure, with gaps

and holes, and dangling -OH and organic groups. The network can undergo annealing if energy is provided to the gel, for example via thermal treatments, which yields denser oxides.

The typical sol-gel reaction can be described as an inorganic polymerization process. The precursors are usually organic complexes of metal ions, dissolved in an organic solvent, or water [113]. The sol-gel reaction is an example of soft chemistry, because it happens in an aqueous solvent, at low temperatures and at environmental pressure.

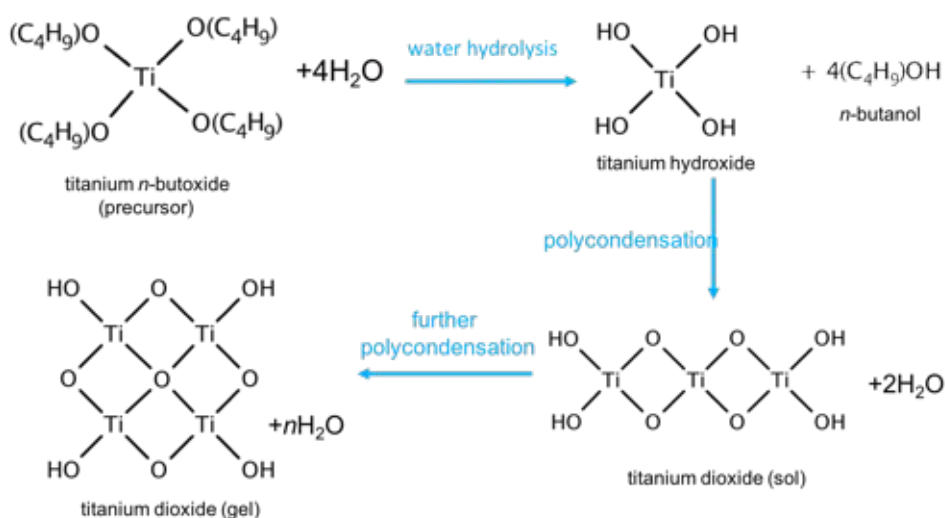


Figure 1.21: Schematic of the sol-gel process. Metal-organic precursors in solution undergo hydrolysis, which creates -OH groups. These -OH groups will then undergo a series of condensation steps with elimination of water and formation of a more or less extended network (called sol or gel).

The reaction kinetics can be tailored by operating on several parameters, for example concentration, temperature, solvent or solution pH. By modifying the precursors, for example by complexation of the metal cation, or by changing the organic ligand, the reaction can be faster or slower. This allows to control composition down to the atomic level, and their structure. The control over reaction rate is very important, as a fast and uncontrolled reaction may result in precipitation of a poorly defined material.

1.9.0.1 *Nonaqueous/nonhydrolytic route*

The condensation reaction usually occurs in presence of water, but another class of reactions can occur even in absence of water, called nonaqueous, or water-free sol-gel mechanism [114, 115]. In such reactions, where water is virtually not present, an alternative source of oxygen must be identified, and it is provided by the solvent (alcohols, aldehydes, ketones or ethers), or by the organic moiety of the precursor itself (alkoxides or acetylacetonates).

Sometimes water can be produced by the reaction itself, so strictly speaking non hydrolytic is not correct, and a better definition would be “non aqueous”, that is, the solvent is not water [116]. Therefore even in absence of water hydrolytic pathway can occur.

Aprotic condensation reactions involve the elimination of a small organic molecule. There are four classes of such reactions:

1. metal halide with alcohol, with alkyl halide elimination;
2. ether elimination;
3. ester or amide elimination; and
4. aldol-like condensation with hydrolysis of the metal alkoxide.

The advantages of such a reaction are several: simple reactions occurring at very low temperatures and with volatile byproducts that are easily removed; avoiding any other organic solvent; better control over homogeneity and stoichiometry of mixed oxides [115].

1.9.1 *Sol-gel and electrospinning*

The sol-gel method combined with electrospinning is a powerful and flexible way to fabricate one-dimensional materials containing metal, metal oxide or metal chalcogenides. It has been widely used to produce nanowires, after calcination and annealing [117], and hollow structures have been produced as well.

Sol-gel method has been employed to produce a variety of hybrid materials, for example metal-polymer, metal oxide-polymer, sulfide-polymer and so on. Such fibres can be followed by calcination to

convert them into ceramic materials or metal oxide/ceramic composite fibres. Through electrospinning, nanoparticles can be synthesised, with a good dispersion in the matrix. Usually, a sol-gel solution is first prepared in the presence of the polymer and then the mixture is electrospun [118].

Nonaqueous route for electrospinning demands for a controlled atmosphere in order to avoid any possible role of atmospheric moisture in the reaction. Therefore the spinning solution should be prepared and transferred into the syringe in anhydrous conditions.

One of the goal of the project is to disperse the metals in the polymer as homogeneously as possible. To achieve a good dispersion and improve compatibility, the sol-gel route was settled upon as an eligible technique. The sol-gel technique relies on organic precursors the would hydrolyse and polymerise during the electrospinning process, creating a network within the polymeric bulk. The metals of choice for the modification of the electrospun polyurethane were zinc and titanium. The organic precursors are titanium(IV) tetra-normal-butoxide and zinc acetate dihydrate, whose structures are shown on Figure 1.22.

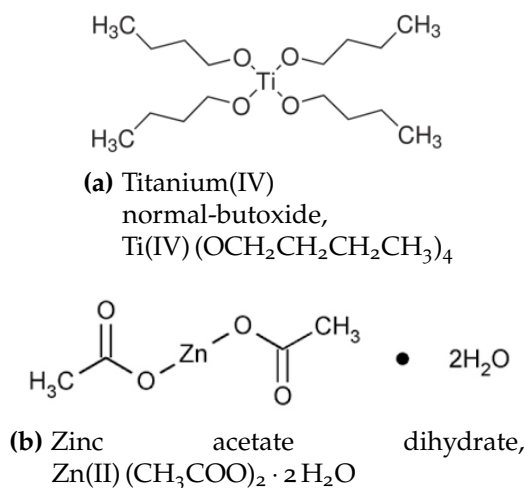


Figure 1.22: Chemical structures of Ti and Zn organic precursors.

1.9.1.1 Sol-gel route for titanium dioxide

Titanium dioxide can be easily prepared via a sol-gel reaction, starting from a titanium precursor (namely, an alkoxide). The titanium

alkoxide solution undergoes a condensation reaction to create a network (called gel) where the titanium atoms are connected by oxygen atoms. The network is usually amorphous, as not all the alkoxide radicals leave during the reaction and remain in the structure, leaving defects, and the reaction occurs too quickly for the atoms to create a crystalline lattice.

Titanium alkoxides tend to react vigorously with water, and an uncontrolled polymerisation could be initiated, leading to gellation and precipitation during the electrospinning process, therefore it is necessary to modify them with a ligand in order to slow down the reaction. For example, a bidentate ligand, such as a carboxylic acid (formic or acetic) create a complex and can be electrospun and mixed with the polymeric matrix.

Sol-gel reaction mechanism usually needs water to occur, but it can be thermally activated as well [114]. At the same time, as the electrospinning process is done in air and not in a controlled atmosphere, the atmospheric water may activate the reaction. Therefore it is difficult to state whether a sol-gel reaction is absolutely water-free or not. Either way, an oxide is obtained.

1.9.1.2 Sol-gel routes to zinc oxide

Usually, zinc oxide is produced following thermal treatment, but several routes to obtain ZnO at low temperatures (room temperature or mild thermal treatments) are reported in literature, mainly based on solution chemistry, such as hydrolysis of zinc salts or alkoxides dissolved in organic solvents, through microemulsion, or electrochemistry [119].

Zinc oxide can be easily prepared via a sol-gel reaction, much alike the titanium dioxide being employed previously in my experiments [120]. Unlike titanium, though, zinc organic compounds are stable in air and water and are therefore less hazardous and easier to handle and react. Only Sinji Harada *et al.* [121] reports the production of a hybrid material by directly mixing the precursor and polyurethane in the same vessel and electrospinning it onto the target.

Zinc acetate dihydrate has a good solubility in a polar solvent such as dimethylformamide (DMF) [122], and is not as sensitive to atmos-

pheric hydrolysis as titanium precursors. Therefore, a quantity of zinc acetate was directly added and mixed to a polyurethane (Z6A1, Biomer Technology, UK) solution in DMF.

In the case of nonaqueous sol-gel reaction, zinc metallorganic compounds are provided with energy through heating, in order to promote polymerisation of the precursors and facilitate the sol-gel reaction. Alkylamines are often added to the solution to complex the zinc metal centre and offer a finer control over the reaction routes. Eventually, non-hydrolytic routes may lead to a lower surface concentration of hydroxy-groups, adsorbed water and organic macromolecules [119].

1.10 RESEARCH AIMS

As it has been explained in Section 1.2.10, the current shunt catheter suffers from a high rate of failure, and, if the valve is to be excluded, the main reasons are bacterial colonisation and obstruction by inflamed or healthy tissue. Another issue that has been flagged in literature is the design of the fenestrations, with the number and layout being criticised for its lack of rationale and low hydraulic efficiency. Both the chemical nature of the standard material and the hydrodynamics of the design lead to poor lifespans and the necessity of frequent revisions of the device, with evident discomfort to the patient and higher risks associated with repeated surgery.

While silicone is a widely employed material for catheters, especially owing to its flexibility and biocompatibility, it exhibits several disadvantages, including being prone to bacterial colonisation. One of the underlying reasons for increased cell and bacterial adhesion on PDMS is that silicone, albeit exhibiting a neutral surface, has been associated with a high contact angle (hydrophobic).

In the general search for new materials and a new design for a shunt catheter, previous research, presented by Suresh & Black [5], suggested the use of a medical grade polyurethane instead of silicone. Their work proposed the use of a microstructured electrospun surface as an alternative to the present silicone catheter device. This different, porous design, as opposed to a continuous surface model, would offer several advantages over PDMS. An electrospun catheter would offer a natural pathway through which the CSF would be absorbed and escape through the microporous structure.

The contact angle of a polyurethane surface, unlike PDMS, is generally around 90° , which indicates a surface neither hydrophilic nor hydrophobic. The wettability of polyurethanes can be explained by their unique chemical nature, which can be simplified as a combination of two different chemical segments exhibiting quite different properties. The main constituent of a polyurethane is a polyol, defined by a long carbon backbone, which is joined to another polyol by diisocyanates. The urethane bonds between isocyanate group and alcohol group are polar and able to create hydrogen bonds, while the

long carbon backbone of polyols is non-polar and hydrophobic. The mixture of the two segments creates a wettability in between.

A biomedical grade polyurethane, provided by Biomer Technology Ltd, is the subject of this work as a replacement form PDMS.

To increase hydrophilicity of the polyurethane, grafting or modification of the surface by introducing hydrophilic moieties was pursued.

The present work recognises that, as a consequence of the much larger surface area to volume ratio of an ES catheter, and surface area exposed to CSF, the potential for cell-surface interactions (microbial as well as autogenous) is far greater. Therefore, the need to develop a catheter material with intrinsic anti-adhesive properties arises, to impart microbial resistance on the one hand, and to minimise mammalian cell-surface interactions on the other.

The present work focuses not on the production *ex-novo* of a polyurethane, but rather on the modification of an existing, medical-grade polyurethane, specifically, to impart intrinsic microbial resistance and minimise mammalian cell-surface interactions by limiting viability and increasing the apoptosis rate. Biomer Technology provides a range of biocompatible polyurethanes for a variety of biomedical applications. The immediate difference between each polyurethane of the range is their HS/SS ratio, which impacts on their mechanical properties. After evaluating each available polyurethane according to their mechanical properties and their readiness to be electrospun, grade Z6A1 was chosen as the most suitable for this work. A sample of cast polyurethane was used as a reference throughout the work.

In order to modify the wettability of the polyurethane, and to confer bioactive properties to the fibres, two kind of inorganic modifiers were added to the matrix of biomedical grade polyurethane. The materials of choice for the modification of polyurethanes were coordination compounds of two transition metals, zinc and titanium. Both these metals were investigated for their bioactivity and antiseptic properties. Moreover, the process method aimed at producing a composite material, whereby the microstructure of the polyurethane was modified by the metal compounds, and the surface properties, in particular its wettability, were influenced accordingly. The materials were incorporated via a sol-gel reaction into the polyurethane.

Wettability is a property that depends not only on the chemistry of the surface, but on the morphology as well. A characterisation of the surface properties was carried out by means of Atomic Force Microscopy and Force Mapping. In order to compare the performance of the electrospun materials with the standard catheter material, a sample of medical grade silicone, PDMS, was used throughout the experiments as a negative reference.

Following their characterisation, materials were exposed to cell from neuronal tissues in order to evaluate their compatibility, toxicity and their influence on viability of cells. An immortalised human astrocyte cell line was chosen for this purposes. Their morphology, adhesion and motility on electrospun surfaces was compared to the standard material, PDMS.

Finally, the efficacy of such materials against bacterial colonisation was tested, using a common bacterial strain found on explanted devices: *Staphylococcus aureus*.

To summarise, the aims of the work described in this thesis were threefold:

1. to achieve the modification of the surface of a biocompatible polyurethane with inorganic modifiers (in order to enhance its wettability) via a sol-gel route and verify the influence of such modification on the physical and chemical properties of the surface;
2. verify the influence of such modification on the growth, viability and motility of immortalised human astrocyte cells; and
3. verify the effectiveness of this modification in limiting bacterial colonisation. The modified materials were cultured with bacteria commonly found in the skin flora and accounting for the majority of shunt colonisations. Growth and proliferation of bacteria were tested against standard controls.

Eventually, the ultimate goal of this work is to lay the foundation for pre-clinical trials required in order to demonstrate beneficial outcomes *in vivo*.

1.11 THESIS OUTLINE

Based on the review of the state of the art, this thesis presents a catheter with a different design, namely with a microporous surface made of a biomedical grade electrospun polyurethane. A wettable surface might improve antibacterial properties and reduce cell adhesion, therefore, in order to modify polyurethane wettability, the materials are modified with titanium and zinc (see Section 1.10).

In Chapter 2 the effects of adding titanium and zinc complexes is analysed and discussed, in particular their impact on the microstructure of the polymer, and the subsequent change in the surface structure. Furthermore, the effect on the morphology of the electrospun materials is investigated, and the properties of a suitable scaffold, ready to be tested for its biological properties, are defined.

In Chapter 3 the functional properties of such materials are discussed, and a surface analysis of the different materials are conducted via Atomic Force Microscopy and Atomic Force Mapping, in an attempt to determine the extent to which these modifications effectively change the wettability properties of the materials at a microscopic scale.

Chapter 4 deals with the translation of the properties of such materials in a biological environment. In particular, its effect on growth and viability of immortalised astrocytes cell line (U373 MG) is assessed. The adhesion of such cells to the substrate is evaluated via a detachment assay and by tracking the motility of cells on different substrates through time lapse microscopy. These data are used to evaluate how effective the new materials are in reducing the adhesion of cells as compared to PDMS.

Finally, substrates are exposed to a common bacterial strain responsible for shunt catheter failure, namely *Staphylococcus aureus*, and the effects on the bacterial cultivation are discussed, in order to assess how the new materials compare to the standard against infection.

From the data collected through such biological assays, an assessment of the suitability of modified electrospun materials as an alternative to the current material used for shunt catheters is made in Chapter 5.

FABRICATION AND CHARACTERISATION OF MODIFIED ELECTROSPUN POLYURETHANE

2.1 INTRODUCTION

Electrospinning is a flexible technique used to produce materials made of usually randomly aligned polymeric fibres with a very high length-to-width ratio, and high specific surface.

With the aim of producing a porous and permeable material for shunt catheters, this chapter focuses on the synthesis of an electrospun polyurethane membrane, functionalised either with titanium and zinc, and the morphological analysis of the same, while at the same time comparing it with a similar electrospun surface containing no metals as a benchmark. Polyurethane is modified with titanium and zinc via a sol-gel reaction that will happen simultaneously with the electrospinning process. In this chapter, the morphology of the fibres (in particular their diameter distribution), as well as the effectiveness of the sol-gel reaction, along with some considerations on the distribution of titanium and zinc within the fibres.

The morphological structure of titanium and zinc is discussed, as well as the impact that electrospinning and metals make on the microstructure of polyurethanes themselves.

2.1.1 *Materials selection*

As discussed in Section 1.6, polyurethanes are biocompatible polymers and have a long history of application in biomedical devices, especially in the cardiovascular field, for example balloons, flexible catheters, heart valves and blood vessel grafts. Their good flexibility is matched by appropriate mechanical resistance. This makes polyurethanes a suitable alternative to silicone for shunt catheters. It should be noticed that, unlike polyurethane, polydimethylsiloxane cannot be

electrospun, because it cannot be dissolved in a suitable solvent for electrospinning in its polymeric form.

Biomer Technology Ltd. provides a wide range of medical grade polyurethanes, which are listed in Table 1.4. They are biocompatible and have a proved record of being successfully used for other medical devices. Of these, Z6A1 in particular was selected for use in this research.

The decision was based in part on the ease with which each polymer could be electrospun: the range of available polyurethanes was tested according to their propensity to being electrospun, and while some grades were more difficult to be electrospun at the conditions of the laboratory environment (in particular, they proved to be particularly sensitive to humidity and voltage set-up), some others were more versatile and workable, in particular Z6A1, providing reproducible results.

Furthermore, Z6A1 grade has a higher concentration of hard segments. This would make the change in microstructure provided by the addition of titanium and zinc more evident and easily detected. Therefore Z6A1 has been used as the material of choice throughout this research. A sample of unmodified electrospun Z6A1 (reference to as ES) and unmodified cast Z6A1 (referenced to as 'cast') are used as controls in each analytical technique.

2.1.2 *Electrospinning*

Electrostatic spinning relies on the creation of a strong electric field between a material-oozing needle and a target. The charged solution, emerging from the tip of the needle, is dragged and elongated by the electric field and lands on the target in the form of a very thin fibre. Eventually, a mat results as the stacking of multiple fibres with no preferential alignment.

The modification of electrospun fibres with titanium and zinc was achieved via a sol-gel reaction. Sol-gel is usually conducted in solution, but in the case of electrospinning, no water should be introduced into the polyurethane:DMF solution, to avoid a disordinate polymerisation of the polyurethane in solution, ahead of the deposition into

fibre form. Therefore, anhydrous route for the sol-gel reaction was attempted. As electrospinning was not conducted in an enclosed environment, water vapour, naturally present in the laboratory environment, should aid the sol-gel reaction during the deposition of the fibres. Besides, one of the precursors, zinc acetate dihydrate, includes two molecules of water in its molecular structure, thus providing the source for water itself.

2.1.3 *Differential scanning calorimetry*

Differential scanning calorimetry (DSC) is a powerful analytical method to get an insight of the structure of a material, and provides the melting and burning temperatures, as well as transformations of the internal structure. DSC is a thermal analysis technique that quantifies the amount of energy that a sample absorbs or releases upon heating the sample at a constant rate (heat flow rate, $\phi = dq/dt$).

While the sample is heated, it absorbs energy at a constant rate, and the curve on the graph is flat. Instead, each change in the quantity of energy that is absorbed by the sample is a transition that is reflected in the differential heat flux relative to the reference (empty pan). Namely, a first-order transition occurs when the sample goes from solid to liquid and melts. This transformation corresponds to a net absorbance of energy by the sample while, at the same time, the temperature does not increase, and the graph exhibits a dip in the curve. A second-order phase change occurs when the internal structure rearranges (crystalline phase changes, for example), and in this case the graph will show a change in the slope of the curve [123].

2.1.4 *Thermogravimetric analysis of polymers*

Among the thermal analyses techniques, thermal gravimetric analysis (TGA) quantifies the weight loss occurring in a sample while bringing it to high temperatures, either in reactive (oxidising) atmosphere (air or oxygen) or in an inert atmosphere (for example, nitrogen). The energy provided to the molecules of the sample allow for chemical bonds to change and break, leading to the formation of dif-

ferent chemical species that are usually shorter than the original polymeric chain and therefore more volatile. The volatile compounds (oxides of carbon and nitrogen such as aldehydes, ketones, CO_2 , water) leave the sample, while the inorganic oxides (ashes) and incombusted organic remains (char) are left in the pan.

Curves obtained by plotting the mass versus the raise in temperature provide an insight on the mechanism of thermal decomposition and the original structure of the polymeric component, while the unburnt residuals of a sample can identify the heat resistant or inorganic components of the material being analysed, and their amount (weight percentage) determined.

2.2 MATERIALS AND METHODS

2.2.1 *Polyurethane selection criteria*

Polyurethanes from the A1 range, series b₉TM, provided by Biomer Technology Ltd. (Runcorn, UK), were chosen as the material for the present study. All the available polyurethanes, namely Z1, Z2, Z3, Z4, Z6 and Z9, were initially screened to determine the most suitable one, in terms of ease to electrospin, flexibility and mechanical properties. While the lower numbers of the range (Z1 and Z3) give soft, prevalently stretchy materials, a sample of Z9, on the opposite end of the range, is tough and not very flexible. Determining the right concentration and the set of parameters that lead to a reliable, consistent electrospun product was another factor to influence the choice of the right polyurethane. Eventually, Z6A1 was chosen as a suitable polyurethane for the project.

Information on the molecular weights are available only for Z3A1 (M_n -143,566, M_w -272,857) and Z9A1 (M_n -100,000, M_w -197,000), so it is inferred that the average molecular weight for Z6A1 should be around 200,000 Dalton [124]. Series A1 polyurethanes provided by Biomer Technology Ltd. are polyether-urethanes made of poly(tetramethylene oxide) (PTMO, polyether diol, molecular structure is shown in Figure 1.9), 1,2-butane diol (Fig. 1.11) and 4,4'-diphenylmethane diisocyanate (MDI) (Fig. 1.10).

2.2.2 *Cast films*

Polyurethane pellets were dissolved in dimethylformamide (DMF, Sigma-Aldrich, UK) to reach an appropriate concentration (15% w/w). A quantity of the solution was then poured into a clean glass petri dish to cover the bottom and dried in the oven under vacuum at 80 °C for 24hr. The cast films were then washed with water and air-dried.

Modified cast films containing Ti and Zn to be used as a direct comparison and benchmark across the testing could not be cast in a way to obtain comparable results to their electrospun modified counterparts. Indeed, the way titanium and zinc modified materials were manufac-

tured (sol-gel method) is sensitive to external humidity. Precursors were added to a DMF:Z6A1 solution, mixed and poured into a clean glass petri dish, and dried in the oven under vacuum at 80 °C for 24hr. Casting method in laboratory conditions, however, could not prevent humidity from interfering with the sol-gel reaction and caused titanium and zinc precursors to precipitate, creating bubbles and visibly dishomogenous areas in the film. Therefore, films produced this way were not deemed suitable for direct comparison with their electrospun counterparts, and were discarded from the rest of the characterisation and testing.

2.2.3 *Electrospinning of the reference sample (ES)*

The electrospinning apparatus, as used for the present project, was composed of the following components: a high-voltage supply (Alpha IV, Brandenburg, Applied Kilovolts Ltd., UK), a glass syringe with a blunt stainless steel needle of 20 G (Vicarey Davidson, UK), a syringe pump (PHD 2000 Infusion, Harvard Apparatus UK), a PVC tube that connects the syringe to the needle, and a grounded stainless steel collecting drum (radius 2.3 cm) connected to a high-speed motor.

Randomly aligned fibres of pristine PU as well as hybrid materials were deposited on a collector rotating at a speed of 200 rpm (corresponding to a linear velocity of 0.48 m/s). After different tests to identify the most suitable voltage/ distance/ flow combination, an ideal voltage difference of 5 kV was applied to the needle and -10 kV to the collector. The syringe pump was set at a very small flow rate of 0.3 mL/h.

The experimental voltage had to be carefully selected, as higher voltages can cause instability in the PU solution, while lower voltages are not strong enough to draw and create fibres. In the case of polyurethanes, it has been noted that the electrospinning process occurs more easily if the needle is slightly positively charged, while the target is negatively charged. As polyurethanes are negatively charged and tend to repel each other, an injection of positive charges might reduce the repulsion between the single polymeric chains. The re-

pulsive charges between chains and fibres during the electrospinning process lead to randomly aligned scaffolds.

One of the major factors influencing the final aspect ratio and morphology of electrospun fibres are the electric field and viscosity of the polymeric solution. As viscosity could not be determined experimentally, the only parameter that could be controlled was the concentration of charges in solution. In the experimental setup of this thesis, the electric field has been kept constant for all samples.

The collecting drum was maintained at a distance of 15 cm from the tip of the needle and the electrospinning process was conducted in a laboratory fume hood. Temperature and atmospheric humidity were recorded using a humidity sensor (Humidity Alert II, Extech Instruments, USA).

A summary of the experimental settings for each sample are reported on Table 2.1.

Electrospun scaffolds were produced following a protocol based on Andrews *et al.* [125]. Poly-ether-urethane beads (Z6A1, from the b_9 'A1' series provided by Biomer Technology Ltd., UK) were vacuum dried in the oven overnight. A solution was prepared by mixing polyurethane pellets with anhydrous dimethylformamide (DMF, Sigma-Aldrich, UK) in a dried glass vessel and leaving the vessel on a rolling mixer overnight. The solution was then transferred into a glass syringe and electrospun. Solution concentration for each sample and their relative electrospinning conditions are summarised in Table 2.1.

2.2.4 *Electrospinning of modified materials*

Samples with increasing concentration of inorganic modifier were prepared. The same molar concentration of metal cation was achieved in correspondent samples in the titanium and zinc set. The charge density of the titanium cation is 362 C/mm^3 , for the Zn(II) cation is 112 C/mm^3 [126]. Molar concentration was prioritised over other factors, in order to be able to compare the effect of the two different metals on the morphology of the fibres and, later on in this work (Chapter 4), their biological effect. A summary of quantities of inorganic precursor/polymer ratio can be found in Table 2.2.

2.2.4.1 Titanium

Titanium dioxide-polyurethane hybrid materials were produced according to the following procedure: titanium n-butoxide (97%, Sigma-Aldrich, UK) was extracted with a fresh hypodermic syringe from its bottle and poured into a vessel where acetic acid had been previously poured. Acetic acid was mixed in large molar excess (1:1 w/w). The solution was then briefly vortexed in order to allow for the acetic acid to complex the titanium precursor and then syringed into the polymer solution. An optimal solution viscosity for Z6A1 in PU for Ti-modified samples was found to be 17% w/w. The jar was mixed for at least 30 minutes on a rolling mixer. The solution looked transparent, clear and homogeneous but verging on yellow. The solution was then transferred into a glass syringe to be electrospun on a cylindrical metallic target.

Three different precursor quantities were chosen arbitrarily as a fraction of the polymer weight, namely $1/2$, $1/3$ and $1/7$, to represent, respectively, three different degrees of modification ($1/2$ being the highest). Each electrospun sample was then washed in water and air-dried.

2.2.4.2 Zinc

Zinc acetate dihydrate (Sigma-Aldrich, UK) was directly added and mixed to a polyurethane solution, 15% w/w in DMF in three different polymer:zinc acetate weight ratios ($1/3$, $1/5$ and $1/10$). The solution was mixed on a roller mixer for 2 hours at a temperature of 60°C in order to catalyse the sol-gel reaction and then aged for 24 hours before electrospinning. The ageing step was introduced to initiate the sol-gel reaction (see for example Turinske *et al.* [127] and Li *et al.* [128]).

The ratios of titanium:Z6A1 and zinc:Z6A1 were chosen in order to yield a comparable number of moles in equivalent samples. The quantities for each sample are specified in Table 2.2.

Table 2.1: Electrospinning parameters for the production of each sample.

	Z6A1/ precursor ratio	short name	PU concen- tration in DMF [w/w %]	needle- target distance [cm]	needle- target voltage [kV]	flow [mL/h]	humidity/ temperature/ dew point [%/ °C/ °C]	rpm
electro- spun Z6A1	-	ES	15	15	+5/-10	0.3	31/ 22.3/ 4.3	200
Z6A1: Ti(O ⁿ Bu) ₄	2:1	Ti2	17	15	+5/-10	0.3	22/ 25.2/ 1.9	200
	3:1	Ti3	17	15	+5/-10	0.3	29 / 20.8 / 2.7	200
	7:1	Ti7	17	15	+5/-10	0.3	28 / 21.1 / 1.8	200
Z6A1: Zn(OAc) ₂	3:1	Zn3	15	15	+5/-10	0.3	24 / 22.4 / 0.9	200
	5:1	Zn5	15	15	+5/-10	0.3	30 / 21.5 / 1.6	200
	10:1	Zn10	15	15	+5/-10	0.3	24 / 21.5 / 0.1	200

Table 2.2: Mass and molar quantities of metal precursors for each sample.

	Z6A1/ precur- sor ratio	short name	m pre- cursor/ mass of Z6A1 [w/w]	MW precur- sor [g/mol]	n [mmol]	final PU concen- tration [%]
Z6A1:	2:1	Ti2	0.46	340.32	1.35	68
Ti(O ⁿ Bu) ₄	3:1	Ti3	0.31		0.91	76
	7:1	Ti7	0.155		0.46	87
Z6A1:	3:1	Zn3	0.3	219.5	1.37	77
Zn(OAc) ₂	5:1	Zn5	0.2		0.91	83
	10:1	Zn10	0.1		0.46	91

2.2.5 Scanning Electron Microscopy and Energy Dispersion Spectroscopy

Electron microscope images of all samples were acquired using a scanning electron microscope (Tabletop Microscope TM-1000, Hitachi High-Technologies, Japan) operating at an accelerating voltage of 15 kV with a 6.88 mm working distance. The samples were first platinum-coated to improve the sharpness of the images with a sputter coater in argon atmosphere (SEM coating system, E5175, Series IIHD, Biorad Polaron Division, USA).

Elemental analysis was performed with Energy Dispersion Spectroscopy (EDS) unit fitted on the same SEM.

The platinum coating adds few layers to the fibres and this might influence the fibre diameter results. The coating thickness can be calculated according to the following equation:

$$d = kiVt$$

where

d thickness of the coating [Å]

V is the voltage setting [kV]

k is a constant depending on the gas and is 0.017 for argon

i is the current: 20 mA

t is the time, 30 s

When substituting the experimental settings into the formula, d is 60 Å (6 nm) per repeat. The coating process is repeated between 4 and 6 times, resulting in a coating of thickness between 24 and 36 nm.

Given the average thickness of the smaller fibre distribution is around 170 nm, the contribution given by the coating is around 14 – 21%, depending on the sample (the smaller the diameter, the higher the contribution).

Fibre thickness was determined by analysing Scanning Electron Micrographs (magnification $\times 10000$) with a plugin (DiameterJ, version 1.018) included in the software ImageJ (Fiji). The protocol is described in Schneider *et al.* [129] and Hotaling *et al.* [130]. The software segmented each pictures into a black and white (binary) picture, therefore each fibre appeared as a white shape against a black backdrop. The software then calculated the semi-distance from the edge to the centre of each fibre, and all semi-distance were collected into bins to create a distribution histogram.

At least three images were acquired from each substrate (magnification $\times 10000$). A separate histogram was produced for each image. By adding all counts together, distributions would merge and become too broad, and the cumulative error would affect the measurements. Instead, fitting was run on each histogram separately with a gaussian fit with Origin 8.6 software. A final diameter average was calculated as the weighted average of the centre of distributions.

2.2.6 *Fourier-transform Infrared spectroscopy*

Attenuated total reflection-Fourier transform Infrared spectroscopy (ATR-IR) was performed using a FT-IR spectroscope coupled with a thermogravimetric analyser (STA449F1 Jupiter, Netzsch, Germany). Spectra were collected from 20 scans, within a range of 400 cm^{-1} – 4000 cm^{-1} using a resolution of 2.0 cm^{-1} .

2.2.7 *Thermal analysis*

Thermal analyses were carried out with a thermogravimetric analyser (STA449F1 Jupiter, Netzsch, Germany). The samples of 10 mg each in a refractive alumina pot were heated from 50 to 700 °C with a single thermal ramp at a heating rate of 10 K/min in nitrogen atmosphere. Baseline calibration was performed at the same conditions with empty pans.

2.2.8 *Statistical analysis*

The quantitative data presented in this chapter (fibre diameter) are expressed as mean values \pm standard deviation.

All experiments were conducted in triplicate ($n = 3$).

Statistical significance was determined following one-way analysis of variance (ANOVA) with post hoc testing according to Tukey's procedure at a 95% confidence level (using Minitab, software version 17).

2.3 RESULTS

2.3.1 *Scanning Electron Microscopy*

The electrospinning parameters used for the fabrication of scaffolds were previously optimised by controlling voltage, flow rate, solution concentration, rotation speed and distance between the tip and the target.

Figure 2.1 shows SEM images of the electrospun scaffolds at three different magnifications.

SEM images of the different substrates show randomly aligned, bead-free and well defined fibres, whose dimensions range in the nano and micrometer domain.

Diameter size frequency distribution examples, as extrapolated from $\times 10000$ magnified images, are shown in Figure 2.2. The example refer to the histogram as produced by the DiameterJ plugin (available with the software Fiji) when applied to a single image. $\times 10000$ magnification has been chosen for diameter analysis because the area of interest is wide enough to collect a good number of fibres, and for the smallest fibres to be big enough for the error associated to the software algorithm to be negligible.

For unmodified PU, the distribution ranges from $0.17\ \mu\text{m}$ to $0.98\ \mu\text{m}$ and the average diameters are collected around at least four major peaks, showing a broad multimodal distribution.

For modified materials, instead, the distribution is narrower and more uniform, leading to a unimodal distribution.

By plotting the variation of the average dimension of the fibres against the concentration of precursor in the initial solution (Fig. 2.3), it appears there is indeed a relation between the two quantities. The higher the concentration of precursor, the smaller the diameter. The relation appears to be linear in materials modified with zinc, while for Ti-modified materials the relation appears to be exponential, although more experimental points would be necessary to confirm it.

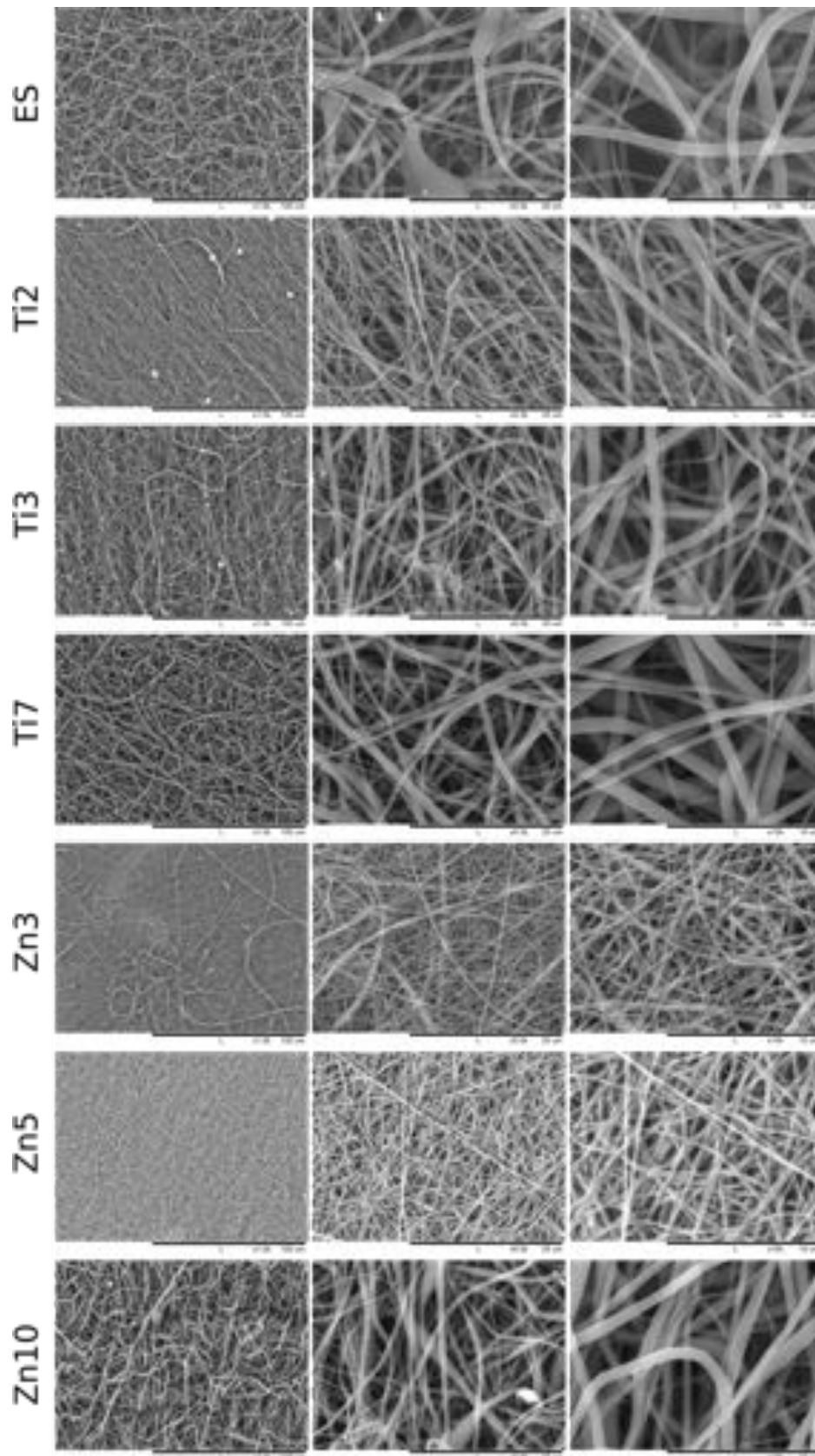


Figure 2.1: SEM images of ES, Ti2, Ti3, Ti7, Zn3, Zn5, Zn10, at x1000, x5000 and x10000 magnification respectively. Size scale is reported at the bottom of each micrograph.

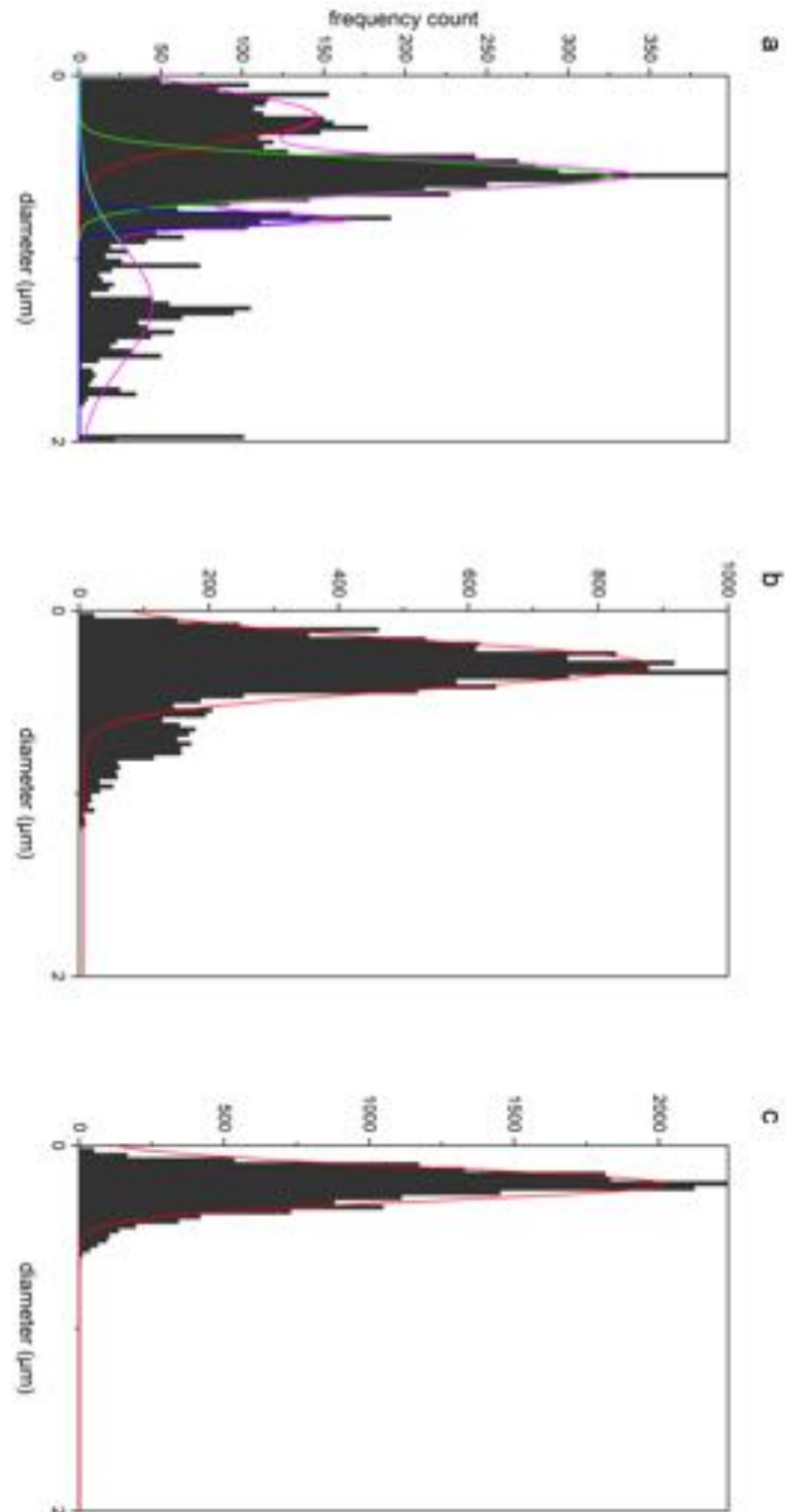
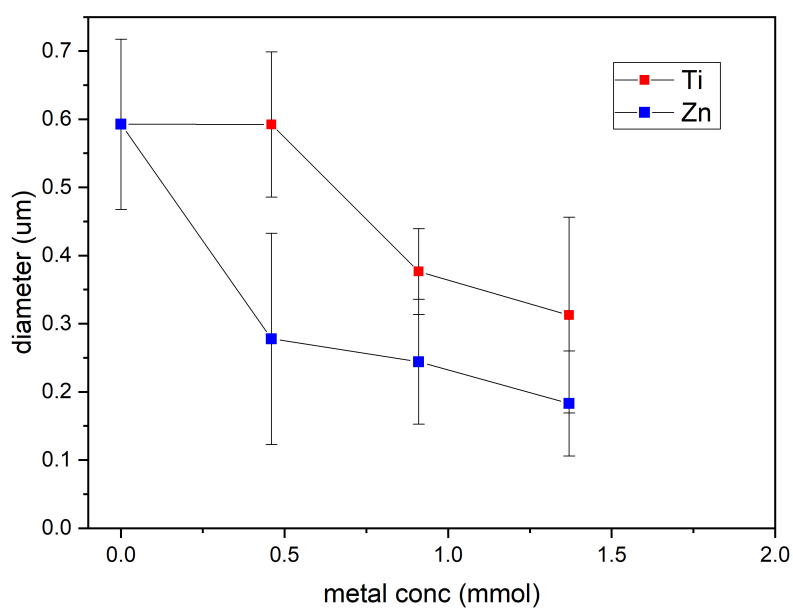


Figure 2.2: An example of gaussian interpolation of distribution histograms of the diameters of the following samples: a) ES, b) Ti₂ and c) Zn₃. From the interpolated curve it is possible to obtain the centre and the size of the distribution.

Table 2.3: Average fibre diameter for Ti and Zn-modified electrospun materials, and unmodified electrospun polyurethane.

	1st peak [μm]	2nd peak [μm]	3rd peak [μm]	4th peak [μm]
ES	0.17 ± 0.06	0.59 ± 0.13	0.85 ± 0.04	0.9778 ± 0.0001
Ti7	0.59 ± 0.11	0.97 ± 0.11		
Ti3	0.38 ± 0.06	0.608 ± 0.002		
Ti2	0.31 ± 0.14	-		
Zn10	0.28 ± 0.15	0.65 ± 0.16		
Zn5	0.24 ± 0.09	-		
Zn3	0.18 ± 0.08	-		

**Figure 2.3:** Average diameter of the first peak plotted against the molar concentration of modifier precursor for each of the two sets of materials, Ti and Zn.

2.3.2 Energy Dispersion Spectroscopy

Energy Dispersion Spectroscopy (EDS) spectra (shown in Figure 2.4) confirm the presence of zinc and titanium on all the modified materials.

The high peak at very low energies accounts for the elements with atomic number lower than 19, in particular the elements that form the backbone of the polymers (carbon, oxygen, hydrogen, nitrogen) and further impurities present in solution.

No element with atomic weight higher than 19 (detectability threshold), other than zinc or titanium, is present in concentrations high enough to be detected, but impurities contribute to the background profile.

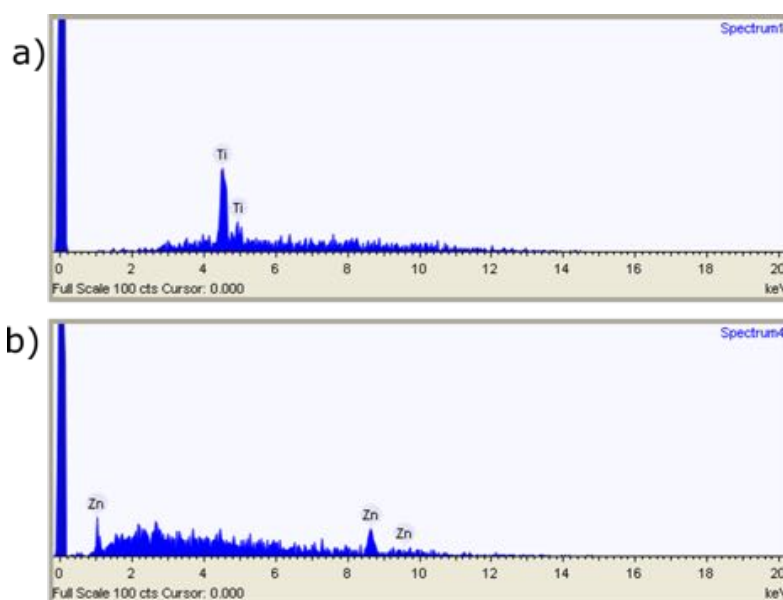


Figure 2.4: Selected Energy Dispersion Spectrogram for titanium and zinc-modified electrospun mats, representing Ti2 and Zn3. The elemental peaks for Ti and Zn, respectively, are indicated. Additional spectrograms pertaining to the remaining samples are to be found in Appendix A.2.

2.3.3 FT-IR

Only the absorbance spectrum for selected samples are reported in Figure 2.5. Small differences in the position of the characteristic bands

between cast and modified samples are highlighted. Inserts report a magnification of the areas of interest, while the exact position of the peaks are reported in Table 2.4.

Table 2.4: FT-IR peak positions for N–H and C=O groups of cast, ES and Ti and Zn-modified samples. A slight shift towards lower wave numbers can be noticed in the NH values for Ti samples, and a shift towards higher wave numbers in the H-bonded C–O values for all the modified samples.

	H-bonded (NH) [cm ⁻¹]	free (C=O) [cm ⁻¹]	H-bonded C–O [cm ⁻¹]
cast	3323	1729	1698
ES	3322	1729	1699
Ti7	3316	1730	1702
Ti3	3316	1730	1702
Ti2	3313	1730	1702
Zn10	3323	1730	1701
Zn5	3320	1730	1701
Zn3	3318	1730	1701

In particular, two of the most characteristic peaks are reported, that is, N–H stretching and C=O stretching. Such bands are indicative of the inter- and intramolecular hydrogen bonds between neighbouring polyurethane chains, namely, between a N–H group on one chain, or on a chain segment and a –C=O group on another chain or chain segment. A hydrogenated bond vibrates at a lower frequency than a non-hydrogenated one. From the spectra, the C=O band is comprised of two superimposed bands, one at around 1730 and the other at 1700 cm⁻¹, which may suggest the presence of both the hydrogenated and non-hydrogenated forms in both modified and unmodified samples.

Modified samples exhibit lower peak intensity, probably due to the lower polyurethane ration in the material. The height of the peaks is diminished accordingly.

Ti-modified samples show a shift in the N–H vibrational frequency to lower frequencies, as well as a broadening of the peak, and this shift is proportional to the quantity of modifier in the material. This

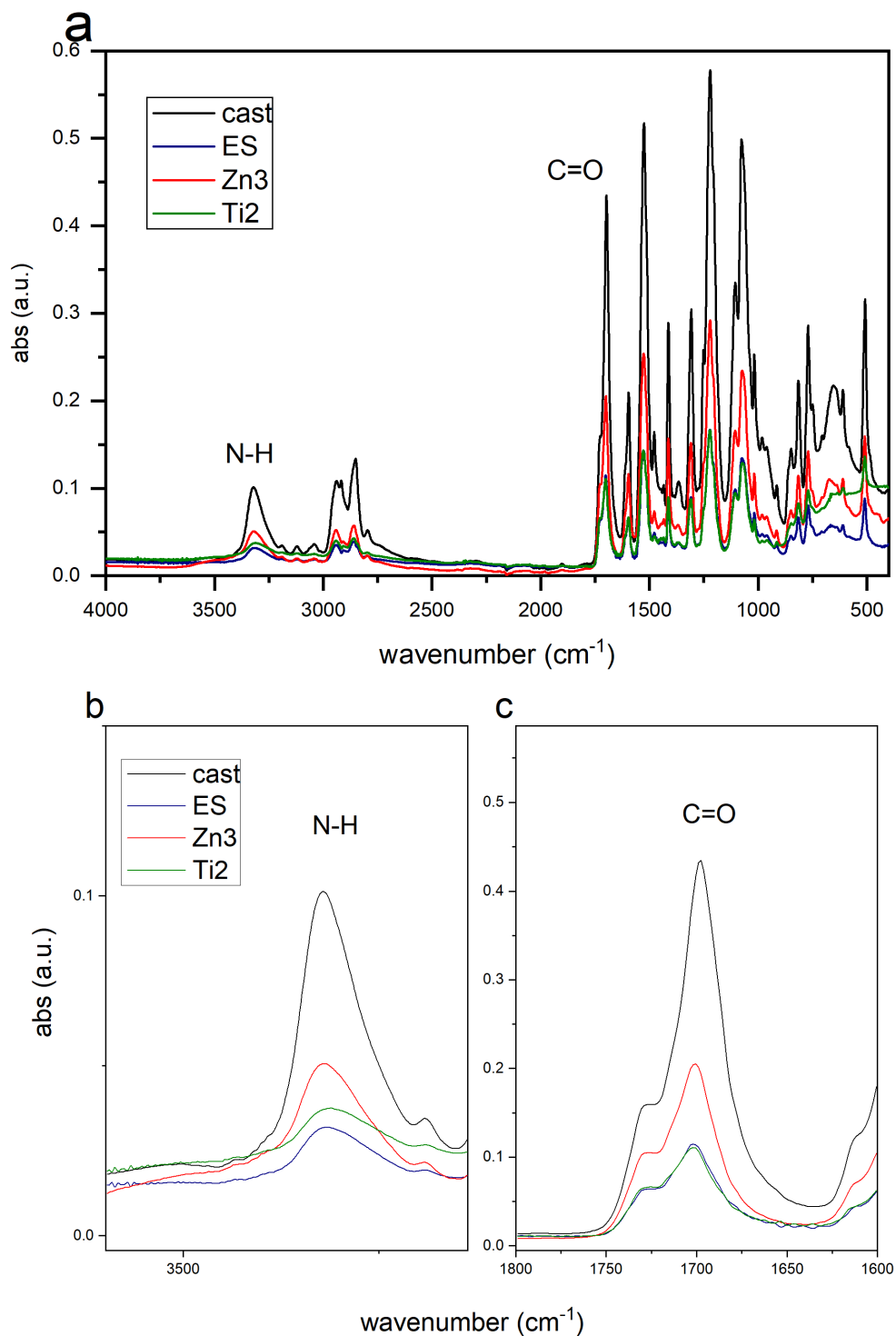


Figure 2.5: a) Absorbance ATR-IR spectra of cast, ES, Ti2 and Zn3 modified samples taken in the 4000 cm⁻¹ to 400 cm⁻¹ region. Inserts b) show details for N-H and C=O vibrational modes. Additional spectrograms pertaining to the remaining samples are to be found in Appendix A.3.

seems to suggest an increase in bonds engaged in hydrogen bonds, and, therefore, a higher degree of N–H bonded to C=O.

Zn-modified samples, instead, do not exhibit substantial differences as compared to cast and ES materials.

A small shoulder is present around 3450 cm^{-1} in the spectra of Zn3 and Zn5 samples, suggesting the presence of free (not bonded) –NH groups [83, 131].

No broad and strong –OH band can be seen, so there might be little free –OH. Most of the –OH bonds are interacting with the –NH group.

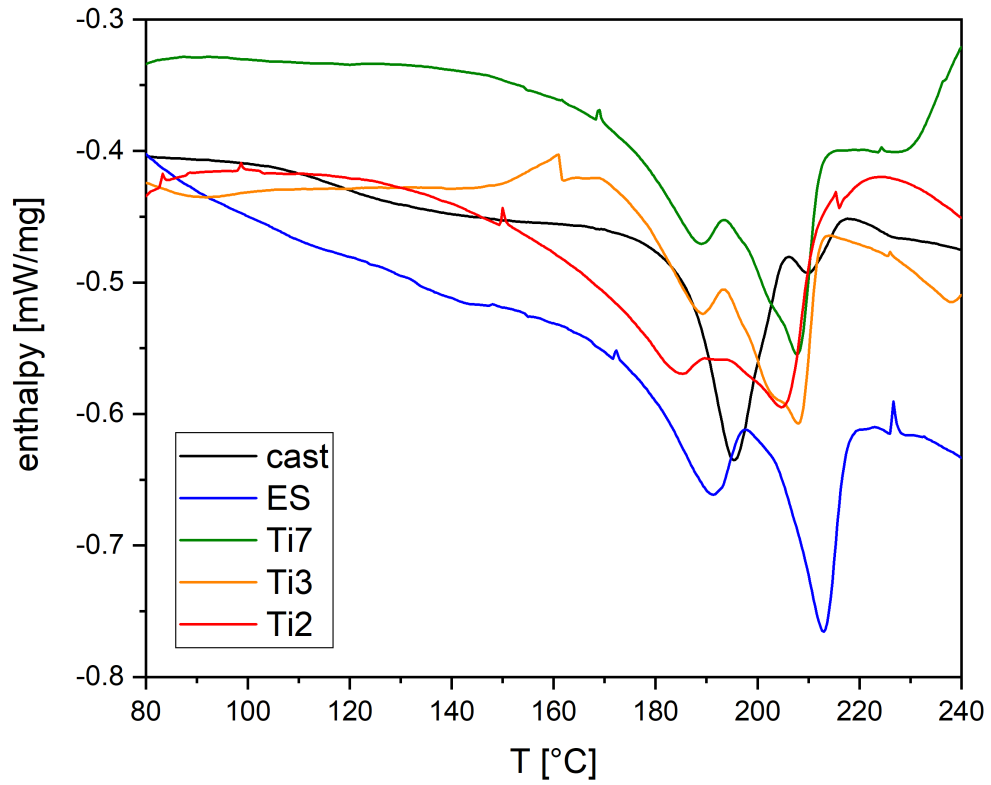
Inorganic materials present a fingerprint region exhibiting peaks at lower wave numbers; these peaks very often overlap with secondary vibrational modes of polyurethane bonds, though, contributing to the background. Therefore, FT-IR does not provide any more information on the bonds between the metallic centres (Zn and Ti) and other functional groups. Still, peaks on 700 – 600 region of Ti2 and Ti3 are better resolved than the other samples and can be attributed to Ti–O–Ti vibrational modes [132]. Zn3 has a peak at 445 cm^{-1} that could be attributed to the Zn–O bond as well [133].

2.3.4 Differential Scanning Calorimetry

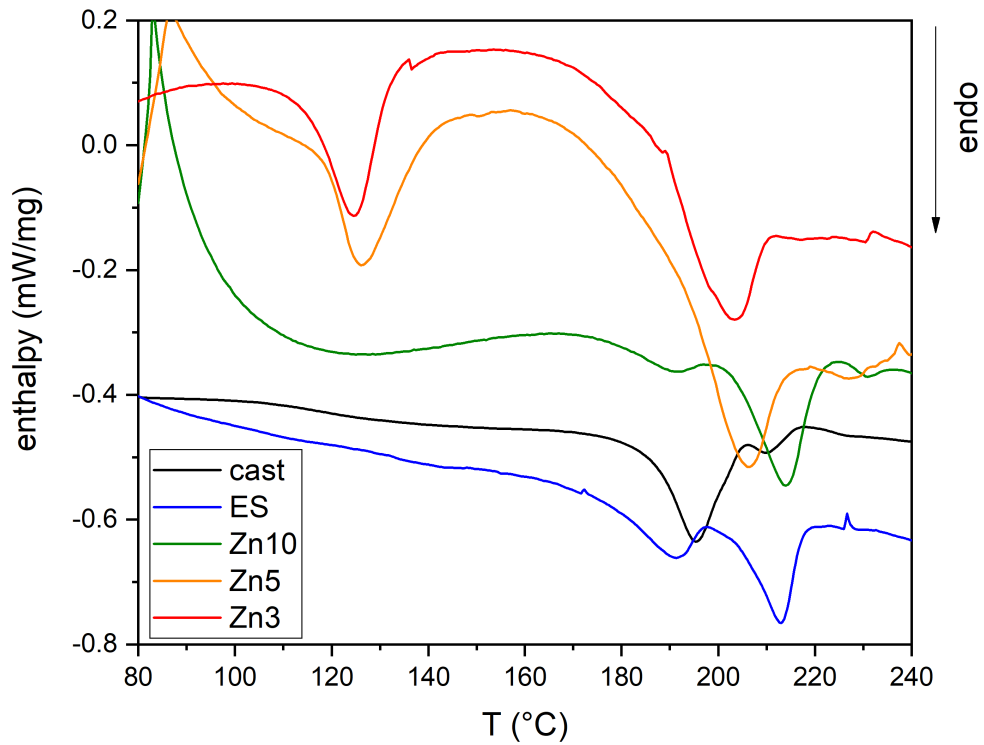
Differential calorimetry curves for Ti and Zn modified samples are shown in Figure 2.6, while details of the peaks are reported in Table 2.5. The temperature range for the thermograms is reduced to focus on the phase change region.

According to the producer documentation, polyurethanes of the b₉ series melt at around $230\text{ }^{\circ}\text{C}$ and degrade beyond $280\text{ }^{\circ}\text{C}$. Most of the materials show a melting temperature ranging between $185\text{ }^{\circ}\text{C}$ to $215\text{ }^{\circ}\text{C}$, exhibiting two separate endothermic curves. The peaks are distant from the onset of thermal degradation, which occurs beyond $300\text{ }^{\circ}\text{C}$ (as evinced by DTG curves), and no overlapping between melting and degradation occurs.

DSC thermograms show that cast film and ES mats have similar shape, but the melting points are shifted towards lower temperatures for the ES sample. Furthermore, the energy needed to melt the crys-



(a) DSC thermograms for Ti2, Ti3, Ti7 and ES.



(b) DSC thermograms for Zn3, Zn5, Zn10 and ES.

Figure 2.6: Thermograms (DSC) of modified samples plotted against the unmodified sample, ES.

tals, corresponding to peak II and III, is remarkably different between the cast and ES sample, whereby the ratio of the areas under the first and the second curve is almost inverted.

Ti-modified samples follow the ES pattern, where the first peak is smaller than the second. The area under the second peak tends to grow smaller as the quantity of titanium increases. The temperature of each peak shifts slightly towards lower temperatures as the quantity of titanium increases.

The same trends described for Ti samples are valid for Zn samples, too. Melting peak III gradually shifts to lower temperatures. For sample Zn5 and Zn3, it is impossible to distinguish two peaks, as type II peak, following the trend seen with Ti samples, becomes less intense and merges with type III peak, which has shifted to lower temperatures.

Besides, both Zn3 and Zn5 exhibit a peak at low temperatures (125 °C), which are not present in any other graph. These two peaks correspond to peak in the TGA thermograms (see 2.7), which are not present in the other samples, and they might be attributed to coordination water loss (2%). Zinc acetate dihydrate includes two molecules of water per molecule. Boiling point for water, which is usually 100 °C, might be elevated by 25 °C by a shielding effect provided by the surrounding polymeric matrix and by the coordination energy.

Table 2.5: Temperature points for peak II and peak III and, in brackets, melting enthalpy for reported samples, as determined from DSC curves.

	Type II melting point [°C] (Melting enthalpy [W/g])	Type III melting point [°C] (Melting enthalpy [W/g])
cast	195.3 (1.6)	209.7 (0.12)
ES	191.3 (0.8)	213.0 (1.29)
Ti7	188.7 (0.39)	207.7 (1.27)
Ti3	189.3 (0.31)	208.0 (1.34)
Ti2	185.7 (0.27)	204.7 (1.01)
Zn10	191.0 (0.25)	214.0 (2.02)
Zn5	-	206.5 (2.94)
Zn3	-	203.5 (2.48)

2.3.5 Thermogravimetric Analysis

For the sake of clarity, the derivative thermogravimetric curves (DTG) are shown in Figure 2.7, and the peaks are reported in Table 2.6. The original TGA curves are reported in Appendix A.4.

Table 2.6: Temperature for each mass loss stage for cast, electrospun and modified materials, as determined from peaks in the TGA graphs.

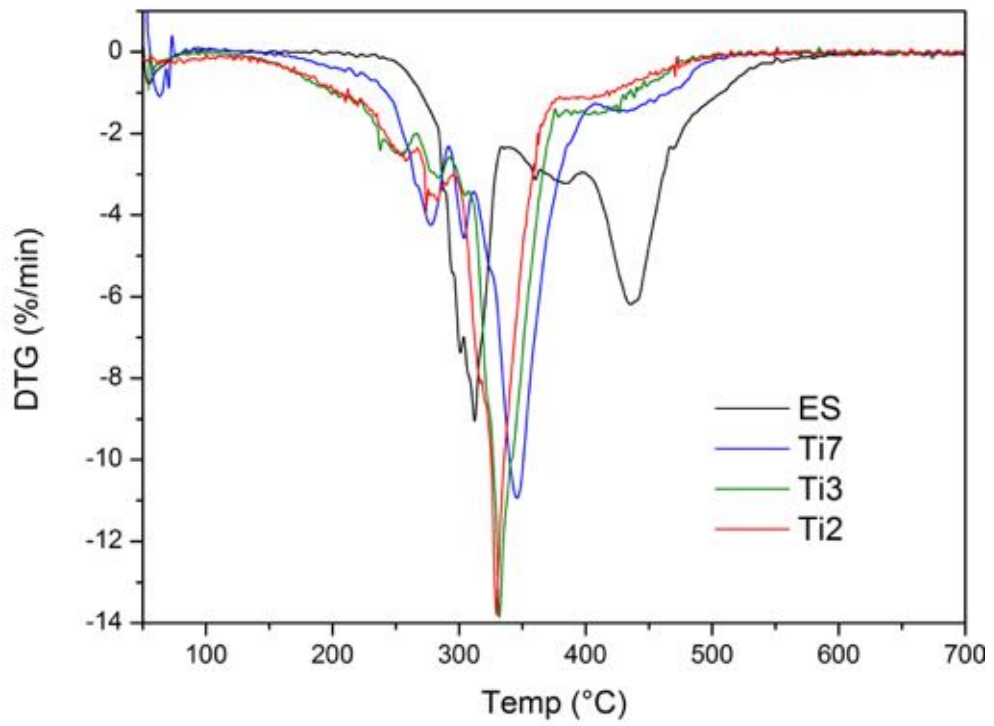
	peak I [°C]	peak II [°C]	peak III [°C]
cast	344	-	-
ES	312	385	436
Ti7	276	303	347
Ti3	256	285	331
Ti2	259	282	329
Zn10	295	379	435
Zn5	266	343	432
Zn3	254	331	427

The unmodified electrospun shows three distinct peaks, and while the first and the third are quite clear, the second one is smaller, broader and partially overlapped with the third one.

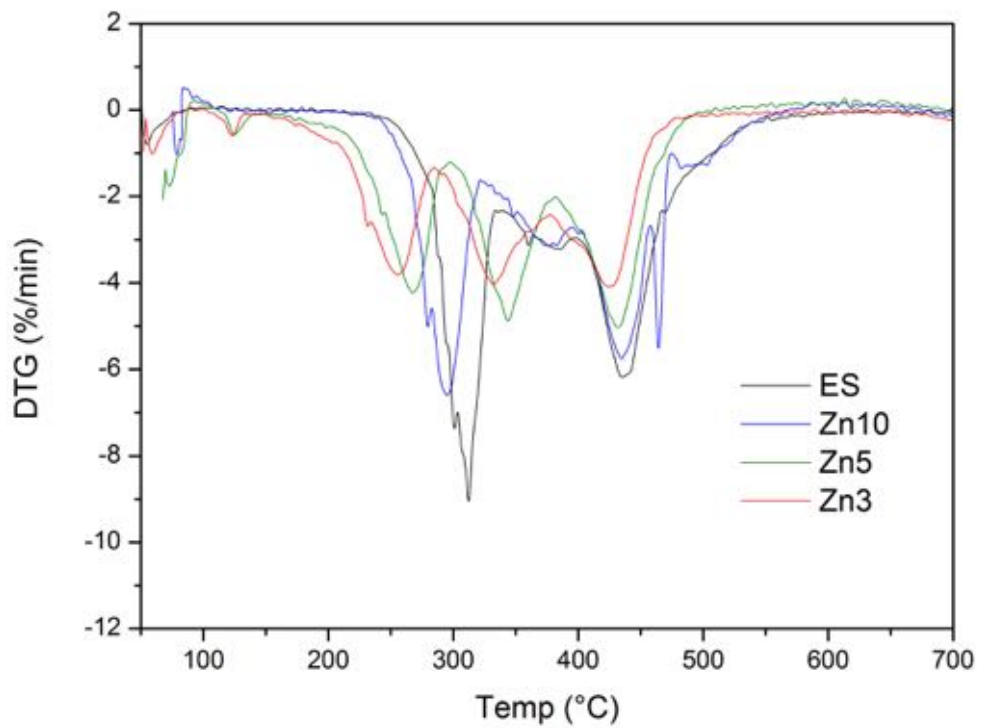
In the case of titanium-modified samples, a shift of the peaks to lower temperatures is observed; in particular, the third peak appears at lower temperatures than the second peak for the unmodified material. As the Ti content in the modified materials increases, the second peak merges with the third one.

Zinc-modified samples show a profile that is more similar to the unmodified material. In general, peaks are shifted to lower temperatures, however the shift is bigger for the first peak, which is smaller and broader, especially for the Zn3 sample, while the second peak appears to be bigger as compared to the unmodified material.

Zn3 and Zn5 exhibit a peak at low temperatures (around 125 °C), which are not present in the other samples, and they might be attributed to coordination water loss (mass loss about 2%, which corresponds to the weight ratio of molecular water as calculated per formula). Zinc acetate dihydrate includes two molecules of water per molecule. Boiling point for water, which is usually 100 °C, might be



(a) Ti-modified samples.



(b) Zn-modified samples.

Figure 2.7: DTG curves for electrospun materials modified a) with Ti, b) with Zn, against the unmodified samples ES.

elevated by 25 °C by a shielding effect provided by the surrounding polymeric matrix and by the coordination energy.

2.3.6 Mass loss

At the endpoint of the TGA run, set at 700 °C, all samples present some charred remains in the pan. The quantity of residue for the unmodified electrospun sample has been considered to be the organic residue (char), and such char has been subtracted from each of the other samples to calculate the relative mass of inorganic component, which is reported in Table 2.7.

The inorganic mass does not correlate precisely with the quantity of precursor added to each sample (the calculated mass, theoretically derived from the chemical reaction, is reported in Table 2.2). Still, the quantity of inorganic char in the modified samples increases with the quantity of precursor. The amount of inorganic ash or residues remaining following decomposition of the Zn-modified samples is remarkably higher than the ash in the Ti-modified samples.

Table 2.7: Mass percentage of char in the pan as determined by TGA curves. The third column is calculated by subtracting the value of ES from the other samples.

	total leftover mass [%]	inorganic mass [%]
ES	9.09	-
Ti7	14.12	4.93
Ti3	13.92	4.73
Ti2	17.96	8.77
Zn10	16.89	7.81
Zn5	22.21	13.13
Zn3	24.54	15.46

The final quantity of inorganic component in the modified materials amounts to a limited fraction, comprising up to 8.77% and 15.46% of Ti and Zn-samples respectively, as reported in Table 2.7. When degraded in nitrogen atmosphere, PU tends to leave a char residue up to 10 – 20%. Char residue occurs more often for polymers containing aromatic moieties, and it is proportional to the content of the aromatic

content (which is more difficult to oxidise and decompose, especially under nitrogen flow). Indeed Z6A1, the polyurethane grade used in this experiment, contains aromatic rings in the HS (see Fig. 1.10). Mass loss depends on the content in polyol as well, because it contributes to the overall oxygen content of the sample and eventually to its degradation [134].

The amount of inorganic ashes is different to the quantities as theoretical calculated, and the amount of ashes in the zinc-modified materials is higher than the correspondent Ti-samples. Charring reactions and mechanisms might be different depending on the metallic ion, which may act as a catalyst for the thermal degradation.

2.4 DISCUSSION

Electrospinning process is a flexible process that allows to produce a range of polymeric fibrous materials. Its extreme versatility derives from the number of parameters it is possible to vary; each of these parameters have a different impact on the final product.

Fibre morphology and porosity

Electrospinning technique was successfully used to manufacture a range of polyurethane substrates, both un- and modified. Fibres look neat and well formed, not fused together and with a narrow dispersion of diameters.

Unmodified electrospun fibres (ES) show a multimodal distribution (Table 2.3 and Figure 2.1), with fibres diameter distributed around more than a single size. This phenomenon can be explained by the splaying processes (see Section 1.7.4.2). The initial polymer solution was viscous (at a concentration of 15%w/w, Table 2.1), which is usually one of the conditions that favours splaying. Furthermore, Z6A1 itself, which is a polyurethane grade rich in hard segments, has a high charge concentration. It is therefore possible that a non-uniform distribution of charges on the surface of the droplets oozing from the nozzle might occur, leading to splining and branching of the fibres, and eventually a multimodal distribution of sizes.

The modification of electrospun fibres with titanium and zinc was achieved via a sol-gel reaction. The introduction of precursors in the polyurethane solution proved to help and stabilise the polyurethane and make the manufacturing process more stable and reliable.

In fact, while the zinc and titanium organic precursors do not bear a charge overall, they readily dissolve and separate into their constituent ionic moieties within the polymer solution, which increases the conductivity of the solution. Therefore, given same electric field and needle-collector distance, smaller fibres, and a narrower diameter distribution are expected. For each set of modified polyurethanes, the concentration of charges in solution was varied (Zn 10, 5 and 3 and Ti 7, 3 and 2 have increasingly high content in metal precursor) and this had a direct impact on the diameter distribution of the electrospun fibres, given the increase in conductivity of the solution.

Priority was given to achieving the same molar concentration for corresponding samples, but in general, when zinc was added to polyurethane, smaller diameters were obtained. The charge density of the titanium cation is higher than zinc (II) cation (362 C/mm^3 and 112 C/mm^3 respectively), but the need to complex titanium isopropoxide with acetic acid might screen the effective charge of the titanium ion and reduce its overall contribution to the solution conductivity. Therefore, the overall conductivity of the zinc-modified polyurethane solution is higher and the fibre diameter is smaller.

The diameter of the zinc modified scaffold is much more uniform throughout the different samples (Zn10, Zn5 and Zn3). The difference of the average diameter between sample Zn10 and Zn3 is only 10 nm (see Table 2.3).

Although the area of pores was not calculated, SEM micrographs show a high porosity well distributed on the surface and a good interconnectivity of the pores. The dimensions of the pores is usually proportional to the diameter of the fibres. In an electrospun material, pores are not a 2D structure, as they develop in depth across the item. Importantly, they are interconnected and allow the scaffolds to be permeable to fluids, including biological fluids such as the CSF. As discussed in Section 1.5.3, conventional catheters have only a limited area open to absorption. This design causes an increase in shear pressure around the apertures. On the contrary, an electrospun design would absorb and drain CSF via capillary forces as well as hydraulic permeability, and pressure would be distributed along the whole length of the surface, rather than on a limited amount of fenestrations.

One of the aims of this research is the synthesis of a hybrid material, whose structure is a blend of organic polyurethane chain and an inorganic active modifier, namely zinc and titanium. To increase zinc and titanium effectivity and their dispersion within the organic backbone, a sol-gel route has been opted for (Section 1.9). Following a sol-gel reaction, titanium or zinc organic precursors should create a network intertwined with the polymeric matrix, and titanium or zinc ions should be finely dispersed throughout the fibres.

In order to confirm the effectivity of the sol-gel process, the successfully electrospun scaffolds have been analysed with a series of meth-

*Chemical
modification*

ods, and the results are here discussed, focussing on both chemical and microstructure modification .

As discussed previously (Section 1.9), polymerisation is usually started by water molecules and proceeds in a very fast way. The initiation of the polymerisation reaction needs to be avoided before electrospinning starts, as the gel would network and that would increase the viscosity of the solution, becoming impossible to electrospin. In order to control the sol-gel process, the precursors are then reacted with species that can form coordination complexes and shield the electrophilic metallic centre from water molecules. Titanium(IV) alkoxides are very sensitive to atmospheric moisture and must be complexed (for example, with acetic acid) in order to slow down their reactivity. Instead, zinc oxide acetate is more stable in air. At the same time, DMF acts as a coordinating or chelating agent through the nucleophilic $-N-$ centre. Zn(II)-DMF complexes have been reported in literature [135], and it can be supposed that similar structures are present in the DMF-zinc acetate-Z6A1 solutions as well. In order to aid the formation of a gel from Zn acetate precursor, heating and ageing are provided.

FT-IR spectrographs (Fig. 2.5) exhibit a small shift of the N-H vibrational mode from its bonded to free form, as the inorganic fraction is small and not all of it interacts with the NH groups. Furthermore, no clear peaks can be attributed to the inorganic material in the fingerprint region, at wave numbers lower than 650 cm^{-1} . They might overlap with other vibrational modes of the polyurethanes.

The sol-gel reaction occurs in air, either via a non-aqueous mechanism, or because of water provided by atmospheric humidity or by the solution itself, given that zinc acetate salts contain water in their molecular structure itself. Condensation reaction may continue even after deposition; during the washing stage and afterwards, with ageing of the sample, humidity may change the free molecules into a gel.

Sol-gel occurs at low temperatures and the energy provided by the process is not sufficient to induce the structure of the gel into more ordered (crystalline) phases. No strong inorganic bands can be seen, as calcination or other form of thermal treatment should be needed

to increase the order of the gel. Therefore, it seems that titanium nor zinc are both in an amorphous phase.

Even during a thermal ramp-up provided during the DSC thermograms (Fig. 2.6), no recrystallisation (phase transition) in the area analysed, up to 700 °C, can be seen. In particular, titanium dioxide has a transition from anatase to rutile around that temperature. This supports the idea that the titanium is present in an amorphous, polymeric phase, not dense enough to be further packed into crystalline forms.

As zinc is responsible for a less evident internal modification, it can be inferred that zinc does not interact with the polyurethane matrix. It is to be determined whether it is finely dispersed within the matrix, either in its elemental form, as clusters or oligomers, or, given its inability to interact with the matrix, it is prone to aggregation and separation.

Further testing would be necessary to assess the structure of the modifiers, for example X-ray diffraction (to clarify whether they are crystalline or amorphous), UV-vis (crystalline TiO₂ absorbs in the UV region of the spectrum), or X-ray photoelectron spectroscopy (XPS, to define the chemical bonds and structure).

Even though they are not in a crystalline phase, further analysis will focus on the impact of these metals on the surface properties of the modified materials (Chapter 3), and on their biological implications (Chapter 4).

All samples appear to be dry and do not show any water loss around 100 °C. However, samples with higher concentration of Zn modifier exhibit a loss of around 2% weight at 125 °C, which explains the endothermic curve for samples at higher concentration (Zn5 and Zn3, Fig. 2.6). This is probably coordination water included into zinc acetate dihydrate.

All the samples have been characterised after at least 10 days from the production, and samples were prepared within few days from each other, to make sure that the ageing of the samples was kept consistent. No stability studies have been conducted on the materials, so it is not known if either modifier (titanium and zinc) leech from the matrix or react in a solvent (especially aqueous, or biological fluids).

The chemistry of titanium and zinc in biological fluids is complicated and can give origin to complexes, oxides and hydroxides.

One of the scopes of this project is to determine the distribution of the functional materials across the fibre. In particular, it is desirable to be able to determine whether the modifiers are evenly distributed across the fibre, or more concentrated either in the core or, more to the point, on the surface, being the outermost layer the interface with the environment and the section that interacts with the biological materials. The ideal modified nanofibres should possess a modifier-rich surface to be able to exhibit biological activity, even though the electrospinning process, based on local concentration of charges, might lead to a higher concentration of modifiers in the core of the fibres.

*Modification of
the internal
structure*

Polyurethanes are typical biphasic polymers. From a mechanical point of view, they can be modelled as microcomposite, with a “filler” (hard segments) dispersed in a “matrix” (soft segments). Z6A1, the polyurethane grade that has been employed in this study, has a high concentration of hard segments.

Of the samples investigated in the present research (Fig. 2.6), cast, electrospun and all of Ti samples exhibit two curves at higher temperatures, while in Zn samples curve II is merged with curve III for sample at higher filler concentration (Zn5 and Zn3). In general, there is a slight shift of the peaks to lower melting temperatures as the metallic content increases.

The difference between casting and electrospinning internal structure appears quite evidently on the DSC thermograms (Fig. 2.6). From the analysis of the area under the curves (Table 2.5), the cast film have a higher content in biphasic mixing, while the electrospun materials are richer in hard segments (crystalline phase) to melt. This seems to suggest that cast films are richer in crystallites, and given their abundance, crystallites are statistically forced to mix with the amorphous phase, rather than creating a perfect biphasic structure.

It was not possible to cast a control sample of Ti and Zn-modified polyurethane. The manufacturing technique (sol-gel) was not successful in reproducing within the vacuum oven a comparable result to the electrospun correspondent. Indeed, titanium precipitates and the re-

sults is an inhomogeneous film. For this reason, no modified control is available.

When a polyurethane is dissolved in a solvent, the hydrogen bonds become loose, HS are separated from each other and the polymeric chains are coiled and linear. If polyurethane is then cast and allowed to dry, this process is slow and allows for enough time for the biphasic structure to form again. The thermal energy provided during cast film formation is enough to let the solvent evaporate, but it is not enough for the chains to drop on the highest-energy conformation.

All of the electrospun samples, both modified and unmodified, show a different curve shape than the cast film. For the cast film, curve II is deeper, while for the other samples curve III is deeper than curve II. In the case of electrospun materials, crystallites are present in lower quantity and they tend to segregate. The energy provided during the DSC scan is employed mainly to melt the hard segments.

During electrospinning process, the short formation times are theoretically not long enough for the HS to align and form the hydrogen bonds again. The quick evaporation of the solvent freezes the polymeric chains in their position. Furthermore, the stretching experienced during the process by the fibres breaks the HS and keeps them apart. While annealing increases the transition temperature and leads eventually to curves merging into a single main peak at melting point by increasing the order of the polyurethane HS, electrospinning process seems to have an opposite effect on polyurethane, that is, the peaks shift to lower temperatures, and the HS are broken down and kept afar.

On top of the effect imparted by the electrospinning process, another effect can be observed in the modified samples as the as the metallic content increases: the peaks become broader and less deep. The width and peak of curves are linked to the HS distribution. The longer the HS, the easier to form crystallites. However, adding metallic species might interact with the hard segments, physically, by blending with the polymeric chains, and chemically, by creating bonds with the functional groups and interfering with the hydrogen bonding. This leads to a reduced amount of crystallites within samples, and a wider distribution of the crystallite size.

More generally, another trend is evident from the DSC thermograms shown in Figure 2.6, i.e. the decrease of melting point passing from cast to electrospun material and as the quantity of modifier increases. It can be argued that titanium and zinc modifiers disrupts in a way the crystalline order by intermingling with the polymer and preventing a closer packing, or preventing the formation of bigger crystalline domains (which accounts for a broader size distribution and a broader curve) and allowing the formation of crystal type II.

This effect is much more clear with titanium. Both curve II and III are shifted towards lower temperatures and become broader. In case of zinc, curve II does not shift remarkably, while curve III shifts and broadens, until curve II merges with curve III as the quantity of modifier increases (Fig. 2.6). This seems to suggest that titanium mixes better with the polymeric matrix, unlike zinc, and therefore it has a bigger impact on the modification of the internal biphasic structure of polyurethane.

The shifts in vibrational modes noticed in the FT-IR spectrographs (Fig. 2.5) support the idea that hard segments are broken down by both electrospinning and the addition of metal fillers, especially Ti.

In fact, a small red shift of around $6\text{--}9\text{ cm}^{-1}$ is observed in the N–H stretching going from the cast film or as-received polymer and the electrospun polymers, which suggests a difference in environment of the polymeric chain, maybe a different crystalline form. Crystallinity in polymers is usually given by hydrogen interactions, and such a frequency shift can support the idea of a different crystalline order as provided by DSC. The shifts are modest, but present, for Ti while for Zn there is only a smaller shift towards lower wave numbers.

Thermal behaviour of polyurethanes is dominated by the content in hard segment (HS), so that the degradation stages and the temperature at which each stage occurs depend on the crystallinity index and on the specific hydrogen bonds that the hard segments create in each specific polyurethane.

Typically, a TGA curve for polyurethanes exhibits three peaks. The first peak (lowest temperature) corresponds to the depolymerisation of the PU into more volatile components, and occurs at around 310°C , at a temperature around 90°C higher than the melting point; the sec-

*Interaction
between
polymer and
modifiers*

ond peak is related to the rearrangement into dimers and trimers of such small, volatile components; and the third peak shows the burning of such rearranged components.

This structure can clearly be traced in the DTA graph for the unmodified ES sample (Fig. 2.7). The degradation mechanism for the Ti and Zn modified samples appears to be quite different instead. Zn modified samples follow the ES pattern at all concentrations. On the other hand, Ti modified samples show the disappearing of one of the three peaks, the middle one, which tends to merge and overlap with the third one as the concentration of Ti increases. Furthermore, the first two peaks are less deep than the third one, indicating that most of the mass loss occurs at the third stage.

DSC curves suggest that the intertwining network of titanium or zinc interact with the HS, and therefore less energy is needed to break down the urethane bonds, which correspond to the first DTG curve. This might be explained as a penetration of the inorganic network with the polyurethane chains, which leads to a less densely packed structure, which determines that less energy is required to break down the polyurethane chains. Therefore, thermal stability changes with Zn, as degradation starts at lower temperatures, and even more dramatically with Ti, for which the final thermal degradation occurs at a lower temperature than for the ES sample (329 instead of 436 °C, a 106 °C difference, Table 2.5). However, Zn modified samples show a pattern that is more similar to the non modified samples. This result can be compared to the FT-IR analysis. The N–H bond shift for the Zn samples is less evident than for the Ti ones (Fig. 2.5).

Addition of inorganic material might change the density of the fibres by changing the packing of the HS and their distribution within the bulk of the material. Zinc-modified materials degrade at higher temperatures compare to the titanium one (the oxydation peak for Zn is around 430 °C, compared to 330 °C for Ti-modified samples, Table 2.6), which may suggest that their structure is more densely packed.

It may be argued that the Zn acts as a thermal catalyst and accelerate the decomposition in the first stage [136]. Zinc stabilises the products of the second stage rather than the first one. Both Ti and Zn might accelerate degradation by forming complexes and acting as

catalysts. Zinc cation is a Lewis acid and might coordinate with the oxygen in the isocyanate group $-NCO$, therefore the carbon is more electrophilic and more reactive with other moieties [137]. Moroi [138] reports other examples of degradation of polyurethane mediated by transition metal ions. The metal complexes mixed to the polyurethane do not act as thermal resistants, but they rather achieve the opposite effect of weakening the bonds between the hard segments and loosening the otherwise more densely packed structure.

In Ti modified materials, a more intense third peak may mean that the first stage is stabilised and that much of the polymer leaves in the third stage, which is the opposite mechanism that happens for unmodified Z6A1. This effect has been called labyrinth or mass transport barrier effect [139]. The samples are shielded from the oxidative degradation, the inorganic network rich in surface $-OH$ traps the volatile components, which therefore tend to leave the sample only at the second stage. Titanium seems to stabilise more the first stage, to entrap the imides and the ureas, acting therefore as a barrier forbidding them to leave. The second stage is enhanced on these samples, and it may be argued that Ti acts as a better catalyst for the third stage.

From the DTG curves analysis, it can be inferred that titanium is finely dispersed within the polymer structure. The metal ions interact with the polymeric chains, breaking down the hard segments by coordinating with the urethane bonds. The microstructure of the polyurethane is modified so that thermal degradation occurs at lower temperatures. As evidenced by TGA thermograms, a certain degree of coordination between the final polymer and the inorganic network occurs. Such interaction suggests the inorganic network is well dispersed within the matrix. Furthermore, the interaction between the HS of the polymer and the inorganic network suggests the breakdown of the HS and the blending of the two networks. The evidence collected seems to suggest that titanium does create an inorganic network within the polyurethane matrix, which is intertwined with the polyurethane chains.

On the contrary, zinc seems to be less well dispersed. Probably, zinc acetate is present in its molecular form, maybe in small clusters

or oligomers, rather than in a polymeric form. It remains to be determined whether zinc is concentrated on the surface or rather in the bulk of the material, and whether it can be released from the material by reacting with the external environment. There is no evidence zinc is in crystalline form. Zinc acetate is soluble in water, and zinc, depending on the pH of the solution, can react and turn into hydroxides, oxide and complexes, therefore, if zinc is not intertwined and interlocked with the polyurethane matrix, it is to expect that it might react and dissolve when fibres are immersed into a water environment.

In the experimental set-up used in the present research, the needle was always positively charged (see Methods Section 2.2), which may force positively-charged chemicals to migrate to the core of the fibres, while attracting negative charges to the surface. Metallic ions are positively charged, albeit shielded by several negatively-charged complexing radicals, and they are expected to be more concentrated in the bulk of the fibres, however they might migrate on the surface of the fibres during the drying process, along with the polar hard segments.

Bonino *et al.* [140] reports the effects of varying the needle charge on the distribution of charges on the fibres. If the electrospun polymer is charged itself, it will experience attraction or repulsion from the charged walls of the needle, even though the effect is buffered by the free charges in solution. Hence, the final fibre will have a different charge distribution depending on the polarisation of the electric field. Namely, a positively charged needle will attract oxygen and nitrogen-rich moieties (concentrated in hard segments), while pushing the soft segments, which are apolar, away and inside the flow. In a neutral, thermodynamically stable environment, the soft segments (rich in -C-H bonds and with lower free energy) would segregate to the surface instead. On top of this process, Reneker & Yarin [100] describes how free charges in solution tend to migrate from the liquid bulk to the surface and become static while fibres dry out.

In order to confirm the presence of titanium and zinc in the fibres, and distribution within the fibres of the same, EDS has been employed (Fig. 2.4). While the presence of titanium and zinc has been detected in each and all samples, however, EDS penetration length is in the

*Distribution of
Zn and Ti on
the fibre*

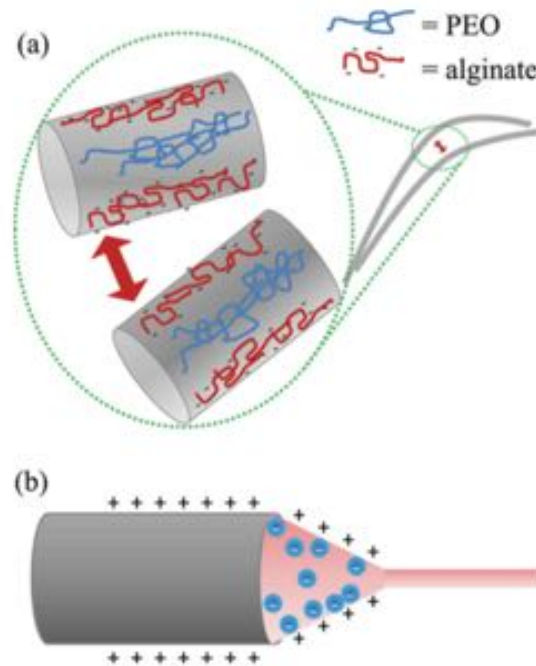


Figure 2.8: This schematic, reproduced from Bonino *et al.* [140], illustrates how the positive charged needle (b) can attract the negatively charged polymers to the surface during the electrospinning process (a). Fibres will then exhibit fixed surface charges and experience repulsion between each other.

order of $2\ \mu\text{m}$ to $3\ \mu\text{m}$ which is longer than the thickness of each fibre, therefore the information provided by the EDS spectra refers to the composition of the whole fibre, if not of multiple fibres, and is not limited to the surface. EDS analysis does not provide an useful insight of the distribution of the metals across the fibre.

As Zn-modified fibres are remarkably smaller than Ti-modified fibres, they possess a higher specific area, and it is to expect that difference between the two groups of materials derive from these properties as well.

2.5 CONCLUSIONS

As a result of the morphological and structural analysis of the electrospun modified and unmodified fibres, the following points can be established:

- it is possible to produce modified polyurethane fibres, which are straight and smooth-looking, exhibiting no beading or splaying. The fibre distribution for modified materials is unimodal and narrow, as opposed to a four-modal distribution exhibited by ES samples. In particular, zinc-modified samples have a very narrow distribution and range of the average diameter of Zn3, Zn5 and Zn10 samples is narrow as well;
- it is not clear how the metallic filler is distributed in the modified materials, in particular whether the metal content is concentrated on the surface or the core of the fibre, or instead distributed evenly throughout the fibre section, although thermal analysis seems to suggest a good distribution across the fibre for Ti-modified samples, while Zn-modified samples do not suggest dispersion of zinc within the polyurethane matrix;
- the electrospinning process itself changes the microstructure of Z6A1 polyurethane by breaking down the crystalline domains and blending the biphasic structure;
- by adding titanium to the polyurethane solution, the microstructure of the final electrospun fibres is further modified and the internal biphasic structure is even less segregated, by way of the interactions occurring between the metal cations and the moieties in the hard segments.

In particular, a change in the structure of Ti-modified samples seems to indicate the sol-gel reaction was effective in case of titanium and the final material is interspersed and mixed with the polyurethane matrix.

In zinc-modified samples, Zn is incorporated into the structure of the polyurethane, it seems like it is still complexed by acetic acid and it may be present as small clusters or oligomers of zinc. The main change induced by zinc is the diameter and morphology of fibres, with smaller diameters, narrower distributions and neat and straight fibres.

Both titanium and zinc have an amorphous structure within the fibres.

FUNCTIONAL PROPERTIES OF MODIFIED ELECTROSPUN SURFACES

3.1 INTRODUCTION

This chapter illustrates the impact of the morphological and structural changes described in the previous chapter on the surface topography and chemistry of the modified materials previously manufactured, in order to analyse their different functional properties, especially their ability to absorb biological fluid. In particular, it investigates the presence of titanium and zinc on the surface, and how the absorbency properties of the materials change when modified with such metals.

In order to characterise the surface at the microscopic scale, Atomic Force Microscopy is employed. Atomic Force scans will provide not only topographic images of the surface, but the distribution of hard and soft domains on the surface, providing clues on the distribution of the titanium and zinc modifiers on the surface as well. Atomic Force Mapping is used to analyse the adhesion properties of the materials.

Contact Angle Goniometry images are used to investigate the wetting properties of the surface of modified and unmodified materials at a macroscopic level.

3.1.1 *Contact Angle Goniometer*

Contact angle goniometer is a common technique used to evaluate the wetting properties of a surface. It is based on the observation that the shape of a droplet of liquid on a surface depends on the interactions between the liquid phase and the solid phase (see Section 1.8).

If the surface tends to have an affinity interaction with the liquid, the droplet will tend to maximise its contact area with the surface,

and the angle between the horizontal surface and the liquid phase will be higher than 90° and closer to 180° (Table 1.5). If the liquid is repulsed by the surface, the angle will be lower than 90° and closer to zero. If the liquid is polar (usually, water), and the drop spreads out, the surface is called hydrophilic, on the opposite it will be defined as hydrophobic.

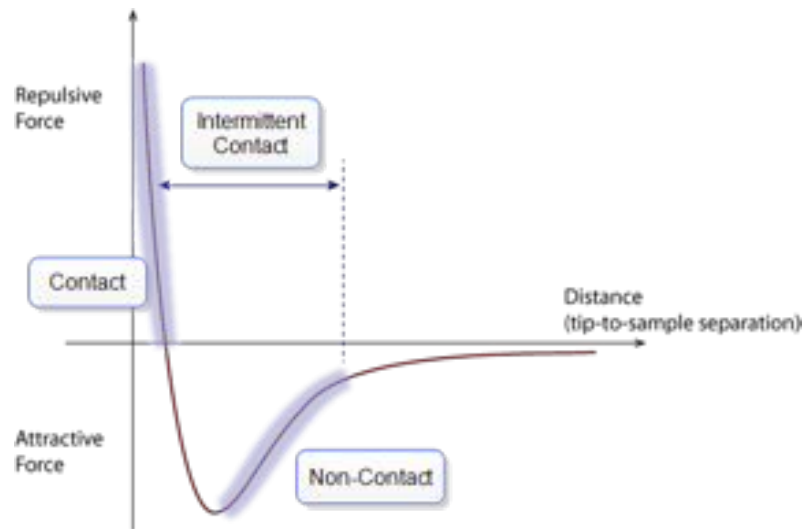
3.1.2 Atomic Force Microscopy

Atomic Force Microscopy (AFM) is a surface analysis technique that allows to reproduce the topography of a surface at a very small scale and a very high resolution. Atomic force microscopy is based on the interaction forces between a very sharp tip held above a surface and the surface itself. While the tip is scanned over the surface, it follows the profile of the surface itself, bending up and down along the contour of the sample and providing a measurement of the height. Combining the height value (z) with coordinates x and y for each point, a three-dimensional map of the surface is generated [141].

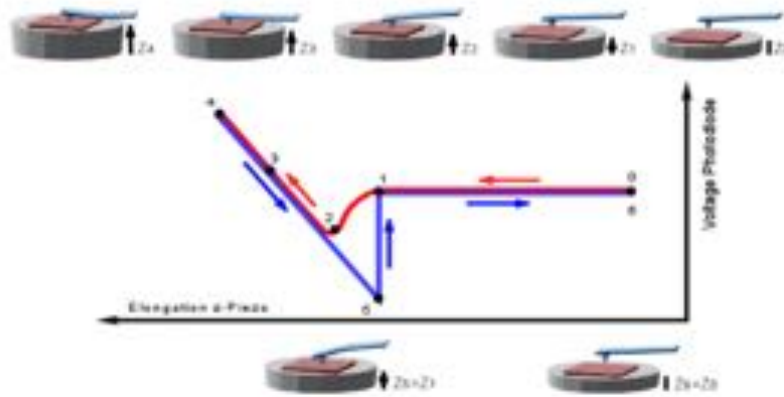
AFM is based on the dispersive forces that arise between the molecular orbitals of the atoms of two surfaces. Dispersive forces, of the order of 0.1 nN to 1.0 nN, measured as free energy as a function of the distance between the tip and the surface itself, can be described by Figure 3.1a. When the distance between tip and surface is wide, the attraction is weak and approaches zero. As the distance decreases, the attractive component is stronger until the graph reaches a minimum. As distance decreases further, the force first becomes zero when it reaches a couple of angstroms and then, at very low distances, the tip experiences a repulsive force. The ideal curve here described is called a Lennard-Jones potential curve [142].

In a real AFM, when a tip is approached to the surface until it touches it, the graph is better described by the graph shown in Figure 3.1b.

The probe is the assembly of a very sharp tip at the end of a long (100 μm to 500 μm) and narrow cantilever. The cantilever is in turn attached to a platform to make it easier to handle and mount it on the head of the AFM scanner.



(a)



(b)

Figure 3.1: Tip-surface interaction graphs [143].

The tip is only few micrometres tall and very sharp so as to ideally terminate with only few atoms. In practice, the actual radius of a fresh probe is around few nanometers (5 nm–50 nm). As well as speed at which scans are taken, resolution depends critically on the sharpness of the tip as images are a convolution of the tip geometry and the features of the sample, but it can reach the nanometer scale and beyond [144].

Cantilevers can be of different shapes, but commonly they are rectangular, triangular or trapezoidal. The materials they are often made of is silicon or silicon nitride (Si_2N_3). The shape and the material will contribute to determine the probe spring constant and therefore the

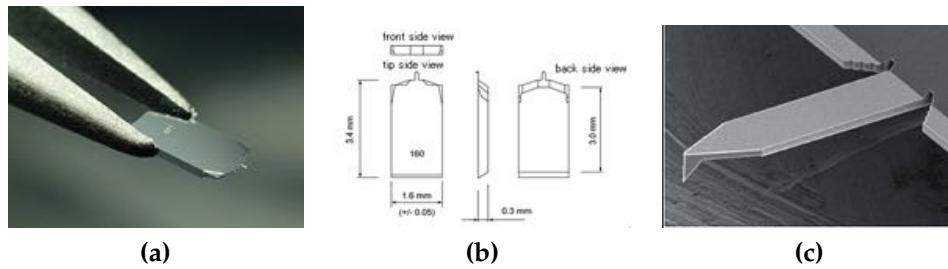


Figure 3.2: Cantilever Olympus AC160TS used in the present work.

interaction between the tip and the sample. For example, silicon nitride cantilevers have lower spring constant. Cantilevers are mounted over a shaker piezo that can vibrate them through a whole range of frequencies.

The way a typical AFM works is shown in Figure 3.3. A piezo-electric actuator moves the probe over the sample surface while a laser beam is shone on the reflective back of the probe. A four-segmented photodetector receives the reflected beam and provides a reading based on the vertical deflection of the probe, as well as the side deflection. The long optic pathway of the laser beam amplifies the position of the tip, therefore the photodetector can detect the minimal difference of coordinates between the calibration position and any other position (deflection), which is interpreted as a height value and transformed into a map. The laser beam must be aligned to the centre of the photodetector before starting scanning [145].

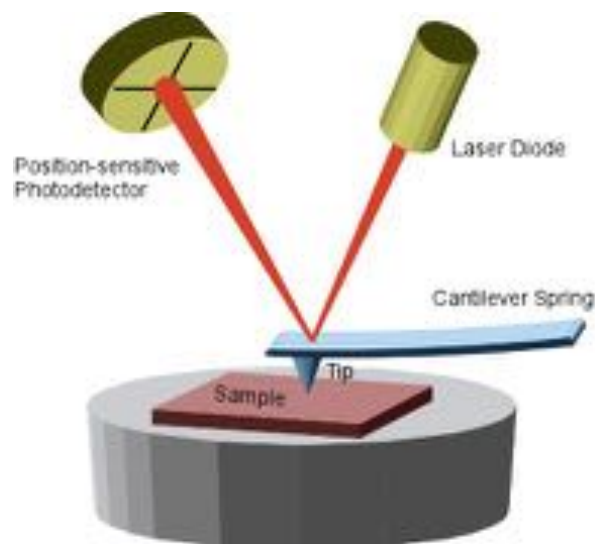


Figure 3.3: Basic diagram of an AFM [146].

AFM can be either built with the tip scanning over the surface, or the sample being moved underneath the cantilever. Either way, the movements are governed by a piezoelectric element that is able to transform a change in dimension into a voltage difference, which can be fed back into a calculator. The piezoelectric piece is extremely sensitive: each volt corresponds to a change of a fraction of nanometer, and vice versa.

The feedback loop is an essential element of the AFM. By trying to keep one of the parameters constant (frequency/force/height), the system brings back the tip on the surface. For example, by setting the frequency constant, as soon as the frequency changes, the driver will change the position of the cantilever slightly, in order to bring the frequency back to the set point. Therefore, the z piezo movement will be the height element information, as a sum of the tip deflection and the cantilever movement. Other feedback loops keep the tip at a constant height or constant force over the surface [142].

The probe is moved over the sample with a raster scanning motion. Scan rate must be slow enough to allow for the loop to adjust, especially around edges and slopes (grooves, nanoparticles and other small features). On the other hand, extremely slow rates can make the scan last too long and make it subject to thermal drifts.

3.1.2.1 *AFM modes*

Based on its set up, AFM can be operated in different modes [147]:

CONTACT MODE : the tip is continuously in contact with the surface and it is kept in the repulsive region of the curve. A constant force (how hard the tip pushes on the surface), or constant cantilever deflection (constant height, where the tip is kept at a fixed height above the sample) are set as the feedback parameter. This is the usual mode for atomic resolution AFM.

Contact mode can develop very high pressure on the sample as the contact area is very small and even if the forces applied to the surface are very small, they can damage it. Therefore contact mode does not allow to get good pictures with soft samples, such as polymers and biological tissues;

NON-CONTACT MODE : the tip is kept slightly away from the surface, at 50 Å–150 Å and made to resonate at or near its resonance frequency, so it can be defined as almost contact;

TAPPING MODE : the cantilever is set vibrating at high frequency, at or very close to the resonance frequency, and is allowed to touch the sample for a very short time. The amplitude of the oscillation is in the range of 20 nm–100 nm when in free air. This mode develops low lateral drag forces, which is relevant when scanning polymeric surfaces.

In tapping mode, the feedback loop is the oscillation amplitude. When the tip approaches a feature, for example a bump, the space for it to vibrate is narrower and the oscillation amplitude changes accordingly. On the opposite side, when there is more space to oscillate, the amplitude increases and approaches the free air value. The feedback will then bring the tip to retreat or approach the surface in order to bring back the amplitude value to the set point.

In tapping mode the tip spends less time on the surface, therefore elastic deformation force applied to the surface are smaller and they can be recovered by the material. Lateral force are minimised, therefore the deformation (or the damage) of the sample is limited. Furthermore, other side interactions that can modify the sample itself are avoided. For example, in the case of loose elements on the surface, such as biomolecules or fibres, they are not dragged around by the tip, and, when the surface is covered by a thin layer of condensed water vapour, the tip avoids the attraction from the water meniscus. Therefore, tapping mode is the preferred mode for soft and biological samples.

Normally, AFM provides a 3D representation of the surface and information about profile roughness and size of morphological features.

However, the interaction between the tip and the surface provides a wealth of extra information about the surface itself, including chemical interactions and mechanical properties. Furthermore, AFM can be modified so as to interact with the surface through different forces,

for example with conductive and magnetic materials, or to work in fluids and therefore permitting to image biological samples.

3.1.2.2 Phase mapping

The phase shift is the difference between the free end (air) and the drive frequency, and it can be between 0 and 180°.

The force tip can be roughly identified as the ratio between the set point amplitude and the free air amplitude, although there are many more factors, for example the tip contact area and the energy dissipation. However, three regimes can be identified: high (10 – 25%), moderate (40 – 70%) and low force (75 – 90%). High force and low forces lead to opposite phase mapping, where hard segments and soft segments appear once as the high spots and low spots on the other hand [148].

Darker and lighter areas alternate on the surface, which can be traced back to the alternating of harder and softer domains which characterise the chemistry and physics of polyurethanes, as described by Sakamoto *et al.* [149].

With an increasing need to determine the interaction of biological molecules with the biomaterial surface in applications such as medical devices and implants, different techniques other than contact angle are required [144].

Phase retrace depends on the interaction between the tip of the cantilever and the material. Wettability and contact angle measurements (free energy) on the macroscale can be ultimately reduced to the nano- or molecular scale interaction between water molecules and the surface, and such interaction receives contributions from free charge distribution and molecular polarity. On a different scale, geometrical factors such as surface roughness and morphology play a significant role.

Papers in literature report contrasting conclusions when interpreting the coloration of the areas, depending on experimental conditions, for example closeness of the AFM tip to the surface. Highly dissipating domains (for example, hydrophilic domains that are richer in –OH groups, can bind water moisture from the air and result in a higher interaction with the cantilever) have been linked to darker

colours, while less dissipating areas appear as brighter areas, as long as phase angle differences due to adhesion contrast are not particularly high [150–152].

Another study conducted by O’Dea & Buratto [153] compares images of the same surface taken in both repulsive and attractive mode. According to the study, darker shades correspond in both modes to hydrophilic areas, but while in attractive mode a dark colour indicates highly dissipating areas, in repulsive mode the same colour indicates lower dissipating areas. Therefore, different sources of dissipation must exist for each mode.

Wang *et al.* [154] discusses issues connected with tapping mode used to image the surface of the samples. Phase range depends on many factors, so different images cannot be compared directly. In tapping mode, the level of force applied to the surface has a dramatic influence on the data collected, in particular phase contrast data. Specifically, as the amorphous chains have a lower surface energy, they tend to segregate on the surface, therefore masking the crystalline domains with a very thin layer (only few angstrom thick, according to Hashimoto *et al.* [155]). By applying a different force to the cantilever, the domain structure can appear more or less clear underneath the surface [156].

3.1.3 Force mapping

The AFM probe can be used as a nanoscale indenter to obtain measurements of mechanical nature of the surface. This technique is called force mapping. The tip is lowered down to the material until it pushes onto or into the surface, entering repulsive mode, and leaves a small indentation, until deflection reaches a certain set point. Based on the slope of the force/displacement curve, the elastic modulus of the substrate can be derived.

The measurement depends on the mechanical properties of the cantilever itself (hence, the necessity of calibrating its spring constant) and therefore the force values cannot be taken as absolute. However, they can be compared to each other.

A typical force/distance graph can be split into six stages, as follows (Fig. 3.1):

1. flat segment: the tip travels towards the surface;
2. snap-in: the cantilever experiences sudden attractive forces towards the surface, for example, capillary forces;
3. repulsive segment: the cantilever bends upwards and the slope of this segment depends on the elastic properties of the surface. When the repulsive force reaches a set off point, the tip stops its run;
4. withdrawal and repulsive segment (opposite direction): the tip is mechanically withdrawn from the surface and it is still in close proximity with the surface;
5. pull-out point: the tip experiences attractive, adhesive forces that keep it stuck to the surface until the tip overcomes such forces and it is able to detach from the surface. The pull-off force is measured as the minimum tension required to remove the tip from the sample surface;
6. flat segment: as the distance increase, the interaction between the tip and the surface goes back to zero.

The amount of energy used to extract the tip from the material after the indentation (step 5) is related to the properties of the surface, in particular charge interactions (van der Waals and electrostatic), viscoelastic properties and wettability.

Indeed, in normal atmospheric conditions, every surface is covered in a very thin layer of water molecules (few water molecule units), present in the air and adhering on any surface. This water layer, whose thickness and structure are influenced by the interaction between the surface and the molecules of water (wettability), adds an adhesion layer between the tip and the surface that can be traced back and quantified via the retraction (pull-off) force. This kind of layer creates what are called capillary forces between the tip and the surface. The adsorbed water layer does not evaporate easily, according to Kelvin's law [157].

Therefore, the pull out area is related not only to the viscoelastic properties of the surface, but to the adhesion forces as well, and can be used to characterise the surface itself. For example, capillary forces are expected to be higher on hydrophilic surfaces.

In addition to this, the combined forces are affected by the surface topography, and depends on surface energy characteristics of both the tip and the sample. Contaminant layers present on the surface produces attractive capillary forces as well.

A discussion of the polar dispersion forces contribute to the overall retraction (adhesion) force is presented in Patra [158]. By analysing the relationship between macroscopic contact angle measurements and the retraction force, they found an exponential relationship of the retraction force with the total surface energy and in particular a more linear relationship with the polar contribution. Polar contribution arises from the dipole-dipole interaction or dipole-charge interaction, for example hydrogen bonding.

The paper concludes that the adhesion force corresponds to the energy necessary to break down the hydrogen bonding of the water layer. While hydrophilic surfaces usually favour hydrogen bonding across the thin layer and interactions with the hydrogen atoms presents on the surface, with the OH groups and with charges, more hydrophobic surfaces favour hydrogen bonding along the thin layer itself.

Therefore, if the tip is pulled off perpendicularly from the surface, it needs to break the bonds present along the water layer and, once the pull off force is higher than such interactions, a sharp detachment occurs, while, on a hydrophilic surface, the bonds to be broken are parallel to the tip itself and the retraction force is lower.

3.2 MATERIALS AND METHODS

3.2.1 *Materials*

Tested described in this section were conducted on selected materials as prepared according to the materials section 2.2.

Controls were cast films of polyurethane (Z6A1), as a flat benchmark, and electrospun polyurethane (Z6A1), as unmodified fibres. Modified electrospun polyurethane with the highest concentration of modifier was chosen for both titanium (Ti₂) and zinc (Zn₃) modifier. The highest modification was chosen in order to be able to highlight the difference between modified and unmodified materials. A selection was rendered necessary by time constraints.

3.2.2 *Contact angle*

Surface wetting properties were quantified using contact angle goniometry, using a Contact Angle Goniometer (DSA30, Krüss GMBH, Germany).

A drop of a non volatile liquid, usually water (but other liquids can be used as well), is carefully placed on the desired surface by using a syringe operated via a manual screw. A camera is aligned with the surface and is used to take a good contrast, black-and-white snapshot of the sessile drop on the surface, from which the contact angle between the surface of the drop is calculated.

A narrow segment of dry material (3 mm width) was cut and fixed to a microscope slide via double-sided tape. The slide was positioned and clamped on the CAG elevated stage and aligned to the camera. A 10 µL droplet of deionised water was delicately produced close to the surface by manually turning the screw of a syringe. Once both the surface and the drop were in focus on the camera, the droplet was deposited on the surface and a snapshot was taken immediately afterwards.

Contact angle values were measured by the in-built drop shape analysis software. Each measurement was repeated on at least 5 different

dry locations for each sample, and then an average and SD was calculated.

3.2.3 Atomic Force Microscopy

Morphology images and surface properties were collected with an Atomic Force Microscope (MFP – 3D Bio AFM, Asylum Research, Oxford Instruments, UK) in non-contact mode in air with a scan size $10\ \mu\text{m} \times 10\ \mu\text{m}$, scan density 256 points/line, scan rate 0.4 Hz, using AC160TS cantilevers (silicon, uncoated, spring constant 26 N/m) with a tip radius of 7 nm. The AFM was operated in ambient with a vibration isolation system. The tip was oscillated normal to the surface and was driven to a frequency close to the cantilever resonance frequency (300 kHz).

Images were recorded on different areas of the samples in order to increase representativity of the whole item.

Cast films were imaged on both the side in contact with the air and with the glass, at different scales, from $80\ \mu\text{m}$ to 200 nm (side length). Random section profiles of the $1\ \mu\text{m}$ images were taken and the peaks measured via the in-built options of the imaging software, along with ARgyle Light (version 20121.1.4.11) and Gwyddion (version 2.49, Czech Metrology Inst., Brno, CZ).

3.2.3.1 Force mapping

Force mode was operated on the same Atomic Force instrument utilising cantilever vibration free amplitude in air. In order to be able to image single fibres resting on a hard surface, electrospun samples were prepared by electrospinning on glass microscope slides mounted on conductive tin foil, while cast samples were simply cut from larger films. Using AFM, the position of an individual fibre was located by imaging the surface before indenting. This was performed in an attempt to ensure that the derived quantities (effective modulus) were based on the nano-indentation of a single fibre rather than the compound effect of nano-indentation and the movement of the electrospun mesh as a whole. Indentation was then carried out using the AFM probe (AC160TS) to a fixed cantilever displacement of 200 nm.

Oliver-Pharr was then used to calculate the modulus for each indent from the first 40% of the retraction curve. The microscope collected ten force values per line, ten lines in total, creating a 10x10 grid per picture, on a 10x10 μm portion of the surface.

Adhesion values were collected on the same day in a chamber with no environmental control, but with weather conditions non changing considerably during the day. Humidity and temperature are detected with a humidity sensor (Humidity Alter II, Extech Instruments, USA). Humidity was $36 \pm 3\%$ and Dew Point $8.8 \pm 1.2^\circ\text{C}$.

The adhesion force curves were analysed with the in-built imaging software (ARgyle), which produces a map of the adhesion values as pixels arranged on a matrix and visualised as a black and white scale, where darker colours correspond to the glass substrate. The adhesion value matrix was exported on a spreadsheet. Each matrix was confronted with the colour map, and the values corresponding to the fibres were collected and averaged, and an overall weighed average and SD was then calculated. The glass value was subtracted from the average value. At least 10 measurements were taken for each sample, and three samples from each material (cast, ES, Ti2 and Zn3) were imaged. Analysis was limited to samples with the highest concentration of modifiers, because of time constraints.

3.2.4 *Statistical analysis*

The quantitative data presented in this chapter are expressed as mean values \pm standard error or standard deviation.

All quantitative experiments (contact angle measurement), were repeated for $n = 5$.

Statistical significance was determined following one-way analysis of variance (ANOVA) with post hoc testing according to Tukey's procedure at a 95% confidence level (using Minitab, software version 17).

3.3 RESULTS

3.3.1 Contact angle

Contact angle values were obtained through a static contact angle goniometer, with a sessile drop technique, using water as liquid phase in atmospheric conditions. The water drop tends to be absorbed by the electrospun layer, and dispersed thanks to capillary forces. Therefore the sessile angle changes very rapidly after the first few seconds after being deposited, with the drop spreading over the surface, and the angle decreasing gradually towards smaller values. The time development of water drops on substrates is shown in Fig. 3.4.

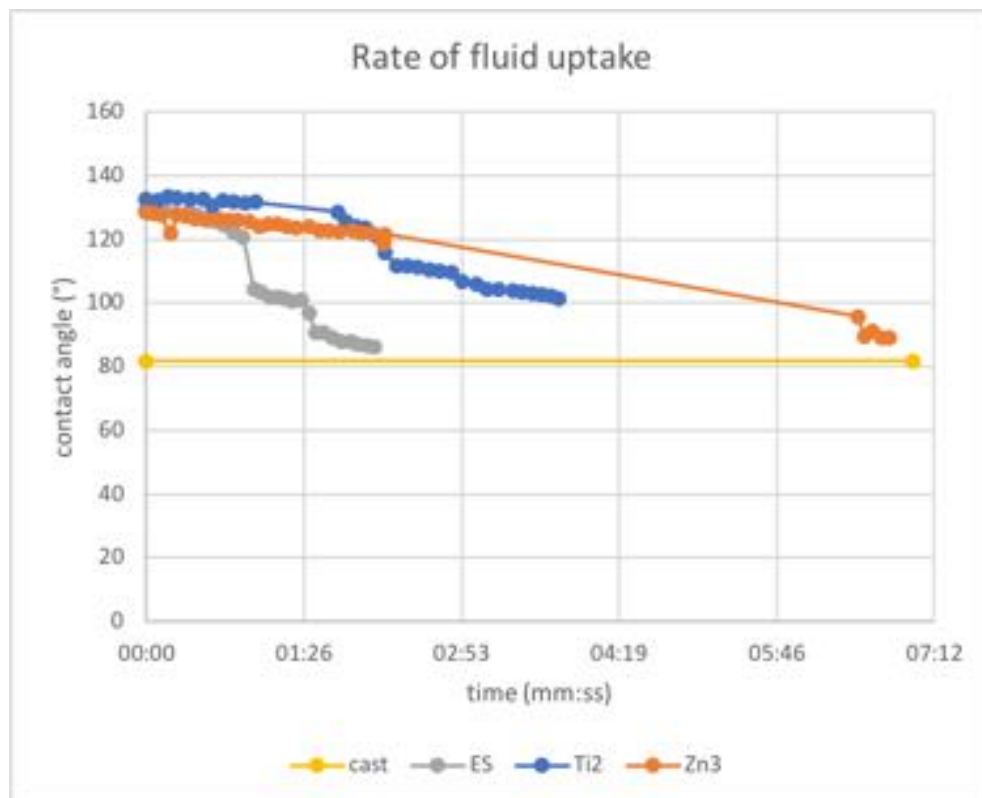


Figure 3.4: Development of contact angle over time on ES polyurethane, Ti2 and Zn3 modified surfaces. Contact angle drops from values around 130° down to around 80° within minutes.

In order to compare different substrates, an average of the contact angle after a cut-off time of 5 seconds was taken. Results are reported in Figure 3.5.

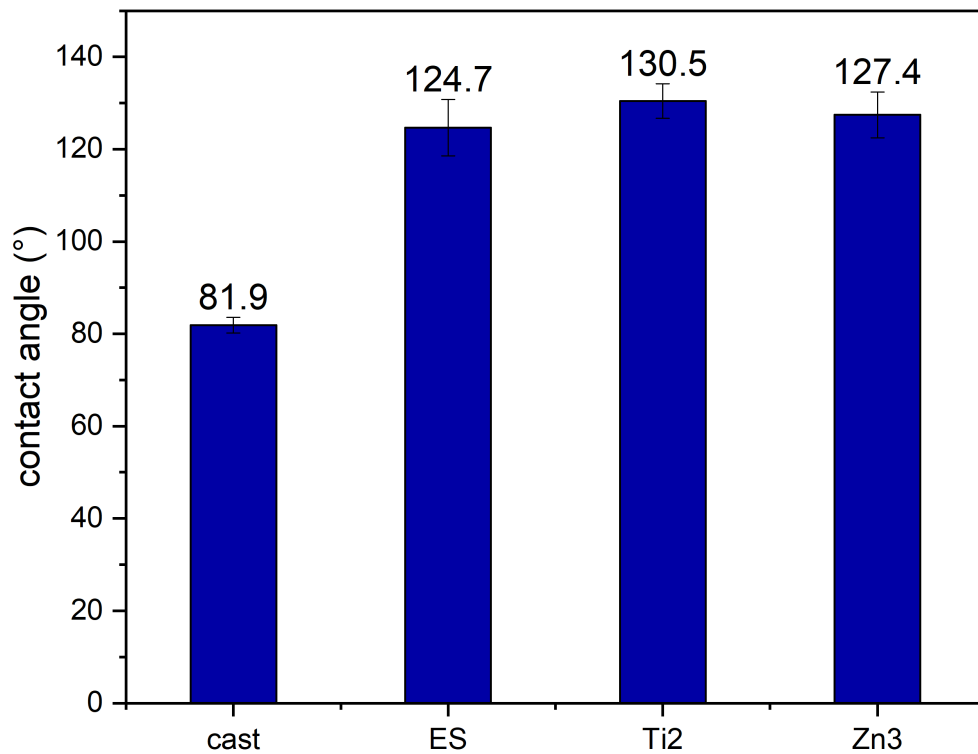


Figure 3.5: Contact angle measurements and SD ($n = 5$) for cast and ES polyurethane, Ti2 and Zn3 (modified electrospun). CA is not significantly different for any of the electrospun materials.

As shown in the graph, cast film value ($81.9 \pm 1.7^\circ$) is compatible with angles previously reported in literature (for example, $86.51 \pm 0.19^\circ$ [159]).

Contact angle values at $t=5s$ do not differ significantly across all the electrospun surfaces, either modified or unmodified (ES, Ti2 and Zn3), and measures around $127 \pm 3^\circ$.

3.3.2 Atomic Force Microscopy

3.3.2.1 Surface morphology

Multiple scans of cast and electrospun materials, both modified and unmodified, were obtained at different magnifications. AFM topographical and phase contrast data are obtained simultaneously during scanning, providing a one-to-one correspondence of the height and phase data as shown in the figures, along with the scale of the colours associated with the pictures.

As a reference, portions of cast Z6A1 were imaged, on both sides (air-exposed and glass-exposed) as well. Scans of the cast material (Fig. 3.6) show two very different morphologies whether on the air-exposed surface or the side in contact with the glass bottom of the Petri dish. While the air-exposed surface exhibits dome-like structures, with a curvature ray of $20\ \mu\text{m}$, the glass side exhibits a finer structure, with an average distance between the bumps of $67\ \text{nm}$ (Fig. 3.6c).

The scans in Figure 3.7 reproduce the morphology of electrospun surfaces. Fibres are randomly aligned and superimposed. They are smooth and well defined, not fused together, so much that they can be plucked and moved around by the tip of the AFM (Fig. 3.8 showing artefacts), evidence that they are quite flexible and individually deposited.

AFM provides a three-dimensional scan of the surface, unlike SEM micrographs (Fig. 2.1), and a wealth of information on the depth of pores can be derived (Fig. 3.10), albeit affected by the cantilever vertical range and tip convolution effect.

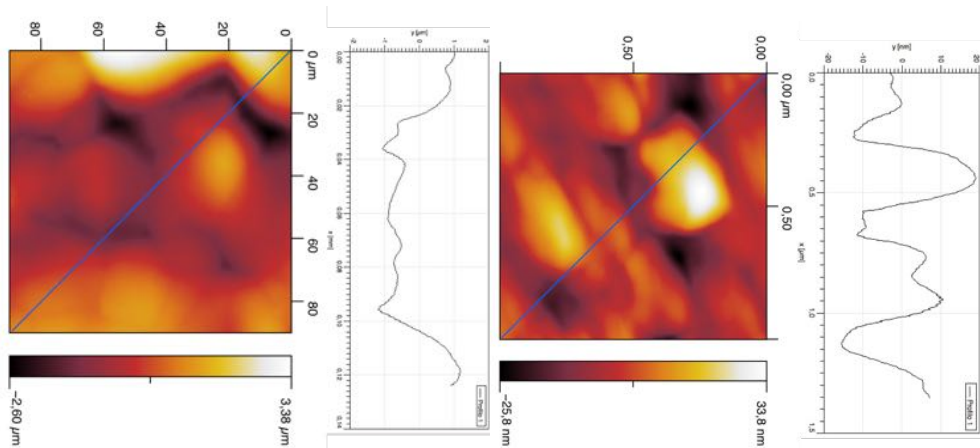
A difference in morphology can be noticed between modified and unmodified fibres: while ES fibres look clumped and bundled together, modified fibres (Zn3 and Ti2) are more straight and individually defined.

Examples of profiles of single fibres are reported in Figure 3.11. While on the Ti2 fibre a single bump can be identified, the Zn3 exhibits a profile with several profile features. The average roughness, as calculated by extracting single profiles of fibres with the software, is comparable on all electrospun surfaces at around $11\ \text{nm}$.

3.3.3 *Phase retrace images*

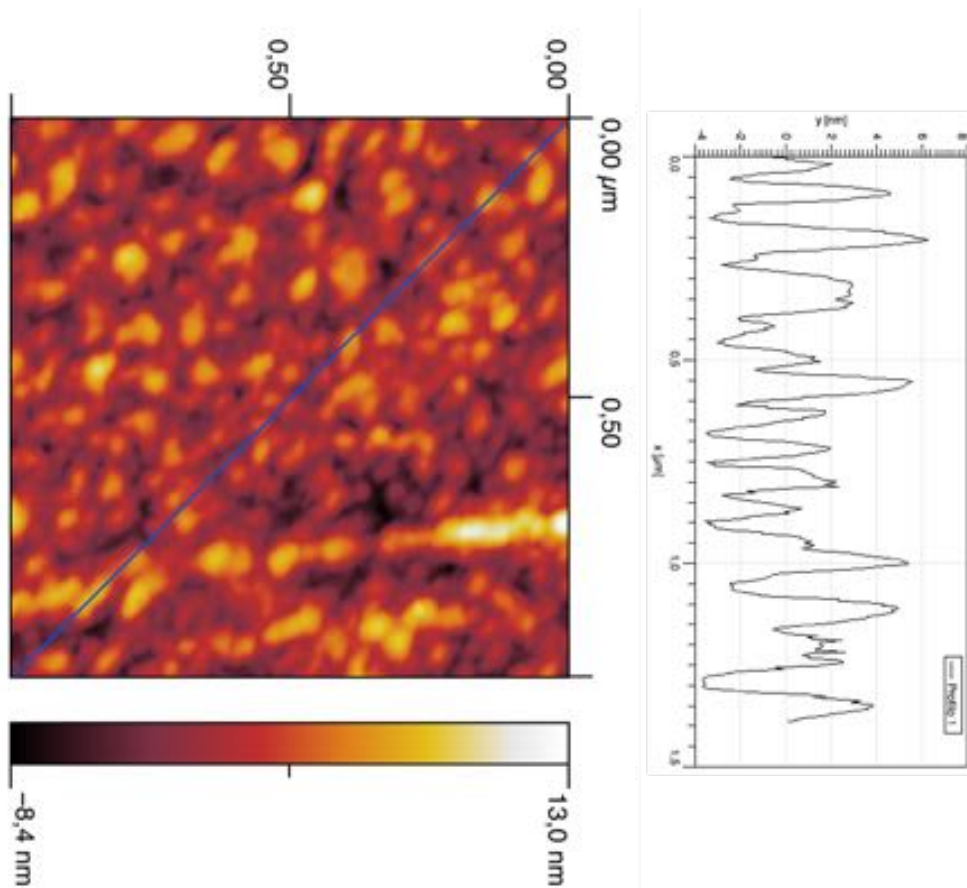
Phase retrace images are reported in Figure 3.7 next to the respective morphological image.

On ES and Ti2 fibres, phase contrast colour maps exhibit a fine structure of small irregular patches. The interspace between patches is small, and it might be attributed to the distribution of hard and soft segments on the surface of the fibre.



(a) Z6 cast, air side, 90x90μm.

(b) Z6 cast, air side, higher magnification (1x1μm).



(c) Z6 cast, glass side (1x1μm)

Figure 3.6: AFM scans of cast Z6A1 at lower and higher resolution, on both glass and air-exposed side, and an example of the height profile of the glass side.

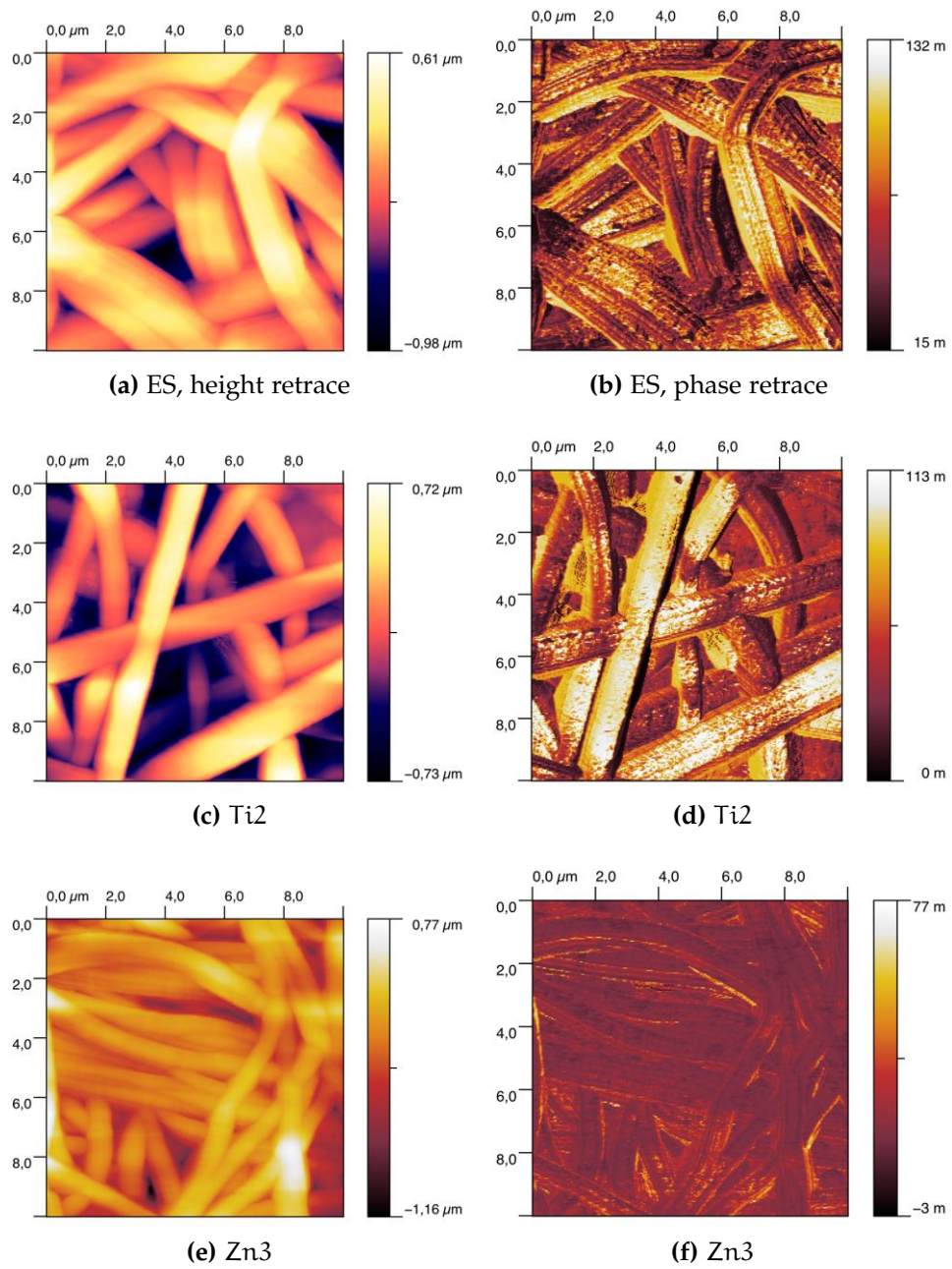


Figure 3.7: 10x10 μm AFM scans of electrospun materials, height profile on the left and phase retrace on the right. The height and phase difference scale is reported next to each picture.

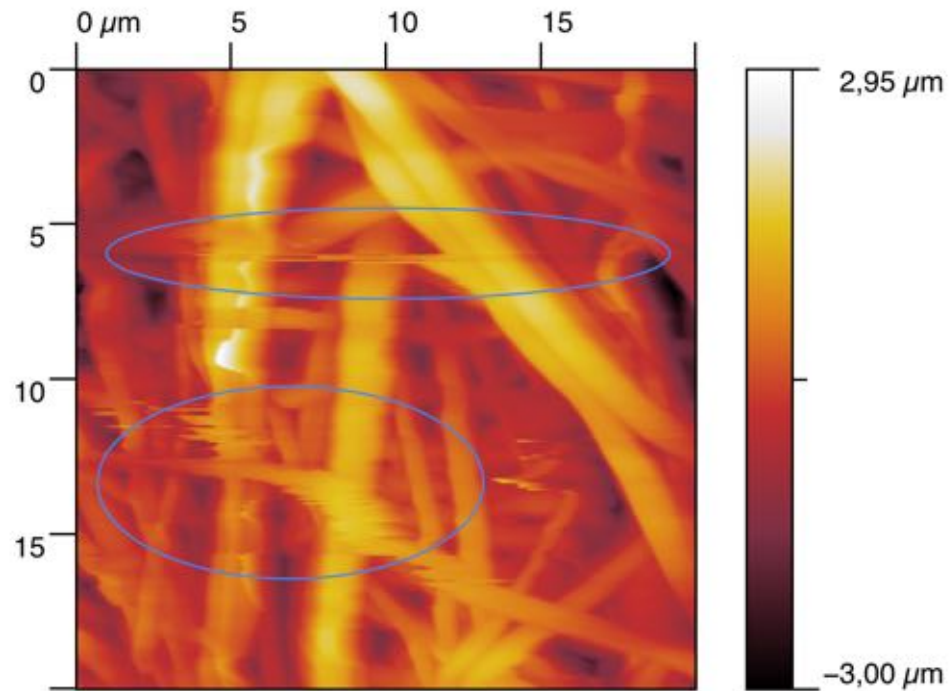


Figure 3.8: $20 \times 20 \mu\text{m}$ AFM scans of Z6A1 electrospun. The two main artefacts are due to loose fibres being plucked by the AFM tip during the sideways scan movement.

Phase retrace image of Zn3 sample show small bumps of darker colours, in correspondence to the bumps present on the height profile (Fig. 3.11b). Such bumps are scattered along some of the fibres and perpendicular to the main axis, looking like stripes. The contours of the features are defined and clear.

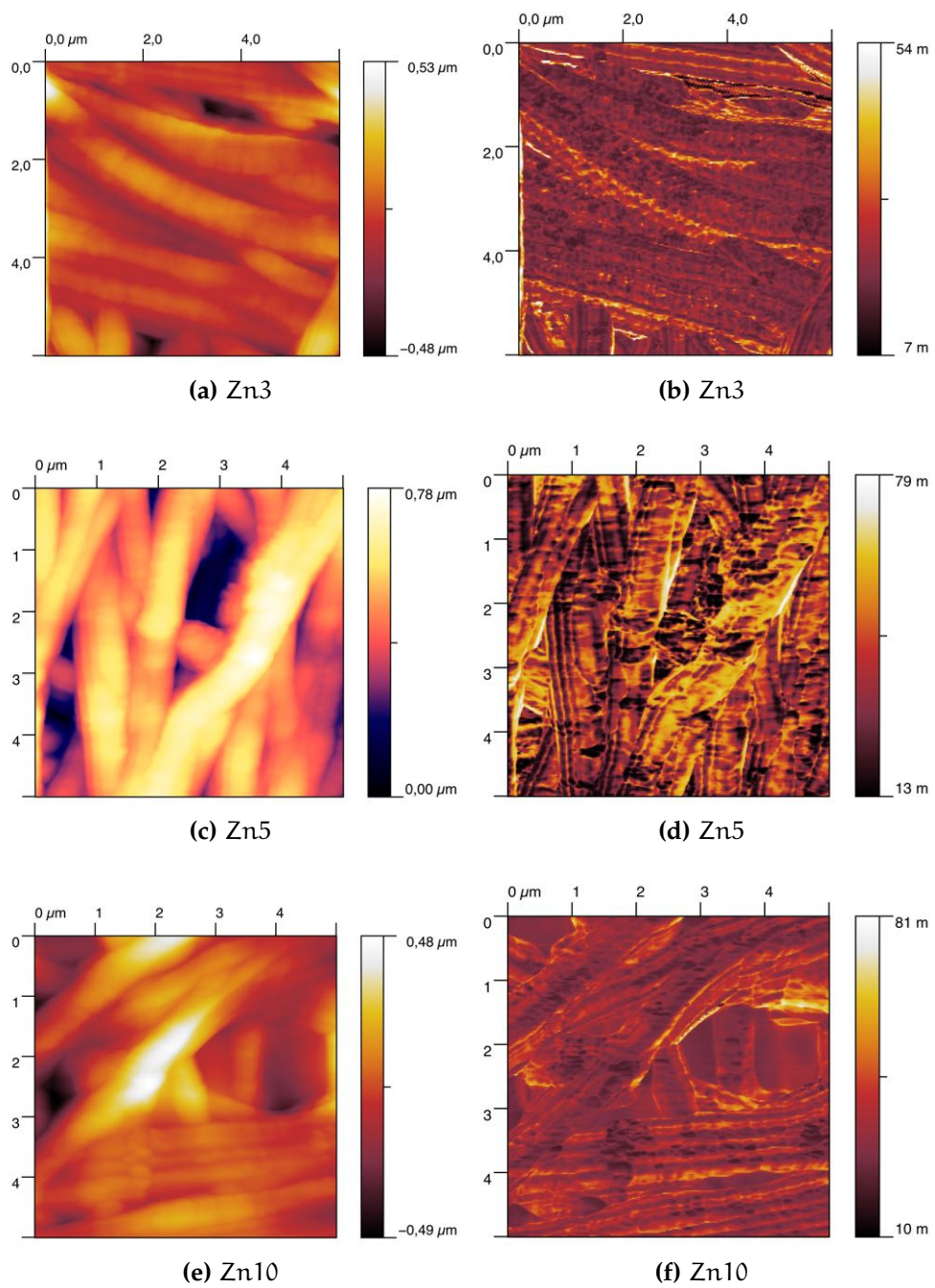


Figure 3.9: 5x5 μm zoom-in AFM scans of Zn-modified electrospun materials, height profile on the left and phase retrace on the right. The height and phase difference scale is reported next to each picture.

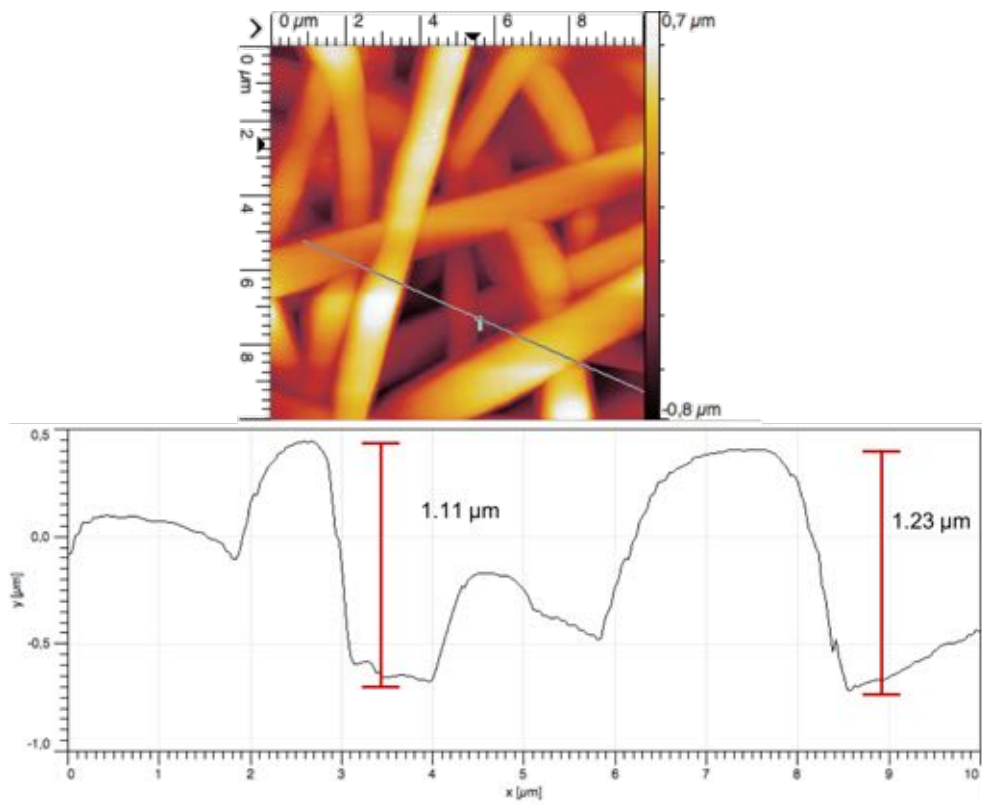
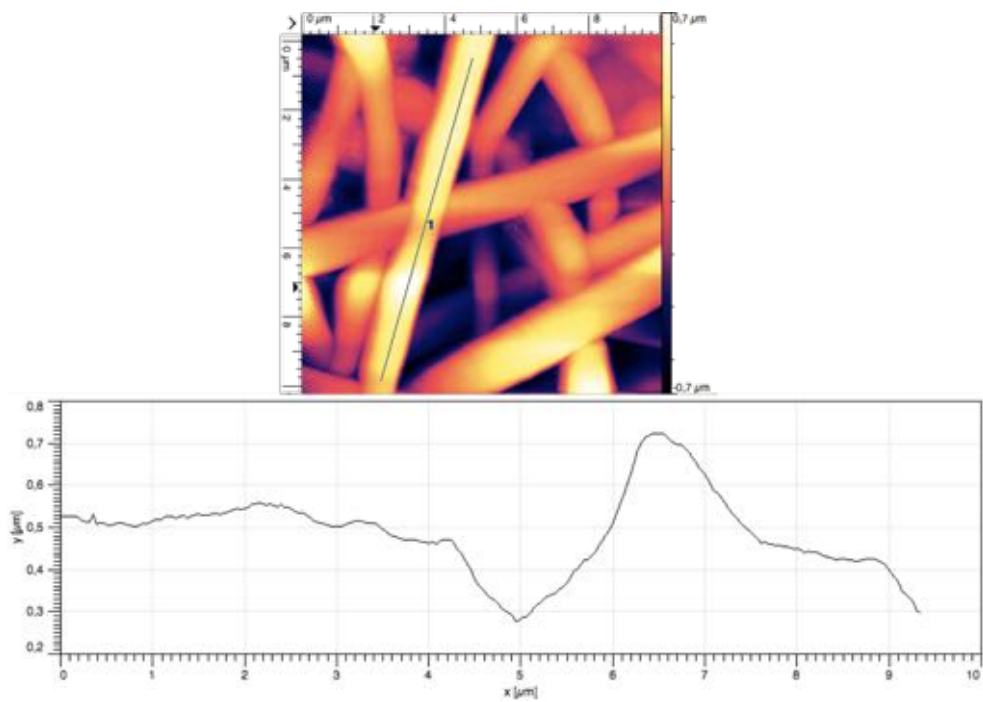
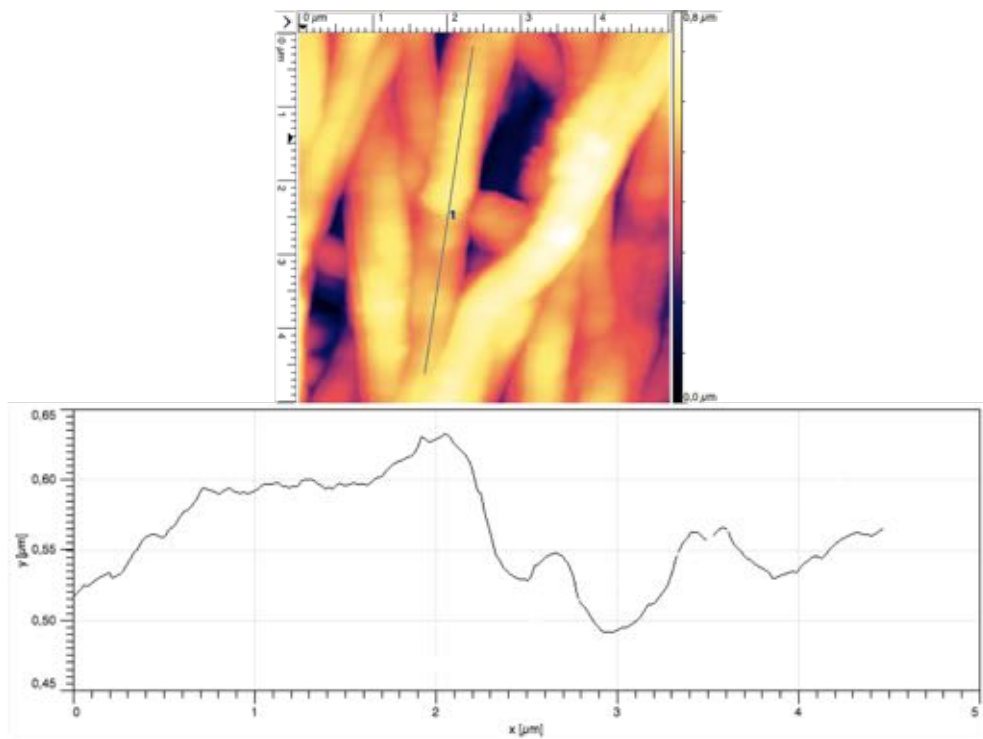


Figure 3.10: Example of height profile of selected pores (marked) on Ti2 scan.



(a) Ti2 height profile of the marked fibre.



(b) Zn3 height profile of the marked fibre .

Figure 3.11: Profile of selected single fibres on Ti2 and Zn3.

3.3.3.1 Force mapping

Pictures in Figure 3.12 show values of adhesion force as obtained from force mapping on single fibres for Zn3 and Ti2 sample deposited on glass microscope slides, cast film (glass side) and mat fibres for ES. Adhesion force values are calculated by the in-built AFM software and are reported as gradation of black and white on a 10x10 grid (ten force values per line, ten lines in total).

Values corresponding to the where fibres lie (lighter colours) are collected and averaged, and the value for glass (dark colours) are subtracted from the average. Results are reported in graph shown in Figure 3.13.

Sample Ti2 exhibits the highest adhesion value, while cast polyurethane has the lowest, and ES and Zn-modified exhibit adhesion values that are not significantly different.

These results are certainly affected by the limitations of the method. Adhesion is not only influenced by the nature of the surface, but by the atmospheric conditions. The results are obtained by a number of scans performed on the same day, but not in an environment-controlled chamber, and the slight changes in humidity, temperature and pressure can influence the results.

Furthermore, the resolution at which the force maps have been obtained is low, with one pixel corresponding roughly to the width of a fibre. When the tip hits the border of the fibre, side effects can affect the nominal result.

AFM tip geometry, penetration depth and contact area all have an influence on the measurement of the sample adhesion force and modulus. The morphology of the sample surface itself can bear an impact on the measured modulus due to variation of the local contact area. The curved morphology of the fibres as compared to a flat surface of the cast polyurethane do introduce a certain variability. Around fibre boundaries, convolution and smearing effect due to finite sized contact area influence the reading.

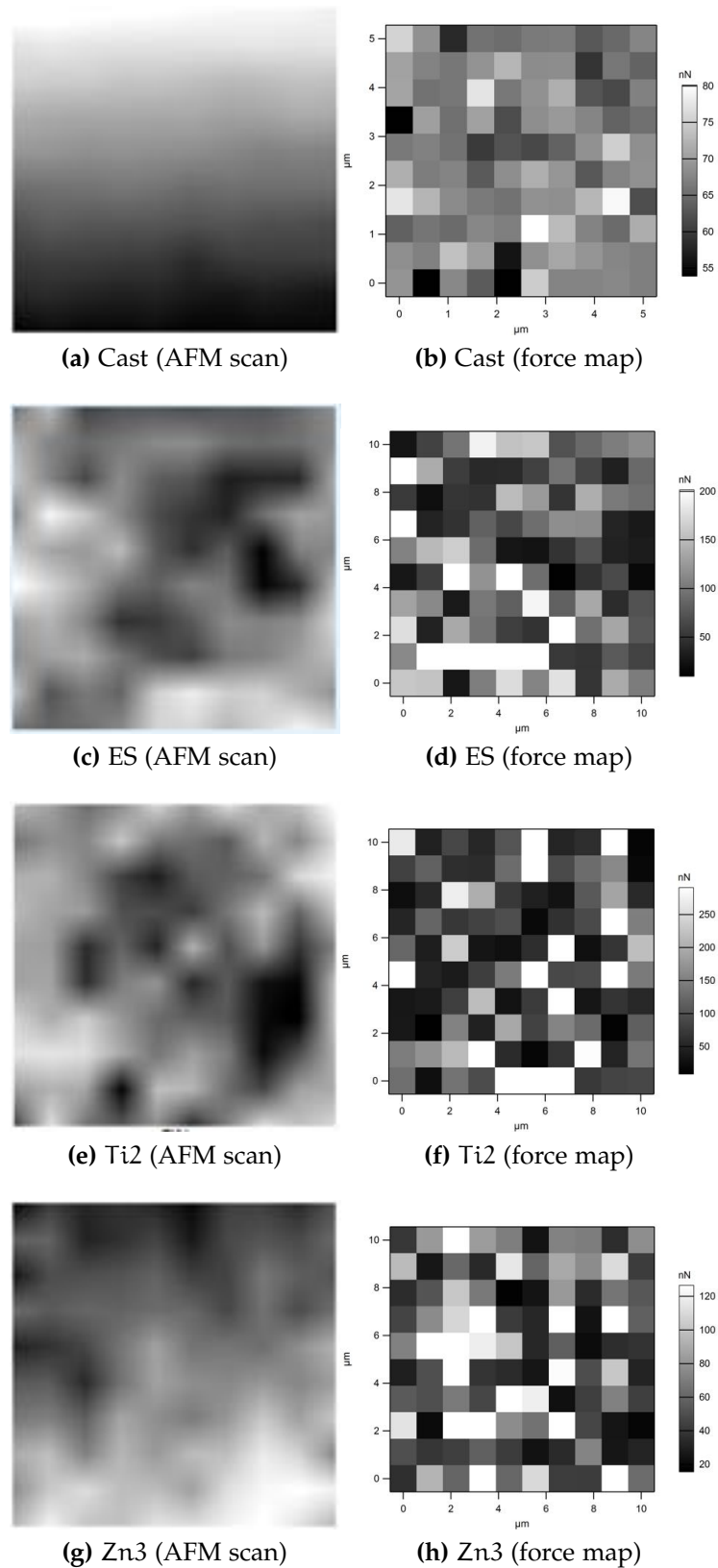


Figure 3.12: Adhesion force mapping scans (on the right) along with a low-resolution AFM height scan produced by the software together with the force map (on the left).

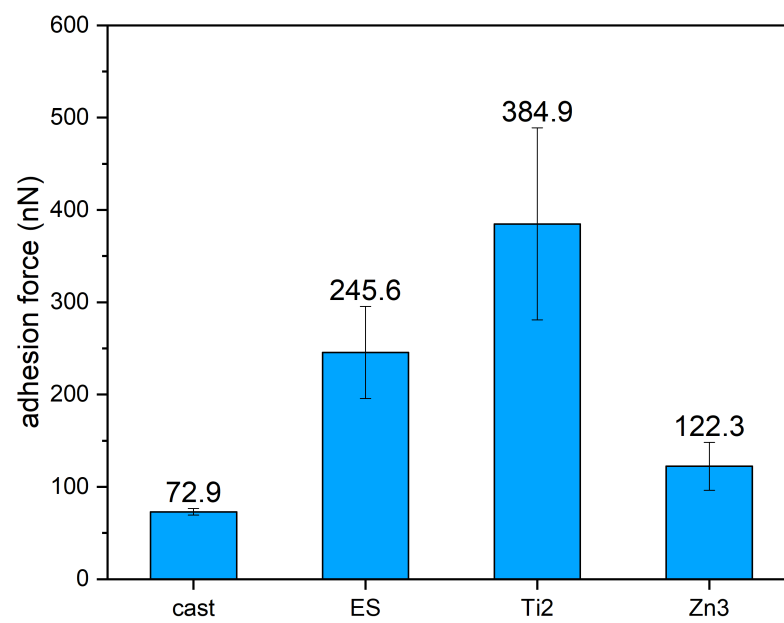


Figure 3.13: Adhesion force values and SD ($n = 3$) for cast and ES polyurethane, Ti2 and Zn3 (modified electrospun).

3.4 DISCUSSION

AFM images were used for a topographical reconstruction of the surface and show how manufacturing influences the surface morphology and topography.

*Morphology
characterisation*

For example, the topography of cast samples (Fig. 3.6) is particularly interesting. The two sides of cast films are different: both exhibit dome-like structures, but dimensions of the domes are separated by three orders of magnitude depending on whether the polyurethane was in contact with glass or air (67 nm on the glass versus 20 μm on the air side). This difference depends on the solvent evaporation rate (kinetic factor) and on the interaction between the polyurethane and the glass surface or air, respectively (thermodynamic factor).

As noted previously (Section 2.4), in the case of solvent casting, the polymeric phase separation can be considered complete and hard and soft domains are easier to image with AFM. Under the experimental casting conditions, solvent removal occurred over the course of hours, allowing for a slow, complete phase separation. Instead, on electrospun fibres the microdomain separation occurs on a smaller scale, and segregation is not as easy to detect.

Microphase separation first occurs in solution, during solvation of the polymer, with subsequent crystallisation of the hard segments as the solvent evaporates. The blocks of hard segments are frozen into domains of limited size. In fact, the polyurethane hard segments have a high glass transition temperature even under slow solvent removal conditions which may allow crystal growth, so the formation of large crystals and spherulites of hard segment is inhibited. Given the lack of spherulites, the bulk of the polyurethane cast film is transparent and it is smooth (on the macroscale).

These same microdomain separation appears differently on electrospun fibres and modified fibres. As shown by individual fibres profiles (Fig. 3.11), Ti-modified fibres are usually smooth, confirming the dispersion of the metal ions and no corrugation or formation of a rough surface. Some height features can be noticed on Zn-modified samples. This is particularly evident on phase-contrast pictures, ow-

ing to a better lateral contrast, providing finer details than the height pictures.

The mapping of the polyurethane surface is of key importance as the distribution of hard and soft domains influences not only the mechanical properties, but the interfacial properties as well, such as charge distribution, polarity and wettability, which can be all explained through the exact chemistry exposed to the surface by the polymeric chains. The charge distribution and polarity determine the behaviour of the polyurethane surface in a biological environment, for example how the proteins adsorb and how the surface influences cell adhesion (these aspects are discussed in more details in the following chapter).

*Modification of
the surface
properties*

While fibres exhibit a smooth morphology (Fig. 3.7), phase-contrast imaging shows a different situation at a smaller scale. Darker and lighter areas alternate on the surface, which can be traced back to the alternating of harder and softer domains which characterise the chemistry and physics of polyurethanes.

The soft-hard segment segregation is more evident on the images of cast samples (Fig. 3.6c). The hard domains appear as small bumps at regular intervals (between 50 nm–100 nm). The microphase domains on electrospun materials are much smaller and finely dispersed.

The modified materials have been inspected for any signs of segregation of inorganic fillers. In general, Ti-modified surfaces look homogeneous at the micrometric scale, therefore the dispersion of inorganic material is expected to be good (Fig. 3.7).

Zn samples (Figure 3.9) exhibit some features with a stripe-like shapes. These stripes are both present on the morphological and on the phase-contrast maps, where they appear with a notable different, darker colouring. These areas are not artefacts and are present at different magnifications and over several scans, without changing position nor appearance. It could be ruled out that they do not belong to the fibres themselves.

The different colouring might suggest that these areas are different from the rest of the fibre they belong to, possibly areas where the inorganic components is present in higher concentration or has separated from the polymeric component and created a structure that is almost

a particle on the fibre. Therefore, a different colouring could indicate a difference in mechanical or chemical properties.

It must be underlined that phase shift tend to follow the change in morphology, with a change in curvature resulting in a change in the phase shift values because of a coupling effect between the tip of the probe and the surface.

It is not straightforward, however, to assign the hardness of the material to the phase colour, as papers in literature report contrasting conclusions depending on experimental conditions, for example closeness of the AFM tip to the surface.

Images shown in the results section (Fig. 3.7) were normally taken in moderate range. In moderate force tapping, higher spots correspond to both high phase values and darker colours. As high phase shift corresponds to high modulus or harder domains, darker domains on the phase retrace images can be attributed to harder domains, or domains with higher dissipating properties (richer in polar groups, such as $-OH$ and $-NH$, as harder domains are). It is possible therefore to associate these domains to an accumulation of zinc cations, or clusters, on the surface of Zn-modified samples. Zinc segregates on the surface of the surface and does not seem to be mixed as much as titanium within the fibres. This might have an impact on how the surface interact with the biological environment.

Such structures have not been detected on the titanium-modified samples or on unmodified samples (ES) (Fig. 3.7). While this does not surprise on ES samples, it is curious that no similar feature is present at all on Ti samples. As discussed in the previous chapter, elemental analysis shows that these fibres do contain titanium. It may be supposed that, for these samples, the inorganic phase is more uniformly distributed throughout the polymeric matrix and is well incorporated in the fibres, probably inside, and not concentrated on the surface. This observation is supported by the results described in the previous chapter.

As the mixing of modifiers appears to be different between Ti-modified and Zn-modified samples, the distribution of charges over the surface of these materials could be different as well. In order to

*Surface
adhesion*

verify this idea, information on adhesion at a microscopic level was collected via atomic force mapping, with data collected every 1 μm .

From the collected data reported on Figure 3.13, titanium modified fibres exhibit a higher adhesion than all other samples. Unmodified electrospun materials show an adhesion value higher than cast PU, while zinc-modified surfaces exhibit adhesion values not different than cast polyurethane.

Surface chemistry and charges determine the adhesion force the tip experiences when retracting from the surface. Results presented in Figure 3.13 seem to suggest that electrospun fibres are easier to penetrate and that the adhesion force exerted on the tip is higher than the cast material. Interestingly, the most adhesive material is Ti-modified material. This can be explained as the structure of titanium-modified fibres is sensibly modified by the titanium structure (see Section 2.4) and this might make it easier for the AFM tip to penetrate in the fibres. Furthermore, the surface might have a different charge distribution and result in a higher “stickiness” on the surface when interacting with the AFM probe.

On the contrary, the fact that zinc modified fibres compared with the cast surface might suggest that addition of zinc does not modify sufficiently the surface chemistry and the internal structure of the fibres themselves. Peculiar structures were observed at high concentrations of zinc-modifier, which leads to think that zinc segregates rather than blend with the polyurethane structures. These results are coherent with observations derived from thermogravimetric data as discussed in Section 2.4. Maybe because the materials are not homogeneously distributed throughout the fibres, for Zn modified materials the adhesion force is not dissimilar to the value for electrospun material.

Finally, Contact angle goniometry is a common technique that relates the surface tension between a surface and a liquid to the surface energy and wettability of the surface itself.

Rate of fluid uptake

Wettability is determined both by the chemical properties of the surface and the morphology of the surface itself. In the case of electrospun materials, the morphological contribution overshadows the chemical properties, therefore all electrospun polyurethane materials,

both modified and unmodified, exhibit a similar initial value, as reported on Figure 3.5. The initial contact angle for all electrospun materials appears to be much higher than the value recorded for the cast sample, and it can be explained by the Cassie-Baxter model, that is, the fact that a rougher surface creates a multitude of air pockets that makes the surface, at least initially, hydrophobic.

This initial hydrophobicity, however, is not a permanent feature of the surface. In fact, thanks to the capillary force owed to the creation of pores in the microscale, the droplets are absorbed very quickly by the surface and the contact angle drops to lower values within few minutes. The porosity and permeability of these surfaces are such that they allow for the droplet to be absorbed. So, although the initial static reading is high, the dynamic behaviour of fluid on electrospun surfaces supports their use for a catheter, as they would be able to absorb the fluid they get in contact with.

While these results do not provide data on the contribution of the Ti and Zn modification, they do offer an insight on the effectiveness of the electrospun surface. Electrospun fibres absorb fluid by capillarity, and the speed at which all electrospun scaffold absorb the liquid droplet can be related to their effectiveness at absorbing and draining away biological fluid even without the application of negative pressure. Scaffolds made of nanofibres act better at dispersing the fluid than a continuous surface (especially when as hydrophobic as MSDS), regardless of their individual modifications, therefore making electrospun surfaces an apt potential candidate for catheters.

In order to make this testing stronger, further controls should be introduced, such as a negative/hydrophobic control (PDMS) and a positive/hydrophilic control (polycaprolacton, PCL, which is easy to fabricate in an electrospun form). Controls would allow a direct comparison of modified electrospun materials.

In general, sessile drop contact angle measures the wettability properties of a macroscopic area which are an average of the properties over that area. In particular, the morphology of the electrospun surface probably has more influence than the properties at small range. Importantly, however, contact angle drops from higher values very rapidly, therefore an initial high value does not represent an inca-

capacity of the surface to absorb water efficiently. On the contrary, all electrospun surfaces behave similarly, being able to absorb fluid by capillary forces through the micropores of the surface. These results support the use of electrospun polyurethane as an alternative material for catheters, given their ability to sustain a continuous flow of fluid through the surface.

3.5 CONCLUSIONS

In general, neither surface retrace nor phase retrace could highlight any inhomogeneity on the surface in unmodified and titanium-modified materials, but some inhomogeneous areas appeared on Zn-modified samples, in the form of darker stripes or spots. The darker shade may suggest that zinc concentrate and segregate from the polyurethane, creating clumps visible on the surface of fibres as spots.

Materials were analysed via force mapping as well, and adhesion values were obtained. Surface adhesion is highest on titanium-modified fibres and electrospun fibres as compared to the cast polyurethane, suggesting that the addition of titanium has an effect on the fibres surface. Such results suggest that a different distribution of charges leads to a different adhesion value when the AFM tip penetrates the fibres.

On the other side, zinc-modified fibres do not exhibit an adhesion value much different than the cast material. Zinc-modified materials, as described in the previous section, do not hint at a different internal structure, hence the adhesion properties are not dissimilar from the cast polyurethanes.

Regardless of their differences at the micro and nano-scale, although the initial contact angle reading seems to indicate electrospun materials are (apparently) hydrophobic (high contact angles are probably due to air pockets between fibres), the drops of water are absorbed by the materials within minutes. All electrospun materials seem efficient at absorbing the fluid, thanks to their microporous structures, therefore making them all suitable candidates in the search for materials that can drain away biological fluid to be employed in the manufacturing of catheters.

BIOCOMPATIBILITY ASSESSMENT

4.1 INTRODUCTION

The present chapter aims to verify how the scaffolds, modified via a sol-gel route with titanium and zinc, interact with a biological environment.

Their compatibility with regard to neuronal epithelial cells, which is the cell type that is closer to the tissue the shunt catheter comes in contact with, is tested via a viability and apoptosis assay, to verify whether the modified materials succeed in reducing viability and proliferation of astrocytes on the surface.

Furthermore, the adhesion of cells is evaluated via a detachment assay and analysis of motility, and these are related to the features of the scaffolds, in order to assess whether they are successful in reducing astrocyte attachment.

Lastly, a bacterial strain (*Staph. aureus*) is grown on the materials, in order to check their ability to inhibit the proliferation of bacteria and limit risks of bacterial contamination.

4.1.1 *Cell apoptosis*

Apoptosis is considered the ordered and active process through which cells ultimately die. Apoptosis can follow either an intrinsic pathway, when the cell initiates self-destruction mechanisms because it senses stress, or an extrinsic pathway, when stimuli come from external sources, such as other cells or the environment [160].

The intrinsic pathway includes DNA damage that cannot be rectified by internal repair mechanisms. External stimuli, instead, involve cytokines such as Tumor Necrosis Factor (TNF). Conditions that can provoke the immune cells to produce TNF include a number of biological or chemical cues, for example, exposure to radiation, viral

toxins, elevated temperature, toxic substances, and, particularly, radicals (Reactive Oxygen Species, ROS).

Both pathways involve the activation of caspases, a group of proteases, that degrade proteins.

A cell undergoing apoptosis shows a series of characteristic morphological changes. Early alterations include:

- Caspases break down the cytoskeleton, leading to the retraction of the lamellipodia, cell shrinkage and rounding of the cell;
- The cytoplasm has a dense and darker appearance, and the organelles are tightly packed;
- A process called pycnosis, a hallmark of apoptosis, occurs, whereby chromatin undergoes condensation into compact patches against the nuclear envelope;
- The nuclear envelope becomes discontinuous and the DNA inside it is fragmented in a process referred to as karyorrhexis. The nucleus breaks into several discrete chromatin bodies or nucleosomal units due to the degradation of DNA;
- eventually, the cytoplasmic fragmentation attracts macrophage removal of the cell material.

Exposure of the apoptotic proteins (caspases) to metal ions can influence apoptosis. Titanium and zinc can be both involved in Reactive Oxygen Species reactions, and zinc has been shown to have an active role in apoptosis regulation [161]. In this chapter, their influence over apoptosis of astrocytoma cells will be monitored and evaluated.

4.1.2 *Cell adhesion*

Harris & McAllister [3] report the role of adherent cells in the obstruction of catheters. When a surface is exposed to a biological fluid, it is immediately covered by multiple biological macromolecules, such as lipids, carbohydrates and especially proteins. Such macromolecules mediate the subsequent adhesion of cells or bacteria,

via a range of interactions: secondary and dispersive forces, electrostatic interactions, hydrophobic/ hydrophilic interactions and hydrogen bonds, and coordination chemistry. Proteins then mediate the adhesion mechanisms of cells on the device surface.

In order to quantify the force necessary to detach cells from a scaffold, a number of methods are described in Christ & Turner [162]. Generally, these assays can be divided into three categories, according to the way force is applied to cells to detach them:

1. centrifugal force: they are based on centrifuges that are commonly available in laboratories to apply forces normal to the surface in order to detach cells;
2. hydrodynamic shear forces: they use fluid flow chambers to apply shear stress on adhering cells;
3. single-cell micromanipulation: they rely on micropipettes, AFM or another kinds of probe to apply highly-localised forces to a single cell in order to detach it.

Furthermore, detachment assays can belong to two categories, according to whether they apply to a single cell or a population of cells.

In cell population assays, increasing forces are applied to different repeats of a cell culture and the remaining adherent population is quantified. Typically, the adhesion strength value at which 50% of the cells detach is determined. These studies provide an averaged force over the whole population of the sample, and it is appropriate to assess the effect of environmental variables.

In contrast, single cell methods involve detaching a cell at a time, and are useful to relate the force to other properties of a cell, such as spread area, volume, phenotype, and focal adhesion [162].

Although the mechanism of cell detachment in a real catheter environment is via hydrodynamic shear stress, the method that has been chosen for this work is a population assay via centrifugal force, which is indeed normal to the surface. The centrifugal method is described in details in Section 4.2.

4.1.3 *Cell motility*

Cells that are capable of migrating usually exhibit a type of front-rear polarisation, which means, different morphology and molecular structures between the front and the rear of the cell. At the front the cell develops either flat ruffling (lamellipodia) or thin protrusions (filopodia). Upon adhesion to a substrate, cells probe the environment using such nanometer scale processes. Lamellipodia explore the environment before attaching securely and moving the cell forward. Filopodia anchor the membrane and facilitate movement. Lamellipodia and filopodia are examples of membrane structures called cell protrusions.

Cells extend their protrusions in every direction on flat surfaces. However, as soon as the surface present morphological features, protrusions tend to follow the surface profile closely. While the front part of the cell polymerises actin filaments in order to extend the front of the cell and reach out, the rear part uses acting to create bundles of filaments (called stress fibres) that hold and pull the cell together and forward to the front part. This way the cell can proceed and advance [163].

Filopodia movements are isotropic, that is, they have no specific direction for their spreading or retracting movements [164]. Filopodia movement occurs in three stages: expression of filopodia, followed by focal adhesion and finally movement/protrusion, or retraction of the filopodia. The quality of focal adhesion determines the direction of movement, the contact area between focal adhesion points and surface. This is the reason why astrocytes tend to move along rather than across ridges. Protrusions tend to stay longer and be more stable along the fibre direction rather than across.

4.2 MATERIALS AND METHODS

4.2.1 *Viability and apoptosis assays*

Viability (cell proliferation) is usually measured indirectly via one of the available colorimetric assays. The mechanism they are based on is similar for all of them. Cells are exposed to a certain amount of dye (dissolved in the culture medium) for a period of time. The dye is taken up by alive cells and metabolised. After a determined amount of time the dye is collected and the absorbance in the UV-vis range is measured. This value is then related to a standard to determine the amount of dye that has been metabolised, which is proportional to the cell activity, which in turn is assumed to be related to the amount of alive cells.

The dye assay that was used for the present study was AlamarBlue, provided by Invitrogen. AlamarBlue is based on the dye resazurin, which is reduced to resorufin by alive cells. Resazurin is not cytotoxic and does not affect cells, and therefore alamarBlue is not an end-point assay and another viability assay can be performed on the same cell sample at a later time point. AlamarBlue is a highly sensitive assay and, by way of a calibration, it can be used for a quantitative analysis of cells in the sample.

The apoptosis assay (Cell-APOPercentage Apoptosis Assay, Biocolor Ltd., UK) is based on a dye that is selectively imported only by those cells which are entering the apoptosis cycle. Necrotic cells (with a damaged cell membrane) cannot retain the dye and therefore are not included in the count.

The apoptosis assay provides useful information complementary to the viability assay. While the viability assay quantifies the cells that are alive but do not offer any indication whether such cells are thriving or not, the apoptosis assay establishes how many cells are actually undergoing a programmed cycle of death.

4.2.2 *Cell type and culturing methods*

With the aim of exposing the materials to a biological environment as closely related to the human brain as possible, the cell type chosen for this set of experiments was a human glioblastoma astrocytoma cell line called U373 MG, supplied by the European Collection of Authenticated Cell Cultures (ECACC). Cells of this line come from a sample of human brain tissue and are of the adherent type [165].

Cells were cultured in T-flasks in Eagle-modified Dulbecco medium (EMDM) at 37 °C, 5% CO₂. Once cells reached confluence, they were subcultured twice a week up to passage number 36, after which they were discarded.

To passage cells, flasks were first washed twice with versene, treated with trypsin in versene to detach them, then transferred into a tube and centrifuged at 1400 rpm. The natant was discarded and the cells were resuspended in medium. A suitable fraction of the suspension is then pipetted into a new flask while the rest was discarded (when not needed for an experiment).

4.2.2.1 *Cell viability and growth*

Materials were cut in rounded sections with a punch (diameter 6.4 mm) and were secured to the bottom of each 96 well plate using 205 µm-thick double sided tape (Transparent Double Sided Plastic Tape, Tesa, Germany), in three replicates. Three plates were seeded using different populations (passages) of cells and treated as different repeats ($n = 3$). As controls, tape and materials without cells were added as well, in order to verify for false positives. Poly(dimethylsiloxane) (PDMS, Silastic MDX4210, Dow Corning Corp., USA) was used as negative control. Silastic MDX4210 biomedical grade elastomer was prepared according to the manufacturer's instructions. Approximately 20 mL of the combined solution was injected into the base of each well and allowed to cure at 50 °C for 12 h before seeding with cells. Each plate was sterilised by exposure to a UV lamp for 20 min (Daro UV Systems Ltd UK).

Cells were collected from the bottom of a T-flask using trypsin at around 75 – 80% confluence, then centrifuged to remove trypsin and

resuspended in medium. Cell density was adjusted and cells were seeded at an initial concentration of 6400 cells/well, equivalent to 20 000 cell/cm², and cultured for 9 days altogether.

Cell viability was assessed quantitatively at three different time points, 48, 96 and 192 h (respectively, 2, 4 and 8 days) by using a viability assay (AlamarBlue Cell Viability Reagent, ABDserotec, Kidlington, UK). DMEM medium mixed with dye (at a concentration of 10%) was added to each well and incubated for 5 hours, as per protocol provided by the producer, after which time the medium/dye solution was removed from each well, and transferred to a fresh cell plate for reading. Absorbance reading was taken at two wavelengths, 570 and 600 nm, with a plate reader (Multiskan GO, Thermo Fisher Scientific Oy, Finland), and the absorbance values were then elaborated according to the instructions provided by the producer.

Each assay was repeated on three different plates, in order to be able to calculate an average and standard deviation. The AB% reduction was converted to cell number via a calibration that was carried out at each time point by seeding cells at different densities and reading the UV-vis absorbance after 5 hours. The slope of the fitted line provides the relationship between AB% reading and number of viable cells (an example can be seen in Figure 4.1).

4.2.2.2 *Cell apoptosis*

Cell apoptosis was detected by means of Cell-APOPercentage™ (Biocolor Ltd., UK). This assay is a dye that is imported selectively by cells undergoing apoptosis. Necrotic cells cannot retain the dye and are not stained, while alive cells are not permeable to the dye.

U373 were seeded at a density of 20 000 cell/cm² and incubated at 37 °C, 5% CO₂. At three time points, namely after 48, 96 and 192 h (2, 4 and 8 days), apoptotic assay was run according to the indication provided by the producer and hereby described (Cell-APOPercentage™, Biocolor Ltd., UK).

Dye (5% volume of the medium) was added to the culture medium and incubated at 37 °C for 30 minutes, then the dye was removed and each well was delicately washed twice with PBS, making sure that cells were not detached and removed. Then trypsin (10 µL) was

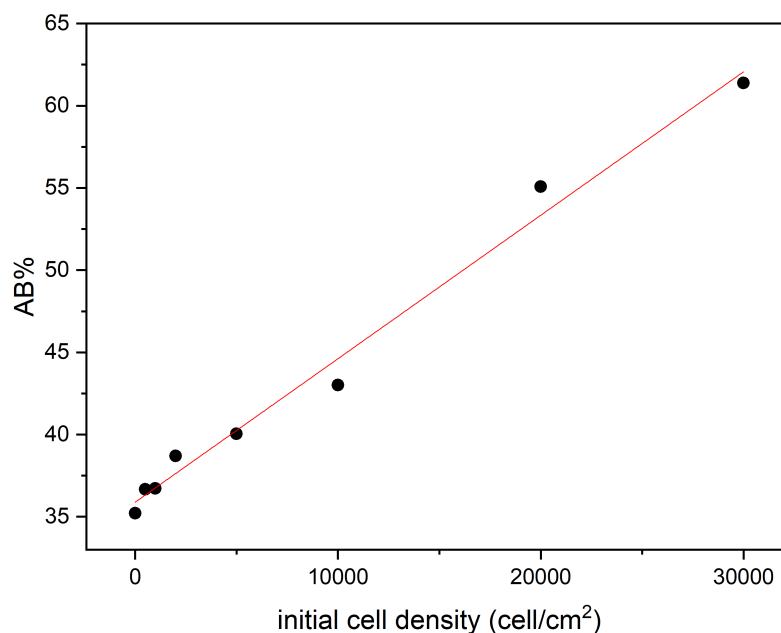


Figure 4.1: Example of calibration curve for AlamarBlue assay. Every time the viability assay was performed, a cell plate with cell seeded at increasing cell densities was incubated for 5 hours and the AlamarBlue percent reduction calculated as per protocol. From the linear relationship between cell density and AB%, it is possible to calculate the number of cells on the main experiment.

added and incubated for 10 minutes at 37 °C. After 5 and 10 minutes the plates were gently tapped to detach cells. Then, the dye release solution (provided with the assays) was added (100 μ L) and the plate was shaken for 10 minutes. The solution was then removed and absorbance at 550 nm was read with a plate reader. Data are reported as the average of repeats ($n = 3$). The average blank contribution (release dye) is subtracted from each value.

As electrospun materials adsorbed dye which was not partially dissolved and brought in solution by the release agent even when no cells are present, the average value of the background dye was collected and subtracted from the electrospun materials as well. Relative apoptosis was obtained by normalising the values of each material population to the positive control (TCP).

Images of cells exposed to the assay after 9 days were taken with a microscope. As the scaffolds are opaque, images were possible only for the TCP, PDMS and cast samples, which are see-through.

4.2.2.3 *Live/dead assay and DAPI assay*

Cells were cultured for different time periods on three 96 well plates, whose bottom was modified to expose cells to different substrates. At each time point, namely after 48, 96 and 192 h (2, 4 and 8 days), a plate was washed with sterile PBS. The live/dead assay (Invitrogen/Thermo Fisher, UK) was removed from the freezer and brought to room temperature. Calcein-AM is green-fluorescent and detects esterase activity, denoting therefore alive cells, while red-fluorescent ethidium homodimer-1 can permeate the cell membrane only when the latter is damaged and, therefore, it stains only apoptotic cells. An appropriate PBS solution of the two chemicals (calcein-AM $2\ \mu\text{mol}/\text{dm}^3$ and ethidium homodimer-1 $4\ \mu\text{mol}/\text{dm}^3$) was prepared and added to each well (150 μL). After cells are incubated for 30-45 minutes at room temperature, pictures are ready to be taken under an optical microscope (ZOE Fluorescent Cell Imager, BIO Rad, USA).

For the nucleus-staining assay, cells were immobilised with a 10% solution of formalin for 10-15 minutes, in order to make the cell membrane permeable to dye. Cells were washed three times with PBS, after which each well was covered with 150 μL DAPI stain at a concentration $300\ \text{nmol}/\text{dm}^3$. Cells were incubated for 5 minutes protected from light. After removing the stain solution, cells were washed three more times with PBS and imaged using the microscope blue filter.

Because many materials are opaque and the microscopes are light-through, it was not possible to obtain good images of cells on some of the substrates, which are therefore not reported.

4.2.2.4 *Cell detachment assay*

The present protocol, based on centrifugal force and on a population method, has been modified from Chu *et al.* [166] and Schlie *et al.* [167].

96-well tissue culture plates were modified to allow the polymeric scaffolds to provide the base of the wells. A small round section of material was cut out with the use of a stud and fixed to the bottom of a 96 well plate with 205 μm -thick double sided tape (Transparent

Double Sided Plastic Tape, Tesa, Germany). A row was added to account for the tape toxicity, one for the PDMS as negative control and finally a row was left unaltered to provide the positive control, tissue culture plastic (TCP). Silastic MDX4210 biomedical grade elastomer was prepared according to the manufacturer's instructions. Approximately 20 mL of the combined solution was injected into the base of each well and allowed to cure at 50 °C for 12 h before seeding with cells.

Cells were seeded on the thus modified 96 well plates at a concentration of 6400 cells/well, or, given the well surface is 0.32 cm², 20000 cells/cm². After being seeded, cells were incubated for 1 hour in an incubator (37 °C, 5% CO₂) to allow for them to start attaching to the substrates.

After one hour, the medium was carefully removed, in order to increase the density difference between the cell and the surrounding environment. Each plate was then mounted upside down on a centrifuge (Centrifuge 5804 fitted with Rotor A-2-DWP, Eppendorf, Germany) which has been modified to support cell plates, and centrifuged each at a different rpm (500, 1000, 1500, 2000, 2500). The centrifugal force was perpendicular to the bottom of the plate and pulling in the external direction, as shown on Figure 4.2. A plate was prepared for each rpm, plus an extra one for rpm = 0, six in total.

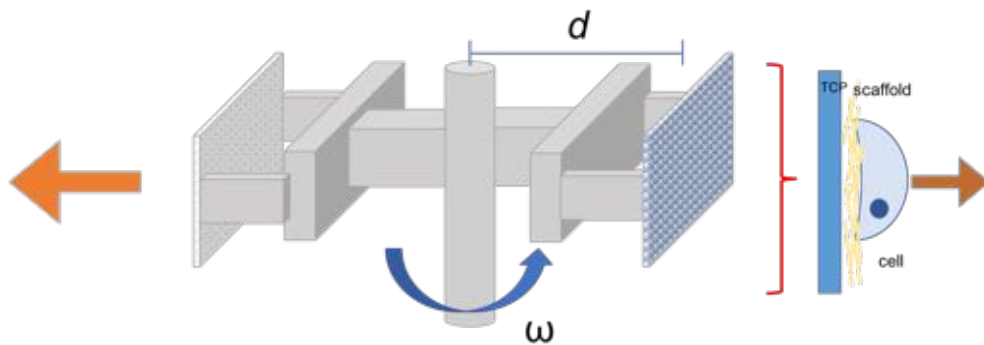


Figure 4.2: Schematic of the centrifuge setting. d is the length of the rotating arm, from the pivot to the bottom of the cell plate. The centrifugal force pulls outwardly and perpendicularly to the bottom of the cell plate.

After each centrifugation cycle, each plate was washed once with PBS very delicately to remove unattached cells, which otherwise would adhere again to the scaffolds, and the medium was replaced with a solution of medium and AlamarBlue (10% v) and incubated for 5 hours. After such time, the content of each well was transferred to a fresh plate and the absorbance value was read with a plate reader (Multiskan GO, Thermo Fisher Scientific Oy, Finland) at 580 and 600 nm, according to the producer's instructions. One reference plate was simply turned upside down for 5 minutes after the medium was removed, in order to provide a reading at 0 rpm and with force gravity as pulling force (baseline).

For each plate, AB% reading was calculated and turned into cell number, by referring to a calibration plate. AlamarBlue is linear with the number of cells and has a high sensitivity threshold. AlamarBlue is not an end-point dye and is not toxic. The experiments were repeated in triplicate, with a minimum of 3 repeats per material.

The dynamics of cell attachment as depending on time and force is described in Schlie *et al.* [167]. Cell attachment dynamics (and its opposite, the detachment process) can be described with a first-order kinetic equation. By defining the incremental number of cells as adhesion rate $R_{ad}(F_{ad})$, a quantity dependent on the force applied to the cells, we can describe the change in number of cells being detached as

$$\int_{N_0}^N \frac{dN_F}{N_0} = -R_{ad}^F \int_0^F dF$$

where N is the number of cells (as determined by the AlamarBlue assay) as a function of the force, so N_F refers to the adherent cells after each centrifugation step, and N_0 refers to the cells subjected to just gravity (upside down cell plate). Force is expressed in RCF (relative centrifugal force in g units).

From this formula, a derivation of R_{ad}^F can be calculated as

$$\ln \frac{N_F}{N_0} = -R_{ad}^F \cdot F_{ad} \quad \Rightarrow \quad N_F = N_0 \cdot e^{-R_{ad}^F \cdot F_{ad}}$$

According to the definition of adhesion force, F_{ad} occurs at the detachment of half the initial cell population: $N_F = N_0/2$.

$$\frac{N_0}{2} = N_0 \cdot e^{-R_{ad}^F \cdot F_{ad}} \quad \Rightarrow \quad F_{ad} = \ln 2 - R_{ad}^F$$

By plotting the cell population after being centrifuged (N_F) against the respective centrifuge force, R_{ad}^F for each material can be derived, and finally F_{ad} for each material.

F_{ad} is expressed in g units as RCF (relative centrifugal force), which is correlated to rpm (rotation per minute) by the formula

$$RCF = \frac{d\omega^2}{g}, \text{ where } \omega = \frac{2\pi \cdot \text{rpm}}{60}$$

where d is the length of the centrifuge rotating arm (130 mm), ω is a function of rotations per minute (rpm) as per $2\pi \cdot \text{rpm}/60$ and g is the gravitational acceleration, all expressed in SI units (see Fig. 4.2).

4.2.2.5 Cell motility

To quantify cell motility, cells were seeded on modified glass coverslips. Materials were electrospun directly on glass coverslips, so to cover the glass with the desired material: unmodified Z6A1 electrospun polyurethane, Ti and Zn-modified electrospun polyurethane. Each coverslip was secured at the bottom of a petri dish with 205 μm -thick double sided tape (Transparent Double Sided Plastic Tape, Tesa, Germany, thickness 205 μm). Besides, a round sample of cast Z6A1 polyurethane was cut and secured, as well as a round sample of PDMS. Each plate was sterilised by exposure to UV light for 20 min (Daro UV Systems Ltd, UK).

Human glioblastoma astrocytoma cells U373 MG were suspended in HEPES-enriched medium (EMDM). HEPES is a buffer that counteracts the acidisation of the medium due to cellular respiration cycle. Cells were seeded at an initial concentration of 20 000 cell/ cm^2 , equivalent to 6400 cells/well. Cells were incubated for 1 hr at 37 °C, 5% CO_2 , so they could fall to the bottom of the petri dish and adhere

lightly. After one hour, each petri dish was retrieved from the incubator and brought under the microscope. In order to maintain the petri dish at a constant temperature, a heated stage set at 37 °C was used. The stage was covered with a small aluminium foil dome to create a chamber around the sample and isolate it thermally. To limit water evaporation from the petri dish, each dish was wrapped in parafilm.

Time lapse videos were taken with a fluorescence microscope (Zeiss Axiovision Imager Z1, Karl Zeiss Microscopy GmbH, Germany) for at least 4 h, magnification $\times 40$ and a picture every 60 seconds.

4.2.3 Bacterial cultures

The antibacterial activity of polyurethane composite fibres was determined by means of Colony Forming Unit (CFU) counting plates using Gram-positive *Staphylococcus aureus* (*S. aureus*, NCTC 8325) as a bacterial strain.

Staphylococcus is a Gram-positive, round-shaped (coccal) bacteria species. It is a static bacteria strain that is frequently found on skin and therefore it is easily transmitted to the patient possibly by contact with the patient's skin itself, being present on 20% of adult population (and this figure increases when considering the hospital population). *Staph. aureus*, together with *Propionibacter acnes*, accounts for most of the contaminations of the revisions of shunt catheter (13-25%) [168, 169].

Staph. aureus carriage is asymptomatic and it is not harmful; the main risk associated to this bacteria strand is autoinfection. In fact, *Staph. aureus* is one of the five main causes of hospital-acquired infections, which can be treated with antibiotics, even though a certain resistance to antimicrobial drugs has been developed recently by some strains, such as MRSA (Methicillin Resistant *Staph. aureus*).

An overnight culture of bacteria in medium was prepared by picking a single colony from an establish culture and transferring it into a universal containing 5 mL sterile lysogeny broth (LB) and shaken at 150 rpm and 37 °C overnight until it reached mid log phase.

A 96 well plate was modified with the following materials: Z6A1 (cast and ES), Ti2, Zn3 and PDMS. Silastic MDX4210 biomedical grade

elastomer was prepared according to the manufacturer's instructions. The combined solution was injected into a Petri dish and allowed to cure at 50 °C for 12 h to produce a sheet. Each material was cut with a metal punch into a round disc (diameter of the discs 6.4 mm) to fit to the bottom of the well and secured to the bottom with 205 µm thick double-side transparent tape (Transparent Double Sided Plastic Tape, Tesa, Germany). A negative and positive control column were included on each plate: bare tissue culture plastic (TCP) as positive control and a column filled with sterile medium as a negative control. In case the negative control appeared contaminated at the endpoint of the experiment, the whole plate was discarded.

As a sterilising method, each 96 well plate was sprayed with a 70% isopropanol solution until all the rows and materials were completely submerged and let dry overnight in a sterile flow cabinet. Inoculation and counting were carried out in a class II sterile cabinet.

Each well was inoculated with 1% of bacterial strain culture in sterile LB medium (200 µL per well) and incubated for 24 hours at 37 °C, 5% CO₂.

After 24 h, the number of colony forming units (CFU) was counted on agar plates following standard procedure for serial dilutions. Each plate was shaken for one minute at 60 rpm in order to make sure the suspension was homogenous. From the suspension, 20 µL of inoculum was taken from each well, transferred into 180 µL fresh LB, mixed well by pipetting 20 times, then diluted again. This progressive dilution was repeated for 7 times. Each passage is a 10-times dilution (a log unit). From each the last 3 dilutions (that is, 10⁻⁵, 10⁻⁶ and 10⁻⁷), 10 µL were seeded ten times on agar plates and incubated overnight (100 µL in total). Such serial dilution process leads to diluted solutions that allow for single bacteria to grow isolated from each other. Each viable bacteria, or colony forming unit, would generate overnight a single visible colony. The following day, the total number of CFU were counted from plate whose dilution exhibits between 3-30 colonies. It is possible to work out the concentration in the original suspension by multiplying the average number of CFU by the dilution factor. The total number of colonies was reported as CFU/mL, and the repeats were averaged (n = 6) and compared.

The same protocol was followed for a second set of sample. However, these plated were exposed to UV light (using a Daro UV Systems Ltd UK lamp) for 20 mins after sterilisation with 70% isopropanol solution and inoculated straight afterwards.

Antibacterial efficiency (ABE), expressed as a percentage, was calculated as:

$$\text{ABE}\% = \frac{(C - S) \times 100}{C}$$

where C and S (CFU/mL) is the averaged number of viable colonies on the positive control and on each sample, respectively.

4.2.3.1 SEM images of inoculated materials

Three samples of materials were fixed to the bottom of a disposable petri dish with double sided tape, sterilised with 70% isopropanol solution and let dry overnight in a sterile cabinet. Afterwards, they were inoculated with a 1% overnight *S. aureus* culture in sterile LB medium and incubated for 24 hr, after which they were gently rinsed twice with sterile LB medium and let dry completely in a flow cabinet. They were sputter coated with platinum and SEM micrographs are taken with a scanning electron microscope (Tabletop Microscope TM-1000, Hitachi High-Technologies, Japan).

4.2.4 Statistical analysis

The data presented in this chapter are expressed as mean values \pm standard error or standard deviation.

All quantitative experiments with mammalian cells (AlamarBlue assay, apoptosis assay, cell detachment assay) were repeated in triplicate ($n = 3$) for each experimental time point, with a minimum of three repeats per material. Bacterial cultures were performed $n = 6$.

Statistical significance was determined following one-way analysis of variance (ANOVA) with post hoc testing according to Tukey's procedure at a 95% confidence level (using Minitab, software version 17).

Whenever significantly different, results were marked by way of asterisks on graphs.

Data were normalised in some cases with respect to the Tissue Culture Plastic (TCP) samples, which represent the positive standard (see Fig. 4.4).

4.3 RESULTS

4.3.1 *Mammalian cell viability*

The effect of modified and unmodified materials on human glioblastoma cells (U373) was evaluated by direct contact culture method. To analyse possible toxicity of the tested materials, cells were grown in contact with polymeric samples for up to 9 days, and a viability assay was performed at three time points to quantify the number of viable cells on each material according to the protocol described in Section 4.2. PDMS (silicone hydrogel) was chosen as the negative control as it is expected to be less conducive to cell growth. Tissue culture plastic, on the other hand, served as the positive control, being specifically treated to increase cell adhesion.

Viability is measured indirectly as the amount of dye resazurin being reduced to resorufin by alive cells. Proliferation is therefore expressed as the amount of dye being reduced (AB%), which is directly proportional to the number of living cells. To convert the AB% into a cell number, a linear calibration curve is plotted from a second plate seeded at the same time of the main experiment by plating an increasing number of cells to obtain a sufficient number of calibration points (Fig. 4.1).

Graph shown in Figure 4.3 shows the viability of cells on different substrates, as measured at different time points, namely 2, 4 and 9 days (48, 96 and 216 h) after being seeded. Results have not been normalised over the TCP value in order to reduce derived uncertainty and to show the natural time evolution on each substrate.

Double sided tape, used to hold the materials in place to the bottom of the 96 well plates, does not inhibit cell viability and it is therefore considered as non toxic and it does not have adverse effects on the experiment results.

The highest cell count occurs on the positive control (TCP), the lowest density of cells is exhibited by zinc-modified substrates, in particular those with higher concentrations of zinc (Zn5 and Zn3). Titanium-modified samples exhibit a lower number of viable cells if compared to the positive control, too, although the reduction is not as low as

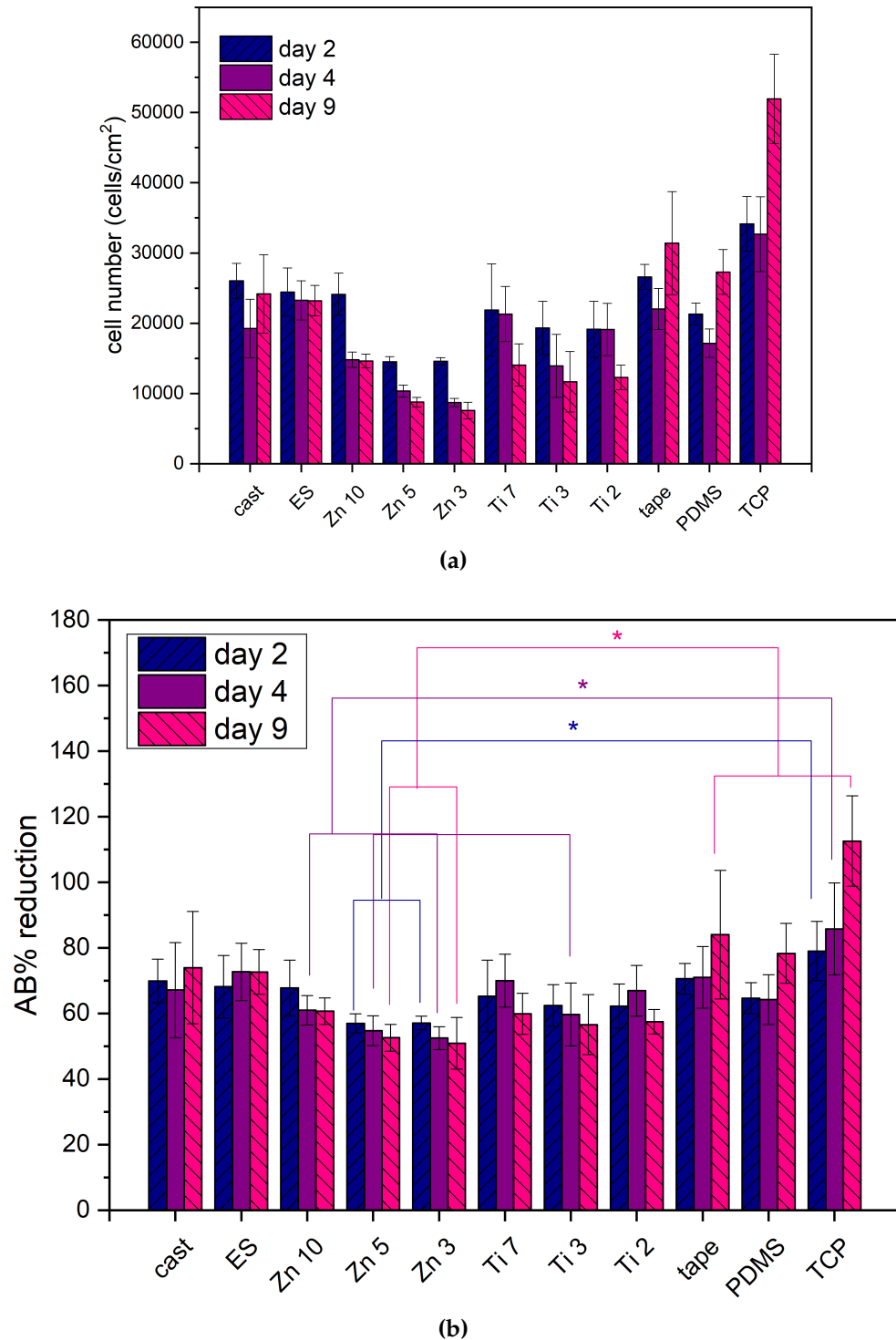


Figure 4.3: Quantification of viability in U373 cells, expressed as mean percent reduction of AB for U373 cells grown on cast PU, untreated ES PU, positive control (tissue culture plastic, TCP) and negative control (PDMS) evaluated after 48, 96 and 216 h in culture. Bars represent standard deviation and $n=3$. Results are shown for each material population as number of cells (a) and percent reduction (b), from three independent experiments. (*) indicates a significant difference ($p < 0.05$) in cell viability compared to the positive control (each relevant time point is indicated by a different colour) determined by one-way ANOVA and Tukey's post hoc analysis.

Zn-PU, and not significantly different from PDMS, cast film or simple ES polyurethane.

As far as growth in time of cell population is concerned, some surfaces prove to be more conducive than others. In general, modified electrospun materials show a lower cell conductivity over time, with cell density declining over observing time. On the contrary, density increases on TCP and PDMS, while it stays constant on cast and ES surfaces. If on the first time point (2 days) the cell count is pretty similar on all the substrates, with time the effect of each substrate becomes more evident, and cells thrive and grown on TCP, while viability of all the other substrates becomes lower.

On both negative and positive controls, cell count increases significantly between day 2 and day 9. However, growth on PDMS is slower, even after 9 days, and the total number of viable cells amounts to around the half of the cells on TCP.

Statistical analysis was run only on the AB% values. Whilst at no time point any of the electrospun substrate, either modified or unmodified, is significantly different from PDMS (negative control), the trend that has been observed within a 9-day period might indicate that the difference between modified substrates and PDMS might widen after a longer period of time.

Both Zn5 and Zn3 are significantly different from the positive control (TCP) at all time points, and additionally Zn10 and Ti3 are different from the positive control on the second time point (after 4 days).

4.3.2 *Cell apoptosis*

The amount of apoptotic cells has been quantified through a colorimetric assay and results are reported on Figure 4.4 as absorbance values. No calibration test has been run, therefore absorbance has not been converted into absolute number of cells; they have been normalised against the positive control (TCP) for each time point, instead.

PDMS has a comparable or lower number of apoptotic cells than TCP, as cast polyurethane and electrospun polyurethane do as well. As for modified electrospun substrates, Zn5 and Ti3 exhibit an apoptotic rate which is quite higher than the TCP control, while Zn10 and

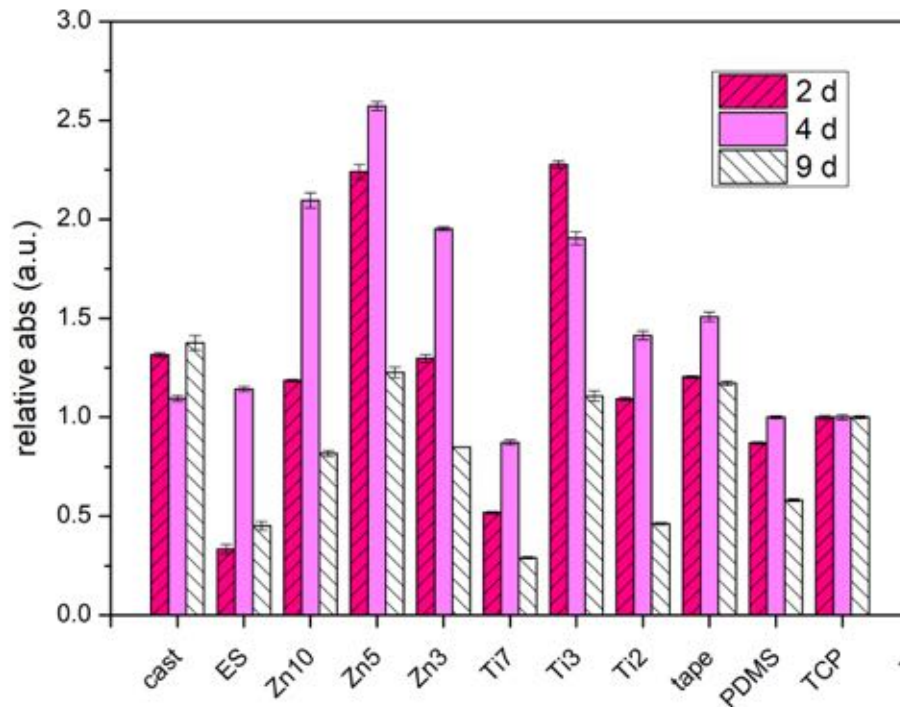


Figure 4.4: Quantification of apoptotic rates in U373 cells, evaluated after 48, 96 and 216 h in culture. Bars represent standard deviation ($n=3$). Results are shown for each material population normalised to the positive control (TCP), from three independent experiments.

Zn3, and Ti7 and Ti2 have lower or comparable results to the positive control.

Analysing the time evolution of apoptosis over the duration of the experiment, it is striking that, for many samples, the second time point exhibited a higher number of apoptotic cells than the other two time points. At the third time point almost all samples registered a lower number compared to the second time point.

Inverted microscope brightfield pictures of apoptotic cells (Fig. 4.5) after 9 days show cells that have taken up the assay dye on different substrates. While on PDMS almost all cells are coloured in red, both on cast polyurethane and on TCP only part of cells are dyed. In particular, on cast PU red cells appear to be clumped and rounded, having lost adhesion, and are distributed uniformly across the sample. Instead, TCP population show whole areas of died cells, and separate areas of still thriving cells.

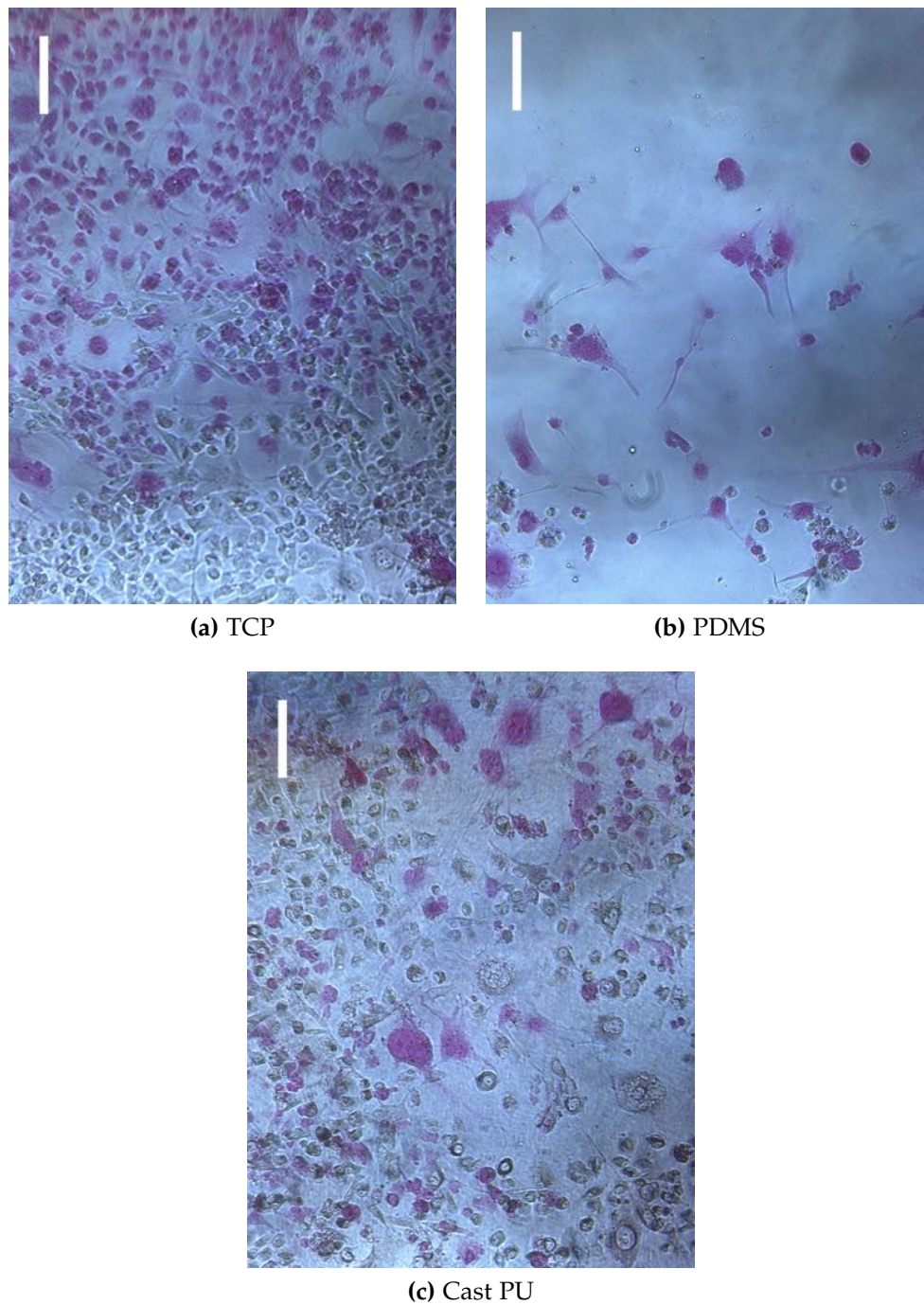


Figure 4.5: Brightfield images of U373 cells grown on a) tissue culture plastic, b) PDMS and c) cast polyurethane for 9 days (final time point) and stained with apoptosis assay. 20x magnification, scale bar 100 μm . Red-coloured cells have initiated the apoptotic cycle, while transparent cells are intact. Large patches of cells are apoptotic on all surfaces.

In order to compare the apoptotic rate against viability, and assuming that both assays are linear with number of cells, a ratio between the absorbance units from the apoptosis assay and the AlamarBlue assay has been calculated and it is reported on Figure 4.6. Even though it is an arbitrary quantity, it suggests the relative ratio of apoptosis as compared to the quantity of viable cells on each substrate and for each time point. In particular, this ratio is almost constant over time, and small, on substrates such as cast and tissue culture plastic. It is small as well on some electrospun materials (ES, Ti7, Ti2) and on PDMS, while it is very high on Zn5, Zn3 and Ti3. In particular, on the second time point (4 days after seeding), the ratio is abnormally higher than the other two time points on all the electrospun substrates.

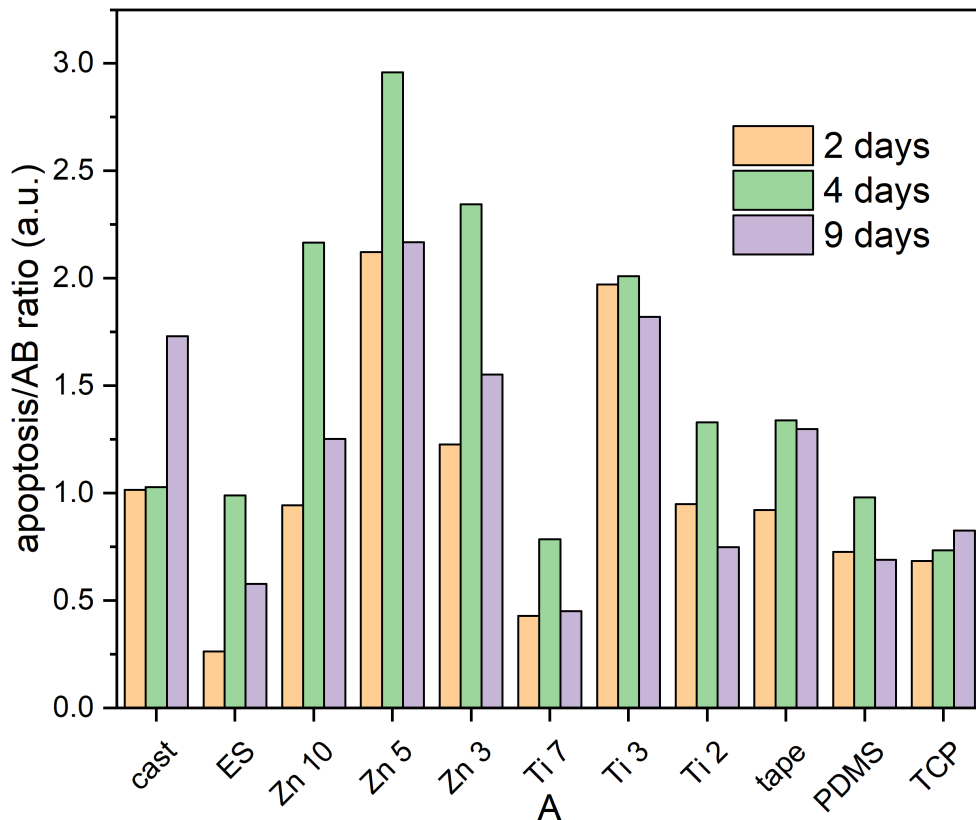


Figure 4.6: Ratio of apoptotic cells versus viable cells on each substrate at each time point, as obtained by dividing the absorbance values from the apoptosis and the alamarBlue assay. On all electrospun scaffolds, and on PDMS, the second time point exhibits an excess of apoptotic over viable cells.

4.3.3 *Live/dead and DAPI assays*

Fluorescence microscope images of U373 astrocytes after 48, 96 and 72 h after staining with DAPI and Live/Dead Assay are presented in Figure 4.7 and 4.8, respectively. Only selected materials are shown, as ES, Zn and Ti modified materials are opaque and it is impossible to take any picture of them with an inverted microscope. The reference sample is represented by cells cultivated in the absence of polymer specimens, on bare TCP. Light microscopy images provide results for the morphological characterisation of the cells.

Images show the number of cells increase with time on all transparent substrates. However, cell density is higher on TCP and cast PU substrates, while on PDMS cells tend to cluster together in big clumps, surrounded by few isolated cells.

Morphology of cells on patterned substrates is different from flat, soft surfaces such as PDMS. In particular, PDMS seems to be less conducive to cell growth and development, with fewer cells scattered on the surface and mainly isolated from each other, or grouped in big clusters. This scenario does not change significantly over the timescale of the experiment. Cells that are clumped together are not adhering onto the surface, with the effect of looking rounded and less spindle-shaped.

On the other hand, the phenotype of cells on other substrates is typical, spindle-like and with extended protrusions, indicating that the cells are exploring the environment and spreading.

4.3.4 *Cell adhesion*

Median detachment force is derived from a detachment assay via the centrifugation of cell culture plates, as described in the methodology section. Average detachment values are reported in Figure 4.9.

The uncertainty on the values is high, and it may be accounted for by the fact the quantities are derived indirectly, and each passage of the protocol contributes with some uncertainty to the final value. Furthermore, the variable nature of the scaffolds themselves may influence the amount of force needed to detach cells. Indeed, SD is

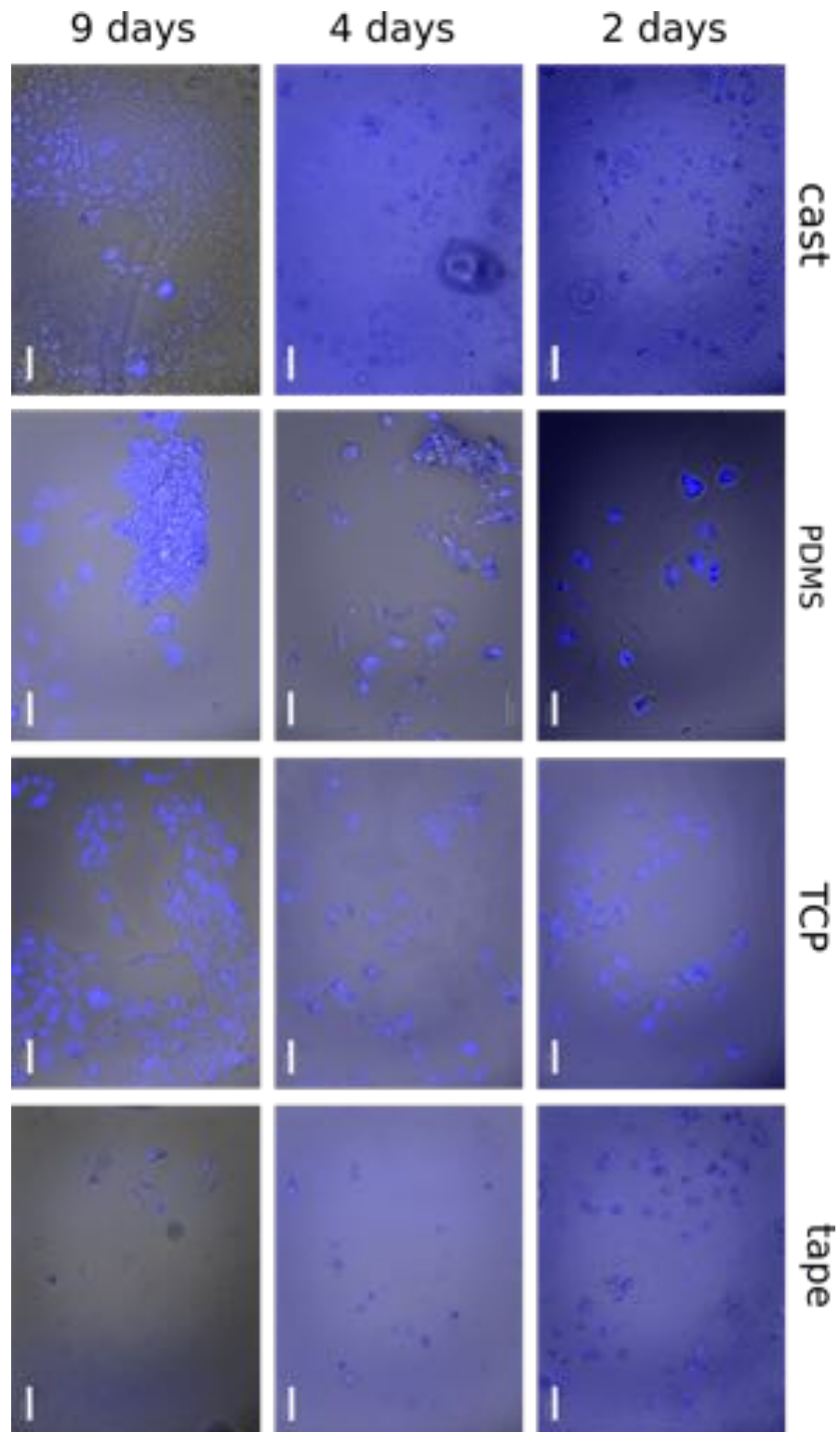


Figure 4.7: Fluorescence images of U373 astrocytes taken after 48, 96 and 216 h in culture on cast polyurethane, PDMS, TCP and tape samples, 20x magnification, scale bars 100 μm . Nuclei of fixed cells are stained blue with DAPI and images superimposed to brightfield pictures.

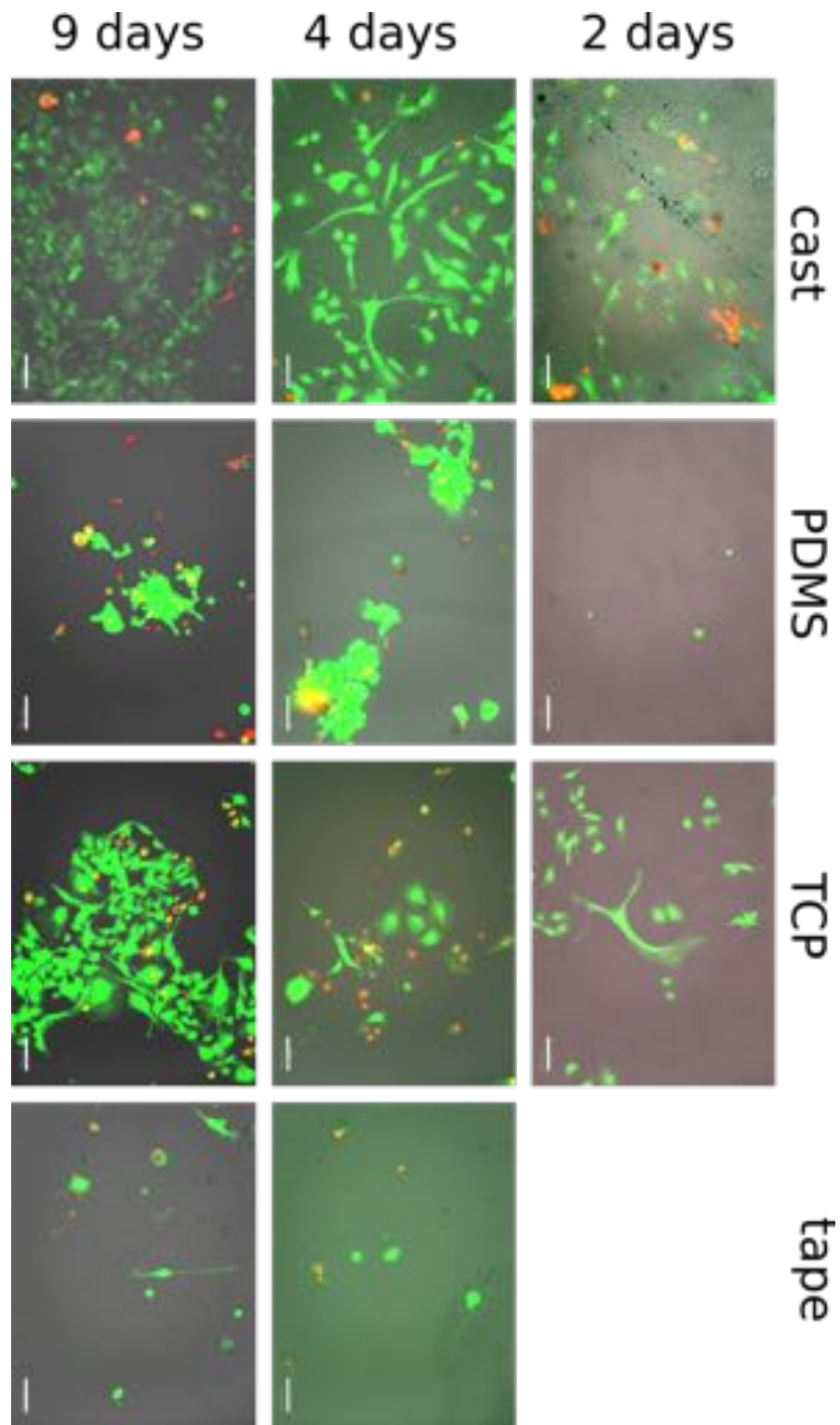


Figure 4.8: Fluorescence images of U373 astrocytes taken after 48, 96 and 216 h in culture on cast polyurethane, PDMS, TCP and tape samples, 20x magnification, scale bars 100 μm . Live cells are stained green (Calcein-AM) and dead cells are stained red (ethidium homodimer-1). Scale bars 100 μm .

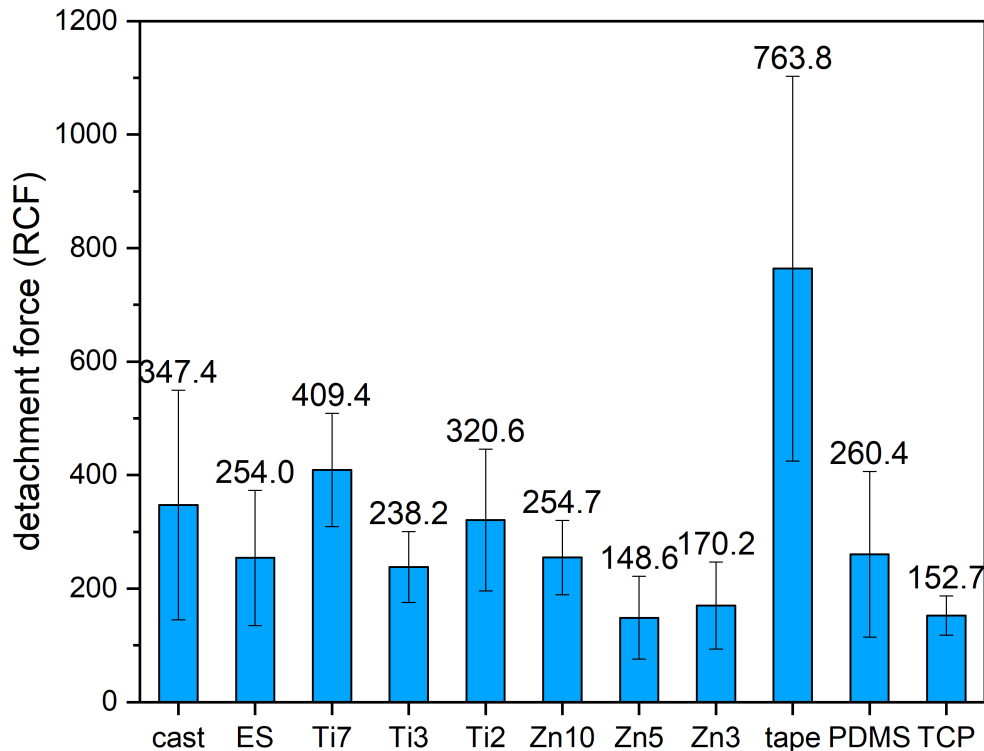


Figure 4.9: Orthogonal detachment force, as obtained via a centrifugation assay, expressed in relative centrifuge force (RCF), bars showing standard error ($n = 3$).

relatively smaller for a standard flat surface such as TCP. Finally, the outlined method describes the average force for a cell population, and it needs to account for variations present between different cell populations.

Nonetheless, it is interesting to note that the highest detachment force is required for tape, which is naturally an adhesive surface, while TCP, a flat surface cells might find it more difficult to adhere and grip to in the timescale of the experiment (60 minutes), registers one of the lowest detachment force values.

On modified electrospun surfaces, the materials with a higher modifier load (Ti2 and Zn3) require smaller detachment forces than samples with low amount of modifier, and Zn samples generally exhibit lower cell adhesion values than Ti samples.

Average cell detachment force was plotted against the size of each surface features, to verify whether the size of the fibres has any influence on the cell attachment to the substrate (Fig. 4.10a). Bearing in

mind the size distribution and the uncertainty affecting detachment force measurements, a linear dependence of detachment force on fibre size is exhibited by the electrospun modified materials, which have a narrower diameter distribution (Fig. 4.10b). While the ES sample does not fit into the model, it needs to be reminded of the multimodal size distributions nature of ES samples.

4.3.5 *Cell motility*

Dynamic cell behaviour of U373 astrocytes was observed using time lapse function on a brightfield microscope.

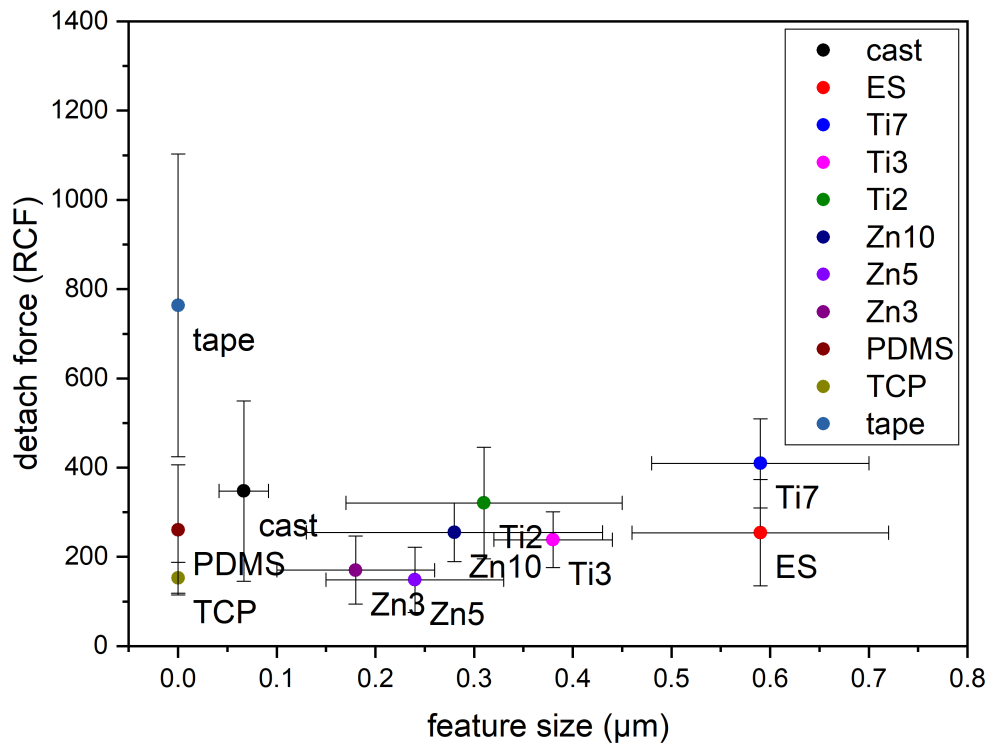
1 hour incubation has been chosen as a cut off time for the present study. One hour is sufficient for cells to start adhering, and microscope images (Fig. 4.11) show that cells are definitely adherent, while at the same time it does not let cell adhere too strongly to the substrate. A limitation of the seeding time was necessary, in order to limit the impact of cell division, apoptosis and detachment, which would invalidate the results. Some cells are still rounded and no cell shows a spread and elongated morphology, and they show lamellipodia and other features of an adhering membrane.

A number of isolated cells on ES, Ti2, Zn3 and PDMS scaffolds have been followed at high magnification and frequent imaging rate, in order to observe closely their movement on the surface. Selected frames of such videos are reported on Figure 4.12. The cell reported for the Zn-modified sample, in particular, exhibits an interesting behaviour.

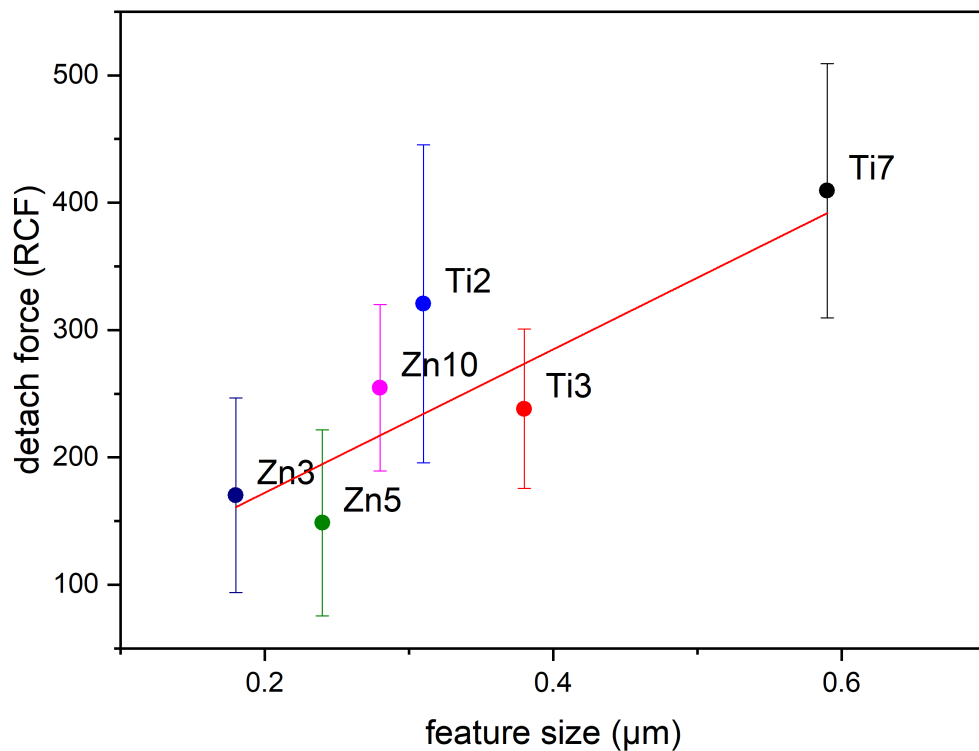
On all samples with fibres, cells move along the fibre, often using the intersections of fibres at small angles as corners to attach and move forward. Fibres act as anchorage sites where cells attach. In particular, cell prefer attaching wherever fibres, crossing at different angles, form a narrow corner, maybe because two or more fibres are adjacent and close to each other and offer more points of contact.

On PDMS, instead, the tracked cell does not move very quickly. The extrusion does not explore the environment but just proceeds ahead.

The cell on Zn-modified substrate (Fig. 4.13) moves along a zig-zag pathway, changing abruptly direction several times in the timescale observed and following a track determined by the fibres. It is possible



(a) Average detachment force plotted against features size



(b) Zoom on the electrospun modified materials.

Figure 4.10: Average detachment force plotted against features size for all substrates. PDMS and TCP were simplified as completely flat, while in the case of ES, whose fibre distribution is multimodal, the most representative one has been chosen. The second graph shows a linear fitting model applied to the modified electrospun materials.

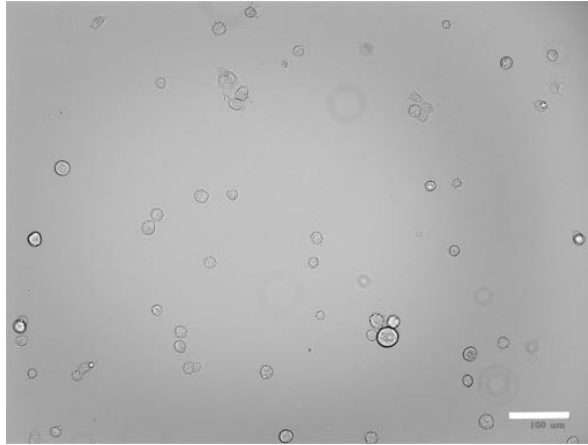


Figure 4.11: Brightfield image of U373 cells after 60 minutes incubation at 37°C, 20x magnification. Scale bar 100 μm. While some cells are still rounded, some exhibit ruffles at the edges and few have started spreading.

to see filopodia at the edge of the membrane explore the fibres and follow the pathway laid out by them. The exploring protrusions the cell uses to sense the environment before deciding for a direction are clearly visible. When the cell moves on, it leaves behind small filaments that remain attached to the fibres.

Another difference among substrates involves the cell shape: they appear elongated and not simply spread out when there are morphological clues, while on TCP flat surface the shape is more circular. Lamellipodia are more prevalent than filopodia on the latter.

4.3.6 *Bacteria morphology and biofilm formation*

Bacterial adhesion tests were conducted and the substrates exposed to bacterial colonies were qualitatively examined by Scanning Electron Microscopy.

SEM micrographs, reported in Figure 4.14, show the growth of *S. aureus* on four different surfaces, three of which electrospun fibrous materials, and a flat surface (PDMS), after 24 h.

On electrospun substrates, clumps of bacteria are visible on the surface. Bacteria are nested between the fibres, especially where multiple fibres create corners and edges. At the same time, after 24 h there is no formation of a thick biofilm on electrospun substrates, but they

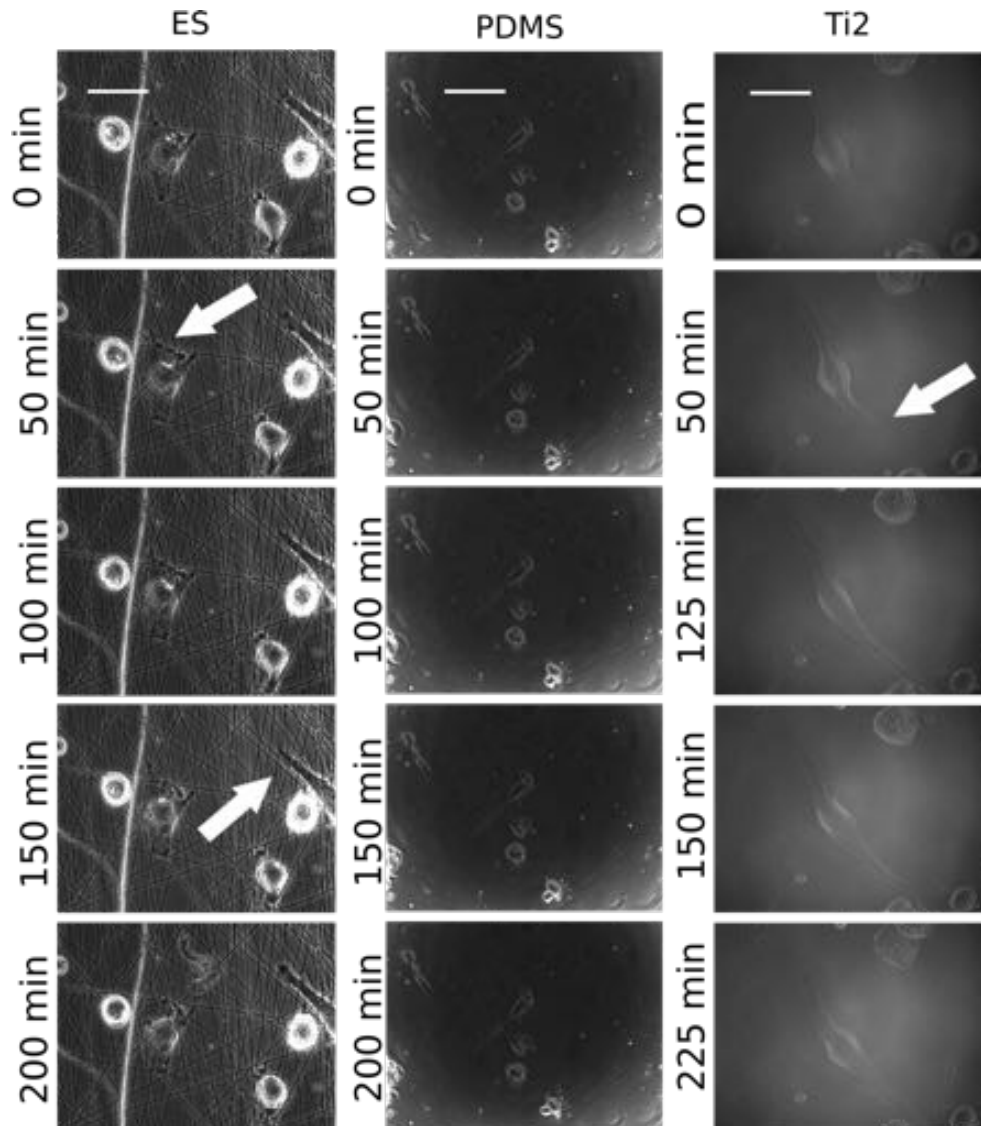


Figure 4.12: Cultures were incubated for 60 min after cell seeding at 37°C, 5% CO₂ and followed by recording under a time-lapse microscope every 60 seconds at a 40x magnification for at least 3 hours. Scale bar 100 μm. Selected images are shown. Time lapsed between snapshots is indicated next to each image. Filopodia exploring the environment can be seen on cells advancing. Especially on ES sample, darker spots can be seen where the cell grips to the fibres, and small filaments remaining attached to the electrospun fibres as the cell moves on.

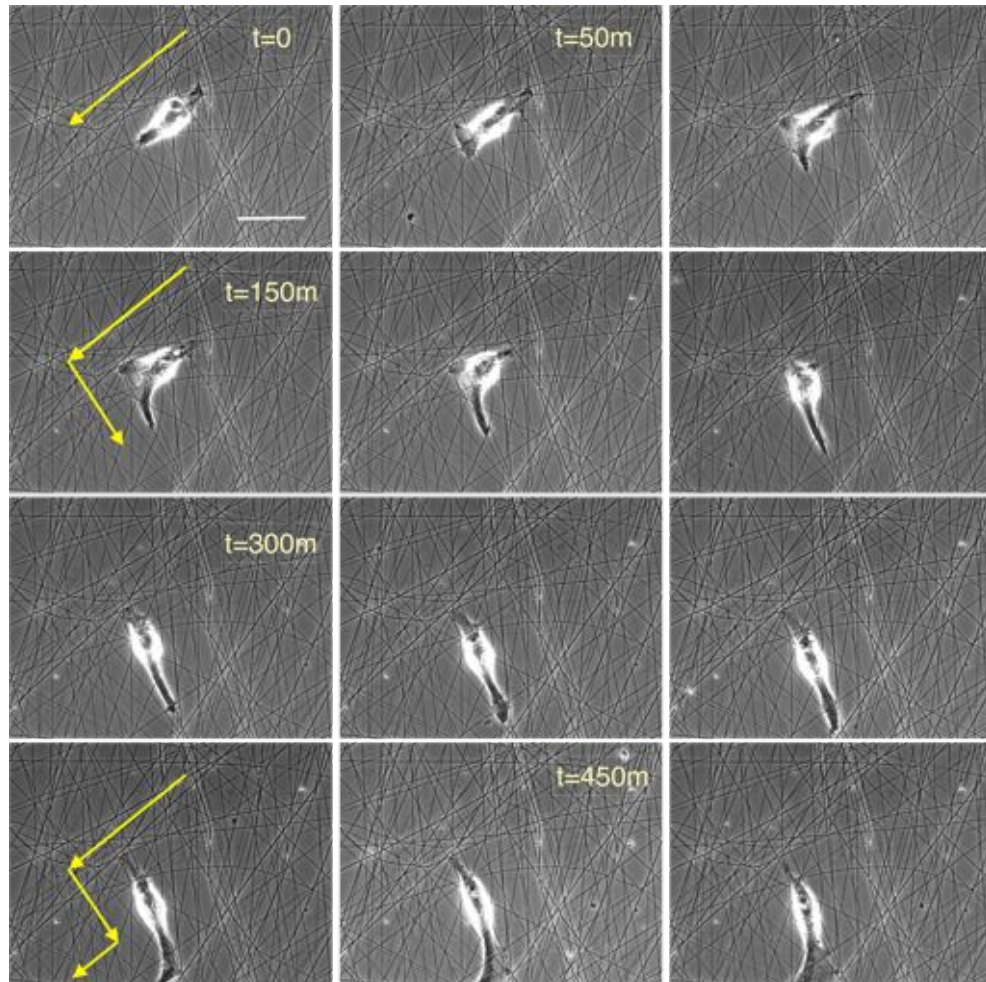


Figure 4.13: Single cell moving on Zn3 fibres electrospun on a glass microscope slides. Cultures were incubated for 60 min after cell seeding at 37 °C, 5% CO₂ and followed by recording on a time-lapse microscope every 60 seconds at a 40x magnification for 10 hours. Scale bar 100 μm. The interval between the selected images is 50 mins.

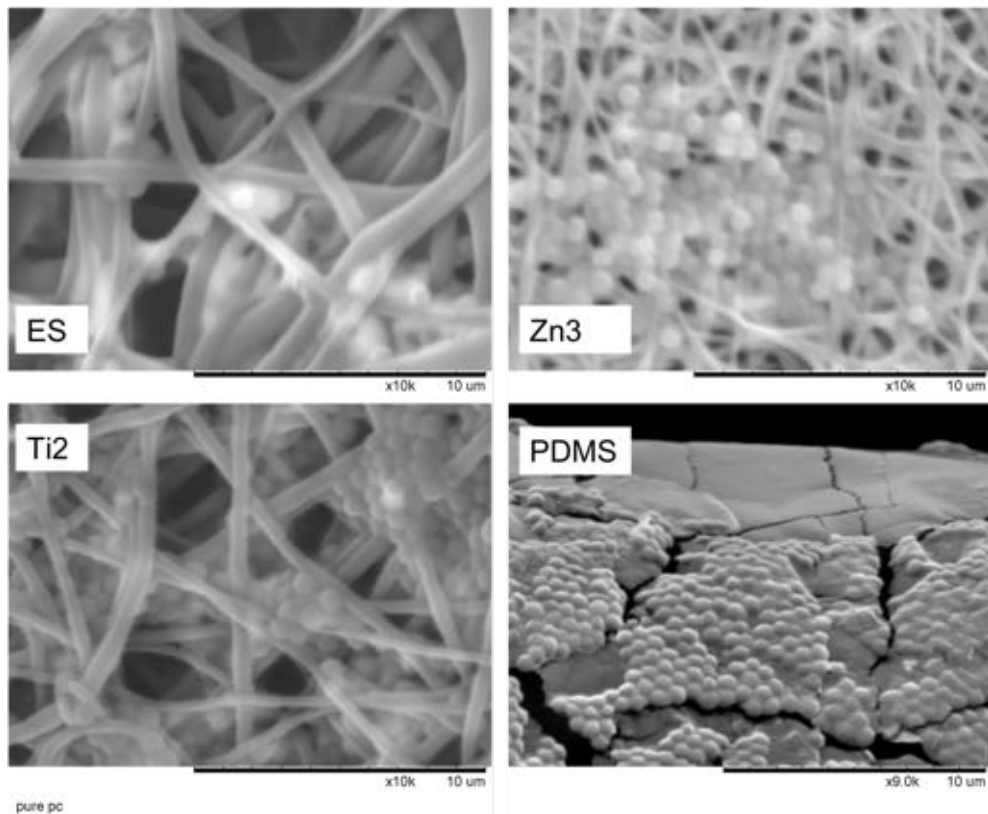


Figure 4.14: Scanning electron micrographs of bacterial cultures on different materials, gold-coated, after 24 hr. Magnification is x10k for Zn, Ti and cast materials, and x9k for PDMS. Scale bar reported on each micrograph.

are grouped into small and separate formations, and sometimes single isolated bacteria appear as well.

On PDMS, bacteria are present only on the rough edges of the samples and aggregate in extended and continuous colonies, while the smooth top of the samples do not show any biofilm formation.

Cast film (not shown) did not report the presence of any bacteria. It was not possible to check the presence of colonies on the sides of the samples because of their limited thickness.

4.3.7 *Bacteria viability*

Bacteria viability was determined by colony counting method, as described in the Methods section.

The viability of *S. aureus* on silicone, cast PU, plain electrospun PU and Ti- and Zn-modified PU, upon and without exposure to UV and expressed as antibacterial efficacy, is shown in Table 4.1. Results expressed in \log_{10} units are reported in Figure 4.15.

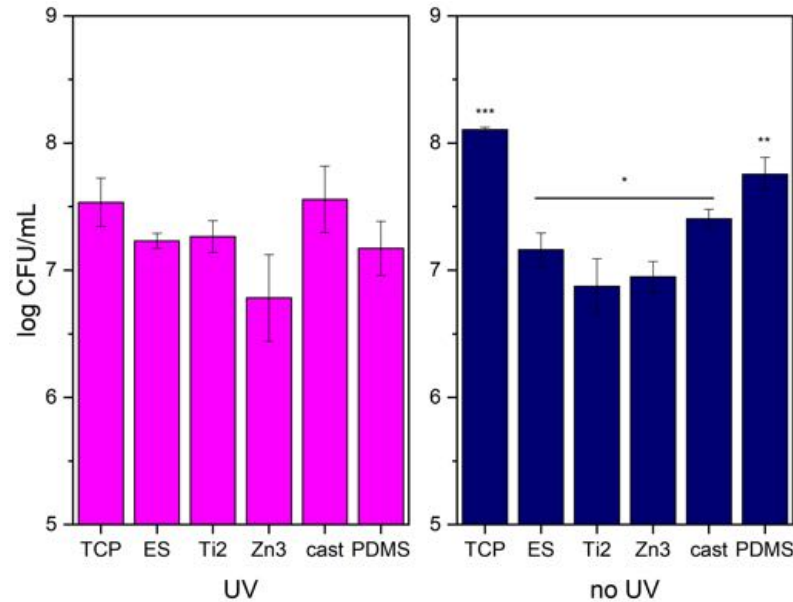


Figure 4.15: Comparison of the Colony Forming Units, expressed in logarithmic units, on TCP (positive control), electrospun PU (ES), Ti and Zn-doped electrospun PU, cast PU and PDMS, with and without exposure to UV light. Bars represent standard error ($n = 6$). (*) indicates a significant difference ($p < 0.05$) in CFU determined by one-way ANOVA and Tukey's post hoc analysis.

The positive control (TCP) shows the highest amount of CFU for both sets of experiments. All CFU counts on other samples are significantly different without UV treatment. Upon irradiation, however, cast PU exhibits a similar amount of CFU, even though the standard deviation for this sample is quite high. PDMS is conducive to bacterial colonisation, showing a very low reduction in colonies and an ABE of around a half for both sets of experiments.

All electrospun materials, instead, seem to be more effective in reducing bacterial colonisation. In particular, titanium-modified electrospun membranes report a 90.24% ABE, and zinc-modified membranes a similar value of 91.85%. However, these values are much lower after UV exposure.

Table 4.1: Antibacterial efficiency (ABE%).

	ES	Ti2	Zn3	cast	PDMS
no UV exposure	86.57	90.24	91.85	78.63	44.41
after UV exposure	64.10	64.92	56.45	5.99	57.78

When plotting the number of CFU/mL against the specific size of features on non-flat surfaces (that is, cast film, ES, Ti2 and Zn3), the scatter plot can be fitted with a quadratic function, with a minimum at around $0.5\ \mu\text{m}$. Cast film was used with the glass-side surface up, which exhibits a multitude of small bumps, as characterised in Section 3.3.2.1.

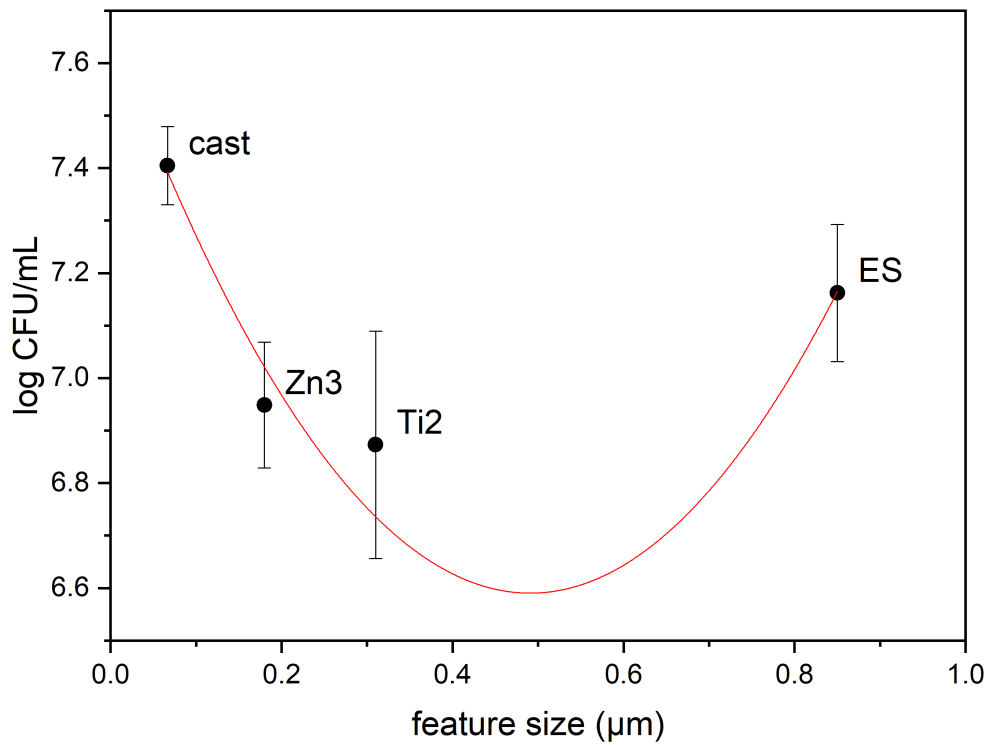


Figure 4.16: Plot of *S. aureus* colony forming units (expressed in log units of CFU/mL) against morphological surface feature size for non-flat surfaces (cast, ES, Ti2 and Zn3). Cast film was used with the glass-side surface up. Fitting with a parabolic function was performed.

4.4 DISCUSSION

The results from viability and apoptosis assays shed some light on the effects of different materials on cell growth and viability.

Cell viability and growth

The viability of cells on different substrates was quantified via the AlamarBlue assay at three time points, namely on 2, 4 and 9 days after cell seeding.

From the graph shown in Figure 4.3, polyurethane either in its electrospun or cast form do not exhibit a significant difference in results. Viability is lower on modified electrospun materials than on unmodified ones, and the difference between unmodified and modified polyurethane increases over time. While the morphological shift from a flat to an electrospun surface does not affect viability when cells are cultured on cast and ES surfaces, when comparing these two substrates to the modified electrospun polyurethanes, the change in charge distribution, or fibre dimension, does affect cell viability indeed. Such effect is particularly strong on Zn-modified materials, which indeed exhibit the greatest reduction in fibre diameter as compared to Ti-modified and unmodified materials.

As evidenced by viability results, unmodified electrospun polyurethane compares to PDMS, and can be well considered an alternative to it, as they both discourage cell viability. The number of cells seems to increase over time on both positive (TCP) and negative (PDMS) controls, while on modified electrospun substrates it seems to decrease. PDMS, on the other side, does not encourage apoptosis more than TCP, while the apoptotic rate is lower for ES samples, maybe because the surface resembles better their natural tissue (ECM), as opposed to a flat surface.

As shown by light microscope images (Fig. 4.8), cells on PDMS tend to grow close to each other in clusters, and clump together. Cells that are adherent and spread on the surface are isolated from each other, enter the apoptosis cycle and eventually die within the time frame of the present experiment. Thus, PDMS is less conducive to cell growth than other materials it has been compared to. Viability count shows that the number of viable cells increases with time, though.

While PDMS is not cytotoxic *per se*, it is not conducive to cell proliferation and growth, exhibiting a large number of apoptotic cells (Fig. 4.5).

Growth and viability of cells on Ti and Zn-modified materials is low and not significantly different than PDMS, the negative control. From the viability data and rate of cell apoptosis it seems that smaller fibres do not encourage growth and thriving of cells. Indeed, fibres diameter determines how big the area of interaction between cell and material is, and eventually determine cell fate, possibly through the spacial control of cell adhesion sites.

The viability assay measures the amount of alive and active cells, but it does not provide any indication on the stage of life cycle those cells are at. For example, cells may be entering the apoptotic cycle, but they would still convert the viability dye. To add information complementary to AlamarBlue, an apoptosis assay was therefore performed in parallel.

The apoptotic assay is based on uptake of dye by cells undergoing apoptosis. Necrotic and healthy cells are impermeable to the dye, therefore the results are related only to the population of cells undergoing death cycle (Fig. 4.5). The ratio of cells entering the apoptosis stage, reported on graph shown in Figure 4.6, is higher on some modified materials (especially for Zn5, Zn3 and Ti3) than on flat and unmodified surfaces (cast, ES, PDMS and TCP) or scaffolds with low filler ratio (Zn10 and Ti7), and especially on the second time point. Apoptotic cells does not vary significantly with time on smooth surfaces, while on electrospun materials it reaches a peak and then decreases.

Metallic zinc, in particular, is known for interacting with astrogloma cells by decreasing adhesion and proliferation, and for participating in a number of biological processes. Zinc can control oxidative processes, by taking part in reactions as a co-reagent. For this reason, an excess of zinc can lead to an excess in reactive oxidative species (ROS), creating distress in cells and leading to the apoptotic process.

Indeed, apoptosis can be initiated by radicals, and that can explain the fact the apoptosis is higher on Zn and Ti-modified fibres than unmodified ones. The higher apoptotic rate observed on day 4, and es-

pecially on Zn-modified substrates, could be explained by the release rate of zinc into solution. The different structural form of Zn and Ti compounds within the fibres, as well as their different chemical nature and the reactions they take part in, might explain why the rate of apoptosis is different, but especially higher for Zn-modified materials. Zinc can be leached by fibres, while titanium, which is more intertwined with the polyurethane matrix, does not. Furthermore, the higher specific surface area of fibres with higher modifier content might explain why apoptosis rate is higher on these substrates. If these fibres release chemicals, the smaller the diameter, the more efficient the release will be from smaller fibres. In that case, a study would be necessary to determine the release time frame.

A way to determine and isolate the effect of modified fibres on cell cultures would be using as cell culture medium, medium that has been in contact with the substrate only. After determining the optimum contact time, the medium would be used to culture cells and their growth and apoptotic rate would be depend only on the chemical factors, rather than on the morphology of the fibres.

Adhesion data (Fig. 4.10b) show how cell adhesion is lower on fibres that have been modified with a higher metal content. The fact that cells are less attached to these fibres and loss of contact is another factor that could initiate their apoptosis. Furthermore, the distribution of charges on the surface, being influenced by the distribution of titanium and zinc (see Section 3.4), might influence the way proteins cover the surface, and therefore, indirectly, the adhesion of cells.

Therefore, modified materials, especially those containing zinc, seem to be effective at reducing adhesion and growth of astrocytes growing on them, and at initiating apoptosis. In particular, zinc-modified fibres, maybe given the fact that zinc is less interspersed with polyurethane and more segregated on the surface, could be more effective at releasing metal ions that regulate cell functions.

Beside colorimetric assays, another method to evaluate biocompatibility and bioactivity of a substrate is the adhesion of cells to the scaffold, and indirectly through their motility on the surface and the development of other typical features of viable cells, for example cell protrusions. Cells move by creating an attachment site at the leading

*Cell adhesion
and motility*

edge, which provides traction, and by simultaneously disassembling the cytoskeleton at their rear side.

Cells cultivated on different substrates, both flat (PDMS) and electrospun (ES, Ti₂ and Zn₃), were imaged with a microscope over some hours to evaluate the movements of single cells.

Many representative cell protrusions were observed probing the environment surrounding the cell (Fig. 4.12). Thereafter, cell protrusions invade the probed area. While on PDMS cells do not move for a long distance over the observed timeframe, movement of cells on electrospun surfaces is purposeful. In particular it is possible to see a number of features at the membrane edge, and orientated protrusions in the direction of cell movement.

It is well known that surface features stimulate the production of filopodia and motility of cells, changing their morphology, and this might be influential on their activity and properties as well. The effect of surface morphology on cell behaviour and contact guidance have been largely explored. A higher surface energy, such as nanostructures on the surface of polyurethane, promotes protein adsorption, leading to improved cell adhesion. Morphological features offer guidance to the cells.

What is quite clear from the time lapse images collected is that cells tend to prefer pathways drawn by the random disposition of fibres on glass (Fig. 4.12). Some cells follow the pathway so tightly, they change their direction very sharply, by almost 90° (Fig. 4.13). In particular, cells tend to follow ridges as if by pulling on a rope. On the contrary, cells on PDMS move in a similar way, but their motion is not directional. This characteristic may be used to direct and channel single cells motion on a surface.

Adhesion values, reported in Figure 4.9, even though affected by high uncertainty, show that a very low force is needed to detach from TCP, a flat surface. On the other side of the spectrum, tape requires the highest force. PDMS, ES and cast require similar detachment forces for cells to be removed from the surface. As far as modified materials is concerned, electrospun materials with higher metal content and smaller fibres seem to require smaller force to detach cells (Fig. 4.10b). This may be explained by the size of the fibres and the

difficulty of cells to develop an attachment in the timeframe of the experiment (1 hour). Attachment on PDMS is not significantly different from values for cast or ES.

The cell line used in these experiments is an adherent line. Mobile cells, and therefore not adherent cells, can undergo apoptosis. Therefore it is to expect that on substrates where the motility is higher, adhesion will be smaller and apoptotic rate higher. A surface promoting cell mobility can therefore be expected to have a lower adhesion.

Cell morphology (Fig. 4.8 and 4.12) is distinctively different depending on the scaffolds. Cells on TCP tend to spread and adhere completely to the surface, adopting a rather round-shaped and flat morphology. On the contrary, cell tend to minimise their contact surface with PDMS and to privilege the contact with other cells, forming lumps.

On all polyurethane surfaces, instead, cells adopt a spindle-like, stellate shape, probably using the features of the surface as grip points. This occurs both on cast PU and on electrospun surfaces. Based on such morphological considerations, micropatterned surfaces encourage a cytotoxic phenotype. Indeed, astrocytes exist in a number of phenotypes, which exhibit both pro-survival ('cytotoxic') and destructive ('cytotoxic') elements. Such components can be dynamically changed by the astrocytes as a response to the topographical cues of the environment. The expression of a more cytotoxic phenotype is associated with healthy astrocytes functions.

As well having an effect on viability and cells growth, modification with Ti and Zn has a major role in inhibiting bacteria adhesion too (Fig. 4.14). The role of metals (Zn and Ti) in contrasting bacterial growth and reproduction can be explained as a multi-pronged approach.

Antibacterial effect

Both titanium and zinc-modified surfaces are effective in reducing bacterial viability (Fig. 4.15). The presence of metal ions may confer bactericidal properties to the surface of treated electrospun materials. In particular, zinc complexes have been shown to have bactericidal activity, mainly due to their formation of complexes that compete with natural iron uptake of most bacteria. Indeed, zinc has a similar electronic configuration with iron and Zn(II) can be

chelated to siderophores (iron-chelating molecules secreted by bacteria in low-iron environments to recruit iron, important for many biological processes). This way, zinc will compete with iron and disrupt iron metabolism within bacteria, leading to their death. Probably the presence of free Zn(II) cations or small molecular clusters (especially concentrated on the surface, as exhibited by AFM scans, see Fig. 3.9) accounts for the effectiveness of Zn-modified samples in reducing bacteria viability.

Furthermore, Zn-modified samples have a higher specific areas given that fibres are thinner (Table 2.3), therefore they have a higher surface capable to interact with the biological environment and, potentially, release Zn(II) ions to contract bacterial colonisation. Although the release aspects in biological fluids has not been clarified, it is likely that unbound zinc cations are leaked into the bacterial lysogeny broth.

As far as titanium-modified materials is concerned, they seem to have a higher surface adhesion, which can be explained with a difference in charge distribution induced by the modifier (Fig. 3.13). This variation in charges could be a factor against bacterial adhesion and growth. *Staph. aureus* has a peptidoglycan membrane which, although less polar than other bacterial species, exhibits a net negative charge. Bacteria experience an attractive field to the modified materials and, upon adhesion, their membrane is depleted of charges, which leads to membrane lysis and bacteria death.

The distribution of charges on the surface, being influenced by the distribution of titanium and zinc (see Section 3.4), might influence the way proteins cover the surface, and therefore, indirectly, the adhesion of bacteria. Albumin adsorbs the most on hydrophobic surfaces, and at the same time acts against bacterial colonisation. Future work should focus on the protein adhesion and distribution on the surface.

Bacteria reduction on modified electrospun surfaces is modest, about $1 \log_{10}$ unit (Fig. 4.15). These surfaces can be described as bacteriostatic rather than bactericidal. The result is however remarkable, considering it has been achieved without the help of broad-spectrum bactericidal drugs or established antibacterial metals such as silver ions.

The large CFU count of bacteria on PDMS, and the large variability, is maybe explained by the fact that PDMS cylindrical samples have a large side area, and, as shown by SEM images, the rough sides are more conducive to a higher growth of bacteria. Probably, the combination of an apolar and smooth surface for PDMS does not encourage bacteria attachment on top, or maybe the adhesion on top is weaker and bacteria are displaced when the samples are prepared.

It has been noticed how the antibacterial efficacy in the current experiment is significantly reduced on all materials upon UV irradiation (Fig. 4.15). UV treatment was kept short (20 minutes) in order to achieve complete sterilisation while at the same time not impacting on the integrity of the surface. Perhaps UV irradiation induces fixed charged on the surface that cause the attraction for bacteria to increase.

The chemical modification of the fibres does not seem to be the only factor influencing the ability of materials to resist bacterial colonisation. From the bacterial viability tests (Table 4.1), it appears that all electrospun materials, both modified and non modified, are effective in reducing the number of viable forming units, regardless whether they are modified or not, while flat surfaces, such as polyurethane cast film and PDMS, are less effective, as they offer a good environment for colonies to form, spread and thrive.

In fact, cast polyurethane does not have any intrinsic antimicrobial properties. The present set of experiments, however, show that there is a significantly different reduction in bacterial colonies on all the electrospun materials, both treated and untreated, as compared to TCP and PDMS. The nanopatterned surface provided by the electrospun materials is sufficient to reduce the ability of *Staph. aureus* to adhere and multiply, maybe by way of isolating bacteria from each other.

Indeed, it appears that disrupting the natural arrangement of cells in the biofilm, and therefore communication and other vital cellular processes, including division and external signal processing, can damage the communication and cooperation between bacteria population. Often, bacteria on electrospun surfaces look nested and isolated, separated from each other (Fig. 4.14). Electrospun surfaces seem to create

a hostile environment, less conducive to create a colony of cooperating bacteria. A surface with morphological features of the same size scale as the organisms adhering on it represents a challenging environment. Bacterial membrane tend to adhere to a surface with as much membrane as possible, and in doing so on patterned surfaces, they naturally tend to stretch, a process that makes the membrane more vulnerable to lysis.

Indeed, when exploring the relationship between the number of bacterial colonies and the size of morphological features of the surfaces they grow on, there appears to be a quadratic dependence, with a minimum colony forming ability when features size is around $0.5\ \mu\text{m}$ (Fig. 4.16).

Shape, size, height and separation distance are all important parameters of the surface features to control bacterial attachment. It has been reported that surface structures are most effective when their size is in the range 50-90% of the length, or diameter, of the settling organism. There is abundant evidence, from the natural world, that structures with size smaller than the protrusions' size reduces settlement and attaching strength. Electrospun fibres produced for this work tend to be in this size range and therefore be effective in contrasting bacterial adhesion.

In conclusion, antibacterial properties of modified electrospun materials can be justified as the concomitant action of different factors, both chemical and morphological:

1. the chemical interference of ions such as Ti(IV) and Zn(II) with the bacterial life cycle, resulting in bacterio-toxicity;
2. the interaction between Zn and Ti ions and chemical moieties of the polyurethane surface and the bacterial surface;
3. the fibre size: smaller fibres drive lower adhesion, breaking up cells and delaying the formation of a biofilm.

4.5 CONCLUSIONS

In the present chapter, the translation of electrospun surfaces into a biological environment has been explored, as a set of preliminary tests to mimic the ventricular environment to which a catheter is exposed in vivo. In particular, samples were tested for their ability to reduce viability and adhesion of neuronal cells, and limit bacterial colonisation on the surface.

When immortalised human astrocyte were cultivated on samples, modified electrospun materials were efficient in reducing viability as compared to the positive control (tissue culture plastic), especially when modified with zinc. Viability data are not significantly different from PDMS (the negative control), therefore the materials being explored in this present thesis are to be considered at least not less efficient than PDMS itself. The positive effect on limiting cell viability might be attributed to the smaller size of fibres, or to the effect of zinc or titanium itself, which, being released into the cell culture medium, might have an impact on the cell regulatory systems.

All modified materials, furthermore, exhibit a higher apoptosis/viability ratio, which suggests a higher apoptotic rate on such surfaces, as compared to both positive and negative controls. The present results, even though affected by a high variability that can be attributed to the variability of the samples themselves, confirm that the newly prepared surfaces are at least partially effective in reducing growth and viability of healthy tissue on them.

Cells exhibit a very different morphology on flat surfaces, such as PDMS and TCP, and nano or micro-patterned surfaces, that is, cast Z6A1 and all electrospun materials. Similarly, cells seem to be more mobile on non-flat surfaces, which could suggest the possibility of a reduced adhesion and therefore minor risk of blockage in the long term. If cells are capable of moving along fibres, while at the same time less prone to colonise the surface, they might avoid the colonisation and blockage of the device.

Modified surfaces seem to be effective in reducing bacterial colonisation of *Staph. aureus*, as well. In particular, all modified and unmodified electrospun surfaces exhibit fewer colonies than PDMS, and

the colonies seem to be more dispersed and less continuous. This might be explained by the synergic effect of metal cations released by the surface, and the size and distribution of the electrospun fibres, that lead to looser contact between single bacteria and disrupt their signalling.

Overall, results from this preliminary set of biological experiments show an improvement of electrospun materials over traditionally used PDMS. They are non cytotoxic, antimicrobial and favour cell mobility.

Further testing is required to confirm these results over a longer time scale, to assess how the influence of the morphology on cell attachment evolve over time.

CONCLUSIONS

5.1 GENERAL CONCLUSIONS

The current shunt catheter, the most common way to treat hydrocephalus, presents a high failure rate and a short lifespan. While research has focused on the valve of the catheter, the proximal and distal catheters have experienced little or no development since they were first developed, especially as far as the design of the fenestration and the material choice is concerned. Obstruction, either from healthy or inflamed tissue or from bacterial colonisation, accounts for most of the proximal catheter failures (Section 1.2.10).

In the search for a new material, or material design, to use in shunt catheters, a different approach has been proposed by Suresh & Black [5], namely to create a nanoporous surface to act as a continuous absorbent surface, instead of a non porous, continuous surface with fenestrations through which the CSF may flow.

Instead of medical grade silicone, the standard material in use at the moment, a medical grade polyurethane was chosen for testing. Polyurethane Z6A1, provided by Biomer Technologies Ltd., is a segmented polymer with good biocompatibility. In order to reduce cell adhesion and blockage, one of the frequent solutions reported in literature is to increase wettability of the surface.

5.1.1 *Successful modification of the surface of a biocompatible polyurethane*

In this work, to modify the native polyurethane, whose wettability is around 90° , precursors of titanium and zinc has been added to the bulk material during the electrospinning process via a sol-gel method.

By adding the precursors, electrospun fibres undergo a dramatic morphological modification. While ES materials exhibit a multimodal distribution with diameter size close to $1\ \mu\text{m}$, modified materials ex-

hibit a narrower and unimodal distribution of diameters, with size as small as $0.18\ \mu\text{m}$ (Fig. 2.1).

Zinc-modified materials exhibit a much narrower fibre diameter distribution, with average diameter being smaller than the unmodified polyurethane. The size can be scaled by adjusting the quantity of inorganic precursor (Fig. 2.3).

Although the the crystallographic state of the inorganic modifier in the fibres could not be determined with certainty, it was probably amorphous, as sol-gel reaction occurred at room temperature and low energy, not sufficient to provide for the formation of ordered crystalline bonds. Nonetheless, Electron Dispersion Spectroscopy and FT-IR spectroscopy data show the presence of titanium and zinc in the finished materials and their interaction with polyurethane (Fig. 2.4).

Having successfully modified the materials, modification occurs over the whole bulk of the material, changing the internal structure of the fibres. DSC and TGA results show how the biphasic separation, typical of segmented polymers such as polyurethanes, and usually less prevalent in electrospun materials, is further broken down, causing hard segments to mix further with soft segments, thanks to the interaction of the polymeric chains with the metal cation (Ti(IV) or Zn(II), accordingly). The internal modification is more evident in the case of titanium-modified materials, with melting point dropping to $205\ ^\circ\text{C}$ as compared to $210\ ^\circ\text{C}$ for cast samples (Table 2.5), while Zn-modified materials do not exhibit the same degree of modification, which leads to the conclusion that, in the case of zinc, sol-gel reaction was partial, leading to the creation of clusters or oligomers, rather than a full network.

The metals are present in an amorphous form, however, adhesion measurements, derived via Force Microscopy, show that electrospun materials, and especially titanium-modified electrospun materials, suggests an effective modification of the surface through the presence of a higher concentration in charges thanks to the contribution of the metal cations (Fig. 3.12).

On the other hand, detailed surface analysis by means of AFM revealed that electrospun Zn-modified materials are not homogenous and there might be a segregation effect (Fig. 3.9).

At a macroscopic level, although the morphology of electrospun materials leads to a certain degree of hydrophobicity, probably explained by micro-pockets of air trapped between fibres, this effect does not last long, and the fluid deposited on electrospun materials is absorbed within minutes, thanks to the interconnecting network of pores typical of electrospun materials (Fig. 3.4). Although pores are in the micrometer range (Fig. 3.10), thus much smaller than the regular fenestrations presented by current catheters, the fact the pores are continuous throughout the surface, and interconnected, make electrospun surfaces effective at absorbing and draining fluid they are in contact with.

5.1.2 *Cell viability is lower on modified electrospun materials*

The modified electrospun materials exhibit a network of interconnected porosity and are effective at absorbing the fluid, which accounts for an improvement over the current catheter design. Now, the effect of these modifications on cell adhesion and proliferation proliferation was investigated, with the aim of evaluating these materials as a potential option for shunt catheters.

From the viability assays (Fig. 4.3), biocompatibility of materials is affected by addition of titanium and zinc. In fact, viability is significantly reduced on modified electrospun surfaces as compared to the positive control ($p < 0.05$). The apoptotic rate is higher on modified materials than flat or unmodified ES surfaces. Higher death rates on such materials might be indicative of lower adhesion; less adherent cells tend to enter the apoptotic cycle.

With a view to using these materials for a catheter, a higher death rate could ultimately lead to an accumulation of cellular debris on the surface of the catheter, which should then have to be removed by macrophages.

The effect of modified electrospun materials on limiting cell adhesion and growth may be explained by at least four factors:

- morphology of the fibres, especially differing diameters;

- surface charge distribution following chemical modification induced by addition of titanium and zinc;
- chemical effect of zinc or titanium themselves in interacting with cells; and
- mechanical modification (the evaluation of mechanical properties were beyond the scope of this thesis, though).

A linear relationship between cell attachment force and the average size of the scaffold was noted for modified electrospun materials (Fig. 4.10), suggesting that adhesion is lowest on thinner fibres, which might explain the significant reduction in viability on Zn3 sample.

Cell detachment and surface adhesion force as measured by AFM exhibit a linearly relation as well, even though only few experimental points were available and the uncertainty affecting such adhesion measurements was high. Further experiments would be needed to explore the impact of each of these individual factors.

Cells growing on PDMS exhibit an elongated shape, but at the same time they grow less densely and tend to clump together. Cells on hydrophobic surfaces tend to prefer to stick together and minimise their contact area with such a surface (Fig. 4.12). Astrocytes with a flat, round-like shape express a phenotype called 'cytotoxic', which is evidence of non-healthy cells. Indeed, the number of viable cells on PDMS is low. The rate of apoptosis is low and constant in time as well, probably linked to the lower density of viable cells.

Cells growing on non-flat surfaces (cast and electrospun materials, both modified and unmodified) show a stellate shape and a polarised morphology, and exhibit a propensity to move on the surface following the topographical clues offered by the surface, especially along the fibres. These features express a cytotropic, or 'healthy', phenotype.

In conclusion, modified electrospun materials seem to be effective in reducing mammalian cell viability as compared to the positive control, increase the rate of apoptosis and encourage motility of the cells exposed to such materials.

5.1.3 Colonisation of *S. aureus* is lower on modified electrospun materials

Finally, the effect of modified materials on bacterial colonisation was assessed. A preliminary assay to verify the properties of the materials when exposed to a strain of *S. aureus* was carried out (Fig. 4.15).

Exposure to UV light does not increase the bacteriostatic properties of the modified materials, leading to the conclusion that titanium or zinc are not activated by UV light.

Results of bacterial cultures on materials not exposed to UV light show how micro- and nanopatterned surfaces are inherently more resistant to bacterial attachment and are effective in avoiding biofilm formation. Electrospun materials are especially effective as compared to the negative control, PDMS, with a significantly different reduction of $1 \log_{10}$ of CFU/mL ($p < 0.05$). This effect could be explained by the combined effect of chemical activity of zinc and titanium being released into the growth broth, and the morphological effect of fibres separating and isolating bacteria, thus making colonisation more challenging (Fig. 4.14).

Even though the time scale for these experiments was limited to 24 hours and to one species (*S. aureus*), and the reduction was limited to one log unit, these results are interesting, as they were achieved without the aid of other common, more effective chemical strategies used to manage infections (for example antibiotic drugs or silver ions).

5.2 RECOMMENDATIONS

Table 5.1 summarises the main findings of the present thesis and results from Suresh & Black [5], and tries to make a comparison between selected candidate materials: standard PDMS, electrospun polyurethane (Z6A1), electrospun polyurethane with added zinc and titanium. These latter, non-standard materials might be helpful in limiting the colonisation and obstruction deriving from neuronal cells and bacterial infection.

The results of the present research support the idea of using a medical grade polyurethane as an alternative material to PDMS. At least under static culture conditions, cell viability is not statistically differ-

Table 5.1: Comparison between selected materials for shunt catheters: standard medical grade silicone (PDMS), electrospun medical grade polyurethane, electrospun polyurethane modified with titanium and zinc. + denotes good or improved feature (as compared to the standard), o denotes no remarkable difference from the standard, and – an absent or worse feature.

	Standard catheter (PDMS)	ES Z6A1	ES Z6A1/Ti	ES Z6A1/Zn
Continuous flowing surface	-	+	+	+
Fast, self-absorbing surface	-	+	+	+
Low astrocyte viability	o	o	o	+
Low astrocyte attachment	o	o	o	+
Low infection risk	-	+	+	+
Ease of manufacturing	+	o	-	-

ent between PDMS and polyurethane. Given the encouraging results of the present research, the translation of some of the results into the current design of shunt catheters might be advantageous.

PDMS suffers from failures that have been described in the literature, but it is an easy material to process and it is flexible, and retains its shape without yielding too many kinks. Electrospun materials are flexible as well, but they might not offer enough resistance to maintain their shape. It would still be advisable to endow the shunt catheter with some of their beneficial properties, for example by electrospinning only the proximal catheter, which has a more linear pathway and is kept open by the positive pressure coming from the ventricle.

In conclusion, an electrospun surface is in fact an efficient filter and can actively block the passage of cells and bacteria from the ventricular environment into the device, avoiding the spreading of dangerous microorganisms from or into the brain environment, while at the same time avoiding the obstruction of a continuous flow of CSF.

5.3 FUTURE WORK

One of the open questions left by this research is a detailed and precise mapping of the surface, which could not be obtained via contact angle and AFM (Section 3.4). The analysis of the chemical distribution of titanium and zinc on the surface would enable to describe the charge distribution on the electrospun fibres, and to correlate such distribution to the microstructural modification. Once a detailed mapping of the surface has been obtained, a closer relationship between surface properties and biological activity can be discerned. To this effect, further analysis could be conducted using Secondary-ion mass spectrometry (SIMS) or Electron Spectroscopy for Chemical Analysis (ESCA) to obtain a more detailed chemical mapping of the surface. Such analytical techniques provide information on the chemical bonds of the materials at a high lateral resolution, and can provide insight on the actual structure of the inorganic part of the modified materials and on their interaction with the organic environment.

Research on the degradations of such materials, and release of degradation products, titanium and zinc ions in a biological environment, especially when exposed to an inflamed tissue, should be conducted.

Further control studies are needed to establish which property of the fibres is more influential and effective in preventing adhesion: the presence of titanium and zinc, the reduced size of the fibres, or the morphology of the fibres itself. Cell adhesion studies should be repeated on single, isolated fibres, so to isolate the effect of fibre size.

It may be of interest to manufacture a thicker layer of electrospun materials in order to perform perfusion studies and verify the results thus obtained in a model that replicates the specific environment of the catheter. Porosity of the electrospun materials should be quantified using, for example, capillary flow porometry.

All biological experiments (in particular cell viability and bacterial colonisation of modified materials) should be performed over a longer period of time, in order to assess the long-term properties of the materials.

The results of the present study, though preliminary, may justify following *in vitro* tests and pre-clinical trials required in order to demonstrate safety and beneficial outcomes *in vivo*, to be followed by phase 1 clinical trials before the results could be translated into a commercial product. In particular, future tests may include cell studies with primary neuronal cells, in order to compare the results from immortalised cells with primary cells. Other experiments could involve the co-culture of two or more cell lines at the same time, including a human macrophage cell line. The hypothesis is that macrophage functions may be improved when exposed to modified materials.

The results from this research could be applied to the design of conventional fenestrated catheters, specifically by creating a micropattern on the surface. One of the conclusions of the present work is that the complex structure created by the non-aligned fibres may be responsible for lower cell adhesion and enhanced antibacterial resistance. By transferring these inherent antibacterial properties to PDMS, for example by etching or engraving a similar pattern in the micro and sub-micro range, the bacterial colonisation rate of the shunt catheter should decrease, thus reducing the need for revision surgery.

Furthermore, patterning promotes cell mobility and it may help shifting cells along the catheter, rather than encouraging adhesion and therefore the eventual blockage of the catheter fenestration. Therefore, an electrospun surface, or patterning with similar features in terms of size and groove shape, could be produced on the surface of the catheter to improve its biological properties without the need for further aids.

Electrospinning surfaces seem to be a quick and efficient way to make a surface more resistant to bacterial colonisation. This application, which confirms other reports in the literature, can be an alternative to antibiotic-impregnated devices, which have the negative consequence of creating antibiotic-resistant bacteria, such as MRSA. This approach could eventually be extended to other medical devices affected by bacterial colonisation.

REFERENCES

1. Lifshutz, J. I. & Johnson, W. D. History of hydrocephalus and its treatments. en. *Neurosurgical focus* **11**, 1–5 (2001).
2. Weisenberg, S. H., TerMaath, S. C., Seaver, C. E. & Killeffer, J. A. Ventricular catheter development: past, present, and future. *J Neurosurg* **125**, 1504–1512 (2016).
3. Harris, C. A. & McAllister, J. P. What we should know about the cellular and tissue response causing catheter obstruction in the treatment of hydrocephalus. *Neurosurgery* **70**, 1589–1601 (2012).
4. Symss, N. P. & Oi, S. Is there an ideal shunt? A panoramic view of 110 years in CSF diversions and shunt systems used for the treatment of hydrocephalus: from historical events to current trends. *Child's nervous system : ChNS : official journal of the International Society for Pediatric Neurosurgery* **31**, 191–202 (2015).
5. Suresh, S. & Black, R. A. Electrospun polyurethane as an alternative ventricular catheter and in vitro model of shunt obstruction. *Journal of Biomaterials Applications* **29**, 1028–1038 (2015).
6. ReKate, H. L. The definition and classification of hydrocephalus: A personal recommendation to stimulate debate. *Cerebrospinal Fluid Research* **5** (2008).
7. Purves, D., Augustine, G. & Fitzpatrick, D. *Neuroscience* 2nd (Sinauer Associates, Sunderland (MA), 2001).
8. Marieb, E. N. *Human anatomy & physiology* 5th, 1249 (Benjamin Cummings, San Francisco, 2001).
9. Damkier, H. H., Brown, P. D. & Praetorius, J. Cerebrospinal Fluid Secretion by the Choroid Plexus. *Physiological Reviews* **93**, 1847–1892 (2013).

10. Aluise, C. D., Sowell, R. A. & Butterfield, D. A. Peptides and proteins in plasma and cerebrospinal fluid as biomarkers for the prediction, diagnosis, and monitoring of therapeutic efficacy of Alzheimer's disease. *Biochimica et Biophysica Acta - Molecular Basis of Disease* **1782**, 549–558 (2008).
11. OpenStax. *Anatomy & Physiology* (OpenStax CNX, 2016).
12. Czosnyka, M., Czosnyka, Z. & Baledent, O. Dynamics of Cerebrospinal Fluid: From Theoretical Models to Clinical Applications. *Biomechanics of the*, 137–167 (2011).
13. Harris, C. A. *et al.* Effects of surface wettability, flow, and protein concentration on macrophage and astrocyte adhesion in an in vitro model of central nervous system catheter obstruction. *Journal of Biomedical Materials Research - Part A* **97 A**, 433–440 (2011).
14. Wagshul, M. E., Chen, J. J., Egnor, M. R., McCormack, E. J. & Roche, P. E. Amplitude and phase of cerebrospinal fluid pulsations: experimental studies and review of the literature. *Journal of Neurosurgery* **104**, 810–819 (2006).
15. Sakka, L., Coll, G. & Chazal, J. Anatomy and physiology of cerebrospinal fluid. **128**, 309–316 (2011).
16. Henry-Feugeas, M. C. *et al.* Origin of subarachnoid cerebrospinal fluid pulsations: A phase-contrast MR analysis. *Magnetic Resonance Imaging* **18**, 387–395 (2000).
17. Wagshul, M. E., Eide, P. K. & Madsen, J. R. The pulsating brain: A review of experimental and clinical studies of intracranial pulsatility. **8**, 5 (2011).
18. Pople, I. K. Hydrocephalus and shunts: what the neurologist should know. *J. Neurol. Neurosurg. Psychiatry* **73**, 17–22 (2002).
19. Brydon, H. L. *et al.* Protein adsorption to hydrocephalus shunt catheters: CSF protein adsorption. *Journal of Neurology Neurosurgery and Psychiatry* **64**, 643–647 (1998).

20. Hühmer, A. F., Biringer, R. G., Amato, H., Fonteh, A. N. & Harrington, M. G. Protein Analysis in Human Cerebrospinal Fluid: Physiological Aspects, Current Progress and Future Challenges. *Disease Markers* **22**, 3–26 (2006).
21. Chrisman, C. L. Cerebrospinal fluid analysis. *The Veterinary clinics of North America. Small animal practice* **22**, 781–810 (1992).
22. Ginsberg, H. J. & Drake, J. M. in *Pediatric Hydrocephalus* 295–313 (Springer Milan, Milano, 2005).
23. Patel, S. K., Yuan, W. & Mangano, F. T. Advanced Neuroimaging Techniques in Pediatric Hydrocephalus. **52**, 436–445 (2017).
24. Vinchon, M., Rekate, H. & Kulkarni, A. V. Pediatric hydrocephalus outcomes: a review. *Fluids and Barriers of the CNS* **9**, 18 (2012).
25. Spector, R., Robert Snodgrass, S. & Johanson, C. E. A balanced view of the cerebrospinal fluid composition and functions: Focus on adult humans. *Experimental Neurology* **273**, 57–68 (2015).
26. Farin, A., Aryan, H. E., Ozgur, B. M., Parsa, A. T. & Levy, M. L. Endoscopic third ventriculostomy. *Journal of Clinical Neuroscience* **13**, 763–770 (2006).
27. Codman® Certas® Plus Programmable Valve <https://www.integralife.com/codman-certas-plus-programmable-valve/product/hydrocephalus-programmable-valves-codman-certas-plus-programmable-valve> (2019).
28. Naradzay, J. F., Browne, B. J., Rolnick, M. A. & Doherty, R. J. Cerebral ventricular shunts. *Journal of Emergency Medicine* **17**, 311–322 (1999).
29. Brain & Spine Foundation. *Hydrocephalus (water on the brain) and shunts* <https://www.brainandspine.org.uk/hydrocephalus-water-brain-and-shunts> (2017).
30. Nakahara, K. *et al.* Shortening of ventricular shunt catheter associated with cranial growth: Effect of the frontal and parieto-occipital access route on long-term shunt patency. *Child's Nervous System* **25**, 91–94 (2009).

31. Madsen, J. R., Egnor, M. & Zou, R. *Cerebrospinal fluid pulsatility and hydrocephalus: the fourth circulation*. tech. rep. (2006), 48–52.
32. Williams, M. A. *et al.* Priorities for hydrocephalus research: report from a National Institutes of Health–sponsored workshop. *Journal of Neurosurgery: Pediatrics* **107**, 345–357 (2007).
33. McAllister, J. P. *et al.* An update on research priorities in hydrocephalus: overview of the third National Institutes of Health–sponsored symposium “Opportunities for Hydrocephalus Research: Pathways to Better Outcome”. en. *Journal of Neurosurgery* **123**, 1427–1438 (2015).
34. Kehler, U. *et al.* Reduction of shunt obstructions by using a peel-away sheath technique? A multicenter prospective randomized trial. *Clinical Neurology and Neurosurgery* **114**, 381–384 (2012).
35. Boch, A.-L., Hermelin, É., Sainte-Rose, C. & Sgouros, S. Mechanical dysfunction of ventriculoperitoneal shunts caused by calcification of the silicone rubber catheter. en. *Journal of Neurosurgery* **88**, 975–982 (1998).
36. Brydon, H. L., Hayward, R., Harkness, W. & Bayston, R. Physical properties of cerebrospinal fluid of relevance to shunt function. 1: The effect of protein upon CSF viscosity. *British Journal of Neurosurgery* **9**, 639–644 (1995).
37. Brydon, H. L., Bayston, R., Hayward, R. & Harkness, W. Reduced bacterial adhesion to hydrocephalus shunt catheters mediated by cerebrospinal fluid proteins. *Journal of Neurology Neurosurgery and Psychiatry* **60**, 671–675 (1996).
38. Brydon, H. L., Bayston, R., Hayward, R. & Harkness, W. The effect of protein and blood cells on the flow-pressure characteristics of shunts. *Neurosurgery* **38**, 498–505 (1996).
39. Anderson, J. M., Bonfield, T. L. & Ziats, N. P. Protein adsorption and cellular adhesion and activation on biomedical polymers. *International Journal of Artificial Organs* **13**, 375–382 (1990).
40. Bayston, R., Ashraf, W. & Bhundia, C. Mode of action of an antimicrobial biomaterial for use in hydrocephalus shunts. *Journal of Antimicrobial Chemotherapy* **53**, 778–782 (2004).

41. Gutiérrez-González, R., Boto, G. R. & Pérez-Zamarrón, Á. Cerebrospinal fluid diversion devices and infection. A comprehensive review. *31*, 889–897 (2012).
42. Jenkinson, M. D. *et al.* The British antibiotic and silver-impregnated catheters for ventriculoperitoneal shunts multi-centre randomised controlled trial (the BASICS trial): Study protocol. En. *Trials* **15**, 4 (2014).
43. Francolini, I. & Piozzi, A. in *Advances in Polyurethane Biomaterials* 349–385 (Elsevier, 2016).
44. Pople, I. K., Bayston, R. & Hayward, R. D. Infection of cerebrospinal fluid shunts in infants: a study of etiological factors. *Journal of Neurosurgery* **77**, 29–36 (1992).
45. Thompson, D. N. P., Hartley, J. C. & Hayward, R. D. Shunt infection: is there a near-miss scenario? *Journal of Neurosurgery: Pediatrics* **106**, 15–19 (2007).
46. Borges, L. F. Infections in neurologic surgery. Host defenses. *Neurosurg Clin N Am* **3**, 275–278 (1992).
47. Kalousdian, S., Karlan, M. S., Williams, M. A. & Bresolin, L. B. Silicone elastomer cerebrospinal fluid shunt systems. *Neurosurgery* **42**, 887–892 (1998).
48. Irminger-Finger, I., Laymon, R. A. & Goldstein, L. S. B. *Analysis of the primary sequence and microtubule-binding region of the Drosophila 205K MAP* (eds Czernicki, Z. *et al.*) *Acta Neurochirurgica Supplementum* **6 PART 1**, 2563–2572 (Springer Vienna, Vienna, 1990).
49. Clyde, B. L. & Leland Albright, A. Evidence for a Patent Fibrous Tract in Fractured, Outgrown, or Disconnected Ventriculoperitoneal Shunts. *Pediatric Neurosurgery* **23**, 20–25 (1995).
50. Achyuta, A. K. H., Stephens, K. D., Lewis, H. G. P. & Murthy, S. K. Mitigation of reactive human cell adhesion on poly(dimethylsiloxane) by immobilized trypsin. *Langmuir : the ACS journal of surfaces and colloids* **26**, 4160–7 (2010).

51. Çağavi, F. *et al.* Effect of hydrophilic coating on microorganism colonization in silicone tubing. *Acta Neurochirurgica* **146**, 603–610 (2004).
52. Arima, Y. & Iwata, H. Effect of wettability and surface functional groups on protein adsorption and cell adhesion using well-defined mixed self-assembled monolayers. *Biomaterials* **28**, 3074–3082 (2007).
53. Cox, J. D., Curry, M. S., Skirboll, S. K., Gourley, P. L. & Sasaki, D. Y. Surface passivation of a microfluidic device to glial cell adhesion: a comparison of hydrophobic and hydrophilic SAM coatings. *Biomaterials* **23**, 929–35 (2002).
54. Gnanaprakasam Thankam, F. & Muthu, J. Influence of plasma protein-hydrogel interaction moderated by absorption of water on long-term cell viability in amphiphilic biosynthetic hydrogels. *RSC Advances* **3**, 24509–24520 (2013).
55. Guevara, J. A., La Torre, J., Denoya, C. & Zúccaro, G. Microscopic studies in shunts for hydrocephalus. *Child's brain* **8**, 284–93 (1981).
56. Epstein, A. K., Hochbaum, A. I., Kim, P. & Aizenberg, J. Control of bacterial biofilm growth on surfaces by nanostructural mechanics and geometry. *Nanotechnology* **22** (2011).
57. Scardino, A. J. & de Nys, R. Mini review: Biomimetic models and bioinspired surfaces for fouling control. *Biofouling* **27**, 73–86 (2011).
58. Ostuni, E., Chapman, R. G., Holmlin, R. E., Takayama, S. & Whitesides, G. M. A Survey of Structure–Property Relationships of Surfaces that Resist the Adsorption of Protein. **17**, 5605–5620 (2001).
59. Matsumoto, H. & Tanioka, A. Functionality in electrospun nanofibrous membranes based on fiber's size, surface area, and molecular orientation. **1**, 249–264 (2011).
60. Samuel, U. & Guggenbichler, J. P. *Prevention of catheter-related infections: The potential of a new nano-silver impregnated catheter in International Journal of Antimicrobial Agents* **23** (2004), 75–78.

61. Xu, L. C. & Siedlecki, C. A. in *Advances in Polyurethane Biomaterials* 247–284 (2016).
62. Richards, H. K., Seeley, H. M. & Pickard, J. D. Efficacy of antibiotic-impregnated shunt catheters in reducing shunt infection: data from the United Kingdom Shunt Registry. *Journal of Neurosurgery: Pediatrics* **4**, 389–393 (2009).
63. Konstantelias, A. A., Vardakas, K. Z., Polyzos, K. A., Tansarli, G. S. & Falagas, M. E. Antimicrobial-impregnated and -coated shunt catheters for prevention of infections in patients with hydrocephalus: a systematic review and meta-analysis. *Journal of Neurosurgery* **122**, 1096–1112 (2015).
64. Zhong, Y. & Bellamkonda, R. V. Biomaterials for the central nervous system. *Journal of the Royal Society Interface* **5**, 957–975 (2008).
65. Hayhurst, C. *et al.* The impact of antibiotic-impregnated catheters on shunt infection in children and neonates. *Child's Nervous System* **24**, 557–562 (2008).
66. Kohnen, W., Schäper, J., Klein, O., Tieke, B. & Jansen, B. A silicone ventricular catheter coated with a combination of rifampin and trimethoprim for the prevention of catheter-related infections. *Zentralblatt für Bakteriologie* **287**, 147–156 (1998).
67. Gower, D. J., Gower, V. C., Richardson, S. H. & Kelly, D. L. Reduced bacterial adherence to silicone plastic neurosurgical prosthesis. *Pediatric Neurosurgery* **12**, 127–133 (1985).
68. Thomale, U. W. *et al.* Perforation holes in ventricular catheters: is less more? *Child's Nervous System* **26**, 781–789 (2010).
69. Galarza, M. *et al.* Basic cerebrospinal fluid flow patterns in ventricular catheters prototypes. *Child's nervous system : ChNS : official journal of the International Society for Pediatric Neurosurgery* **31**, 873–84 (2015).
70. *Ares Antibiotic-Impregnated Catheters - Overview | Medtronic* <https://www.medtronic.com/us-en/healthcare-professionals/products/neurological/shunts/ares-antibiotic-impregnated-catheters.html> (2019).

71. Lin, J. *et al.* Computational and experimental study of proximal flow in ventricular catheters. *en.* **99**, 426–431 (2003).
72. (ed Medtronic) *Products catalogue-CSF Management, Critical Care, Cranial Repair, and Neuroendoscopy* 2017.
73. Galarza, M., Giménez, A., Pellicer, O., Valero, J. & Amigó, J. M. in *Pediatric Hydrocephalus* (eds Cinalli, G., Ozek, M. M. & Sainte-Rose, C.) 1–23 (Springer International Publishing, Cham, 2018).
74. *Ventricular Catheter, Brain Shunt, Hydrocephalus Treatment* | *Anuncia* <https://reflowventcath.com/patients-families/> (2019).
75. Go, K. G., Ebels, E. J. & van Woerden, H. Experiences with recurring ventricular catheter obstructions. *Clinical Neurology and Neurosurgery* **83**, 47–56 (1981).
76. Pettikiriarachchi, J. T., Parish, C. L., Shoichet, M. S., Forsythe, J. S. & Nisbet, D. R. Biomaterials for brain tissue engineering. *en.* *Australian Journal of Chemistry* **63**, 1143–1154 (2010).
77. Bagherzadeh, R., Najar, S. S., Latifi, M., Tehran, M. A. & Kong, L. A theoretical analysis and prediction of pore size and pore size distribution in electrospun multilayer nanofibrous materials. *Journal of Biomedical Materials Research - Part A* **101 A**, 2107–2117 (2013).
78. Sonnenschein, M. F. *Polyurethanes: Science, Technology, Markets, and Trends* 1–417 (John Wiley & Sons, Inc, Hoboken, NJ, 2014).
79. Janik, H., Sienkiewicz, M. & Kucinska-Lipka, J. in *Handbook of Thermoset Plastics* 253–295 (2013).
80. Heath, D. E. & Cooper, S. L. in *Biomaterials Science: An Introduction to Materials: Third Edition* 64–79 (2013).
81. Touchet, T. J. & Cosgriff-Hernandez, E. M. in *Advances in Polyurethane Biomaterials* 1–22 (2016).
82. Sonnenschein, M. F. in *Polyurethanes* 10–104 (John Wiley & Sons, Inc, Hoboken, NJ, 2014).
83. Yeh, F., Hsiao, B. S., Sauer, B. B., Michel, S. & Siesler, H. W. In-situ studies of structure development during deformation of a segmented poly(urethane-urea) elastomer. *Macromolecules* **36**, 1940–1954 (2003).

84. Marois, Y. & Guidoin, R. Biocompatibility of Polyurethanes. *Madame Curie Bioscience Database*, 1–17 (2010).
85. Wiggins, M. J., Wilkoff, B., Anderson, J. M. & Hiltner, A. Biodegradation of polyether polyurethane inner insulation in bipolar pacemaker leads. *Journal of Biomedical Materials Research* **58**, 302–307 (2001).
86. Cardona, M. *Application of advanced material analysis for the investigation of the role of nano-mechanical properties in cell-scaffold interactions* PhD thesis (2016), 2013.
87. Stryjewski, M. E. & Corey, G. R. Methicillin-resistant staphylococcus aureus: An evolving pathogen. *Clinical Infectious Diseases* **58**, S10–S19 (2014).
88. Xu, Y. & Guan, J. in *Advances in Polyurethane Biomaterials* 523–542 (2016).
89. Seymour, R. W. & Cooper, S. L. DSC studies of polyurethane block polymers. *Journal of Polymer Science Part B: Polymer Letters* **9**, 689–694 (1971).
90. Lin, M.-F., Shu, Y.-C., Tsen, W.-C. & Chuang, F.-S. Differential scanning calorimetry analysis of silicon-containing and phosphorus-containing segmented polyurethane. Thermal behaviors and morphology. *Journal of Applied Polymer Science* **81**, 3489–3501 (2001).
91. Tan, H. *et al.* The effect of fluorinated side chain attached on hard segment on the phase separation and surface topography of polyurethanes. *Polymer* **45**, 1647–1657 (2004).
92. Madkour, T. M. & Mohamed, S. K. Heterocyclic and aromatic based polyurethane scaffolds: Morphology and crystallinity studied by X-ray diffraction, small-angle X-ray scattering and differential scanning calorimetry. *Journal of Applied Crystallography* **46**, 980–992 (2013).
93. Koberstein, J. T. & Russell, T. P. Simultaneous SAXS-DSC Study of Multiple Endothermic Behavior in Polyether-Based Polyurethane Block Copolymers. *Macromolecules* **19**, 714–720 (1986).

94. Srichatrapimuk, V. W. & Cooper, S. L. Infrared Thermal Analysis Of Polyurethane Block Polymers. *Journal of Macromolecular Science, Part B* **15**, 267–311 (1978).
95. Yang, W. P., Macosko, C. W. & Wellinghoff, S. T. Thermal degradation of urethanes based on 4,4'-diphenylmethane diisocyanate and 1,4-butanediol (MDI/BDO). *Polymer* **27**, 1235–1240 (1986).
96. Saunders, J. H. & Backus, J. K. Thermal Degradation and Flammability of Urethan Polymers. EN. *Rubber Chemistry and Technology* **39**, 461–480 (1966).
97. Grassie, N. & Zulfiqar, M. Thermal Degradation of the Polyurethane From 1,4-Butanediol and Methylene Bis(4-Phenyl Isocyanate). *J Polym Sci Polym Chem Ed* **16**, 1563–1574 (1978).
98. Duquesne, S. *et al.* Thermal degradation of polyurethane and polyurethane/expandable graphite coatings. *Polymer Degradation and Stability* **74**, 493–499 (2001).
99. Berta, M., Lindsay, C., Pans, G. & Camino, G. Effect of chemical structure on combustion and thermal behaviour of polyurethane elastomer layered silicate nanocomposites. *Polymer Degradation and Stability* **91**, 1179–1191 (2006).
100. Reneker, D. H. & Yarin, A. L. Electrospinning jets and polymer nanofibers. **49**, 2387–2425 (2008).
101. Andrady, A. L. *Science and Technology of Polymer Nanofibers* 1–403 (John Wiley & Sons, Inc., Hoboken, NJ, USA, 2007).
102. Garg, K. & Bowlin, G. L. Electrospinning jets and nanofibrous structures. *Biomicrofluidics* **5**, 13403 (2011).
103. Darrell H. Reneker & Hao Fong. Polymeric Nanofibers. *Polymeric Nanofibers. ACS Symposium Series* **918** (eds Reneker, D. H. & Fong, H.) 1–6 (2006).
104. Thompson, C. J., Chase, G. G., Yarin, A. L. & Reneker, D. H. Effects of parameters on nanofiber diameter determined from electrospinning model. *Polymer* **48**, 6913–6922 (2007).
105. Thanopoulou, K. *et al.* Investigation of anxiety and depression among individuals addicted to substances *SpringerBriefs in Materials* **1**, 36–44 (Springer Berlin Heidelberg, Berlin, Heidelberg, 2015).

106. Kidoaki, S., Kwon, I. K. & Matsuda, T. Structural features and mechanical properties of in situ-bonded meshes of segmented polyurethane electrospun from mixed solvents. *Journal of Biomedical Materials Research - Part B Applied Biomaterials* **76**, 219–229 (2006).
107. McKee, M. G., Wilkes, G. L., Colby, R. H. & Long, T. E. Correlations of Solution Rheology with Electrospun Fiber Formation of Linear and Branched Polyesters. *Macromolecules* **37**, 1760–1767 (2004).
108. Demir, M. M., Yilgor, I., Yilgor, E. & Erman, B. Electrospinning of polyurethane fibers. *Polymer* **43**, 3303–3309 (2002).
109. Teo, W. E. & Ramakrishna, S. A review on electrospinning design and nanofibre assemblies. en. *Nanotechnology* **17**, R89–R106 (2006).
110. Abedalwafa, M. A. *et al.* in *Electrospinning: Nanofabrication and Applications* (eds Ding, B., Wang, X. & Yu, J.) xix–xxv (William Andrew Publishing, 2019).
111. Ogushi, Y. *et al.* Antimicrobial Activity of Ultra-fine Fiber Non-woven Fabrics Produced by Electrospinning. *Seikei-Kakou* **21**, 287–290 (2009).
112. Niederberger, M. & Pinna, N. *Metal Oxide Nanoparticles in Organic Solvents* 230 (Springer Science & Business Media, 2009).
113. Livage, J., Sanchez, C., Henry, M. & Doeuff, S. The chemistry of the sol-gel process. *Solid State Ionics* **32-33**, 633–638 (1989).
114. Niederberger, M. Nonaqueous sol-gel routes to metal oxide nanoparticles. *Accounts of Chemical Research* **40**, 793–800 (2007).
115. Vioux, A. Nonhydrolytic Sol-Gel Routes to Oxides. *Chemistry of Materials* **9**, 2292–2299 (1997).
116. Deshmukh, R. & Niederberger, M. in *The Sol-Gel Handbook* 29–70 (Wiley-VCH Verlag GmbH & Co. KGaA, Weinheim, Germany, 2015).

117. Tiano, A. L., Koenigsmann, C., Santulli, A. C. & Wong, S. S. Solution-based synthetic strategies for one-dimensional metal-containing nanostructures. *Chemical Communications* **46**, 8093–8130 (2010).
118. Lu, X., Wang, C. & Wei, Y. One-dimensional composite nanomaterials: Synthesis by electrospinning and their applications. **5**, 2349–2370 (2009).
119. Cozzoli, P. D., Curri, M. L., Agostiano, A., Leo, G. & Lomascolo, M. ZnO Nanocrystals by a Non-hydrolytic Route: Synthesis and Characterization. *The Journal of Physical Chemistry B* **107**, 4756–4762 (2003).
120. Kolodziejczak-Radzimska, A. & Jesionowski, T. Zinc oxide - from synthesis to application: A review. en. *Materials* **7**, 2833–2881 (2014).
121. Sinji Harada, N., de Araujo, R. B., de Souza, M. A. V., de Santa Maria, L. C. & Wang, S. H. Polyurethane Composite Membranes. *Materials Science Forum* **775-776**, 3–8 (2014).
122. Busuioc, C., Evanghelidis, A., Enculescu, M. & Enculescu, I. Optical and photocatalytic properties of electrospun ZnO fibers. **10**, 957–965 (2015).
123. Suchitra, M. Thermal Analysis of Composites Using DSC. *Advanced Topics in Characterization of Composites*, 11–33 (2004).
124. Tetteh, G., Khan, A. S., Delaine-Smith, R. M., Reilly, G. C. & Rehman, I. U. Electrospun polyurethane/hydroxyapatite bioactive Scaffolds for bone tissue engineering: The role of solvent and hydroxyapatite particles. *Journal of the Mechanical Behavior of Biomedical Materials* **39**, 95–110 (2014).
125. Andrews, K. D., Hunt, J. A. & Black, R. A. Technology of electrostatic spinning for the production of polyurethane tissue engineering scaffolds. *Polymer International* **57**, 203–210 (2008).
126. Rayner-Canham, G. & Overton, T. *Descriptive inorganic chemistry* 6th (W. H. Freeman, 2014).
127. Turinske, A. J. *et al.* Formation of ZnO within flexible polymer fibers. *Journal of Sol-Gel Science and Technology* **65**, 283–286 (2013).

128. Li, H. *et al.* Sol - Gel preparation of transparent zinc oxide films with highly preferential crystal orientation. *Vacuum* **77**, 57–62 (2004).
129. Schneider, C. A., Rasband, W. S. & Eliceiri, K. W. NIH Image to ImageJ: 25 years of image analysis. *Nature Methods* **9**, 671–675 (2012).
130. Hotaling, N. A., Bharti, K., Kriel, H. & Simon, C. G. DiameterJ: A validated open source nanofiber diameter measurement tool. *Biomaterials* **61**, 327–338 (2015).
131. Bower, N. W. Principles of Instrumental Analysis. 4th edition (Skoog, D. A.; Leary, J. J.) *Journal of Chemical Education* **69**, A224 (1992).
132. Pirson, A. *et al.* Synthesis of SiO₂-TiO₂ xerogels by sol-gel process. *Journal of Sol-Gel Science and Technology* **4**, 179–185 (1995).
133. Ghule, K., Ghule, A. V., Chen, B. J. & Ling, Y. C. Preparation and characterization of ZnO nanoparticles coated paper and its antibacterial activity study. *Green Chemistry* **8**, 1034–1041 (2006).
134. Pielichowski, K., Pielichowski, J., Altenburg, H. & Balloff, H. J. Thermische degradation von MDI-basierenden polyurethanen: Charakteristische abhängigkeiten zwischen den zersetzungsparametern. *Thermochimica Acta* **284**, 419–428 (1996).
135. Frischmann, P. D., Gallant, A. J., Chong, J. H. & MacLachlan, M. J. Zinc carboxylate cluster formation in conjugated metal-*macrocycles*: Evidence for templation. *Inorganic Chemistry* **47**, 101–112 (2008).
136. Ma, X. Y. & Zhang, W. D. Effects of flower-like ZnO nanowhiskers on the mechanical, thermal and antibacterial properties of waterborne polyurethane. *Polymer Degradation and Stability* **94**, 1103–1109 (2009).
137. Liu, X., Hao, J. & Gaan, S. Recent studies on the decomposition and strategies of smoke and toxicity suppression for polyurethane based materials. *RSC Advances* **6**, 74742–74756 (2016).

138. Moroi, G. Influence of ion species on the thermal degradation of polyurethane interaction products with transition metal ions. *Journal of Analytical and Applied Pyrolysis* **71**, 485–500 (2004).
139. Gilman, J. W. Flammability and thermal stability studies of polymer layered-silicate (clay) nanocomposites. *Applied Clay Science* **15**, 31–49 (1999).
140. Bonino, C. A. *et al.* Three-dimensional electrospun alginate nanofiber mats via tailored charge repulsions. *Small* **8**, 1928–1936 (2012).
141. Rugar, D. & Hansma, P. *Atomic force microscopy*. 1990.
142. Voigtländer, B. *Scanning Probe Microscopy: Atomic Force Microscopy and Scanning Tunneling Microscopy* **2**, 165–166 (2016).
143. Friedbacher, G. *Atomic Force Microscopy (AFM)* 2011.
144. Ricci, D. & Braga, P. C. *Atomic Force Microscopy Biomedical Methods and* **2**, XIV, 394 (Humana Press, 2004).
145. Eaton, P. & West, P. *Atomic Force Microscopy* 1–256 (Oxford University Press, 2010).
146. AFM (Atomic Force Microscope) - University of Greifswald <https://physik.uni-greifswald.de/en/biophysics-and-soft-matter-prof-christiane-helm/methods/afm-atomic-force-microscope/> (2017).
147. Jalili, N. & Laxminarayana, K. *A review of atomic force microscopy imaging systems: Application to molecular metrology and biological sciences* 2004.
148. Sauer, B. B., Kampert, W. G., McLean, R. S. & Carcia, P. F. TMDSC and atomic force microscopy studies of morphology and recrystallization in polyesters including oriented films. *Journal of Thermal Analysis and Calorimetry* **59**, 227–243 (2000).
149. Sakamoto, H., Asakawa, H., Fukuma, T., Fujita, S. & Suye, S.-i. Atomic force microscopy visualization of hard segment alignment in stretched polyurethane nanofibers prepared by electrospinning. *Science and Technology of Advanced Materials* **15**, 015008 (2014).

150. Schön, P. *et al.* Quantitative mapping of elastic moduli at the nanoscale in phase separated polyurethanes by AFM. *European Polymer Journal* **47**, 692–698 (2011).
151. Tocha, E., Janik, H., Dębowski, M. & Vancso, G. J. Morphology of polyurethanes revisited by complementary AFM and TEM. *Journal of Macromolecular Science - Physics* **41 B**, 1291–1304 (2002).
152. Pickering, J. P. & Vancso, G. J. Apparent contrast reversal in tapping mode atomic force microscope images on films of polystyrene-*b*-polyisoprene-*b*-polystyrene. *Polymer Bulletin* **40**, 549–554 (1998).
153. O’Dea, J. R. & Buratto, S. K. Phase imaging of proton exchange membranes under attractive and repulsive Tip-sample interaction forces. *Journal of Physical Chemistry B* **115**, 1014–1020 (2011).
154. Wang, Y., Song, R., Li, Y. & Shen, J. Understanding tapping-mode atomic force microscopy data on the surface of soft block copolymers. *Surface Science* **530**, 136–148 (2003).
155. Hashimoto, T., Koizumi, S., Hasegawa, H., Izumitani, T. & Hyde, S. T. Observation of “Mesh” and “Strut” Structures in Block Copolymer/Homopolymer Mixtures. *Macromolecules* **25**, 1433–1439 (1992).
156. McLean, R. S. & Sauer, B. B. Tapping-mode AFM studies using phase detection for resolution of nanophases in segmented polyurethanes and other block copolymers. *Macromolecules* **30**, 8314–8317 (1997).
157. Skinner, L. M. & Sambles, J. R. Vapour pressure over curved surfaces—the Kelvin equation. *Contemporary Physics* **12**, 575–593 (1971).
158. Patra, A. in *Quantifying Interactions of Biomolecules with Inorganic Surfaces* 27–40 (Springer International Publishing, Cham, 2017).
159. Seil, J. T. & Webster, T. J. Decreased astroglial cell adhesion and proliferation on zinc oxide nanoparticle polyurethane composites. *International Journal of Nanomedicine* **3**, 523–531 (2008).
160. Campo, M. L. in *Apoptosis: Involvement of Oxidative Stress and Intracellular Ca²⁺ Homeostasi* 17–55 (Springer Netherlands, Dordrecht, 2007).

161. Huber, K. L. & Hardy, J. A. Mechanism of zinc-mediated inhibition of caspase-9. *Protein Science* **21**, 1056–1065 (2012).
162. Christ, K. V. & Turner, K. T. Methods to Measure the Strength of Cell Adhesion to Substrates. *Journal of Adhesion Science and Technology* **24**, 2027–2058 (2010).
163. Zhan, J. S. *et al.* Astrocytes in Migration. *Neurochemical Research* **42**, 272–282 (2017).
164. Fujita, S., Ohshima, M. & Iwata, H. Time-lapse observation of cell alignment on nanogrooved patterns. *Journal of the Royal Society Interface* **6** (2009).
165. PHE Culture Collections https://www.phe-culturecollections.org.uk/products/celllines/generalcell/detail.jsp?refId=08061901%7B%5C%7Dcollection=ecacc%7B%5C_%7Dgc.
166. Chu, L., Tempelman, L. A., Miller, C. & Hammer, D. A. Centrifugation Assay of IgE-Mediated Cell Adhesion to Antigen-Coated Gels. *AIChE Journal* **40**, 692–70 (1994).
167. Schlie, S., Gruene, M., Dittmar, H. & Chichkov, B. N. Dynamics of Cell Attachment: Adhesion Time and Force. *Tissue Engineering Part C: Methods* **18**, 688–696 (2012).
168. Gutierrez-Murgas, Y. & Snowden, J. N. Ventricular shunt infections: Immunopathogenesis and clinical management. **276**, 1–8 (2014).
169. Tong, S. Y. C., Davis, J. S., Eichenberger, E., Holland, T. L. & Fowler, V. G. Staphylococcus aureus infections: epidemiology, pathophysiology, clinical manifestations, and management. *Clinical microbiology reviews* **28**, 603–61 (2015).

APPENDIX

A.1 TIME LAPSE IMAGES OF CELL POPULATIONS

In this Appendix, time lapse images detailing the motion tracking of multiple cell cultivated on different surfaces are presented. This discussion is not of primary relevance to the main body of the thesis, but is included here because it contains data linked to the time lapse images of individual cells presented in Section 4.3 (Fig. 4.12).

A.1.1 *Methods*

To quantify cell motility, cells were seeded on modified glass coverslips. Materials were electrospun directly on glass coverslips, so to cover the glass with the desired material: unmodified Z6A1 electrospun polyurethane, Ti and Zn-modified electrospun polyurethane. Each coverslip was secured at the bottom of a petri dish with double sided tape (Transparent double sided plastic tape, Tesa, Germany), thickness 205 μm . Besides, a round sample of cast Z6A1 polyurethane was cut and secured, as well as a round sample of PDMS. Each plate was sterilised by exposure to UV light for 20 min (Daro UV Systems Ltd UK).

Human glioblastoma astrocytoma cells U373 MG were suspended in Hepes-enriched medium (EMDM). Hepes is a buffer that counteracts the acidisation of the medium due to cellular respiration cycle. Cells were seeded at an initial concentration of 20 000 cell/cm^2 , or 6400 cells/well. Cells were incubated for 1 hr at 37 °C, 5% CO_2 , so they could fall to the bottom of the petri dish and adhere lightly. After one hour, each petri dish was retrieved from the incubator and brought under the microscope. In order to maintain the petri dish at a constant temperature, a heated stage set at 37 °C was used. The stage was covered with a small aluminium foil dome to create a chamber

around the sample and isolate it thermally. To limit water evaporation from the petri dish, each dish was wrapped in parafilm.

Time lapse videos were taken with a fluorescence microscope (Zeiss Axiovision Imager Z1, Karl Zeiss Microscopy GmbH, Germany) for at least 20 h, magnification $\times 10$, a picture every 15 minutes.

Images were exported as videos and uploaded on an university driver. They are available at <https://tinyurl.com/yyg5unjb>.

The barycentre of selected cells was tracked via the Manual Tracking plugin of Fiji software (version 2.0.0-rc-69/1.52n).

A.1.2 *Results and discussion*

Cell paths were tracked manually and their individual position in consecutive frames was plotted as single dots and reported in Figure A.1.

Cells growing on nanopatterned surfaces (cast and electrospun) move purposefully and following morphological cues provided by the interconnecting fibres, as evidenced by the long strikes showed in Figure A.1. Cells exhibit rear/front polarity. Growth cones and protrusions are developed, explore the environment, grip on fibres and move in a precise direction, pulling the cell body along.

On TCP, cells do not move directionally, but tend to gravitate around a centre, rather than pursuing a direction. On PDMS, cells do move along the surface, but the movement seems less governed by the surface, as cells continue advancing in the same direction.

As discussed in Section 4.4, micro- and nano-patterned surfaces are more conducive to motility than flat surfaces. Electrospun substrates mimic the fibrous structure of extracellular matrix and offers the cells contact guidance, as opposed to flat surfaces. Furthermore, the distribution of charges, metallic ions and functional groups on the surface of electrospun fibres may interact with cells and influence their adhesion and movements.

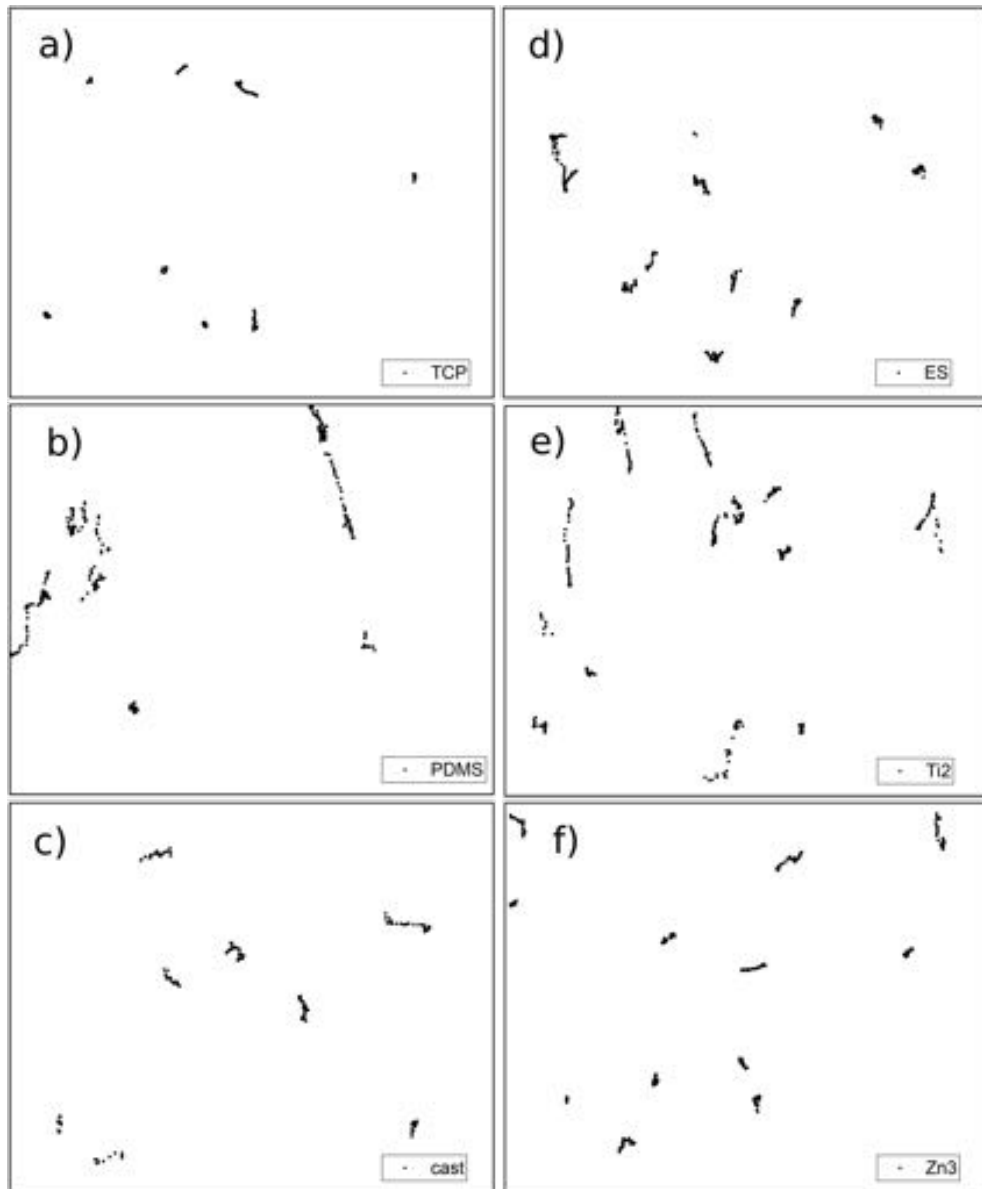


Figure A.1: Paths of cells moving on TCP (a), PDMS (b), cast polyurethane (c), ES (d), Ti2 (e) and Zn3 (f), as tracked with Fiji/Manual Tracking software on videos of multiple cells, magnification $\times 10$, sampling frequency=15 minutes over 20 hours.

A.2 ENERGY DISPERSION SPECTROSCOPY

Additional Energy Dispersion Spectrograms are reported in Figure A.2.

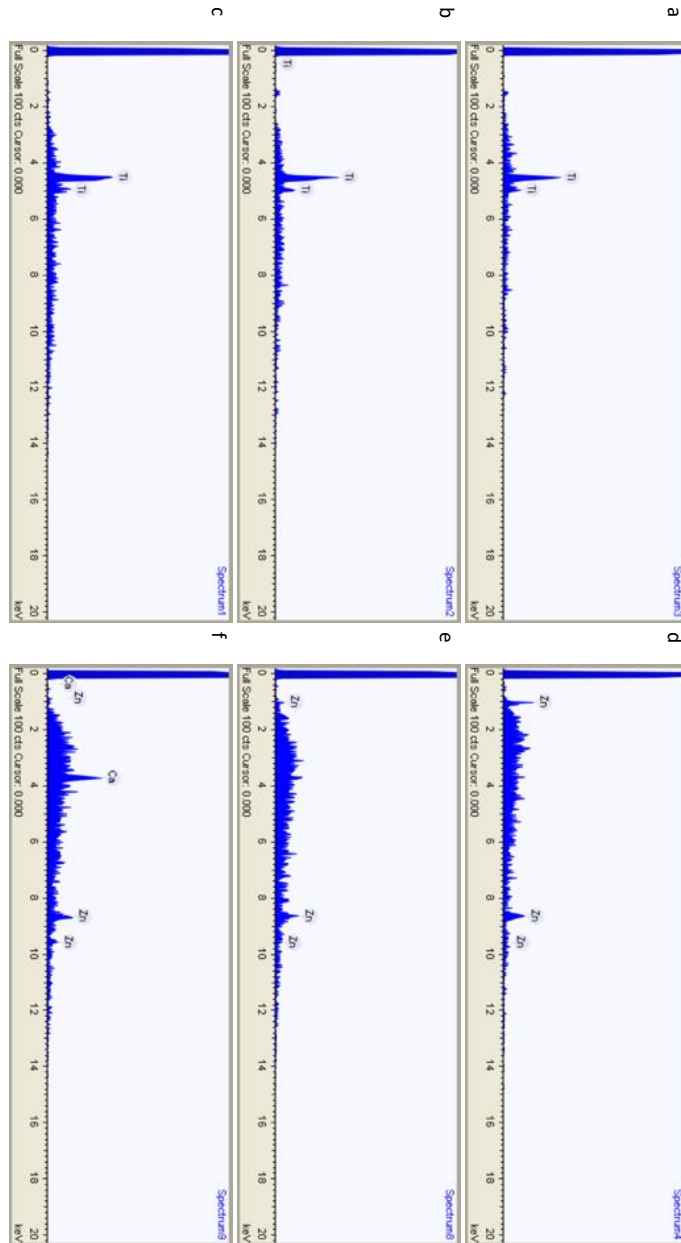
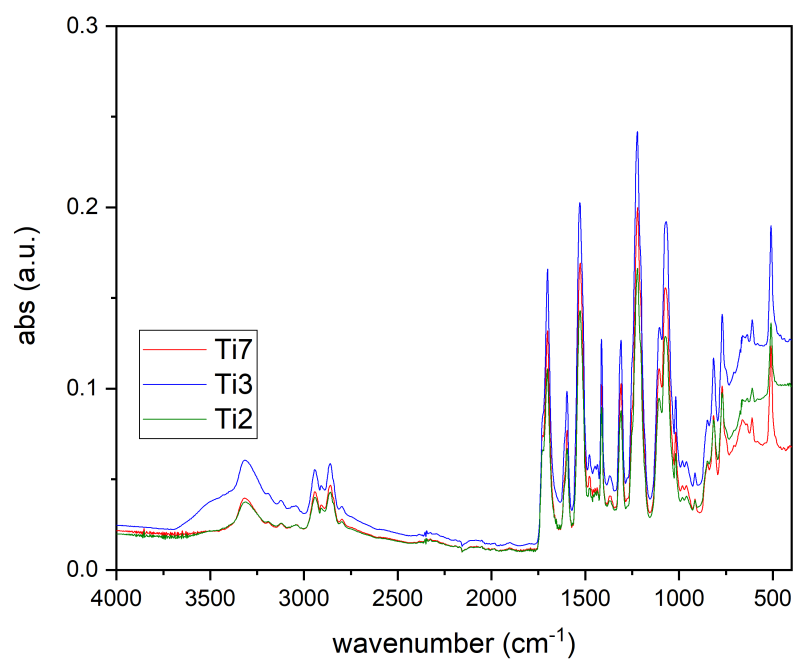


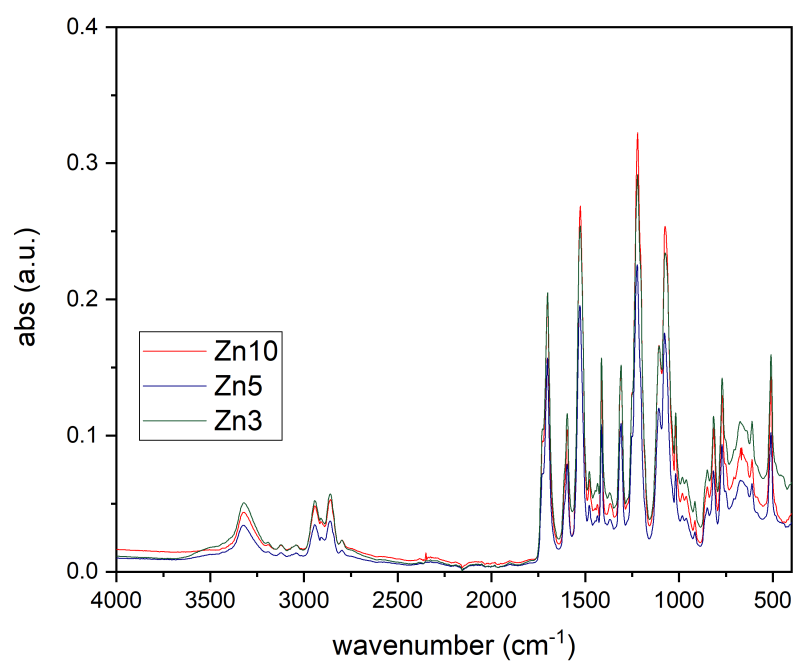
Figure A.2: Energy Dispersion Spectrogram for titanium and zinc-modified electrospun mats, representing Ti₂ and Zn₃. a) Ti₂, b) Ti₃, c) Ti₇, d) Zn₃, e) Zn₅, f) Zn₁₀. The elemental peaks for Ti and Zn, respectively, are indicated.

A.3 FT-IR

Additional FT-IR Spectrograms are reported in Figure A.3.



(a) Ti-modified samples.

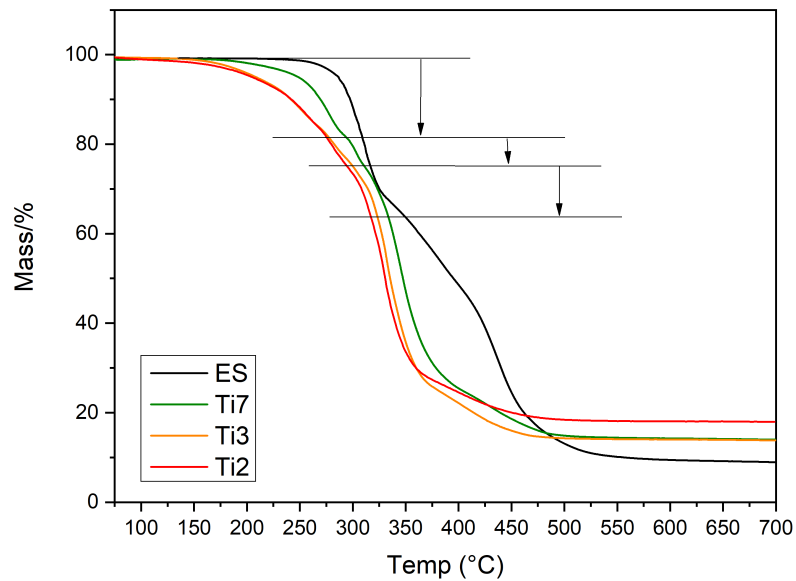


(b) Zn-modified samples.

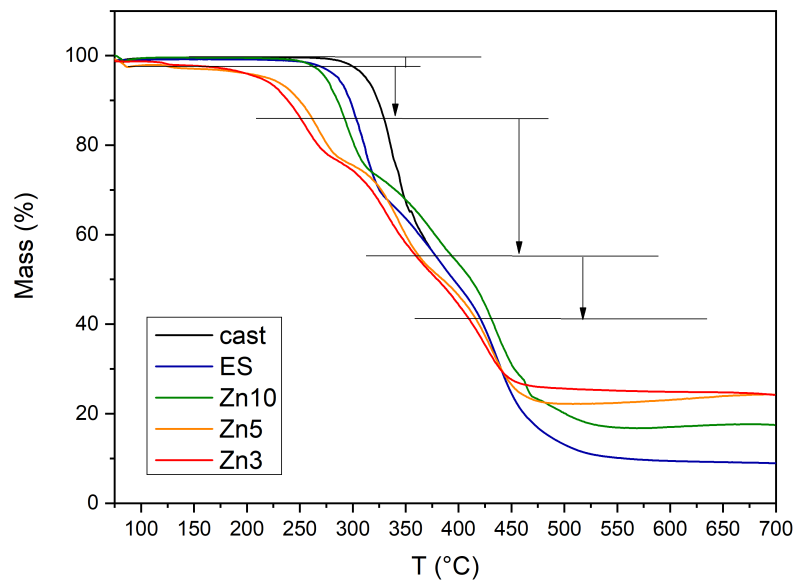
Figure A.3: Additional Absorbance ATR-IR spectrograms of Ti2 and Zn3 modified samples taken in the 4000 cm⁻¹ to 400 cm⁻¹ region.

A.4 THERMOGRAVIMETRIC ANALYSIS

Thermogravimetric curves are reported in Figure A.4.



(a) Ti-modified samples.



(b) Zn-modified samples.

Figure A.4: TGA thermograms for electrospun materials modified a) with Ti, b) with Zn, against the unmodified samples ES.